**UNIVERSITAT POLITÈCNICA DE CATALUNYA**
BARCELONATECH

**Department of Civil and Environmental Engineering**
Division of Geotechnical Engineering and Geosciences

Tesi per compendi de publicacions – Thesis by publications

# Modelling fragmentation in rockfalls

*PhD Thesis*

**Gerard Matas Casado**

*Supervisors:*   *Nieves Lantada*
*Jordi Corominas*

Barcelona, September 2020

**UNIVERSITAT POLITÈCNICA DE CATALUNYA**

**School of Civil Engineering of Barcelona**
UPC BARCELONATECH

# Abstract

The fragmentation process in rockfalls is a complex phenomenon that is not well understood and only a few rockfall simulation models consider it explicitly. Fragmentation significantly affects the evaluation of the hazard and therefore of the risk. This thesis aims to develop a rockfall propagation model that is capable of reproducing the fragmentation phenomenon in rockfalls and to assess its consequences in the risk analysis. Four real-scale tests in a quarry and one laboratory test were performed for a better understanding of the fragmentation process. During these tests, several remote sensing techniques were used to capture the motion of the blocks and the fragment size distributions of the resulting deposit. The analysis of the empirical data acquired confirmed that the mass distribution produced by the fragmentation of a single block can be adequately described using fractal theory. Moreover, it was observed that the envelope of the trajectories of the newly generated fragments adopted the shape of a cone.

The knowledge gathered with these experiments led to the development of RockGIS, a stochastic program based on a lumped mass approach for the numerical simulation of rockfalls and their fragmentation using a fractal model. The model simulates the trajectories of the blocks using state-of-the-art methodologies and implements an innovative fragmentation module to consider block breakage using fractal theory. The code was developed within the framework of the Rockmodels project (https://rockmodels.upc.edu). In the simulation, the parameters that define the sizes of the fragments generated are computed at each impact according to the kinematic conditions. This approach allows different fragmentation patterns to be reproduced depending on the energy conditions of the impacts.

The performance of the RockGIS code was verified and validated by the real-scale rockfall tests carried out and by reconstructing three inventoried natural rockfall events that took place in Spain: a 10,000 $m^3$ rockfall near Vilanova de Banat (Eastern Pyrenees) in 2011, a 800 $m^3$ rockfall in Monasterio de Piedra in 2017 (Zaragoza) and a 10 $m^3$ rockfall on the Ma-10 road (Mallorca). For the calibration of the model different goodness-of-fit indicators were considered depending on the information available in each case study. Two main calibration criteria were used: the runout distance and the size distributions of all the fragments generated. Moreover, the fragment scattering along the slope, the number of blocks crossing a reference line, the position of the center of gravity of the whole deposit and other criteria were used in some scenarios to validate the simulation results. The parametric analysis showed that the model is highly sensitive to the parameters that control the fragmentation process.

The performance of the fragmentation model developed is satisfactory and accomplishes the goal of representing the fragmentation process, as it is able to reproduce the field observations accurately. To use this approach for risk analysis and the design of protective measures, precise calibration is required to ensure the parameters are appropriate for each case study considered. Regarding the risk analysis, fragmentation has both a significant and a contrasting effect on the risk value and should not be ignored. The most significant effect is on the rockfall runout distance. Fragmentation may significantly reduce rockfall propagation if the slope is sufficiently gentle and long. In this case, the new fragments generated mobilize less energy and can be trapped by the topographic irregularities, obstacles and protection works. Conversely, a wide range of block sizes are able to reach corridors running below steep slopes. In such a situation, fragmentation facilitates the divergence of the blocks' trajectories, which increases the probability of impact on people and vehicles and consequently the risk.

# Resum

La fragmentació en despreniments rocosos és un fenomen complex, poc comprès i només alguns models de simulació de caigudes de roques la consideren explícitament. La fragmentació afecta l'avaluació del perill i conseqüentment l'avaluació del risc. L'objectiu d'aquesta tesi és desenvolupar un model de propagació de despreniments rocosos capaç de reproduir la fragmentació i avaluar les conseqüències de considerar-la en l'anàlisi del risc. Per millorar la comprensió del fenomen, s'han realitzat quatre assajos a escala real i un assaig al laboratori. L'anàlisi de les dades experimentals adquirides confirma que la distribució de volums produïda per un procés de fragmentació d'un bloc es pot descriure adequadament mitjançant la teoria del fractal. A més, han permès confirmar la hipòtesi que les trajectòries dels fragments que resulten de la fragmentació d'un bloc es mantenen dins d'un límit en forma de con.

El coneixement recollit en aquestes campanyes experimentals ha permès el desenvolupament de RockGIS, un programa estocàstic basat en una aproximació puntual de la massa per a la simulació numèrica de despreniments rocosos i la fragmentació mitjançant un model fractal. El model simula les trajectòries dels blocs basant-se en les metodologies més recents i implementa un mòdul de fragmentació innovador que contempla la ruptura dels blocs gràcies a un model de fragmentació fractal desenvolupat en el marc del projecte Rockmodels (https://rockmodels.upc.edu). Segons les condicions cinemàtiques, a cada impacte es calculen els paràmetres del model de fragmentació que defineixen els volums dels nous fragments. Aquest enfocament permet reproduir diferents escenaris de fraccionament en funció de les condicions energètiques dels impactes.

El funcionament del codi RockGIS ha estat verificat i validat per mitjà d'assajos a escala real i segons tres despreniments rocosos naturals inventariats que han tingut lloc a Espanya: un despreniment de 10.000 $m^3$ a prop del poble de Vilanova de Banat (Pirineus orientals) el 2011, una caiguda de 800 $m^3$ a Monasterio de Piedra el 2017 (Saragossa) i una caiguda de roca de 10 $m^3$ a la carretera Ma-10 (Mallorca). Per calibrar el model es van considerar diferents indicadors de bondat d'ajust segons les dades disponibles en cada cas d'estudi. Es van utilitzar dos criteris principals de calibratge: l'abast, o distància recorreguda, dels fragments generats i la distribució de volums. A més, en alguns dels escenaris estudiats es van considerar criteris addicionals de calibratge com ara la dispersió lateral dels fragments al llarg del vessant, el nombre de fragments que traspassaven una línia de referència, la posició del centre de gravetat de tot el dipòsit, etc.

Els resultats del model desenvolupat són satisfactoris i compleixen amb l'objectiu de representar la fragmentació en els despreniments rocosos, ja que és capaç de reproduir les observacions de camp de manera precisa. Per emprar la metodologia proposada en l'estimació del risc i el disseny de mesures de protecció, cal un calibratge precís per tal de garantir que els paràmetres seran adequats a cada cas d'estudi considerat. Pel que fa a l'anàlisi del risc, la fragmentació té un efecte significatiu i contrastat sobre el valor del risc i no s'ha d'ignorar. Principalment afecta al càlcul de l'abast màxim dels blocs. La fragmentació pot reduir significativament la propagació dels despreniments si el pendent és prou suau i llarg. En aquest cas, els nous fragments generats mobilitzen menys energia i poden quedar atrapats per les irregularitats topogràfiques, els obstacles i les obres de protecció. Per contra, una àmplia gamma de mides de blocs poden arribar als elements exposats que es troben sota de vessants amb inclinacions altes. En aquests casos, la fragmentació facilita la divergència de les trajectòries de blocs, cosa que augmenta la probabilitat d'impacte amb els elements exposats i el risc conseqüent.

# Resumen

La fragmentación en desprendimientos rocosos es un fenómeno complejo, poco comprendido y sólo algunos modelos de simulación de caídas de rocas la consideran explícitamente. La fragmentación afecta la evaluación del peligro, y consecuentemente la evaluación del riesgo. El objetivo de la presente tesis es desarrollar un modelo de propagación de desprendimientos rocosos capaz de reproducir la fragmentación y evaluar las consecuencias de considerarla en el análisis del riesgo. Para mejorar la comprensión del fenómeno, se realizaron cuatro ensayos a escala real y un ensayo en el laboratorio. El análisis de los datos experimentales adquiridas confirma que la distribución de volúmenes producida por un proceso de fragmentación de un bloque se puede describir adecuadamente mediante la teoría del fractal. Además, han permitido confirmar la hipótesis de que las trayectorias de los fragmentos resultantes de la fragmentación de un bloque se mantienen dentro de un límite en forma de cono.

El conocimiento recogido en estas campañas experimentales ha permitido el desarrollo de Rock-GIS, un programa estocástico basado en una aproximación puntual de la masa para la simulación numérica de desprendimientos rocosos y su fragmentación mediante un modelo fractal. El modelo simula las trayectorias de los bloques basándose en las metodologías más recientes e implementa un módulo de fragmentación innovador que contempla la ruptura de los bloques gracias a un modelo de fragmentación fractal desarrollado en el marco del proyecto Rockmodels (https://rockmodels.upc.edu). Los parámetros del modelo de fragmentación que definen los volúmenes de los fragmentos generados utilizados en la simulación, se calculan en cada impacto según las condiciones cinemáticas. Este enfoque permite reproducir diferentes escenarios de fragmentación en función de las condiciones energéticas de los impactos.

El funcionamiento del código RockGIS ha sido verificado y validado mediante ensayos a escala real y según tres desprendimientos rocosos naturales inventariados que han tenido lugar en España: uno de 10.000 $m^3$ cerca de Vilanova de Banat (Pirineos orientales) el 2011, uno de 800 $m^3$ en Monasterio de Piedra en 2017 (Zaragoza) y uno de 10 $m^3$ en la carretera Ma-10 (Mallorca). Para calibrar el modelo se consideraron diferentes indicadores de bondad de ajuste según los datos disponibles en cada caso de estudio. Se utilizaron dos criterios principales de calibración: el alcance, o distancia recorrida, de los fragmentos generados y su distribución de volúmenes. Además, en algunos casos se usaron criterios adicionales de calibración como la dispersión lateral de los fragmentos a lo largo de la vertiente, el número de fragmentos que traspasaban una línea de referencia, la posición del centro de gravedad de todo el depósito etc.

Los resultados del modelo desarrollado son satisfactorios y cumplen con el objetivo de representar la fragmentación en los desprendimientos rocosos, ya que es capaz de reproducir las observaciones de campo de manera precisa. Para emplear la metodología propuesta en la estimación del riesgo y el diseño de medidas de protección, se requiere una calibración precisa para garantizar que los parámetros son adecuados a cada caso de estudio considerado. En cuanto al análisis del riesgo, la fragmentación tiene un efecto significativo y contrastado sobre el valor del riesgo y no se debe obviar. Principalmente afecta al cálculo del alcance máximo de los bloques. La fragmentación puede reducir significativamente la propagación de los desprendimientos si la pendiente es bastante suave y largo. En este caso, los nuevos fragmentos generados movilizan menos energía y pueden quedar atrapados por las irregularidades topográficas, los obstáculos y las obras de protección. Por el contrario, una amplia gama de tamaños de bloques pueden llegar a los elementos expuestos que se encuentran debajo de laderas con inclinaciones altas. En estos casos, la fragmentación facilita la divergencia de las trayectorias de bloques, aumentando así la probabilidad de impacto con los elementos expuestos y el consecuente riesgo.

# Acknowledgements - Agraïments

Tinc la tesi escrita, el dia està preciós des de la finestra de la meva habitació i em toca mirar enrere per entendre com he arribat aquí. I el primer que em ve al cap és la meva mare Pilar. Quan parlem de què faré a partir d'ara, em diu, com sempre i amb seguretat que podré fer el que vulgui a la vida. I sé que és perquè ella se n'ha cuidat bé que així sigui. Des d'ensenyar-me a córrer i saltar per competir a les olimpíades de l'escola a mig obligar-me a estudiar anglès des de ben petit. L'espai de creixement personal que m'has procurat durant tots aquests anys m'ha permès créixer amb llibertat i amor. Gràcies mama, t'estimo. També m'estimo un munt al meu germà Adrià, amb qui hem tingut algunes èpoques de més o menys proximitat, però de qui la seva confiança en mi ha mantingut sempre la meva autoestima alta. Jo confio en tu i sé que també podràs fer el que vulguis. També han estat importantíssims per mi els meus tiets i cosins, us estimo. I en Joan, que ha estat un referent important per mi, i que sempre s'ha cuidat que no oblidi el que em diu la mama, que puc fer el que vulgui, t'estimo. I la Boira, que en els últims anys m'ha acompanyat a passejar per les muntanyes, és una gosseta preciosa, amor pur.

Als 18 anys tocava triar i m'agradava l'enginyeria, i entre les que m'agradaven la de camins va ser la que més em va cridar més l'atenció. El quart any de carrera va ser molt intens però sempre vaig trobar forats per anar a escalar amb en Salva i/o la Maria. El material d'escalada és car i per començar a sentir-me econòmicament independent vaig decidir aplicar a les beques de suport a la docència, en concret per ser becari de Topografia. L'assignatura m'havia agradat molt, tant que fins i tot un diumenge amb l'Helena i la Luisa vam anar a repetir una anivellació amb un equip molt rústic de l'avi de l'Helena perquè no ens donaven prou bé els tancaments. La Nieves i la Carol em van fer l'entrevista i em van acabar triant a mi. L'any següent quan em va tocar fer el projecte i la tesina de final de carrera, el Josep i la Nieves em van parlar d'un projecte de recerca per al qual havien demanat finançament relacionat amb els despreniments rocosos. Em va semblar tan interessant que hi vaig dedicar els dos treballs.

Per continuar amb la recerca i demanar una beca predoctoral, juntament amb la Cristina, vam haver de córrer a acabar el projecte, i fins i tot el cap d'estudis va entendre la nostra situació i ens va preparar un tribunal especial perquè poguéssim tenir el títol a temps per la convocatòria. Amb la seva companyia vaig gaudir d'aquell esprint per un objectiu comú. No les vam aconseguir cap dels dos, ens van valorar molt malament els plans de recerca (que realment no havíem tingut temps de preparar bé). Vaig treballar tres mesos en una empresa de túnels en practiques però no em va convèncer i ho vaig deixar tot i que volien que em quedes. I al cap d'un o dos mesos de no saber ben bé que fer em va trucar la Nieves explicant-me que els havien concedit definitivament el projecte i que tenia associada una beca FPI. Vaig aplicar i vaig guanyar-la. La meva bona amiga Maria Sevilla, que ja era doctoranda des de feia un any aleshores, em va escriure al dors de la convocatòria de la beca la frase *"Te'n penediràs, muà!"* que vaig tenir present en alguns moments baixos. La Cristina també va aconseguir una beca predoctoral més tard, que lamentablement no va poder gaudir. Comença la tesi doctoral. A partir d'aquest moment, el suport en diferents àmbits de moltes persones ha fet possible la materialització d'aquest treball. I dit això, que potser serà el més semblant a un diari que deixaré per la posteritat, passo als agraïments personals:

Les persones més importants en la realització d'aquest treball han estat, sense dubte, els meus tutors la Nieves Lantada i en Jordi Corominas. Nieves, t'agraeixo moltíssim que m'hagis guiat en aquest procés de doctorar-me, l'ajuda que m'has brindat sempre que ho he necessitat, el suport emocional i la teva altíssima capacitat resolutiva quan a mi m'han mancat forces. A més, el nivell de rigorositat científic d'aquesta tesi no hagués estat pas el mateix sense tu. Jordi, t'agraeixo moltíssim la paciència que has tingut ordenant les meves idees disperses a l'hora de conceptualitzar mètodes, preparar articles i escriure conclusions i la confiança que has dipositat en les meves iniciatives i la meva feina. També valoro molt l'acompanyament durant els meus primers passos en el món de la recerca als congressos on vam coincidir a l'inici. De la mà dels dos m'he submergit en el món de la recerca, del qual tinc algunes crítiques profundes a nivell estructural, però que he gaudit durant aquests anys anant amunt i avall per les muntanyes i llençant rocs amb maquinaria pesada (i moltes hores de programar). Sense la vostra qualitat humana no hauria passat del primer any. Gràcies de tot cor.

En Josep Gili va començar sent tutor de la tesi però per raons burocràtiques només van poder ser dos tutors. Això no ha impedit però que seguís aconsellant-me i guiant-me durant el desenvolupament d'aquesta tesi. T'agraeixo molt que t'hagis cuidat que la meva investigació no virés cap al determinisme extrem, quasi diví, que de ben segur m'hagués portat a culs de sac considerant l'estocasticitat del fenomen d'estudi.

El meu camí hagués estat molt diferent si en Roger Ruiz no hagués passat abans per aplanar-lo. Has estat un referent per a mi i t'agraeixo molt com m'has cuidat tant a nivell personal com acadèmic, donant-me consell i opinió per desenvolupar el codi de simulació, redactar articles, preparar les campanyes experimentals, etc. Estic segur que seguirem compartint coses. Us desitjo el millor per a tu, l'Aina i en Quim!

Agraeix l'esforç i la col·laboració de tot l'equip de treball dels projectes RockRisk i Rock-Models en les diferents campanyes experimentals que s'han realitzat i usat per desenvolupar aquest treball i pel suport emocional: Jordi Corominas, Nieves Lantada, Felipe Buill, Josep A. Gili, Joan Martínez, José Moya, Mª Amparo Núñez, Albert Prades, Càrol Puig, Antonio Abellán, Olga Mavrouli, Raúl Oorthuis, Roger Ruíz i Lluís Saló. Valoro molt el suport a nivell de programació computacional que m'ha donat l'Albert Prades i que ha fet que programar no fos tant solitari. També als companys de despatx Marcel Hürlimann i Clara Alvarado per ajudar-me, assessorar-me i pressionar-me per publicar articles. Una abraçada a tots!

Gràcies als companys de doctorat: Ferran, Gaia, Riccardo, Ningning, Arisleidy, Lu, Celia, Miquel i Raúl per compartir alegries, patiments i una preciosa amistat durant aquests anys. Us desitjo molta sort als que ja us heu doctorat i molts ànims als que esteu acabant. Us estimo!

Vull agrair també als professors Maribel Ortego i Juanjo Egozcue la seva assessoria en matèria de tractament estadístic i anàlisis de bondat d'ajust de les dades una tarda des de la terrassa del C2. Em vau desencallar en un moment crític per tirar endavant l'últim article del compendi.

Je suis très reconnaissant de l'attention que Franck Bourrier m'a portée lors de mon séjour de recherche à Grenoble, ainsi que du bon accueil que j'ai eu de la part de tous les chercheurs et doctorants du centre IRSTEA. Je prends un très bon ami, Vivien, avec qui continuer à faire des projets de montagne.

Agraeixo a Canteras Hermanos Foj i a Canteras la Ponderosa haver facilitat la realització dels assajos de caiguda de blocs a escala real. També agraeixo al Laboratori de Tecnologia d'Estructures i Materials "Lluís Agulló" i al seu personal haver facilitat i ajudat en la realització de l'assaig de comminució.

Durant aquests anys he cotutelat diversos treballs de final de grau i màster i agraeixo a totes les ara ex-estudiantes la seva feina: Miguel Ángel Sánchez, Francesc Rich, Òscar Nabot, Albert Ramon i en especial a l'Ester Parras per la bona feina feta en l'assaig de comminució. En alguns moments d'estancament, dedicar temps als vostres treballs m'ha fet recuperar energia i tenir noves idees per continuar.

L'Ariadna ja em va conèixer com a doctorand i ha vist totes les fases per les quals he passat i sempre les ha portat amb molt optimisme i serenor. Hem tingut un temps preciós junts, estic agraït per cada moment i, tot i que els nostres projectes vitals no hagin convergit, ets una persona meravellosa i m'agradarà seguir al teu costat de la manera que vulguis. Potser ballant? T'estimo :)

Els meus amics i companys de casa en l'última etapa del doctorat, la Mireia i en Pere, m'han cuidat un munt i han estat molt comprensius amb les meves fluctuacions anímiques durant aquest temps. A més, us heu preocupat perquè mantingues un mínim de socialització i us ho agraeixo moltíssim. I l'Anna i en Guillem, que també m'han cuidat molt, gracies bonics. Tots quatre sou unes persones maquíssimes, us estimo molt i estic segur que, sigui on sigui, independentment de la casa, els metres quadrats i les teulades caigudes, el nostre projecte serà xulíssim.

Gràcies als amics i veïns de Baix Pallars que m'han acollit amb els braços oberts aquest últim any de tesi.

# Contents

# Chapter 1

# Introduction

Rockfalls are rapid mass movements generated by the detachment of a rock volume from a slope. They often threaten civil infrastructures, buildings and transportation networks in mountainous regions. These phenomena have great destructive potential due to the high speed and, consequently, the high kinetic energy the rockfall can reach during its propagation.

During the last few years some important accidents due to rockfalls occurred in Spain, some of them causing fatalities. A major rockfall trapped a car in the LV-9124 road on April 2018 producing the death of the two occupants of the vehicle. In 2002 another rockfall affected the same road and in May 2020, the access to the villages of Burgo and Llavorre was closed. A person lost her life in June 2018 while driving along the C-16 road when a rock fragment broke through the roof of his vehicle and impacted her. Another person was killed in a beach in Mallorca when a huge rock detached from the cliff behind the sand on July 2019; 8 people were rescued by the sea in June 2020 as the access to Porto Pi beach in Tossa de Mar was blocked. In the lucky cases where no fatalities occur, the economic consequences of rockfalls can be significant. For example, a major rockfall occurred in CV-428 road near Cortes de Pallás affecting a hydroelectric power station and isolating the village. In December 2019 a rockfall blocked C-13 road between Rialp and Llavorsi. The access to the to the ski resorts was closed for several days. Economical losses in the region were significant as it was high season and the event forced locals to take a 2.5hr detour. Similarly, the C-242 road, which is one of the accesses to Cornudella de Montsant, was closed for three months. The frequency of these events could be increased during the next decades due to climate change (Palomo, 2017) even some authors have found no correlation between warming and rockfall frequency in their countries (Sass and Oberlechner, 2012).

Researchers have developed methodologies to predict, control and mitigate rockfall risk. These methodologies allow to estimate rockfall susceptible areas and the potential runout or maximum reach of the events both using empirical indexes or computer numerical simulations (Dorren and Seijmonsbergen, 2003b). Extensive studies have also been carried out to design mitigation infrastructures and to evaluate the forest contribution as a natural protection. However, until present, few researchers had paid attention to fragmentation of rockfalls during their propagation. In some of the cited cases presented before, fragmentation took an important role on the development of the events. Moreover, rockfall inventories previously collected by our research group (https://rockmodels.upc.edu/en/work-

team) suggested that fragmentation can modify significantly the final behavior of a rockfall (Corominas et al., 2012).

At this point, the main research question was: How does the fragmentation influence rockfall propagation? Fragmentation in rockfalls causes the size reduction of the moving blocks and consequently, the reduction of the kinetic energy of each of the fragments. However, it increases the impacting probability since the number of moving blocks increases. Also the total runout may be affected depending on the topographical conditions since the different block sizes interact in a different way with the ground surface and due to the divergence of the trajectories. All these features generate contrasting effects on the resulting risk value, and thus no direct answer to this question can be given.

This thesis aimed at the understanding of the fragmentation phenomena during rockfalls in order to introduce it in the modelling rockfall propagation. To achieve that, it was decided to follow this work plan: first, to carry out some experimental campaigns including real scale and laboratory tests; and then, to develop a rockfall propagation simulator that incorporates the processes and parameters observed in the field. This tool will allow to model the complete process of risk quantification in fragmental rockfalls.

## 1.1 Thesis objectives

The main goal of this thesis is to increase the understanding of fragmentation in rockfalls and its modelling during propagation. This thesis has three specific objectives:

1. Develop a methodology for the consideration of fragmentation in rockfall propagation simulations.

2. Develop, implement and validate a 3D rockfall propagation code able to consider block fragmentation.

3. Calibrate and validate of the developed code and the fragmentation model.

4. Integrate the consideration of fragmentation in the rockfall quantitative risk assessment method.

Fragmentation is still a very poorly understood phenomena (Giacomini et al., 2009) and few empirical data has been gathered by scientist. To improve the knowledge of the phenomena, the development of testing methodologies at both real and laboratory scales and for inventorying real scale cases is required. Data gathered during the realization of these campaigns will also be used for the calibration and validation of the developed code.

## 1.2 Framework of this thesis

This thesis has been carried out within the framework of the research project entitled "Rockfalls in cliffs: risk quantification and its prevention" with acronym Rockrisk (2014-2016, ref. BIA2013-42582-P,), and funded by the Spanish Ministry of Economy and

Competitiveness (MINECO), and a FPI grant from the MINECO (2015-2018,.ref. BES-2014-069795). The aim of RockRisk project was the quantification of risk induced by rockfalls and providing tools to improve its prevention and protection in case of occurrence and mitigation of its effects. To reach the main goal these three objectives where proposed: 1) definition of potential volumes of breakage in rocky slopes, 2) determining fragmentation of rock masses and their integration into propagation analysis and 3) Rockfall quantitative risk assessment. The content of the present research focus on the second objective.

During the development of the project, several natural rockfall events where inventoried and real scale fragmentation tests were performed in quarries. This knowledge allowed the formulation of a rockfall fractal fragmentation model. The rockfall propagation code considering fragmentation, RockGIS, was developed by the author of this thesis and tested in several real scenarios. However, during the development of the project several other research questions outcropped regarding the data capture process both in natural events and in real scale test. Moreover, the developed tools gave room for improvement through more testing in real cases.

To keep on with these research lines a new project entitled "Characterization and modeling of rockfalls" with acronym Rockmodels (2017-2020, with ref. BIA2016-75668-P, AEI/FEDER,UE) was funded by the Spanish Ministry of Economy and Competitiveness. In this project the three main objectives were: 1) Explicit identification of unstable rock volumes and stability assessment, 2) Validation of the fragmentation model, and 3) Analysis of the propagation and set-up of the RockGIS model. Additionally, and with the experience of the real scale testing campaigns performed during the first research project, this project aimed at the development of a code for the capture of kinematic parameters of the falling of blocks and their fragmentation in the trials of launching of blocks recorded by high-speed video cameras. The obtained kinematic parameters were used as a database for the Fragmentation Fractal Model and the RockGIS model. Also a semi-automatic procedure would be proposed to obtain the spatial distribution of the roughness and the calculation of fragments volumes. This last aspect seeks to find an alternative to the manual procedures to obtain the rock block size distribution (RBSD) at the base of the cliffs that require a long, tedious and often dangerous work.

During the Rockmodels project, which at the time of writing this document was still going on, many improvements on RockGIS were done. In particular, an upgrade of the fragmentation model, which now accounts for the impacting conditions to define the parameters to use when computing new generated fragments; the inclusion of protective structures in the simulations like dynamic barriers etc. A new real scale fragmentation test was been carried which, with all accumulated knowledge, has provided many valuable data on the fragmentation process and allowed a precise calibration. Finally, a laboratory test was performed to investigate the effect of comminution in rockfalls, when several blocks fall together in a stack.

At the time of writing this thesis, the research group is awaiting final confirmation for a new project that will provide continuity to the research lines and allows a technological transfer of all the knowledge obtained to all interested agents, including private companies and public agencies. The interest gathered by the research done during these years and the continuity it is going to have, show the clear interest on the improvement of the methodologies to deal with natural risks.

## 1.3   Thesis Outline

This thesis is presented as a compendium of three publications in journals indexed in the JCR, two as a first author and one as second author. This document brings together and summarizes the research that resulted in the publication of the three articles. This first chapter explain the motivation and objectives of this thesis and the framework of the research projects within it has been developed. The Chapter 2, *Literature review* summarizes the state of the art on of rockfall fragmentation, its numerical simulation and risk assessment. It highlights the points where the research started from. The work of different research groups has been also summarized in this review. Chapter 3, *Understanding fragmentation process*, reports all the experimental research carried out including real scale fragmentation tests, laboratory tests and natural events inventories. The results of all this experimental research are the basis for the development of RockGIS, a 3D propagation numerical code able to consider fragmentation. The description of this code is and its calibration are presented in Chapter 4, *Methodology: Development of RockGIS code*. The obtained results in different scenarios including natural events and real scale tests are presented in Chapter 5, *Results: RockGIS performance and applications*. Finally, Chapter 6 *Conclusions and future perspectives* summarizes the main conclusions obtained from the research and proposes future research lines to continue advancing in the understanding of rockfall fragmentation.

The three publications forming the compendium are:

1. **Matas, G.**, Lantada, N., Corominas, J., Gili, J. A., Ruiz-Carulla, R., and Prades, A. (2017). "RockGIS:a GIS-based model for the analysis of fragmentation in rockfalls". In: Landslides 14.5, pp. 1565–1578. doi: 10.1007/s10346-017-0818-7

2. Corominas, J., **Matas, G.**, and Ruiz-Carulla, R. (2019). "Quantitative analysis of risk from fragmental rockfalls". In: Landslides 16.1, pp. 5–21. doi: 10.1007/s10346-018-1087-9.

3. **Matas, G.**, Lantada, N., Corominas, J., Gili, J., Ruiz-Carulla, R., and Prades, A. (2020). "Simulation of full-scale rockfall tests with a fragmentation model". In: Geosciences (Switzerland) 10.5. doi: 10.3390/geosciences10050168.

Although these were the three articles selected to form the compendium, other works have been published as a result of the research carried out in this thesis. The following table summarizes the total scientific production, including the 3 articles of the compendium. Reference to all these publications is found in appendix #1.

| Publication type | Total | As first-author |
|---|---|---|
| Articles in journals included in the JCR | 5+1 submitted | 2 |
| Articles in peer-reviewed conferences and symposia | 14 | 6 |
| Contributions to non peer-reviewed conferences and symposia | 4 | 4 |

# Chapter 2

# Literature review

A rockfall is a rapid mass movement generated by the detachment of a rock volume from a slope that falls, bounces, and rolls during its propagation downhill (Varnes, 1978; Hungr et al., 2014). Rockfalls often threaten civil infrastructures, buildings and transportation networks in mountainous regions (Chau et al., 2003; Guzzetti et al., 2009; Giacomini et al., 2009; Thoeni et al., 2014; Crosta et al., 2015; Mitchell and Hungr, 2017; Asteriou and Tsiambaos, 2016; Mavrouli et al., 2019).These phenomena have great destructive potential due to the high speed and, consequently, the high kinetic energy the rockfall can reach during its propagation (Hoek, 2000).

In a rockfall, the initial mobilized mass can be either a single massive block or a set of blocks defined by the joint system in the massif. The concept of in situ block size distribution (IBSD) was introduced to describe the initial distribution of block sizes within the rock mass (Lu and Latham, 1999; Elmouttie and Poropat, 2012; Ruiz-Carulla et al., 2017). During propagation, the block or blocks that originally form the IBSD may break on collision with the ground to produce fragments that are smaller than the original ones (Figure 2.1). The term "fragmental rockfall" is used to refer to this phenomenon (Evans and Hungr, 1993; Hungr et al., 2014; Ruiz-Carulla et al., 2015; Corominas et al., 2017) to distinguish from the term "rock avalanche", which refers to masses of fragments that move as a granular flow. The final distribution of the fragments is called the rockfall block size distribution (RBSD). In some cases, a young debris cover is formed on the first impacts where slope gradient is high and some blocks fall above the others producing comminution (Matas et al., 2020b).

There are three main strategies to mitigate the risk from rockfalls (Corominas, 2013):

1. Hazard reduction by means of reinforcement and stabilization works. This strategy aims at decreasing the occurrence probability by making potentially unstable blocks more stable. Examples of stabilization works are anchoring specific unstable blocks using bolts, clearing unstable rock masses by forcing them to fall in controlled situations, areal stabilization using meshes fixed to the slope with bolts etc.

2. Constraining and obstructing the progression of the rockfall mass by means of defense structures with the consequent reduction of its magnitude, velocity, and runout. Dynamic barriers, earth embankments, protection galleries etc. are examples of structures used both to stop or diverge rockfalls.
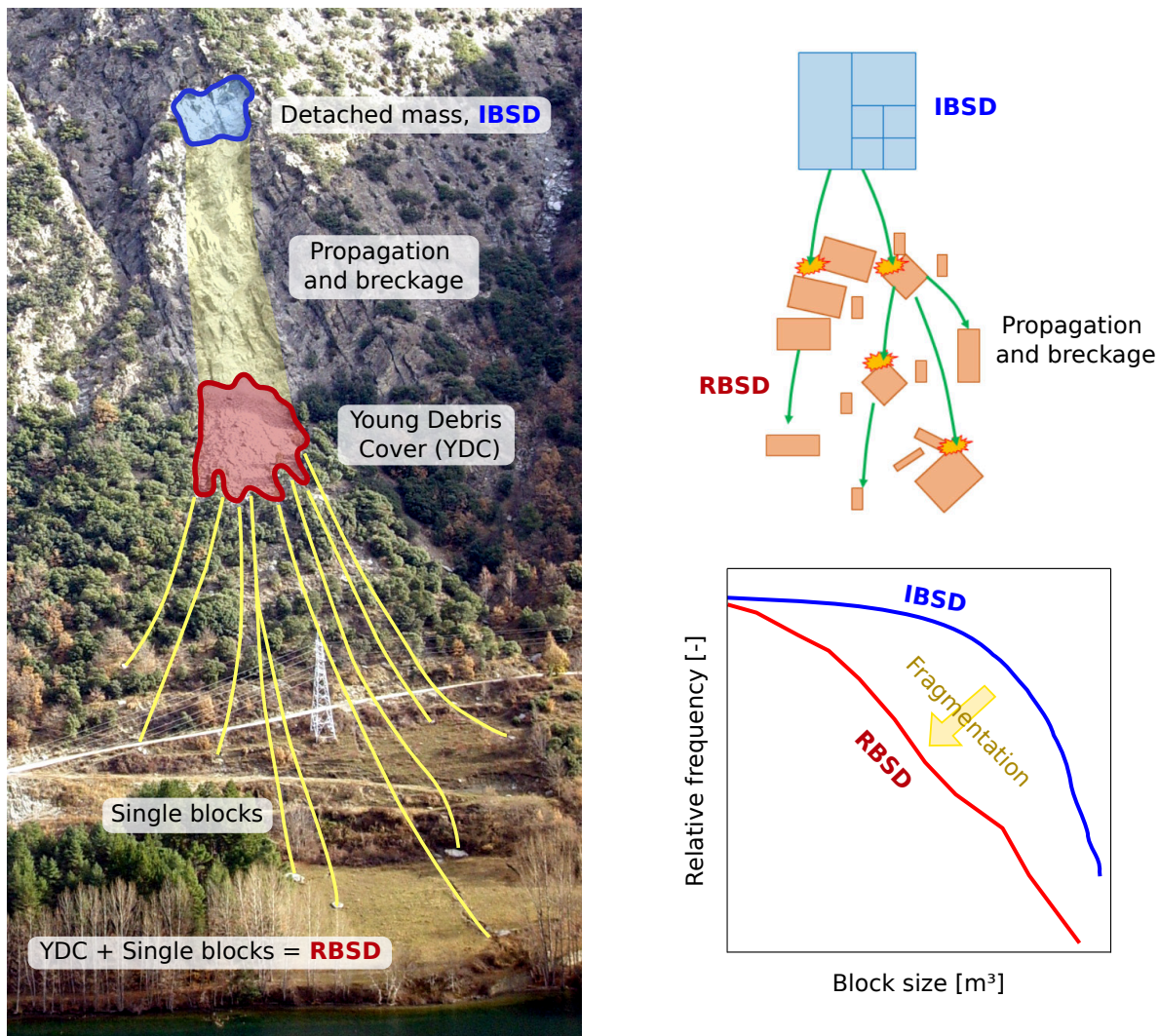
**Figure 2.1:** Example of fragmental rockfall with its conceptualization. An initial block distribution (IBSD) is detached from the cliff, these blocks are mobilized and broken during propagation producing a final different block size distribution (RBSD).

3. Protecting the exposed elements. The purpose is to make exposed elements less vulnerable to rockfall impacts, for example, by constructing sheds and galleries or by reinforcing the protection structure of a backhoe cabin to protect the operator.

For both options 2 and 3, the kinematics of the blocks such as the kinetic energy, velocity, passing height and reach probability must be estimated at the exposed areas. Modern techniques for determining these values use computational simulations for performing trajectory analyses of rockfalls (Volkwein et al., 2011).

Rockfall models simulate the kinematics of the boulders, calculating their movement downslope using Newton's second law neglecting air friction. Some of these models also include explicitly the rolling motion of blocks (Agliardi and Crosta, 2003; Lan et al., 2007), but the study of the interaction of the blocks with the topographic surface during the successive contacts (impacts) is the main scientific challenge in rockfall modelling (Bourrier and Hungr, 2013a).

Considering the blocks unbreakable during their propagation is a common hypothesis in

most of the existing propagation models (Dorren and Seijmonsbergen, 2003b; Volkwein et al., 2011; Turner and Duffy, 2012; Li and Lan, 2015). However, fragmentation is a process frequently observed in rockfalls and it is defined as the separation of the initial rock mass into smaller pieces upon impact with the ground (Hungr and Evans, 1988; Evans and Hungr, 1993). This definition covers both the disaggregation of the block fragments delimited by pre-existing fractures in the initial mass and the generation of new fragments due to the breakage of intact rock (Ruiz-Carulla et al., 2015).

The fragmentation mechanism is considered to be the most complicated and the least understood process in rockfall propagation (Giacomini et al., 2009) and very few contributions address this topic specifically. Two main consequences of the fragmentation are the generation of multiple fragments and the divergence of the fragment trajectories downhill from the impact point. After an impact involving fragmentation, the initial rock mass generates a number of block fragments that can be characterized by a volume distribution (Ruiz-Carulla et al., 2015). Further features are higher bounces, higher post-impact velocities (Agliardi and Crosta, 2003) and the ejection of small fragments (Cuervo et al., 2015). These physical effects may change significantly the way rockfalls interact with the terrain, the defense structures and the exposed elements. In the following sections this effects will be discussed in detail regarding their implications when numerically modelling the phenomena.

The resultant fragments propagate downslope following independent trajectories, which is crucial for the trajectory analyses and for hazard assessment. Note that when the interaction between particles is the predominant mechanism during the propagation of the fragments, a flow-like behavior develops and the process would be classified as a rock avalanche instead of a fragmental rockfall (Hungr et al., 2014). The simulation of the trajectories of a rockfall with or without considering the fragmentation may differ notably. Furthermore, analyses which ignore fragmentation tend to overestimate both the kinetic energy and runout (Corominas et al., 2012). On the other hand, the probability of an impact with the exposed elements is largely underestimated because the blocks generated during fragmentation define multiple and divergent trajectories (Corominas et al., 2012). The possibility of multiple impacts with fences or buildings due to the increased number of blocks have to be added to the list of fragmentation consequences.

## 2.1 Modelling rockfalls

To describe the existing susceptibility or hazard affecting a certain area and for the design of protective structures it is important to describe the movement of a falling rock along a slope regarding its trajectory, kinetic energy, passing height, maximum runout etc.

The first approaches to describe the maximum runout of the blocks were empirical. The Fahrböschung or travel angle was defined by Heim, Albert (1932) as the angle between a horizontal line and the segment connecting the top of the rockfall source to the deposition point. The travel angle has been used to characterize the mobility of rockfalls and rock avalanches (Hsü, 1975; Scheidegger, 1973; Li, Tianchi, 1983; Corominas, 1996) and to define the potentially affected areas (Finlay et al., 1999; Ayala-Carcedo et al., 2003; Jaboyedoff and Labiouse, 2011). This concept was modified by Lied (1977) and later by Evans and Hungr (1993) into the "shadow angle" concept, which links the highest point

of the apex, with the deposition point of the block which stopped the farthest. Figure 2.2 shows the geometrical variables defining both concepts. This approaches are easy to use, since only the topography and the starting point are taken into account, and allow a fast estimation of the potential maximum runout of a susceptible slope. Both methods were applied by Corominas et al. (2003) and Copons et al. (2009) in the Central Pyrenees in order to assess the rockfall susceptibility for a range of rockfall magnitudes. However, these approaches cannot be used for the design of protective structures since the physics of the process is not considered and thus the required dynamic parameters can not be properly stated. A review of these approaches is found in Hungr et al. (2005).
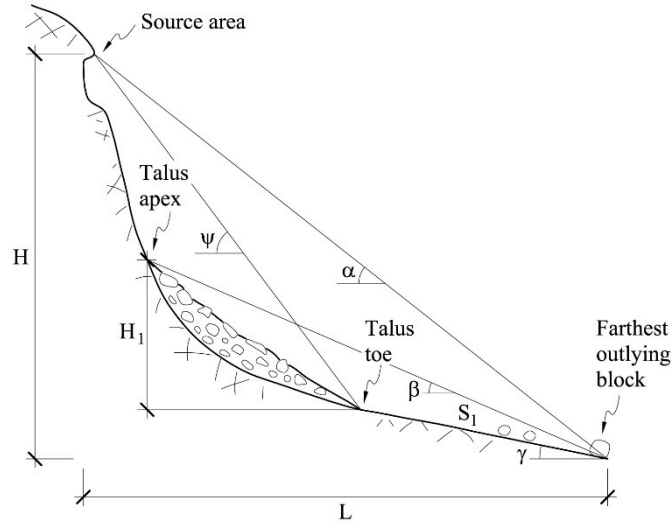


**Figure 2.2:** Geometrical variables: vertical drop (H), travel distance (L), reach angle ($\alpha$), shadow angle ($\beta$), source-talus angle ($\psi$), and shadow distance ($S_1$) (from Hungr et al. (2005))

When the use of computers began to generalize, numerical models which accounted for the dynamics of rockfalls during their descent downslope appeared. These models consider the kinematics of the blocks using different approaches regarding the spatial dimension considered, the physical representation of the block during the simulation and how the interaction between the slope and the blocks is represented. These also called process based models allowed to obtain information on the block velocity, jump heights and spatial distribution, which are the basis for a reliable design and the verification of protective measures. Examples of these models are Rotomap, RocPro3d, Hy-Stone, Rockfall Analyst, CRSP-3D, RAMMS, RokyFor3D. This approach requires the use of several parameters that must be properly set in order to represent faithfully the natural phenomena (Wyllie, 2014). The experience in applying the model and a knowledge of its sensitivity to parameter settings, as well as how to determine model parameter values in the field, is a prerequisite to obtaining acceptable results (Volkwein et al., 2011).

For the calibration and validation of these models, scientist have performed several experimental investigations, which are listed in the great review by (Volkwein et al., 2011), where more than 30 publications regarding experimental testing to calibrate rockfalls models are shown and summarized. However, since the year of this publication, additional tests both in real or laboratory scales have been performed. They show how important the experimental data are for the proper calibration of the numerical models and to reproduce

8

accurately the phenomenon (Asteriou et al., 2012; Gili et al., 2016; Zhao et al., 2017; Cui et al., 2017; Noël et al., 2018a; Asteriou and Tsiambaos, 2018; Wang et al., 2018; Hu et al., 2018; Ye et al., 2019a; Ji et al., 2019; Caviezel et al., 2019; Feng et al., 2019; Lu et al., 2019; Luo et al., 2019).

### 2.1.1 Modelling hypotheses

Propagation models can be classified by how they simplify reality and the hypotheses they consider with respect to the following aspects (Matas et al., 2017):

- **Spatial dimension:** The calculation of the trajectories can be performed in a 2D (Van Dijkem and van Westen, 1990; Meissl, 1998) or 3D space (Agliardi and Crosta, 2003; Dorren et al., 2005; Lan et al., 2007; Leine et al., 2014; Gischig et al., 2015). Some models use a 2.5D approach (Dorren and Seijmonsbergen, 2003a) in which the slope profiles required for performing the 2D analysis are obtained from Digital Elevation Models using algorithms like the maximum slope path for determining the possible propagation direction of rockfalls.

- **Block kinematics:** The kinematics of falling rocks can be described as rolling, sliding and bouncing over the substratum (Ritchie, 1963). However, it is not always necessary to account for all of them to simulate rockfalls, and each model considers different combinations of these types of motion. The kinematics of the blocks is closely related to the shape considered in each model.

- **Block shape:** The shape of the blocks can be explicitly accounted for (rigid body approach) or simplified by treating all the mass of the block as concentrated in one point (lumped mass approach). In the rigid body approach the shape of the blocks can be considered as a sphere or a cylinder, as a 3D mesh (Leine et al., 2014), or as a combination of spheres using the Discrete Element Method (DEM) (Giacomini et al., 2012; Paluszny et al., 2016). Some models consider a combination of both approximations at different stages of the calculation process (hybrid approach). Examples of models using these different approaches are shown in Volkwein et al. (2011).

- **Impact modelling:** Impact detection routines depend on the block shape considered and once the impact with the ground is detected, a rebound model is applied in order to estimate the post-impact velocity of the block. There are several rebound models, from simpler ones that consider only a percentage loss of the velocity with respect to a local coordinate system at the impact point, to the ones that account for the mechanical properties of the ground, impact angle, angular velocity, block size, etc. A review of the different existing rebound models can be found in Bourrier and Hungr (2013a). Some models also consider impacts with trees (Dorren et al., 2005; Dupire et al., 2016; Toe et al., 2018) or mitigation structures such as fences and ditches using specific impact models (Lambert et al., 2013).

- **Dealing with uncertainty:** Every impact of a rock particle is a random process (Bourrier et al., 2009). There are many sources of randomness when performing numerical rockfall analyses, such as the source location, the rock properties, the

initial kinematic conditions, the slope properties during impacts, etc. Li and Lan (2015) present an exhaustive review of how existing models deal with uncertainties.

## 2.1.2  Interaction between block and slope

The interactions between blocks and the slope during the propagation depend on the modelling hypotheses chosen for each simulation code. Different approaches are taken for the sliding, rolling, free falling and bouncing motions of rockfalls. Most rockfall models simulate trajectories as a succession of free fall and bouncing phases since due to the slope surface irregularity, both rolling and sliding motions are more a succession of small bounces (Volkwein et al., 2011; Turner and Duffy, 2012). In the models that explicitly account for sliding and rolling motions, a tangential damping coefficient related to friction is introduced. This sliding friction is, according to Coulomb's law, defined as the normal component with respect to the soil surface of the block's weight. In order to change the motion mode during the simulations, transition criteria have to be defined. Bozzolo et al. (1988) defined the transition from sliding to rolling and Hungr and Evans (1988) and Giani (1992) discussed the transition between bouncing and rolling modes.

When a falling block collides with the slop surface bouncing, or rebound, occurs. Several variables influence on the resultant trajectory of a block after an impact, and it is considered the most difficult to predict type of motion in rockfalls. Figure 2.3 shows the definition of the problem, where the outcoming velocities after an impact must be estimated considering the incident velocities, the topographical conditions, the shape of the block etc. depending on the modelling approaches. In the case of lumped-mass approach, a collinear impact is assumed, which means that the normal to the contact surface passes through the center of gravity of the particle. This assumption implies that no momentum is transmitted by the normal contact force and this permits a separate balancing of momentum in normal and parallel directions to the impact surface (Stronge, 2000).

As per Volkwein et al. (2011), the most common definition of a block rebound involves differentiation into tangential $R_t$ and normal $R_n$ restitution coefficients (Budetta and Santo, 1994; Evans and Hungr, 1993; Fornaro et al., 1990; Giani, 1992; Guzzetti et al., 2002) as defined in equation 2.1.

$$R_n = \frac{V_n^+}{V_n^-} \quad and \quad R_t = \frac{V_t^+}{V_t^-} \tag{2.1}$$

where $V_n^-$ and $V_t^-$ are the normal and tangential velocities of the block before the rebound and $V_n^+$ and $V_t^+$ are the velocities after the rebound as shown in Figure 2.3.

Several authors have performed real scale tests in order to estimate the values of the restitution coefficients in different lithologies and impacting conditions (Piteau and Clayton, 1977; Hoek, 1987; Pfeiffer and Bowen, 1989; Giani, 1992; Azzoni et al., 1992; Evans and Hungr, 1993; Robotham et al., 1995; Chau et al., 1998; Budetta and Santo, 1994; Peng, 2000; Richards et al., 2001; Chau et al., 2002; Giani et al., 2004; Imre et al., 2008; Giacomini et al., 2009; Giacomini et al., 2012; Asteriou et al., 2012; Wyllie, 2014; Sabatakakis et al., 2015; Noël et al., 2018a; Asteriou and Tsiambaos, 2018) among others. Results obtained in these works show that the restitution values depend on the impact velocity, the incidence angle and the incident momentum. Asteriou and Tsiambaos (2018) concluded
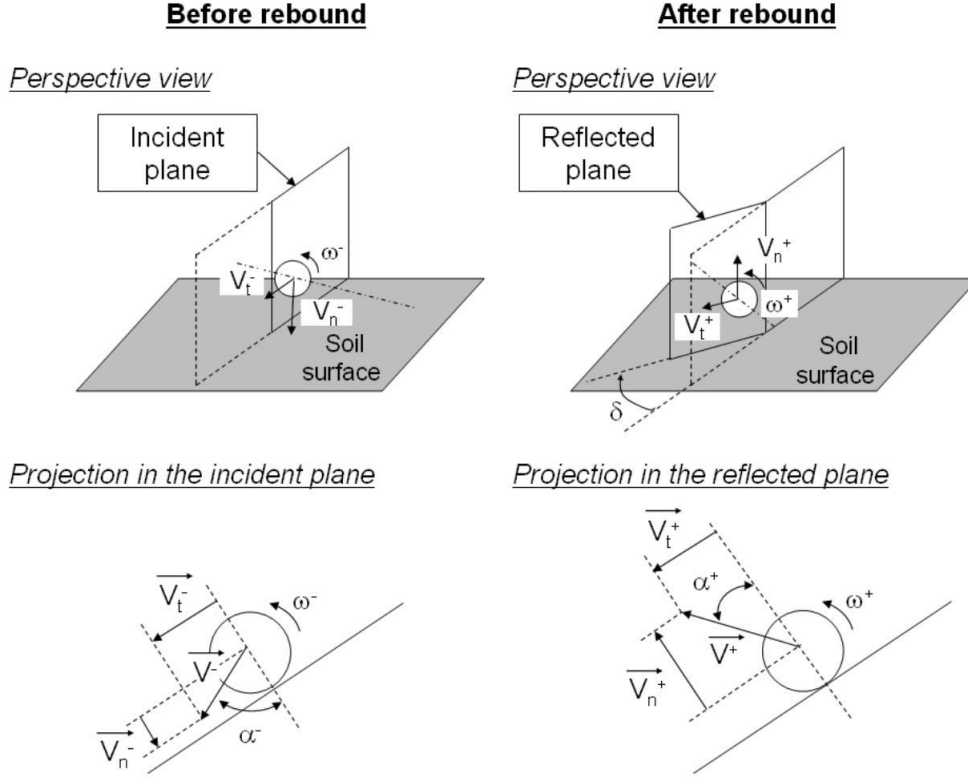
**Figure 2.3:** Definitions of reflected $(V_t^+, V_n^+, \omega^+)$ and incident $(V_t^-, V_n^-, \omega^-)$ velocity components and deviation angle $\delta$ characterizing changes in boulder fall direction due to the rebound (Bourrier et al., 2009).

that (i) the coefficients of restitution (COR) are significantly affected by both the incident velocity and the block mass and they can be better interpreted using incident momentum and (ii) the COR is affected by the stiffness of both the block and the impact surface. Then, scaling functions depending on these variables are used to estimate the COR value at each impact. Some authors, thus, prefer to name this parameters as "restitution factors" instead of "restitution coefficient" since they are not a fixed value but defined by variable functions. In Bourrier and Hungr (2013b), Gischig et al. (2015) and Asteriou and Tsiambaos (2018) reviews of the different approaches to scale restitution factors can be found. These approaches use the incidence angle, incidence momentum or incidence velocity with different mathematical curves to estimate how the incident conditions determine the COR value at each impact, for example using hyperbolic functions (Gischig et al., 2015).

### 2.1.3 Fragmentation in rockfalls

Understanding the fragmentation process in rockfalls is fundamental for the analysis of the rockfall hazard, since it is a critical input datum for calculating the trajectories and the runout of the rock fragments, the encounter probability with the elements at risk and the expected impact energies. The mining industry has historically been the most interested in fragmentation to assess the efficiency of blasting operations (Lilly, 1986; Hudaverdi et al., 2012). More recently, several research groups paid attention to fragmentation as an

important factor in the study of rockfalls (Wang and Tonon, 2011; Bourrier and Hungr, 2013b; Gischig et al., 2015; Sala et al., 2019; Luo et al., 2019) and rock avalanches (Davies et al., 1999; Davies and McSaveney, 2002; Blasio and Crosta, 2015; Blasio et al., 2018). In rockfall events, three main consequences are observed when a block fragments:

1. **Reduction of the initial block size.** This can range from 6 to 9 orders of magnitude in single isolated blocks from 1 to 2 $m^3$ (Gili et al., 2016), and 15 to 18 orders of magnitude in events that mobilize over 20,000 $m^3$ (Blasio et al., 2018). To study the block size distributions, Ruiz-Carulla et al. (2017) proposed a fractal approach in which a finite number of iterations was adopted, based on Mandelbrot (1982) and Turcotte (1986) who had already developed fractal theory to deal with complex natural phenomena. This type of approach has been used to derive the RBSD from the ISBD of past rockfall events (Ruiz-Carulla et al., 2017; Marchelli and De Biagi, 2019). Recently, a continuous approach using fractal theory and the scale-variant fractal probability model has been proposed for rockfalls (Ruiz-Carulla and Corominas, 2019).

2. **Divergence of trajectories.** After breakage, fragments adopt fan-like diverging trajectories from the collision point (Davies et al., 1999; Ruiz-Carulla et al., 2015; Mavrouli and Corominas, 2017; Corominas et al., 2017; Prades et al., 2017; Blasio et al., 2018). Despite the fact that dispersion of trajectories have been observed in rockfalls (Crosta and Agliardi, 2004), few studies have targeted the evaluation of trajectory divergence after fragmentation in rockfalls, including numerical modelling (Zhao et al., 2018) and field experiments (Giacomini et al., 2009; Gili et al., 2016).

3. **Momentum boost effect.** After fragmentation, small fragments may reach velocities higher than big ones (Blasio et al., 2018; Zhao et al., 2018; Ye et al., 2019b; Ye et al., 2019a). Discrete element simulations of the vertical impact of a sphere show that the maximum fragment velocity after breakage can double the impact velocity (Ye et al., 2019b). The distribution of energy after breakage is still unknown and, in some numerical investigations, no correlation has been found between the fragment size and fragment kinetic energy for a given impact velocity (Ye et al., 2019a). So far, only a few studies have attempted to measure the energy distribution after fragmentation in rockfalls (Prades et al., 2017; Guccione et al., 2020).

The combination of these three effects can produce a range of scenarios. Although the fragment size is reduced, the potential increment in velocity due to the momentum boost effect may lead to high energies concentrated in a small area. It has been observed that in this scenario blocks with significantly less energy than the design value can punch out dynamic rockfall barriers (Spadari et al., 2012). This is called the "bullet effect". Moreover, trajectory divergence, combined with size reduction, may have opposite effects depending on the topography. In scenarios where propagation takes place on gentle slopes, the overall runout of the fragments may decrease when compared to the unbroken blocks. This effect disappears on steep slopes (Corominas et al., 2019).

For a better understanding of the fragmentation phenomenon, some authors have used energetic considerations in attempts to understand the effect of the loading rate on the rockfall breakage (Grady and Kipp, 1987; Zhang et al., 2000). Giacomini et al. (2009) performed several fragmentation field tests with emphasis on the influence of the impact

angle in case of foliated materials. In the cited study, the idea of an impact energy threshold to trigger breakage of the blocks proposed by Fornaro et al. (1990) was not confirmed. Recently, Gili et al. (2016) and Gili et al. (2020) performed several rockfall fragmentation field tests in which this concept of an energy threshold was not observed either, but a correlation of the number of blocks generated during breakage and the fractal dimension of the generated volumetric distribution was found (Ruiz-Carulla et al., 2017; Ruiz-Carulla et al., 2020).

## 2.2 Risk assessment in rockfalls

Risk is defined by three basic concepts (Einstein, 1988; IUGS, 1997; Fell et al., 2005; Fell et al., 2008; Corominas et al., 2014): the hazard, the exposure of the elements at risk, and their vulnerability. There can be characterized by both spatial and non-spatial attributes. The growing societal demand for road safety requires managing this risk and places a high priority on the identification of problematic areas to effectively manage the mitigation works (Mavrouli et al., 2019). The hazard refers to the expected magnitude (or intensity) of the event, for example in terms of volume or kinetic energy, and its probability of occurrence (Hungr et al., 1999; Dussauge-Peisser et al., 2002; Chau et al., 2003; Crosta and Agliardi, 2003; Guzzetti et al., 2003; Jaboyedoff et al., 2005; Abbruzzese et al., 2009; Hantz, 2011). The exposure is given by the spatial and temporal probabilities that the element at risk is actually located in the area affected by the potential event (threat) at the time of its occurrence (Ferlisi et al., 2012; Nicolet et al., 2016; Macciotta et al., 2016). Finally the vulnerability is the expected degree of loss of the element at risk depending on the intensity (or magnitude) of the phenomenon and ranging from 0 (no damage) to 1 (total destruction) (Mavrouli and Corominas, 2010; Vallero et al., 2020). An extended description of these required components to estimate risk can be found in recent reviews for landslides and rockfalls such as Lee and Jones (2006), van Westen et al. (2006), Fell et al. (2008), Corominas et al. (2014), Budetta et al. (2016), Ferrari et al. (2016), and Mavrouli et al. (2019).

Risk can be approached qualitatively or quantitatively. Qualitative methods define hazards, elements at risk and their vulnerabilities using qualitative descriptors, such as ranked attributes, weighted indices, rating systems, scoring schemes, ranking matrices and classifications (Cruden and Fell, 1997). Quantitative methods use numerical values or ranges of values instead of qualitative terms to estimate each one of the components of a rick analysis (Ferrari et al., 2016).

The quantitative risk analysis (hereinafter QRA) has received an increasing interest in recent years (Corominas et al., 2014). One of the main advantages of QRA against qualitative methods is that it provides an objective evaluation of risk because the assumptions and uncertainties are declared (Straub and Schubert, 2008). It yields reproducible results, allowing the analysis of different scenarios, the comparison of their results, evaluation of the effectiveness of protection structures and the consideration of risk acceptability criteria. Equation 2.2 shows how risk using QRA approach is calculated (IUGS, 1997; Ho et al., 2000; Fell et al., 2005).

$$R = \sum_{j=1}^{J} \sum_{i=1}^{I} N_i \cdot P(X/D)_i \cdot P(T/X)_j \cdot V_{ij} \qquad (2.2)$$

where:

$R$ : Risk due to the detachment from a cliff of a rock mass of magnitude (volume) $i$ on an exposed element $j$ located at a reference distance $X$ from the source.

$N_i$ : annual frequency of rockfalls of volume class $i$.

$P(X/D)_i$ : probability that the detached rock mass of the size class $i$ reaches a point located at a distance $X$ from the source (reach probability).

$P(T/X)_j$ : exposure or the probability that an element $j$ be in the trajectory of the rockfall at the distance $X$, at the timing of the arrival of the rock fall debris.

$V_{ij}$ : vulnerability of an exposed element $j$ being impacted by a block of magnitude $i$.

This approach has been used in recent publications (Agliardi et al., 2009; Macciotta et al., 2016; Budetta et al., 2016; Moos et al., 2018; Corominas et al., 2019), but requires a special treatment when considering fragmentation as is explained in Chapter 4.

# Chapter 3

# Understanding fragmentation processes

The scientific method is based on empirical evidence. Wikipedia defines empirical evidence as "information received by means of the senses, particularly by observation and documentation of patterns and behavior through experimentation". In this chapter, the procedures used and developed to observe and understand natural behavior of fragmentation in rockfalls are presented. This task was very challenging since only few publications had specifically addressed the characterization of fragmentation in rockfalls when this research started (Ruiz-Carulla et al., 2015). The following paragraphs briefly describe the approaches adopted to gather empirical evidences in this research and then, following subchapters explain each one in detail. The goal of improving the knowledge of the phenomenon is to implement a propagation model that is capable of reproducing fragmetation in rockfalls.

The first approach has been the direct observation of fragmental rockfalls in nature by means of inventories. Once a rockfall occurs lots of information can be gathered from direct observation of the resultant deposit like the maximum runout distance and the block size distribution of the fragments (the RBSD). The main drawback of the study of natural rockfall events is that it is done posterior to its occurrence. It means that the only available data on the field is the final state of rockfall deposit, and no additional features of the process are usually available (i.e. kinematic features). In this scenario back-analysis is carried out to make a virtual reconstruction of the phenomenon. For example, an estimation of the trajectories followed by the generated fragments during propagation can be done by locating the marks they left when impacting on the ground surface or on trees. Also, an estimation of the initial block size distribution of the detached rock mass, the IBSD, can be made by studying the fracture pattern of the massif and using digital surface models of the detached rock mass prior to the event (which are not always available). Despite some natural rockfall events have been recorded by scientist who were specifically monitoring rockfall susceptible regions, or by modern real time early warning systems (Yan et al., 2019), direct observation of natural rockfall events are very infrequent and sometimes they are caught by chance. Although the observation of natural past fragmental rockfalls is essential to understand the phenomenon globally, it usually does not allow a detailed observation of how the fragmentation of a single block occurs.

The second approach has addressed the direct observation of the fragmentation process of

single blocks by means of real scale tests. The goal was to gather empirical information of the fragmentation process that can not be obtained from past natural occurred events. A series of real scale test were performed in controlled scenarios in quarries in the framework of the Rockrisk and Rockmodels projects. These experiments allowed direct observations of the fragmentation process. In this chapter the procedure developed during this research to carry out this experiments is described. However, real scale tests also have some limitations. Heavy machinery is required for their realization, and the range of block volumes that can be tested is limited by its loading capacity. In addition, the reproduction of the fall of a set of stacked blocks together, as it usually occurs in nature, is technically very difficult.

The third approach aimed at observing fragmentation process in scenarios that were unfeasible to reproduce in real scale tests. In natural rockfalls, having a group of stacked blocks that are detached together from the cliffs is a common scenario. To reproduce this scenario, reduced scale laboratory tests were performed to study fragmentation behavior when blocks are subject to overburden stress produced by the stack of blocks over them when impacting the ground. These tests were performed in a controlled environment and more variables controlling the phenomenon could be defined and measured. To the author's knowledge no attempts have been made so far to test the fall of a set of stacked blocks.

Both real scale and laboratory testing approaches introduced are costly and time consuming since they require lot of preparation and the use of expensive materials and machinery. In addition, the treatment of the huge amount of information gathered during their realization is a challenge and requires a lot of processing in order to obtain measurable information. Moreover, there are some details controlling fragmentation process that can not be directly observed using video cameras, accelerometers or geophones, like the propagation of the cracks during fragmentation and the tension waves produced inside the blocks when impacting the surface. The last approach for understanding fragmentation process adopted in this research has been the use the Discrete Element Method to perform numerical simulation of the phenomena. Even just preliminary tests could be done using this methodology due to time constraints, it showed a lot of potential regarding the capacity of performing virtual simulations of real scale tests in different scenarios and observation of the crack propagation and tension waves inside blocks. Note that this is not a direct observational method, since it requires a precise calibration of the model to obtain good results. However, when a model is properly set up it allows testing infinite scenarios that would be impossible to test in real scale tests nor in laboratory scale. Considering the high stochasticity of the fragmentation phenomenon, the ability of statistically testing several possible event scenarios is very appropriate and powerful. In this approach, the main limitation is the available parallel computing potential, since simulations require large computing time.

## 3.1   Natural event inventories

Inventorying a natural rockfall consists of gathering as much information as possible once the event has occurred regarding the total volume of the detached mass, the final position of the blocks in the deposit, the impacting points of the blocs with the slope surface to

reconstruct the trajectories etc. It is an intense field work that allows to characterize the failure mechanism, the present lithology, the topographical conditions of the propagation path, the characterization of the detached mass and the characterization of the final deposit. This information is crucial for rockfall simulations since it determines the initial boundary conditions and allows to calibrate propagation models.

This section summarizes the general process of inventorying a fragmental rockfall. All the data obtained and tools used to collect them are also described. The most important data to obtain in an inventory of a fragmental rockfall are: (1) The digital elevation model, which allows a virtual reconstruction of the same; (2) the in situ block size distribution (IBSD) of the rock mass formerly to the detachment and (2) the rockfall block size distribution (RBSD) of the final deposited fragments. In addition, other data can help to understand each event, such as the position of the impacts, the lithology, the pattern of joints in the massif, etc. To facilitate the comprehension, all the explanation is aided by some examples of natural event inventories carried out during this research.

All information gathered in natural events allows the characterization of fragmentation by using fractal theory (Ruiz-Carulla et al., 2015). This characterization was crucial in this thesis for the development of a methodology to consider fragmentation in a rockfall propagation code.

Figure 3.1 shows an example of a fragmental rockfall that occurred in 2017 at Monasterio de Piedra in the central Iberian Range, NE Spain. It shows the main features of a rockfall: the detachment area, the propagation path and the final deposit. The geological setting in this site corresponds to a series of Mesozoic carbonate rocks, Miocene detrital formations, and Quaternary tufa. An extended description of the site can be found in (Corominas et al., 2019). The following subsections detail the steps of the data gathering process to inventory a fragmental rockfall.

### 3.1.1   Topographic surface model

A three dimension detailed model of the event and the affected area allows a virtual reconstruction of the scene which can be processed and analysed. To obtain this surface model, UAV flights were carried out taking both zenithal and oblique images of the scene. The images were then processed using a photogrammetric software Agisoft Photoscan. To increase the accuracy of the model it is common to use ground control points which are accurately measured using GPS-RTK. Depending on the photogrammetric software, a classification of the 3D points computed from the images in ground, vegetation etc. is required. In the case of Agisoft Photoscan it has a specific module to perform this task. After all processing, a 3D model of the scene is obtained. Figure 3.2 shows an example of the obtained 3D model of the Monasterio de Piedra rockfall including a zoom to the detachment area. This model has been used to generate other subproducts like a digital elevation model, a soil classification, an ortophoto, contours etc. Thanks to the good quality results in terms of ground pixel resolution achieved using photogrammetric techniques and modern UAV, the produced 3D models allow direct identification of joints in the massif and measurement of the size of deposited fragments. With this precise identification of the joints, it is possible to identify unstable rock masses (Francioni et al., 2020). These models are also essential for rockfall simulation since they provide the
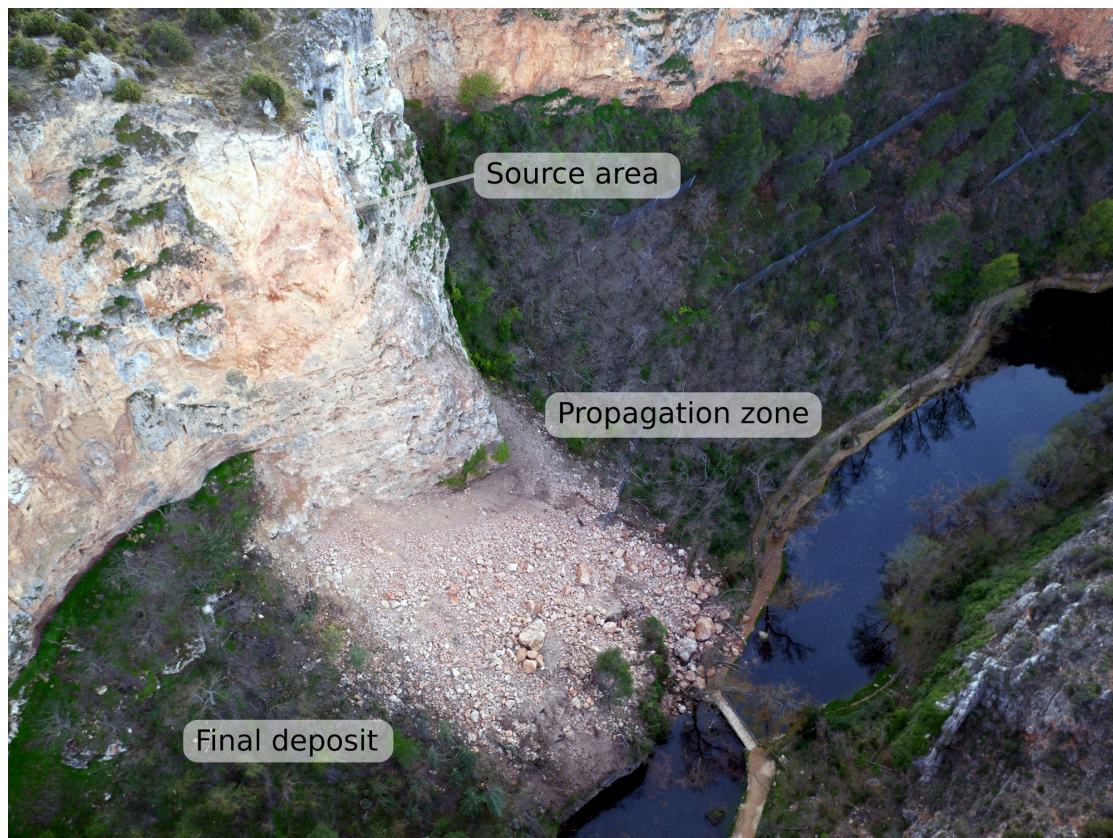
**Figure 3.1:** Aerial photo of the 2017 event in Monasterio de Piedra. The IBSD defines the volumes and positions of the blocks in the source area prior to the event. In the propagation zone these blocks broke and the generated fragments deposited forming the RBSD.

virtual representation of the terrain on which the blocks interact during the computation.

### 3.1.2 IBSD

The in situ block size distribution (IBSD) of the detached mass is required for the simulation of fragmental rockfalls. First, the total detached volume is estimated by computing the difference between digital surface models prior and post event. It is not usual to have a highly detailed surface model of the affected area prior to the event. However, aerial lidar information provided by some governmental topographic services were used in case of large rockfalls. In case no topographical information of the area is available, an heuristic reconstruction of the original detached mass can be estimated by analyzing and extruding the scar. In Figure 3.3 an example of the reconstructed volume in Monasterio de Piedra 2017 event is shown. For this rockfall the total estimated detached volume was 780 $m^3$.
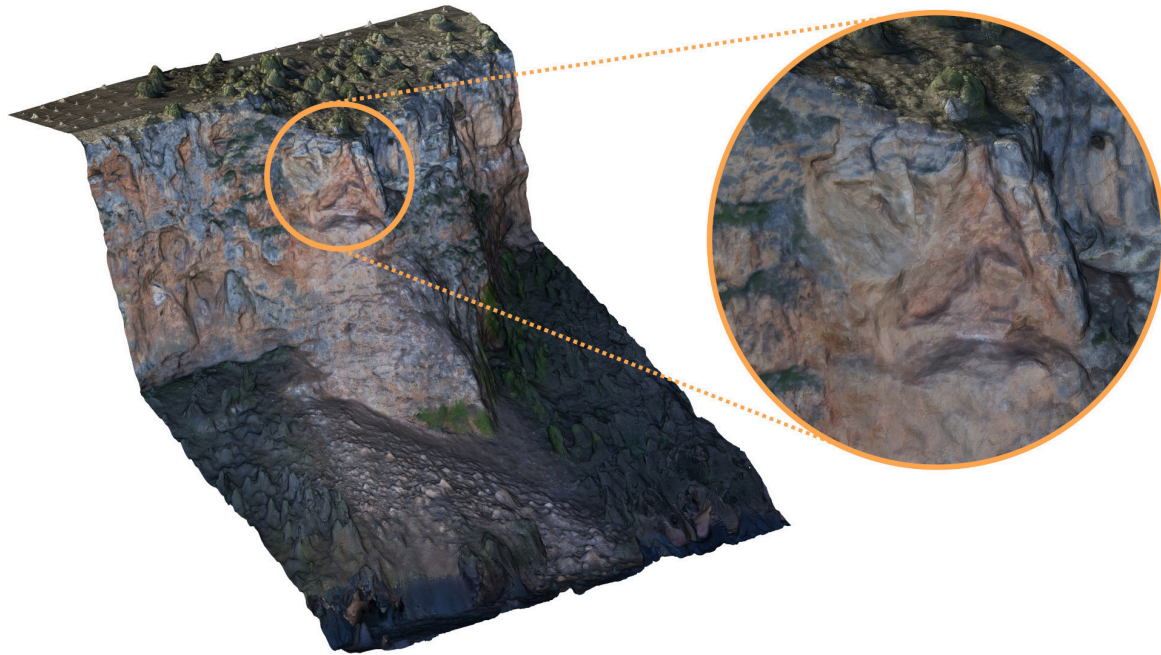
**Figure 3.2:** Example of the 3D surface model obtained by UAV photogrammetry of the Monasterio de Piedra rockfall in 2017. The detachment area is enlarged to appreciate the details.
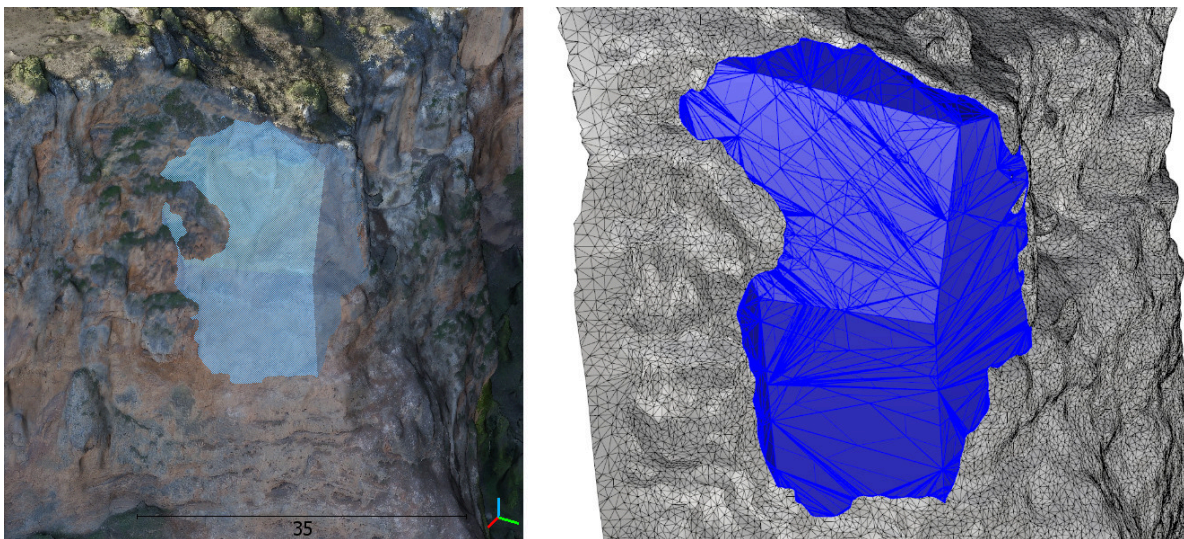


**Figure 3.3:** Example of a 3D reconstruction of the detached mass in the 2017 Monasterio de Piedra rockfall. Image provided by Roger Ruiz-Carulla.

Once the detached volume was estimated and its 3D model isolated, the IBSD was estimated by intersecting the volume with a discrete fracture network (DFN). This DNF was estimated by direct observation of the produced scar and extruding the visually identified discontinuities in the high resolution model. The intersection of the detached volume with the DFN generates a set of polyhedra representing the initial blocks. Figure 3.4 shows the identified set of joints on the detachment zone of the 2017 Monasterio de Piedra rockfall that were used to cut the identified detached volume. Note that this approach assumes an infinite persistence of the joints and thus it may underestimate the biggest volumes.

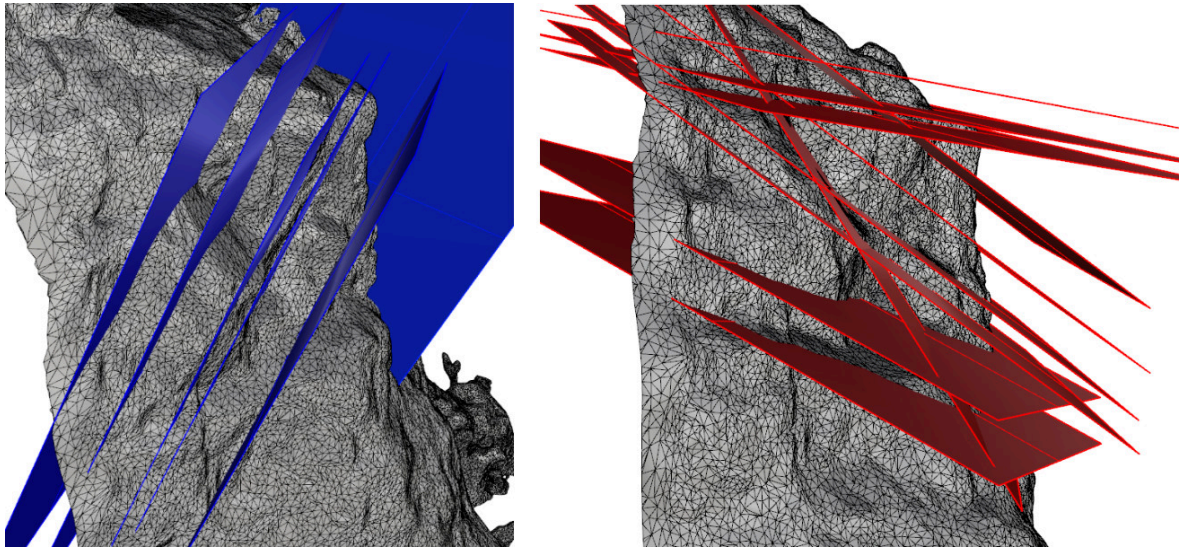Measuring the volume of each one of this polyhedron the IBSD was obtained.



**Figure 3.4:** Main set of joins identified in the massif used to cut the detached estimated volume in the 2017 Monasterio de Piedra rockfall. The result of the intersection of these joints and the volume gave a set of small volumes which correspond to the in situ block size distribution (IBSD). Image provided by Roger Ruiz-Carulla.

### 3.1.3   RBSD

The first step when characterizing the RBSD is the differentiation of the fragments that correspond to the studied rockfall from the ones from previous events. In vegetated slopes it may be very easy if there are not many blocks present on the surface and the paths followed by blocks are easily traceable following ground scars. However, in case of a rockfall occurs on an old debris scree cover this identification may be tricky. The main criteria was then using the color difference between newly generated surfaces on the fragments to identify the most recent ones.

Once the fragments are identified, different approaches are used for the estimation of the rockfall block size distribution of the deposit. The classical is tape measuring the produced fragments. By measuring three axes of each fragment an estimation of its volume can be obtained. This method is slow and force the operator to work on a probably risky zone while gathering data. Moreover, in case of large rockfalls with several thousands of produced fragments measuring them one by one can be unfeasible. Instead of measuring all fragments it is common to make samplings on representative areas in order to make extrapolations of the fragment size distribution (Ruiz-Carulla et al., 2015). However, in the presented study case here a significant part of the deposit was hand measured in order to have a ground truth to compare with other semi automatic methods. Figure 3.5 shows the hand measured area of the deposit including some significant blocks which were georreferenced. In this case the polygons just delimit measuring areas for practical purposes during the measurement.
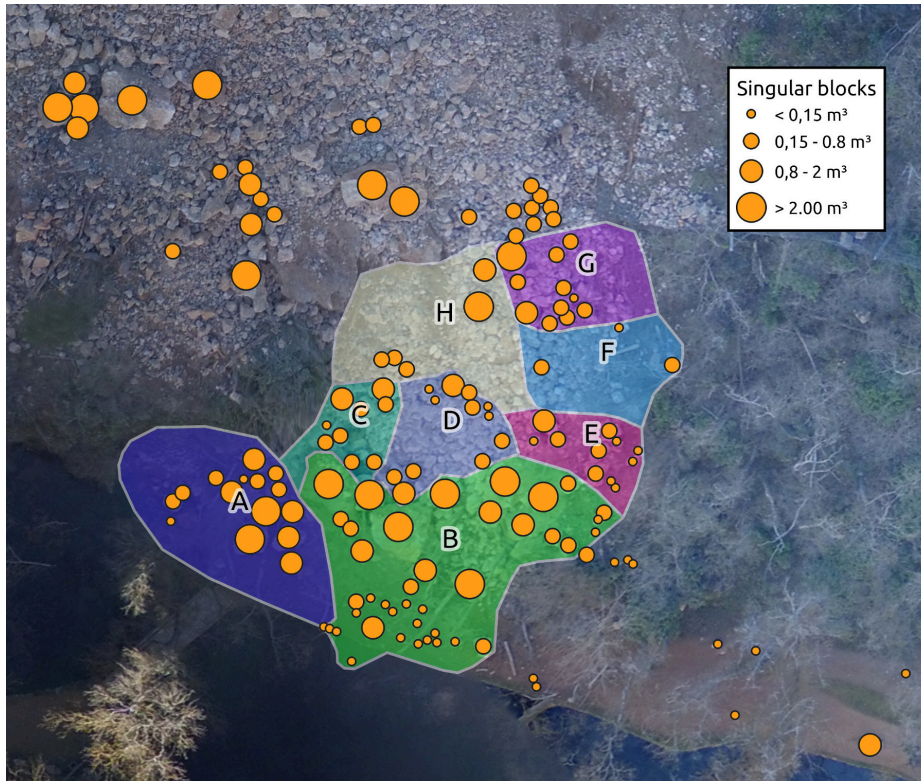
**Figure 3.5:** Part of the 2017 event deposit hand measured using tape. Significant blocks were georreferenced. Zoning shown was used for practical purposes during the measurements.

To overcome these limitations the high resolution digital surface model obtained and its derivative products were used. The fragment size can be estimated both in 2D or 3D using the ortophoto or directly the 3D mesh. In 2D case, all fragments were manually delimited in a GIS environment using polygons and then the area of each polygon was computed. This list of areas was then converted to volumes by using some approaches like adjusting ellipsoids or using relations of X,Y axis and Z axis obtained from manual sampling plots. Modern image segmenting techniques also allow an automatic classification of the blocks. These algorithms analyze raster images and subtract a set of polygons representing the fragment margins. Figure 3.6 shows an example of the segmentation result using ImageQ software. First, the ortophoto is cropped to contain exclusively the fragments produced of the studied event. Image on left of Figure 3.6 shows the cropped deposit for the 2017 Monasterio de Piedra event. Then, the process results in the classified raster image shown on the right side of the same figure.

Even this automatic method is fast, sometimes the segmentation of fragments can be imprecise due to overlapping of fragments or shadows. A combination of manual and automatic segmentation gives great results. The RBSD could also be estimated from the 3D mesh of the deposit. To do so, manual segmentation of the polygons, corresponding to the projection of the fragments on the ortophoto, must be determined and then their volumes estimated. This is a very time consuming process and the bottom part of the fragments is usually not well represented in 3D due to the shadow effect. To improve the RBSD measurement, some authors are working on 3D segmentation algorithms of fragments (Kitahra et al., 2016; Bonneau et al., 2019). These authors face similar limi-

tations than 2D segmentation technique since some stacked fragments may be delimited as a single fragment. The combination of color analysis and 3D segmentation seems very promising. For example, color analysis has been used in point clouds for automatic joint identification on rock massifs (Guo et al., 2019).
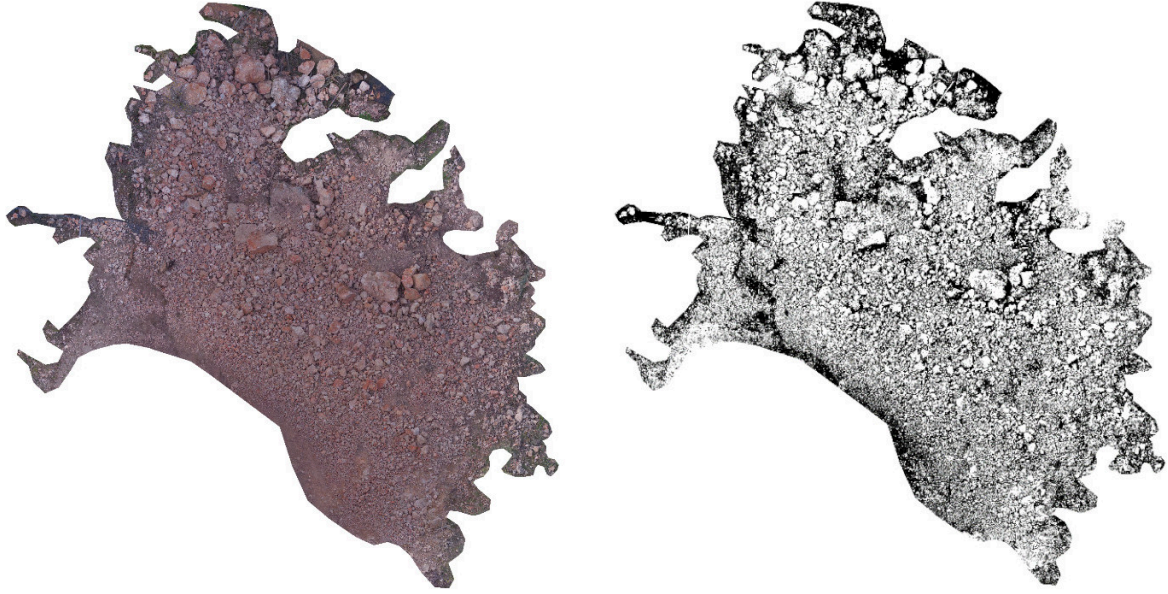


**Figure 3.6:** Automatic classification of the fragments of the 2017 event deposit using ImageQ software. Results give a list of areas corresponding to each identified fragment.

## 3.2   Real scale rockfall fragmentation tests

A total of four real scale rockfall fragmentation tests were performed during the course of this research and in the framework of Rockrisk and Rockmodels projects. These tests were performed in quarries of different lithologies: limestone, granite and dacites. they basically consisted of throwing individual blocks against the slope using backhoes. More than one hundred blocks were tested and more than three terabytes of data were totally recorded. In this section the testing methodology and the obtained results are summarized. The detailed explanations of these tests are found in Gili et al. (2016), Gili et al. (2020), and Matas et al. (2020b).

The aim of these tests was to improve the knowledge of fragmentation phenomena of a single block impacting on a surface. Few experiments had previously addressed direct observations of the fragmentation phenomena in rockfalls (Giacomini et al., 2009) since most of the rockfall experiments focused on unbroken blocks (Dorren et al., 2006; Bourrier et al., 2012; Volkwein and Klette, 2014). The information to be collected in these experiments was the initial volume and 3D shape of the blocks, different video recordings to allow the 3D trajectory reconstruction of the fragments, deposition position of the fragments, fragment size distribution after breakage (RBSD) and seismic recordings of the impacts.

## 3.2.1  Tests set up

The first step was selecting testing profiles inside the quarries. The main criterion for selecting the profiles was having maximum hardness of the impact point to achieve a high percentage of fragmenting blocks. However, in some cases quarry operations restricted the choice of profile. Figure 3.7 shows an example of the profile of testing site #4. In this site the first impact of the blocks was directly against a hard rock plane with a 42º angle.

Then a set of blocks to be tested were chosen from leftover blocks from mining operations. These blocks were first manually measured and photographed so as to later build 3D models. Three ellipsoids were painted around the blocks so as to facilitate its identification in the video footage. In some of the blocks L-Hammer tests were performed to evaluate their strength. Figures 3.8 and 3.9 show the blocks prepared prior to their release in test sites #1 and #3 respectively. The lithology on test site #1 and #2 were limestone and granite respectively.

Several sensors were placed in each one of the testing sites to gather all desired data. Ground control points were placed in each profile to provide scale, and georeference photographs and video images taken. Both printed targets and direct paint on the rock were used. These points were precisely surveyed using GNSS technology. The disposition of the sensors was very similar in all testing sites, and Figure 3.10 shows an example of the disposition of all sensors for testing site #4.

Three high speed cameras recording at 400fps were strategically placed pointing the scene. The location of these tree cameras was strategically designed so as to get best results when performing video-triangulation of the fragments trajectories (Figure 3.11). The used cameras did not have a synchronization function between them since they were cinematographic cameras. Since it was technically unfeasible to directly synchronize these three cameras, a flashlight was placed at the bottom of the slope pointing to a reflective surface so that it was seen in the frame of the three cameras. The flash was fired several times during each release to allow frame synchronization during the post-processing of the footage with a minimal error of 1/400 seconds. Some other cameras were also used to record the tests. In the last test performed, a UAV recorded each of the releases from a zenithal point of view and then captured several images of the deposit that allowed a 3D reconstruction using photogrammetry.
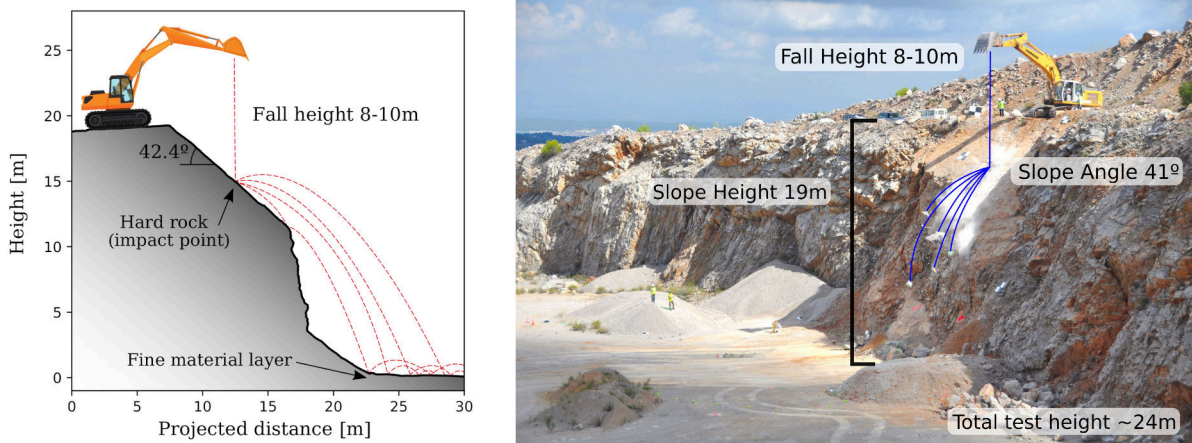


**Figure 3.7:** Selected profile of the testing site #4 (Matas et al., 2020b).

**Figure 3.8:** Blocks prepared for their release in testing site #1 being limestone the block lithology.



**Figure 3.9:** Blocks prepared for their release in testing site #3 being granite the block lithology.
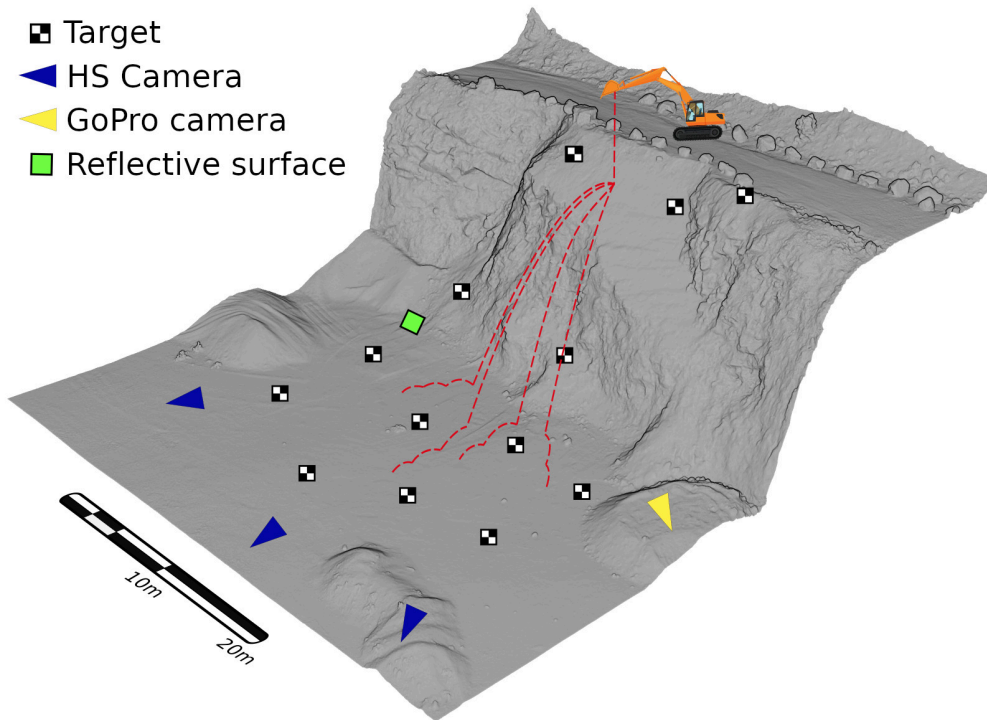
**Figure 3.10:** Position of the sensors used in test site #4 including high speed cameras, other regular cameras, the ground control points and the reflective device used for synchronization purposes.(Matas et al., 2020b)



**Figure 3.11:** One of the high speed cameras used to record the tests and the total station used to georrefenrence the ground control points placed on the scene.

## 3.2.2 Tests realization

During the realization of the tests safety was a priority issue. Once no operator was in the risky area all cameras started recording and the backhoe operator released the block. During its fall, the flashlight was shot several times for synchronization purposes as explained before. A UAV also recorded the releases from a zenith perspective in testing site #4. An example of the release of a block in test site #4 is shown on Figure 3.12.

**Figure 3.12:** Example of the release of a block in test site #4. The time step between selected frames is 0.33 seconds. (Matas et al., 2020b)

Once all fragments were stopped the UAV stopped video-recording and took pictures for building the photogrammetric model of each release. The zenithal UAV recordings at 4K gave great footage of the block fragmentation instant in which the block cracking pattern upon impact can be observed (Figure 3.13). Finally after checking the stability of the slope, measurements of the deposited fragments where done by tape and then another machine cleared the deposition area for the following release (in testing sites where a second machine was available).
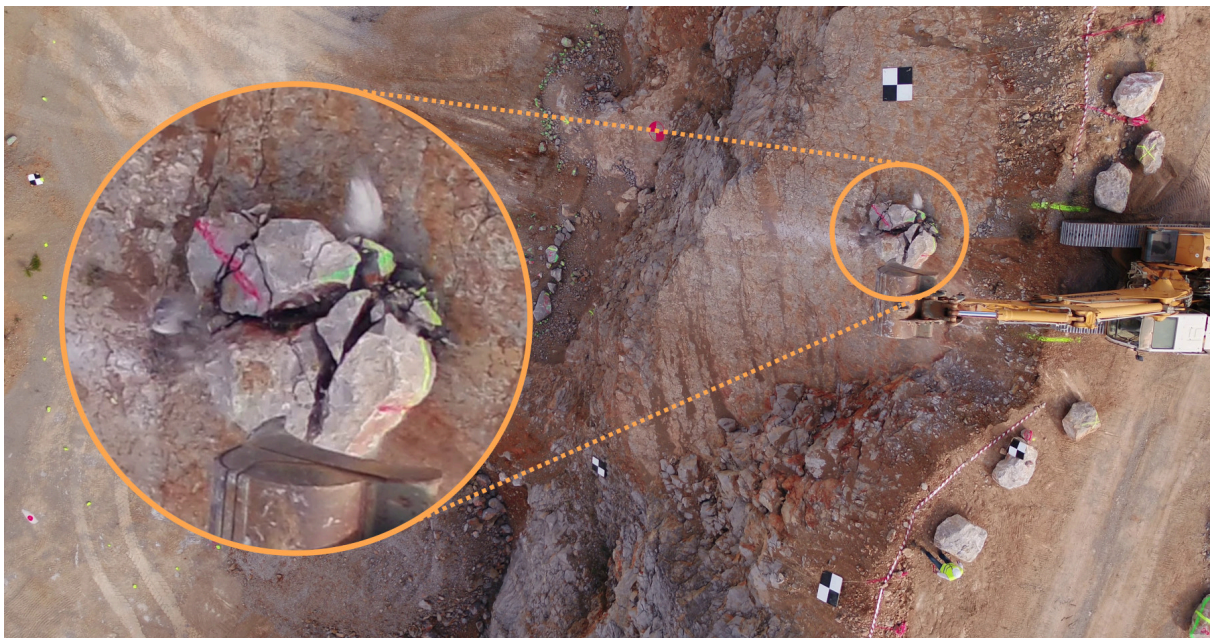


**Figure 3.13:** Detail of the fragmentation process of a block in test site #4 recorded from a UAV. The cracking pattern upon impact is perfectly visible.

### 3.2.3 Data processing and results

All data gathered during the tests was then processed. About 3TB of data were generated in the four testing sites including the high speed video cameras, the UAV zenithal videos and photos, auxiliary cameras footage and seismic signal. Although the methodology evolved after each testing site, the targets of processing all data were the same in the four cases: 1) Measurement of the size of each single released block; 2) in case a block fragmented, obtain its RBSD; 3) extract blocks' trajectories from video footage to determine their cinematics when falling through the slope and 4) correlate the seismic signal with the footage to investigate the effect of fragmentation on the seismic signature of impacts.

**Size of the tested blocks**

Different techniques were used to measure tested blocks before they were released. The simplest one was to hand measure them using tape. This approach requires taking three measurements corresponding to the edges of an approximate polyhedron that contain all the mass of the block. This is a tricky method and may be little subjective. For a better measurements, a 3D circular photo-survey was performed to each block in order to generate a 3D model using photogrammetry. This method gave high precision models of the blocks and allowed to measure their volume, center of gravity, inertial tensor etc. Figure 3.14 shows an example of the resultant model of block #11 in testing site #1.
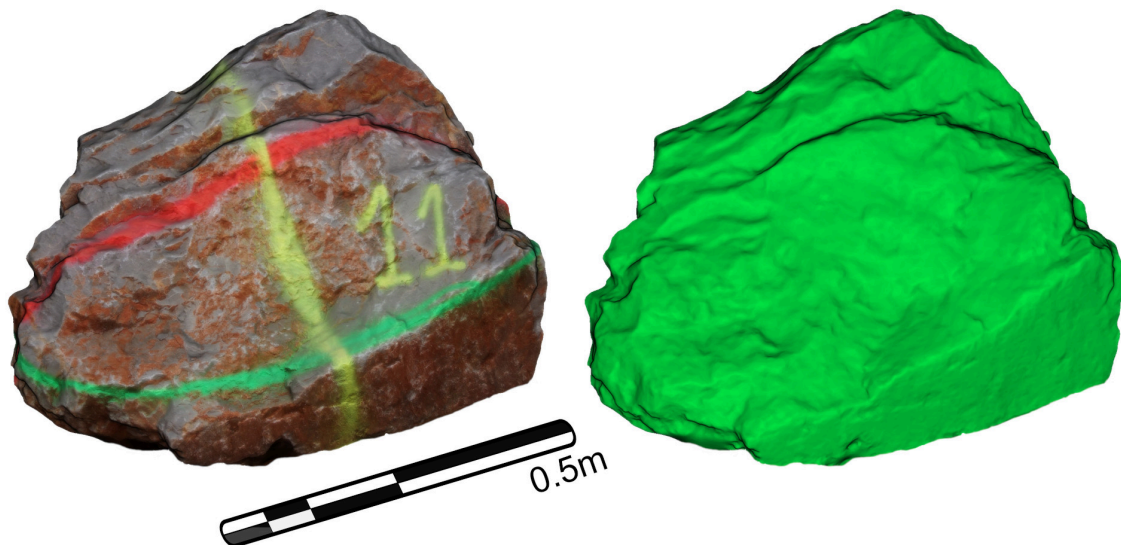


**Figure 3.14:** Example of a 3D model obtained from circular photogrammetry of block #11 in testing site #1. In the left image the texture is shown while in the right just the model with shades to see its details.

**Fragments' volume distribution**

The measurement of the deposited fragment volume distribution, also evolved after each testing site. The basic approach was to measure the fragments by hand using tape. The

criteria in this controlled scenario was to measure all identifiable fragments with a minimum smallest side of one centimeter. Smaller fragments measured where about 1x2x2 cm giving an estimated volume of 4·10-6 $m^3$. As far as the knowledge of the authors, experiments carried out during this research are the first ones to measure produced fragments in a fragmental rockfall with this level of detail.

Hand measuring method was very time consuming but effective and allowed a proper characterization of the RBSD of each release. However, this approach did not georreferenciate the fragment position and doing it using the total station was not feasible. In the last testing site a UAV flight was performed after every block release and allowed a generation of a 3D model of each deposit. Using the generated ortophotos from this models, measurement of all fragments area was manually done by the assistance of the videos to ensure the fragments correspond to the analyzed release (note that even the machine cleared the base of the talus after each release some small fragments could escape the shovel and stay in place). Identified fragments using this method in test site #4 are shown on Figure 3.15.
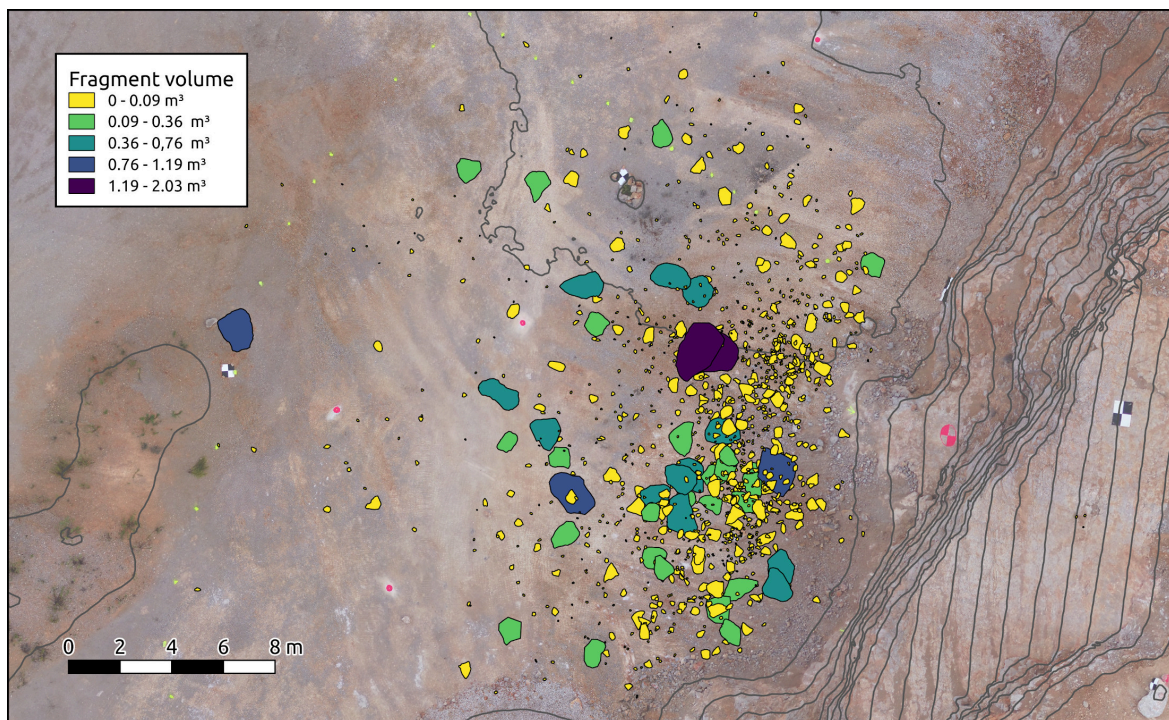


**Figure 3.15:** Superposition of all fragments measured on the ortophoto for each released block in testing site #4. The volume has been estimated from the measured area (Matas et al., 2020b)

This method allowed a proper positioning of the fragments and a measurement of the projected area, which were required for a proper calibration of RockGIS model in this scenario. However, since the RBSD must be expressed in terms of cubic meters, some assumptions had to be taken to transform this area distribution into volume distribution. This procedure is explained in Matas et al. (2020b). An extensive analysis of the obtained fragment distributions can be found in Ruiz-Carulla et al. (2020). Figure 3.16 shows the summary of the fragment distributions obtained for each released block for the four testing sites.
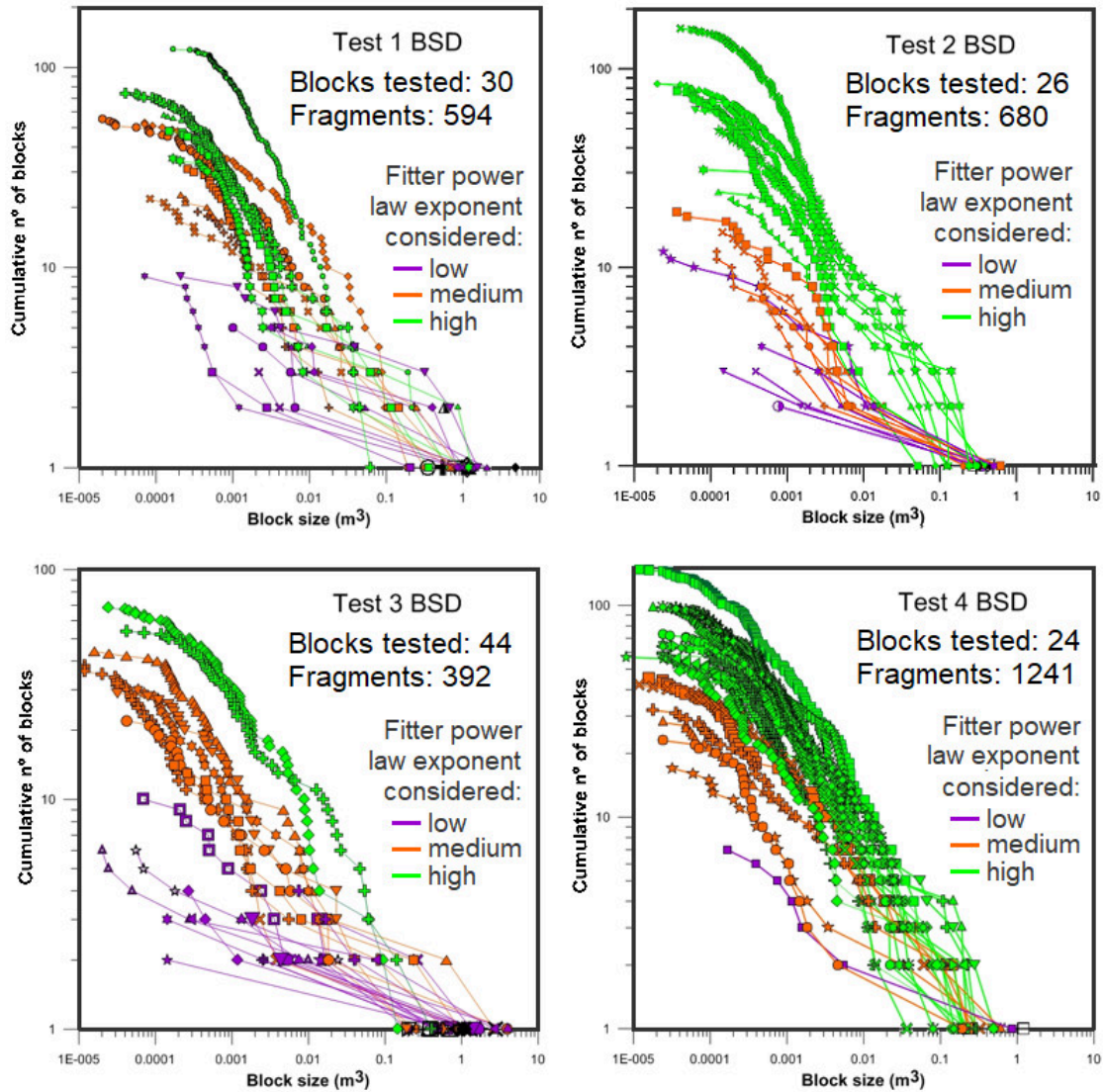
**Figure 3.16:** Block size distributions of all the fragments measures on each tested block, arranged by testing site. The distributions are colored with: low (purple), medium (orange) and high (green) values of the exponent of the fitter power law. (Ruiz-Carulla et al., 2020)

**Block trajectories**

To obtain block trajectories the footage obtained from the high speed cameras were used to triangulate the position of the block and the generated fragments during their release. The footage of these cameras was first synchronized using the flashlight placed in the scene and visible to each one of the three cameras. Then the center of gravity of each tracked block was determined in each of the three frames (corresponding to each camera footage). During the course of the research project, different methods were used to track the displacement of the center of gravity. It was first manually done by clicking on the gravity center of each frame of interest on the three images. This proved to be a very slow and tedious process since when a block broke it could produce several tens of fragments increasing substantially the amount of tracking time. In this first iteration of trajectory capturing process just the biggest blocks produced during fragmentation were measured.

To overcome these limitations, a member of the research group started a new research line for a semi automatic detection of the gravity center of the blocks (Prades et al., 2017). However, in this work just the results regarding the manual tracking of the blocks are included.

Once the gravity centers of the tracked blocks are defined on each one of the three images corresponding to a certain time, the computation of the position in the space is done. To do this computation, cameras must be first oriented and the relative position between then has to be computed. This is done by using the ground control points that where placed in the scenes and precisely georreferenced using GNSS technology and a total station. Once the position of all cameras is known, a spatial intersection of the light ray from the focal point of the camera passing through the marked gravity center point on the image is computed. Due to measurement errors it is very unlikely that the three traced rays intersect in the space and a minimization of the distance between them was performed using least squares to get the final three dimensional position of the blocks. Note that this video triangulation could be done by just using two video cameras pointing at the scene, but the third one proved to add extra accuracy on the intersection process and also reliability in the cases when one camera failed.

An example of the tracking of a block in testing site #1 is shown on Figure 3.17, and the corresponding vertical velocity obtained is shown on Figure 3.18. A non fragmenting block has been chosen in this figure for a better visualization. First, the block is released from the backhoe and it falls freely until it impacts with the inclined plane at an approximate speed of 13 m/s. This first impact corresponds to the first crest on Figure 3.18. Then, it follows a parabolic flight until it impacts again with the ground at 14 m/s, as can be seen in the second crest of Figure 3.18. The direction of the block is much more perpendicular to the impacting surface in this case and more energy is dissipated during the impact. Finally, the block follows little parabolas near the ground before stopping. In these last parabolas negative vertical velocities are observed since the reference system is pointing to the ground and the block has a vertical component towards the sky.

The shown process for capturing a single block trajectory was performed on the biggest produced fragment of each release of testing site #1 and #3. In testing site #2 the cameras had to be placed so far from the scene that the resolution did not allow a proper identification of the gravity center of the blocks in the frames of the video. Data of testing site #4 is being processed by the new in house software being developed at the time of writing this document. Figures 3.19 and 3.20 show the resultant measured trajectories on test sites #1 and #3 respectively. These measurements allow the characterization of the incidence velocity before an impact and the reflected velocity, which characterize the energy lost during the impact. Moreover, when a block fragments, the trajectory followed by each individual fragment is described. After breakage, fragments trajectories were observed to stay within a cone, which lead to one of the main hypothesis of the fragmentation module developed in this work. Figure 3.19 shows an example of a cone observed in the test site #4.
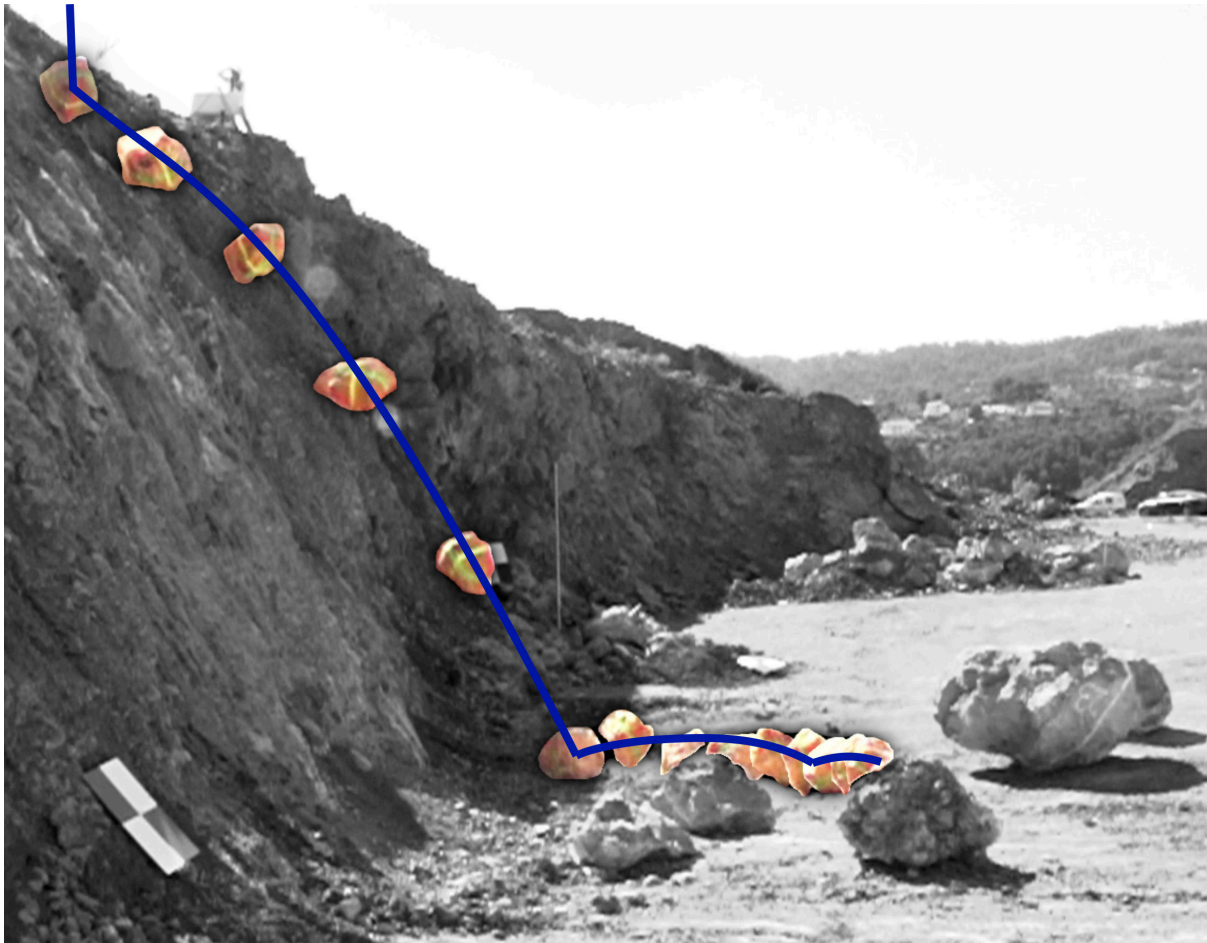
**Figure 3.17:** Sequence of the release of block #25 in testing site #1. For visualization purposes, a non fragmenting block was chosen. There are tho main impacts, the first on the slope and the second on the base of the talus.
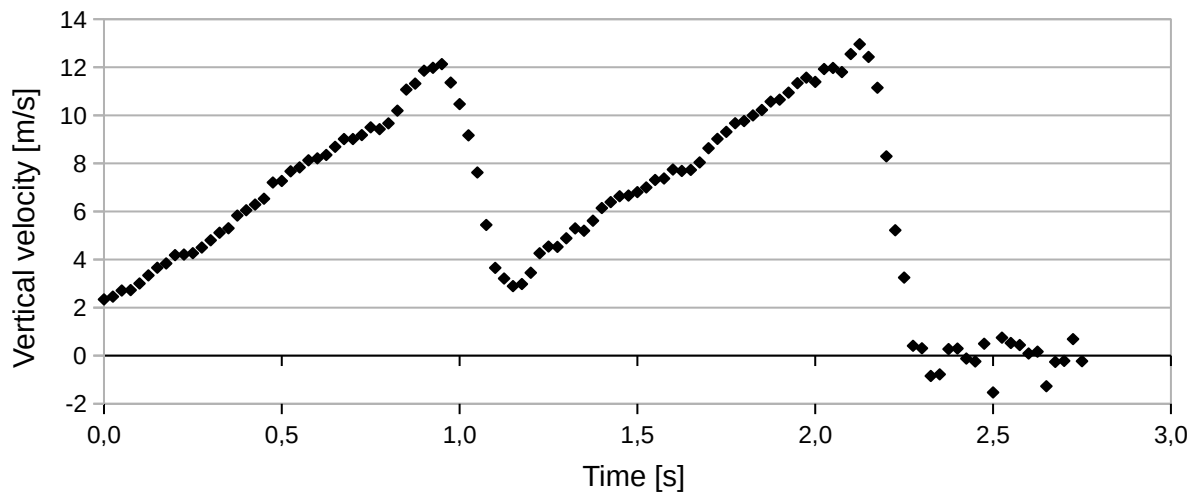


**Figure 3.18:** Vertical velocity profile obtained from video-triangulating block #25 in testing site #1. The two crests correspond to the two main impacts that can be observed in Figure 3.17.
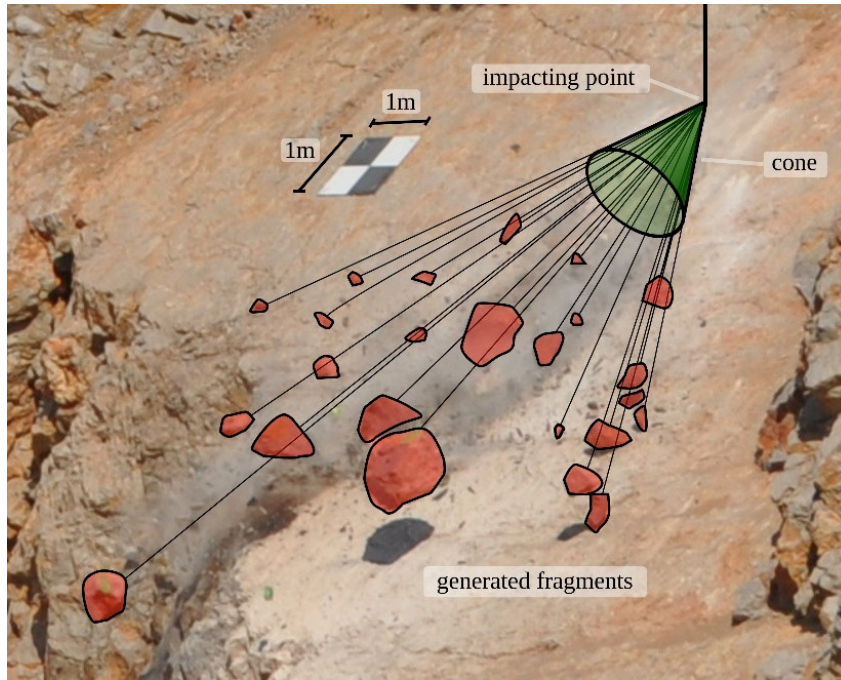
31

**Figure 3.19:** Example of a cone-shaped distribution of fragments produced after the impact of a block against a 42.4° inclined slope surface during a real-scale test performed in this study.
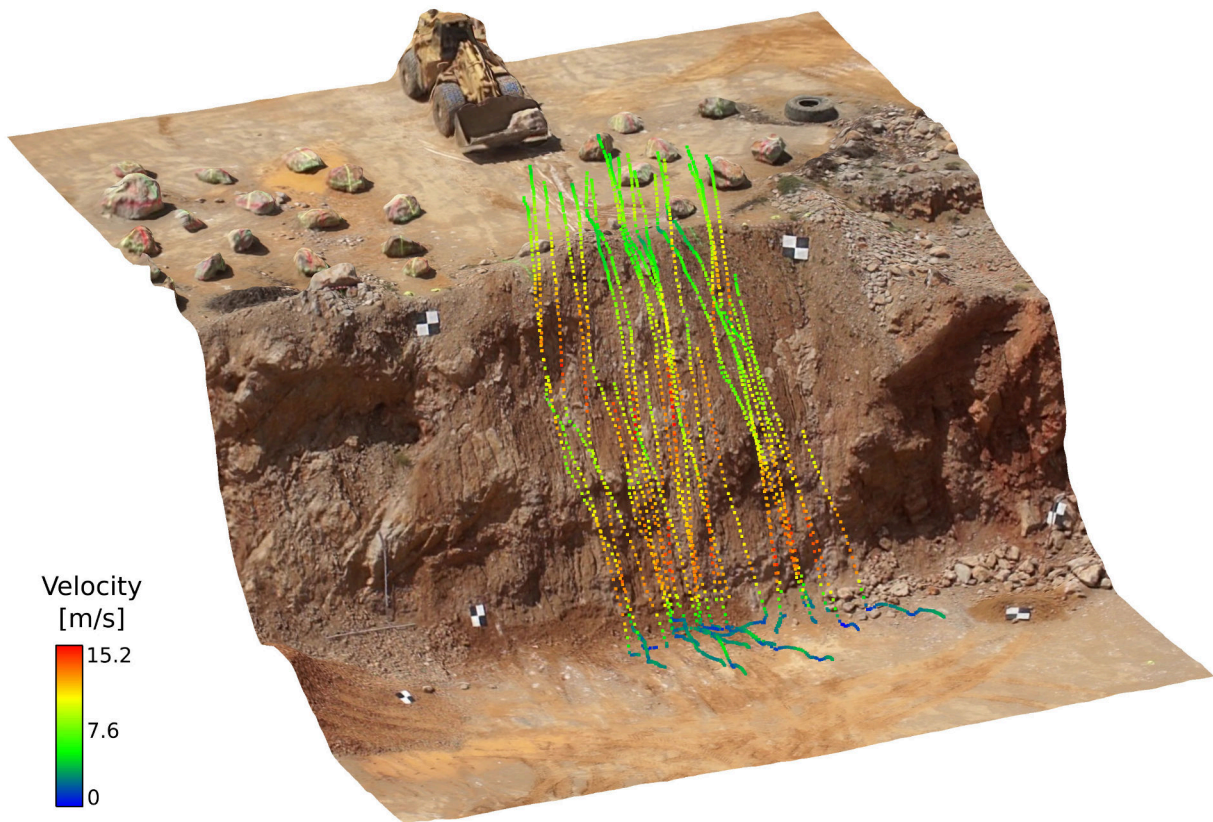


**Figure 3.20:** Measured trajectories of the blocks and, in case of fragmentation, the biggest fragment in testing site #1. Trajectories are overlapped with the 3D model obtained by UAV photogrammetry.

**Figure 3.21:** Measured trajectories of the blocks and, in case of fragmentation, the biggest fragment in testing site #2. Trajectories are overlapped with the 3D model obtained by UAV photogrammetry.
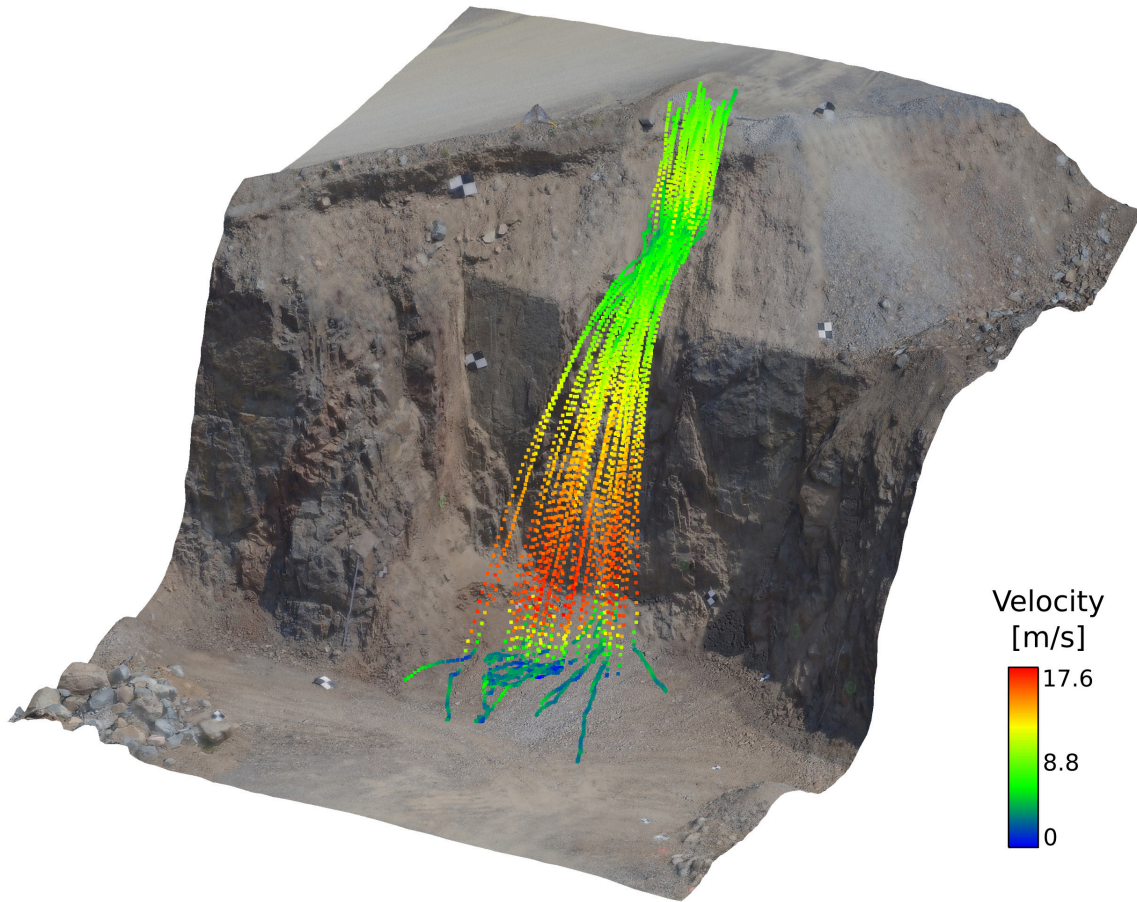
## 3.3   Reduced scale comminution test

Comminution is the breakage mechanism that occurs when multiple stacked blocks impact together. The analysis of inventoried rockfall events suggest that comminution tends to increase with the size of the falling mass (Ruiz-Carulla et al., 2016).

Real scale rockfall tests are typically performed to characterize rockfall motion parameters (Ritchie, 1963; Labiouse and Heidenreich, 2009; Spadari et al., 2012) and very few of these tests study the effect of primary fragmentation (Giacomini et al., 2009; Gili et al., 2016). In some rockfall events, a young debris cover is formed during the first impacts, with a substantial reduction of the particle size. The large amount of small particles generated in the debris cover suggests that beside the breakage of the particles, comminution by crushing and grinding may also occur during the impact. However, as far as the author is aware, the effect of comminution in rockfalls has not been studied yet.

The laboratory experiments done in this research aimed at studying the effect of block confinement on the dynamic fragmentation and on the resultant grain size distribution. The main hypotheses to check are that as lower is the position of a block in the stack: i)

the smaller are the fragments generated, ii) the greater the number of fragments created, and iii) both effects should intensify with the number of stacked blocks. The results have been published in Matas et al. (2020a).

### 3.3.1 Materials

The tested material was selected based on two main criteria. First, the material must be weak enough to break under the impacting energy conditions of the test and secondly, the commercial availability of enough quantity from different colors to be able to distinguish which fragments correspond to each initial piece. The material selected for the test were baked clay bricks. We discarded using low strength concrete pieces because the maximum fall height of our testing site was not enough to reach a high fragmentation degree with this material. Bricks have a standard size of 5 x 10 x 20 cm and five different colors. Figure 3.22 shows a sample of the bricks types with their relative position on the stacks. Their density ranges between 1.81 and 2.24 $g/cm^3$ depending on the color. Three settings were tested to evaluate the effect of the added dynamic load due to piece stacking: single piece, three stacked pieces and five stacked pieces (Figure 3.22).



**Figure 3.22:** Possible stack distribution of bricks tested: single brick, three stacked and five stacked.

### 3.3.2 Test set up

The tests were carried out in the Laboratory of Technology of Structures and Materials (UPC). A device was specially designed to place and release the bricks. It allowed the bricks to fall vertically without rotational velocity (Figure 3.23a). The total fall height was 4.26 m, which determined the impacting energy of the bricks stack. The concrete slab of the floor was protected with a 10mm thick steel plate placed on the impacting area. To stop the fragments ejected after breakage, a wood frame was built around the steel plate. This protective frame had wood boards around the perimeter with a height of 1.2 m and a plastic rack above the boards to allow light to enter the scene (Figure 3.23a).

Each one of the releases was recorded using a high-speed camera recording at 400 fps in HD and a GoPro camera. This high frame rate avoided blurring effect of the bricks at each frame. Since the tests were performed indoor, artificial light sources had to be used. To match light requirements of the high-speed camera, four spotlights were placed pointing the scene with a total power of 4000 W. The camera and the spotlights pointed the scene through holes in the wood boards protected with polycarbonate sheets and metal mesh respectively to avoid melting due to generated heat (Figure 3.23b). Several targets were placed both in the floor and the wood boards to allow cinematic estimations using the video records.
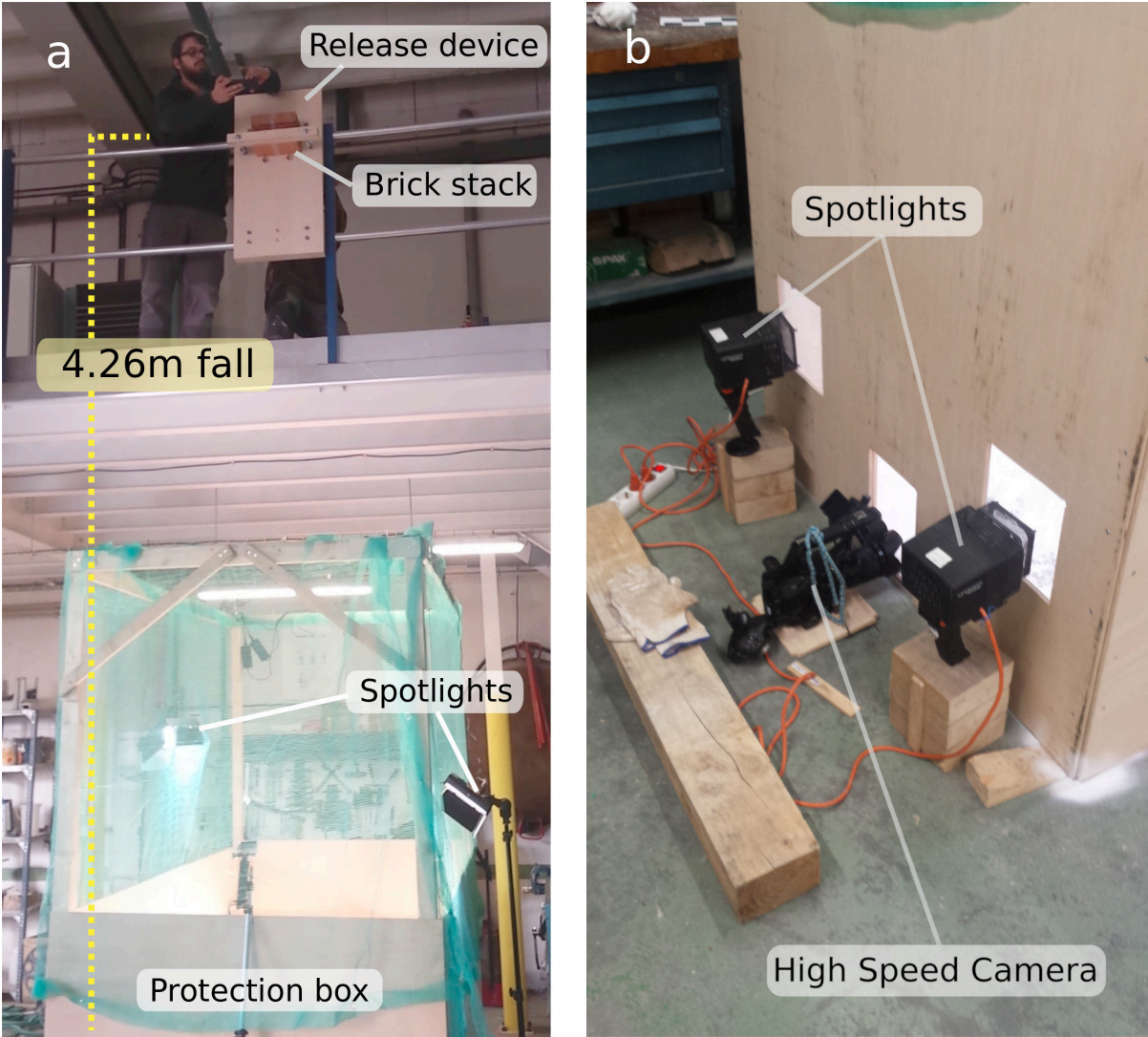


**Figure 3.23:** (a) Experimental test in laboratory with bricks release device and wood frame around the impact area. (b) Position of the high speed camera and spotlights protected by polycarbonate sheet and metal mesh respectively.

## 3.3.3    Test realization

A strict security protocol was designed to minimize risks during the execution of the tests. For each release, the procedure followed consisted of:

1. Placement of tracing paper and graphical targets in the impacting point to record the contact area during impact. In Figure 3.24 the graphical targets just behind the stack of blocks in the impacting point is shown.

2. Turning on the spotlights and the cameras.

3. Security check: everybody is placed and at a safe distance.

4. Release of the bricks' stack (see an example in Figures 3.24 and 3.25).

5. Turning off all cameras.

6. Photogrammetry: place a control volume in the scene for calibration and take a photographic coverage to build a 3D model of the fragment deposit.

7. After each release the tracing paper and all fragments were carefully removed, stored and marked with the release reference number to later proceed to the fragment classification and measurement.
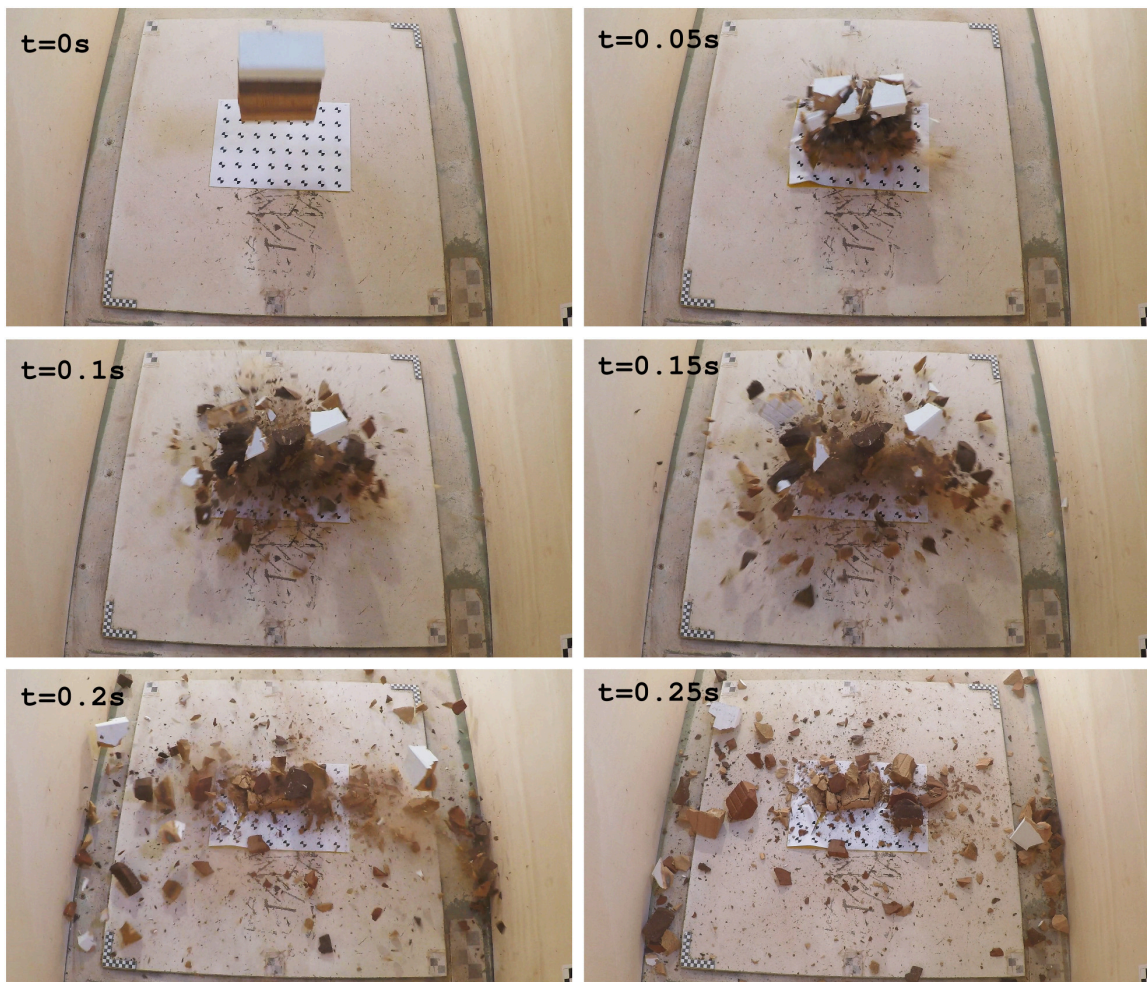


**Figure 3.24:** Sequence of test #60 where a stack of five bricks was dropped. Note how the brick on the bottom stays in place in the last frame.

**Figure 3.25:** Sequence of test #60 from the high speed camera footage. Note that this camera pointed at the scene from the reversed side than footage in Figure 3.24.

### 3.3.4 Data processing and results

The grain size distribution of each brick was obtained to characterize different fragmentation degree for each position within the stack. For each stack, first all fragments where sieved using a 4.76 mm sieve to discard very fine particles or dust. Figure 3.26a shows the sieve used while Figure 3.26b shows an example of the fragments that passed, which were discarded for the measurements. All the fragments retained in the sieve were visually classified by color (based on the position on the stack in Figure 3.27). The average amount of discarded mass was 5%.
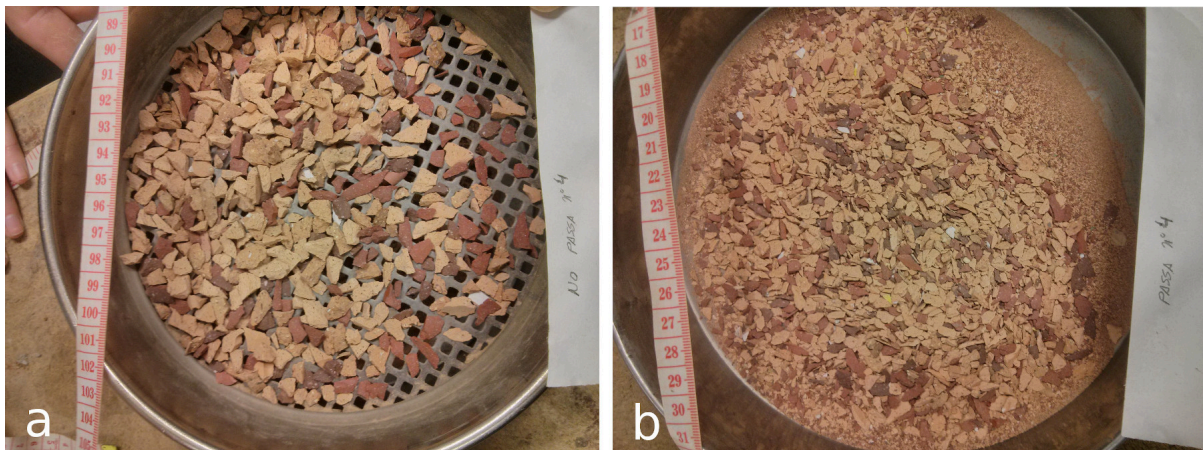


**Figure 3.26:** Example of the sieving used to discard the smallest fragments (a) Fragments not passing through the sieve and considered for the measurements; (b) fragments crossing the sieve and discarded.

**Figure 3.27:** Classified fragments produced by test #60.

Once classified by color, the weight of each fragment was measured using a high precision weighing scale. The weighing scale available in the lab had an old interface to connect to a computer and the measurements had to be manually annotated. This process was extremely slow and to speed it up a semi automatic capturing system was build using a webcam. The webcam pointed the LCD screen of the weighing scales and a specifically designed python code captured the numbers (Figure 3.28). The code used the open source computer vision library OpenCV. When the operator pressed enter key the recording was automatically stored in a spreadsheet file. This trick speed up the process by 3 and was a significant time saving considering that we measured several thousand fragments. Finally, knowing the density of each of the bricks, the weights could be transformed to volumes thus obtaining the grain size curve of each tested brick. This whole process lasted a couple of weeks.
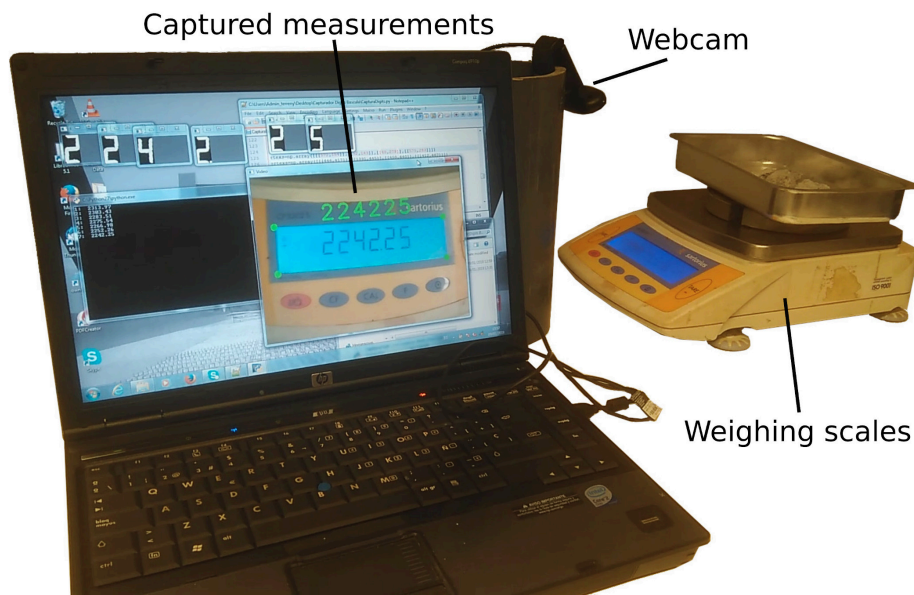


**Figure 3.28:** Weighing station set up to overcome the weighing scales available limitations. A computer vision code with a camera pointing to the LCD screen records the measurement directly to a file.

After the color classification and measurement of the fragments, the maximum volume and number of fragments of each tested brick were known. Moreover, since each color corresponded to a specific position in the stacks, the different fragmentation behavior depending on how many bricks had each one on top was observed.

Figure 3.29a and 3.29b show the grain size distributions obtained on a test of 3 and 5 stacked bricks respectively. The relative position of the bricks within the stack is indicated from 1 to 3 or 5, being the brick "1" the located at the bottom.
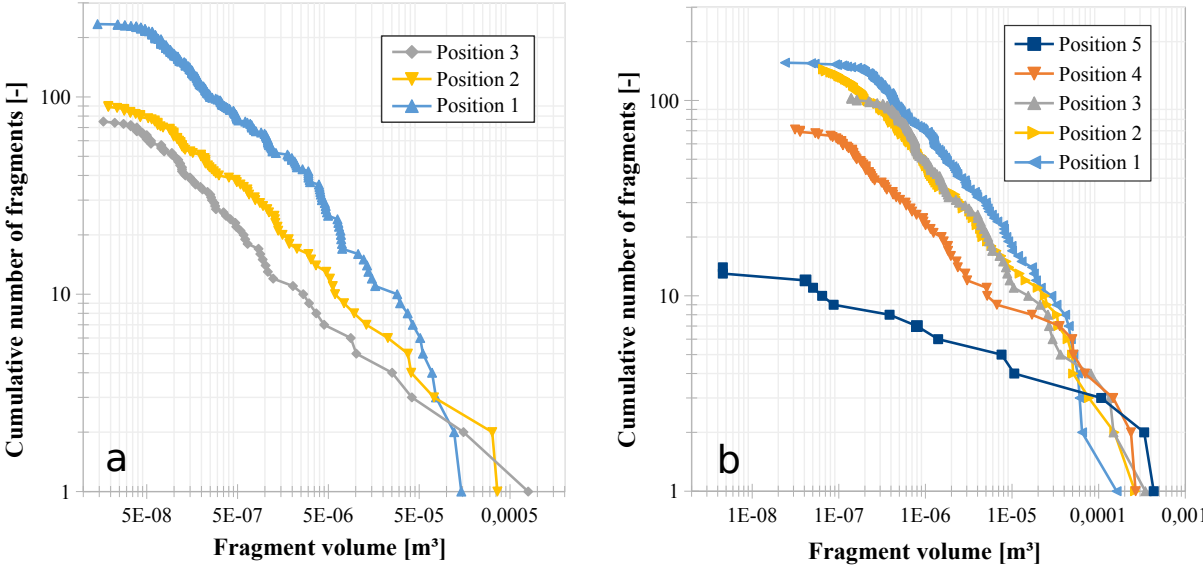


**Figure 3.29:** Cumulative number of fragments against fragment volume in (a) test number 62, corresponding to a 3 bricks stack and (b) test number 33 corresponding to a 5 bricks stack.

The plots 3.29a and 3.29b highlight the influence of the brick position on the number and size of the resultant fragments. The lower the position of the brick, the smaller the size of the maximum fragment and the greater the number of generated fragments. The slopes of the distributions look pretty similar except by brick in position 5 on test 33 (Figure 3.29b) which broke in three main fragments only.

The number of generated fragments on each position of the stacks for 5 bricks tests are shown in on Figure 3.30 It clearly shows how the number of fragments generated increases when lowering the position of the brick on the stack. The maximum number of fragments was 378 for the brick at the bottom position of test #84. The maximum, minimum and average number of fragments generated at each position are shown on Table 3.1. In a few cases, there was a brick that did not break at all. Analyzing the videos, we observed that the unbroken bricks landed on an edge or on top of a fragments' pile of the bottom brick which had already broke.

**Table 3.1:** Statistics on generated fragments depending on the position of the bricks in the 5 bricks stacks. Position 1 corresponds to the bottom brick.

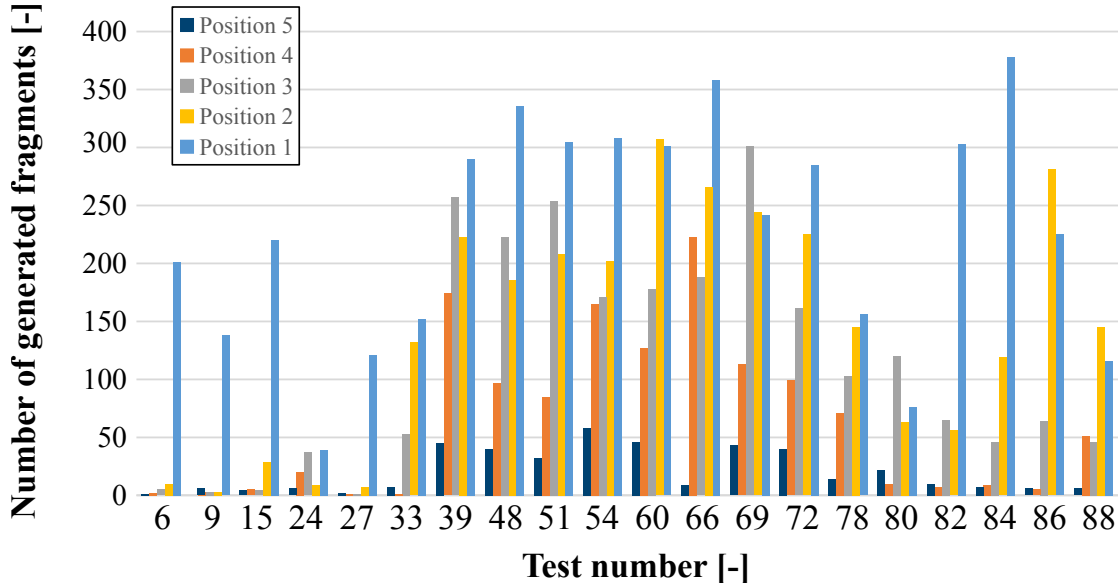| Position | Max # frag | Min # frag | Average # frag |
|----------|-----------|-----------|----------------|
| 5 | 58 | 1 | 20.2 |
| 4 | 223 | 1 | 63.4 |
| 3 | 301 | 1 | 114 |
| 2 | 307 | 3 | 143 |
| 1 | 378 | 39 | 227.5 |



**Figure 3.30:** Number of generated fragments in 5 brick stacked tests for each position in the stack. Position 1 corresponds to the bottom brick while position 5 to the top block in the stack.

In many tests most of the fragments generated by the brick placed at the bottom of the stack remained in place at the same point where they contacted the steel plate (Figure 3.31). In Figure 3.24, a sequence of test #60 (5 brick stack) shows how fragments are quickly ejected except those of the bottom brick, which remain in place. At the first contact with the steel plate, the fragments generated in the outer edge are ejected but the ones at the center cannot escape and tend to stay at the impact point. Then the deposit shows the brick broken in several fragments but maintaining the general shape of the initial brick, as in a puzzle (Figure 3.31).

**Figure 3.31:** Detail of the bottom block of the release #60 (Figure 3.24) The cracking pattern is observed but the fragments in the middle remain in in place like a puzzle

### 3.3.5 Test conclusions

The grain size distribution of fragments obtained from this experimental test confirms that the blocks undergoing greater confinement (which increase towards the lowest position on the stack) generate a greater number of fragments while decreasing their maximum size.

This phenomenon, combined with the reduction of mobility of the confined fragments, which remain in place at the impact point, may explain the formation of Young Debris Cover in real cases where the initial released rock masses are big enough to produce both the confinement and comminution effect. The fragments generated at the edges of the bricks were quickly ejected. In this case, the release velocity increased with the confinement.

When considering fractal theory and adjusting power laws to the fragment distribution of each brick in the pile, the slope defining the curve decreased as higher was the position of the block on the stack. This information is useful when simulating huge rockfalls formed by several blocks since the parameters controlling the fragmentation law may be adjusted consequently so as to reproduce this comminution effect and increase the fragmentation degree of the blocks placed on the lower positions.

As a final remark, many researchers have focused on fragmentation recently since new technologies allow better data acquisition in field and laboratory tests and new methodologies for numerical simulations. However, there are still few publications in which the kinematics of the fragments is analyzed and/or experimentally measured. The energy distribution after fragmentation and subsequent momentum increase of some of the frag-

ments remains as unexplored topic.

## 3.4 Modelling real scale fragmentation tests in Yade

During the realization of this research the author visited the *Institut national de Recherche en Sciences et Technologies pour l'Environnement et l'Agriculture* (IRSTEA) in Grenoble (which has currently been recently renamed INRAE). At this research institute, they have a lot of experience in the study of rockfalls. They have made important contributions in the field of real-scale experimentation as well as in the numerical simulation of rockfalls. For the numerical simulations they have contributed to both stochastic and deterministic approaches using the Discrete Element Method (DEM) for simulating the interaction between rockfalls and forests (Toe et al., 2018) and with different mitigation structures (Lambert et al., 2013; Mentani et al., 2016; Coulibaly et al., 2019; Lambert et al., 2019).

The aim of this research stay was to evaluate the feasibility of performing full scale DEM simulations of the real scale rockfall fragmentation tests performed in quarries (section 3.2) taking advantage of hosts great expertise in the use of Yade DEM code. Stochasticity is a key factor in rockfalls but when performing real scale or laboratory tests the amount of possible configurations is limited (for example regarding the falling height, restricted by the available machinery and the topography of the site or the initial kinematics of the blocks). With a functional DEM model, calibrated with field tests, several thousands of different configurations could be numerically tested for a better understanding of the fragmentation phenomena and the limit would just be the available computing power. Results from this kind of numerical simulations can be used for feeding meta-models that can be implemented in stochastic rockfall simulation programs.

In the short period of time that the stay lasted, it was possible to build a functional model and carry out preliminary simulations with promising results, but an exhaustive calibration of the model was not possible due to time constraints. However, the feasibility of simulating real-scale fragmentation tests was demonstrated and the ground was paved for future lines of research. In this section, the reader will find first a very brief introduction to DEM method including a description of the code used Yade. Then, the build process of the scene in the program, the python code written for the specific analysis of fragmentation and the usage of a High Processing Computer (HPC) to run the simulations are described. Finally the obtained results are shown and discussed.

### 3.4.1 Discrete element method and Yade

The Discrete Element Method (DEM) is a numerical method for modelling the dynamics of solid particles which interact with each other at discrete contact points (Zaho 2017). This method was first proposed by Cundall and Strack (1979) to study the mechanical behaviour of rock at the microscopic level. The use of this method was extended to simulate other materials like liquids and solutions, granular matter, bulk materials, powders and blocky or jointed rock masses.

In DEM materials are represented by rigid spheres or sets of interacting rigid spheres and other geometries. The simulations accounts for particles stress state and kinematic state

of each one (position, linear velocity, rotational velocity and contact forces), updating them at every numerical time step iteration. An explicit integration of Newtons' second law motion is used to obtain the translational and rotational displacement of each particle. Contact forces between particles are calculated using force-displacement contact models (Cundall and Strack 1979; Itasca 2003). It is assumed that the velocity is constant during the time step, then small time steps have to be used to achieve stable numerical solutions. This time step also has to account for the specific conditions of the simulated scene since stiffness of the particles and high linear velocities could produce unwanted results if the time step is too high. In case of particles with high stiffness, high time steps may result in high indentation between particles that produce an extremely large elastic force and make them reach high accelerations that may make the whole simulation unstable. If expected velocities during the simulation are high and the time step chosen is not small enough some particles may be moving in intersecting trajectories but the contact would not be detected by the algorithm. During all the simulation, all spheres state variables are tracked and stored for evolution visualization purposes.

The numerical calculation cycle in DEM starts by detecting the interactions between particles. With the contact points and the overlapping distance, the force exerted by the particles is calculated using the force-displacement models. Once the forces are computed, they are applied to the center of the sphere and particle displacement, velocity and accelerations are computes according to Newtons' second law of motion at each numerical iteration. State variables of all particles are updated and the loop continues by detecting again the contacts between particles in the newly computed configuration (Figure 3.32). This loop continues until some stop conditions are reached, for example a specific number of iterations or a specific state of the spheres like low velocities.
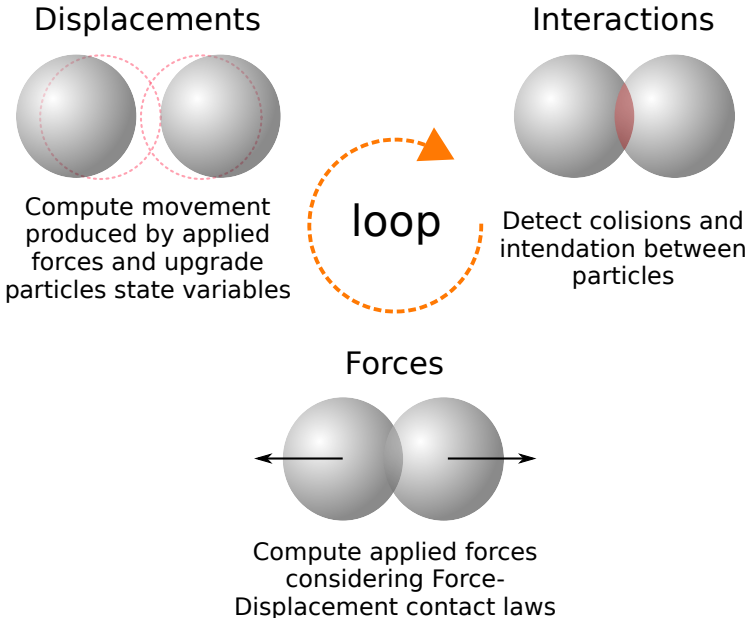


**Figure 3.32:** Calculation cycle in Discrete Element Method

There are several implementations of the DEM method, both commercial (PFC3D, EDEM, Chute Maven etc.) and open source (LIGGGHTS, MFIX-DEM, YADE, PyGranESyS-Particle etc.). In this research, Yade DEM code was used. It is an extensible open-source

framework for discrete numerical models, focused on Discrete Element Method. The computation parts are written in c++ using flexible object model, allowing independent implementation of new algorithms and interfaces. Python is used for rapid and concise scene construction, simulation control, postprocessing and debugging (Šmilauer and Chareyre, 2015).

To build an object in Yade, several spherical particles are filled in a confined space defined by the user. This space is defined by geometric shapes produced by CAD-programs such as stl or meshes. In case of rigid breakable bodies, like rocks, once the shape is filled with spheres bonds are created between them to ensure they are attached and form a rigid structure. These bonds act as a spring between the particles and can use different bonding laws implemented in the code. In case the limit stress is reached in the bond, it breaks. This is how a crack may start in a simulated rock mass.

## 3.4.2 Modelling real scale fragmentation tests in Yade

For simulating the real scale rockfall tests in Yade the first step was to geometrically define the scene. The scene is composed by two main elements: the released block and the ground surface. The shape of each block was obtained, as explained in previous sections, using photogrammetric techniques to build a 3D model. This 3D model is used as a boundary geometry to build the sphere packing. Packing algorithms considering a boundary surface require that all normal vectors point inside the block so as to make a proper intersection. Otherwise, the result is a cube with a hole of the desired shape inside it. This basic pre-process was done using open source software Blender. The packing method used in Yade was random dense pack. Figure 3.33 shows of block #8 original mesh and the obtained packing considering a sphere radius of 2 cm. For this block, a total of 24k spheres with a radius of 2 cm were required. The packing process tends to be slow since several iterations compressing the set of spheres are performed before reaching the desired initial state. However, well-known techniques such as using pre-packed sets of specific sphere radius are accelerate the packing process.
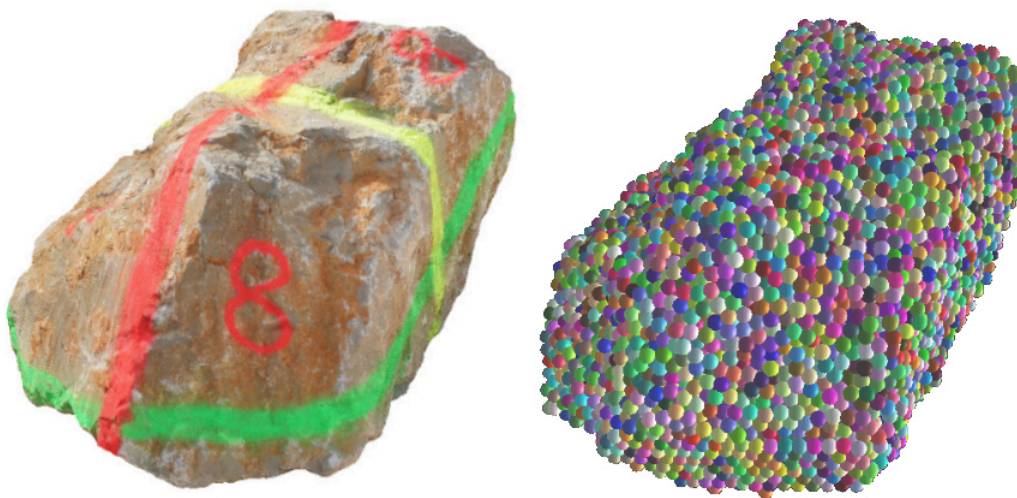


**Figure 3.33:** Example of the sphere packing inside a 3D mesh of block #8 formed by 25k spheres. The radii of the spheres is 2 cm.

Once the packing is done, the particles are bonded together following a linear elastic–plastic law which has proven to be well adapted to simulate cohesive-frictional materials (Scholtès and Donzé, 2013). The material definition used in Yade was the JCFcpMat (Jointed Cohesive Frictional Material). This material definition allows the introduction of joints and allows the simulation of crack propagation inside rigid bodies (Scholtès and Donzé, 2012). The interactions between spheres are created for each sphere with the surrounding spheres at a user defined distance $d = \gamma_{int} \cdot r$ (where r is the sphere radius). This definition of the bindings allow the generation of a bond between particles that are almost together but not mathematically in touch. Figure 3.34a shows the interactions that would be created in case of just considering contacting spheres. In case of considering a value of $\gamma_{int} = 1.5$ the grain interlocking in higher as shown in Figure 3.34b.
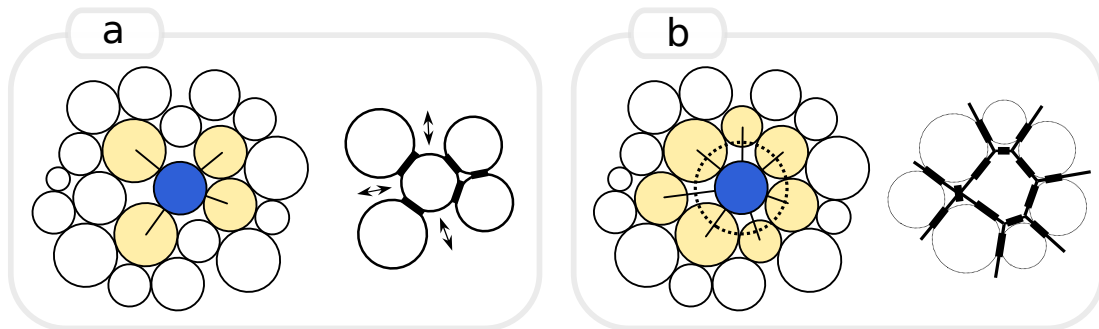


**Figure 3.34:** Example of the effect of the interaction range on the contact fabric and grain interlocking. In (a) $\gamma_{int} = 1$ while in (b) $\gamma_{int} = 1.5$. This figure has been adapted from Scholtès and Donzé (2012).

To complete the block building in Yade, a first single time step must be run in order to detect contacts inside the interaction range, build the actual interactions and finally reset equilibrium distance between particles. The interaction law between particles is considered elastic in compression and traction with a cohesion and a tensile strength to break the interactions and allow breakage. For setting the initial state of the block (velocities), formed by the set of spheres, no specific function was available in Yade and it had to be coded. The known variables extracted from field experimentation were the linear and angular velocities of the block with respect to its center of mass. In DEM when imposing a velocity it has to be done individually to each sphere. Using basic rigid body kinematics physics each particle linear velocity was calculated and imposed using a simple python script. In this point, the block is built in the scene and has the field measured linear and angular velocities.

The material definition used (JCFcpMat) allows, as the name indicates, the consideration of joints inside the bodies. The joints are introduced in Yade as planes and different material properties can be assigned to all spheres intersecting with this planes. Spheres directly interacting with other spheres intersected by the joint plane are also detected and their material properties can also be modified. Figure 3.35 shows the same block that in Figure 3.33 but with two joints. The dark blue spheres are directly intersecting the defined joints planes while the particles in red are interacting with the first ones. In the real scale test performed the boulders were mostly massive. However, when considering natural rockfalls the presence of joints or weak planes is common. Some simulations were

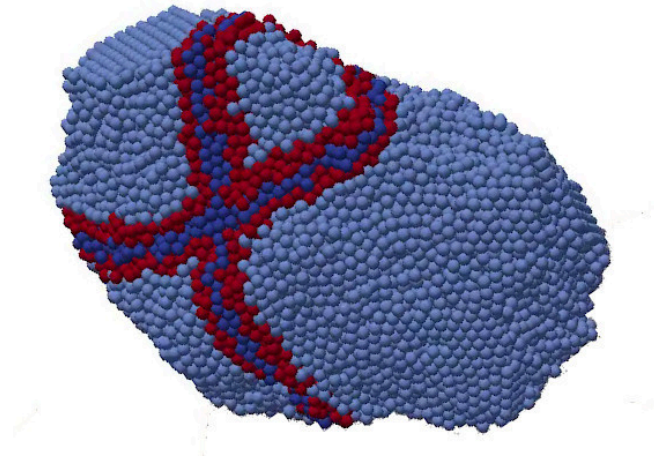carried out considering presence of joints to test the method.



**Figure 3.35:** Example of a block with two joints. Dark blue spheres intersect the defined joint planes. Red spheres do not intersect with the plane but interact with dark blue spheres.

Once the block is built, it is time for the ground surface. The shape of the ground surface was also obtained using photogrammetry, but in this case using photos taken from a UAV (see section 3.2). When using 3D meshes in DEM, it is important to note that there is a singularity line in the intersections of the planes. For smooth contact and avoiding unexpected behavior and computational problems, the use of Pfacets is recommended in some scenarios. Pfacets are polyhedrons composed by three spheres which act like nodes, three cylinders that join the spherical nodes and two triangular facets or planes that cover the cylinder (Figure 3.36). The use of Pfacets overcomes the problems produced in the planes intersections by smoothing the contact with a cylinder or a sphere in the vertexes.



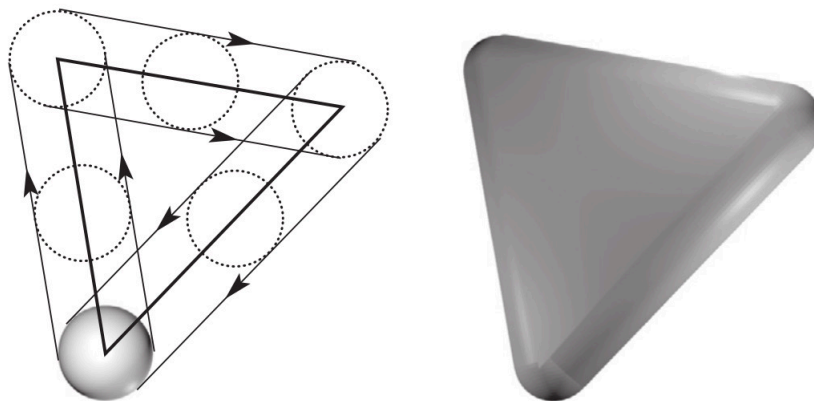**Figure 3.36:** Geometrical definition of a Pfaced composed of three sphere nodes, three cylinders and two facets. (Effeindzourou et al., 2017).

The 3D terrain mesh was very precise and had more than 1M faces. When converting this high number of faces to Pfacets, more than 8M elements would have been considered in the simulations, drastically increasing the computational time due to the high number

of interacting elements in the scene. To overcome this limitation, the mesh was simplified while maintaining its representative geometric characteristics. Figure 3.37 shows the original highly detailed mesh in the left side and the simplified Pfaced mesh in the right side used for the simulations.
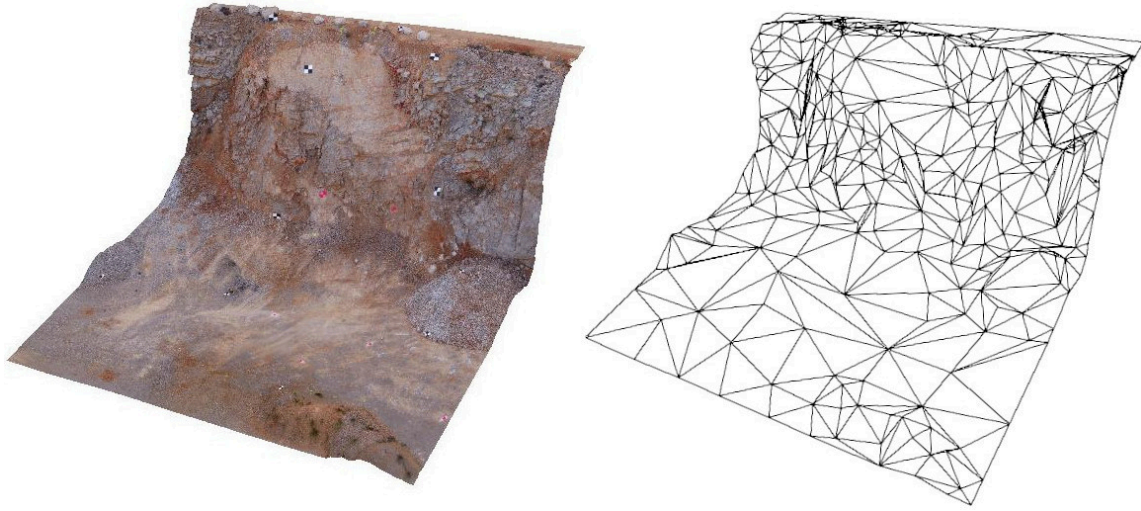


**Figure 3.37:** Simplification of the UAV high definition mesh (left side) to a simplified Pfacet mesh in Yade (right side).

Both the terrain and the block have to be placed in the virtual space reproducing the initial conditions of the release. The positions of the released blocks were recorded during the tests and just a local reference system conversion was required to place them on the right initial position in the simulation. With the elements in place everything was ready to launch the simulation.

As a first approach, the time step used in the simulations was $10^{-6}s$. During the simulation the position and state variables of each sphere were recorded in a vtk file that could then be visualized in the open source scientific visualization software Paraview. Computation time for a whole realization ranged from 10-30h running on eight cores and depended on the number of generated fragments. The most demanding engine in the Yade iteration loop was the interaction one (approximately six interactions per sphere for about 25k spheres). Computations were run on Titani cluster in UPC, a HPC formed by 5 DELL PowerEdge R630 computing nodes running CentOS. Some hacking into Yade code was required in order to compile it in Titani since several dependencies had to be adapted lo local libraries. Once compiled, it run smoothly and a fast parallel queue with a maximum of 6 jobs using 8 to 12 cores during 24h and a slow processing queue with 2 processes for a maximum of 14 days were used depending on the expected duration time of the simulations.

### 3.4.3 Results and discussion

During each simulation Yade exported the state of all spheres in the scene to a vtk file. However, this raw results gave no information about how many fragments were produced nor their volumes since it just stored the stare variables for each individual sphere. A

python fragment segmentation post processing algorithm was developed to identify which subsets of spheres were bonded at each simulation time step. This algorithm recursively looped through all spheres. It takes a first sphere, checks with which neighbors spheres it has an active binding and stores them in a list. Then for each added sphere the process is repeated and all bonded spheres are also included to the list (excluding the ones that are already in the list). Repeating this process until no new bonded spheres are found gives a list of all spheres belonging to the same fragment.

After the fragment segmentation algorithm was run and all spheres where associated to a fragment identifier, the fragment state variables could be computed by finding the gravity center of the fragment considering all corresponding spheres. Then, using again the rigid body dynamics, both the linear and angular velocities of the fragment could be computed. The total fragment volume was also computed by adding all individual sphere mass. After this process, a separate vtk file containing spheres representing each fragment was obtained. Figure 3.38 shows an example of block #8 impacting against a flat plane and the results of the fragment segmentation algorithm. Each red sphere corresponds to a segmented fragment and its size is proportional to the fragment size. In t=0.1s the block has started to break, however since not all bonds are yet broken the algorithm associates all the spheres to a single fragment. In t=0.2s more bonds are broken and the segmentation algorithm properly discriminates between fragments and creates a sphere in the center of mass of each one while storing all state variables (linear and angular velocities, mass, number of spheres etc.)
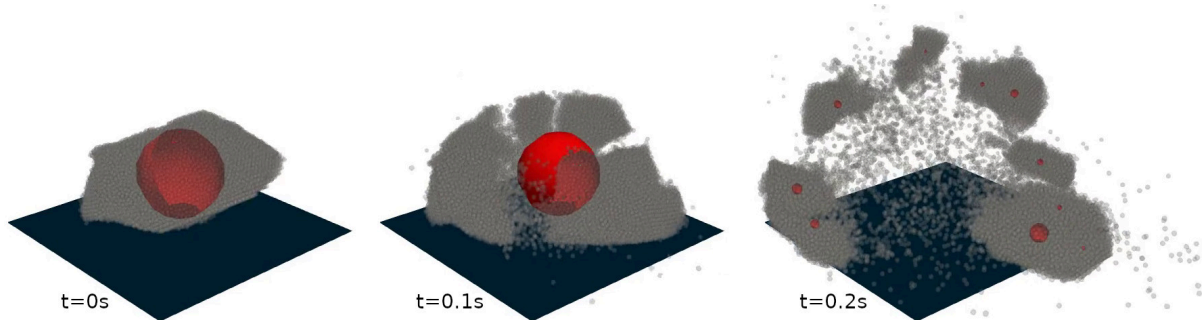


**Figure 3.38:** Example of a fragmentation upon an impact with a plane and the results of fragment segmentation. Red spheres size are proportional to fragment volume.

The simulation of a single block impacting with a plane were able to reproduce fragmentation phenomena including crack propagation and tension waves propagation inside the mass. Figure 3.39 shows an example of a block impacting a plane at 10 m/s and 0.5 rad/s where the color of the spheres depends on the corresponding normal stress. When tension in the bonds reach the critical value they break and causes them to repel each other and a crack begins to spread.

**Figure 3.39:** Example of the normal stress on the spheres forming a block when impacting against a plane at 10 m/s and 0.5 rad/s.

When considering fractures inside the blocks, the simulations gave consistent results. Figure 3.40 shows a sequence of the simulation of a b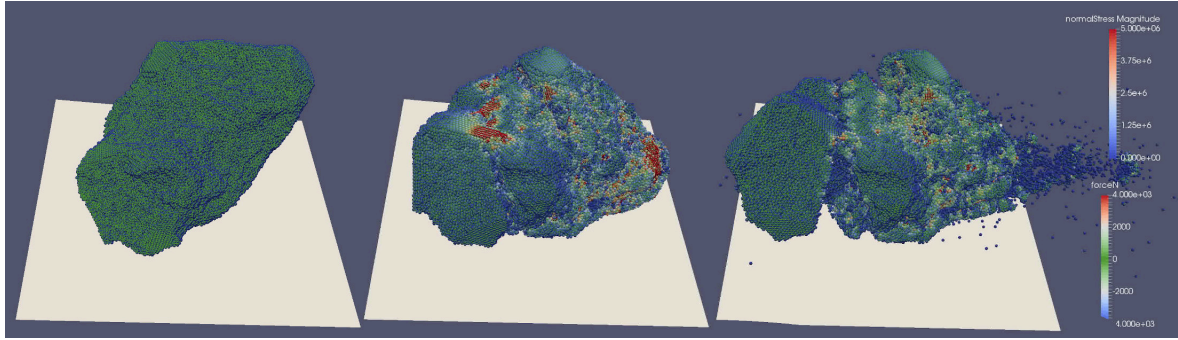lock with an initial weakened plane representing a fracture. When impacting the plane, the first bonds to break are the ones in the weakened plane as expected but rapidly other cracks appear in the massive parts of the block where no joints were imposed. The energy release after bonds brake eject the fragments and convert what initially was just vertical linear momentum into lateral momentum. In this figure, the colors of the spheres represent the remaining bonds with interacting particles with respect the initial bonds. Spheres are blue if no bonds have been broken and red when all bond are broken. Newly generated faces are shown in light blue since approximately half of the bonds have been broken (the ones corresponding to the other side of the new face).

The simulations on the real scenario confirmed the feasibility of performing virtual testing campaigns. Figure 3.41 shows an example of block #8 test with a linear impacting velocity of 8 m/s and a rotational velocity of 0.7 rad/s.

Even the results were really promising, some more work should be done to make this model absolutely functional. The next step would be the calibration of the parameters controlling the definition of the materials and the interactions between the spheres and the surface so as the results match satisfactory the field data. The goodness-of-fit indicators to calibrate the model would be similar to the one shown in Matas et al. (2020b), considering both the size distribution of the generated fragments and the final deposition runout. The model is very sensitive to the stiffness of the materials and the size of the particles used. Both conditions the iteration time step to use and if not properly adjusted it may lead to small computation time steps requiring unfeasible computational time. Although Yade can run in multiple cores, there is a limitation on how many cores increment the real computation speed since at a certain number of cores in between 6-10 depending on the simulation, the overhead produced by the information exchange between the cores counteracts the increase of computation power.
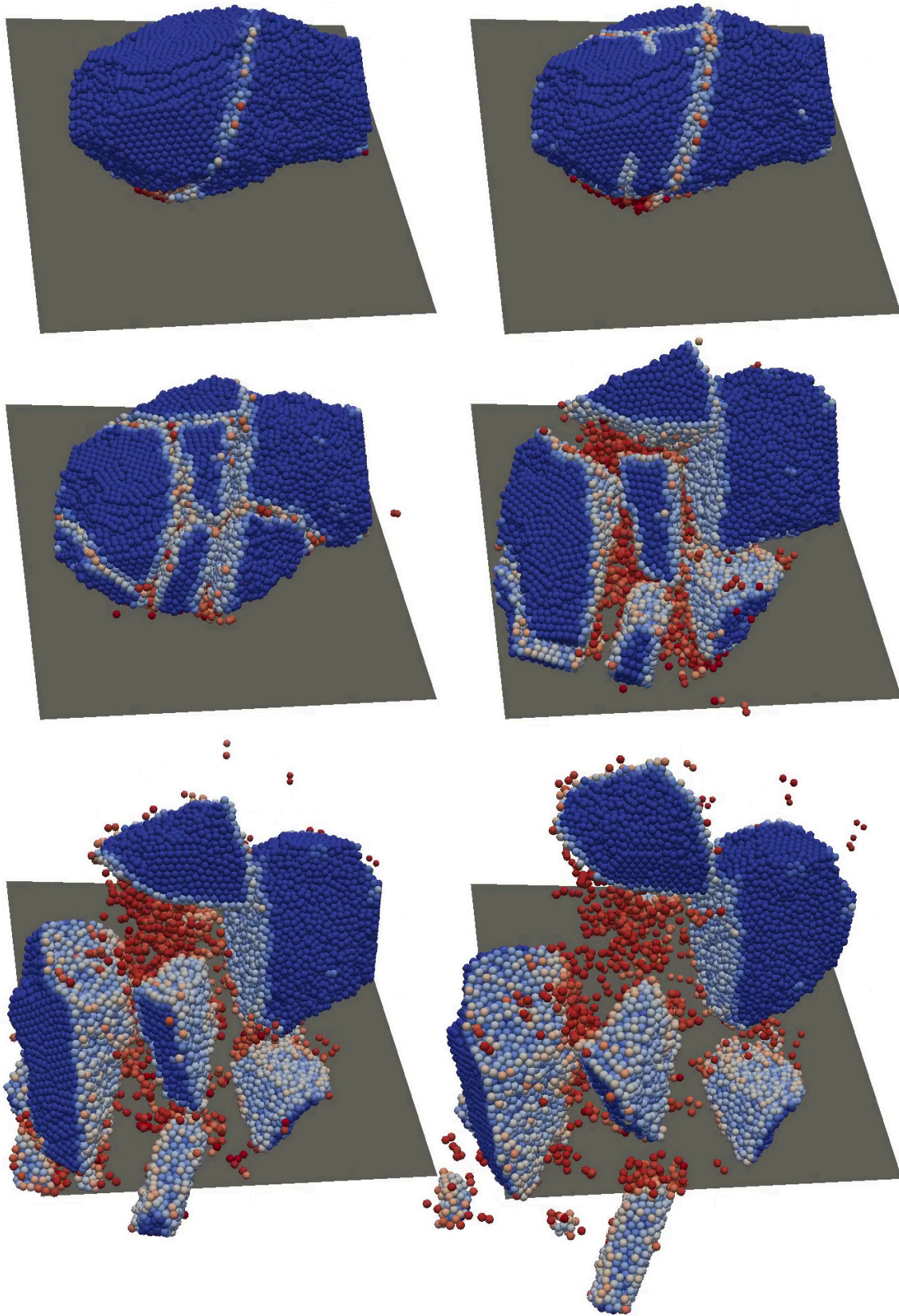
**Figure 3.40:** Sequence of the breakage of a block with a preexisting weak plane representing an internal fracture. Color scale shows the number of initial bonds that are broken (blue none, red all). The crack propagation starts in the weak plane but rapidly several other cracks appear in non-weakened parts of the block and then fragments are ejected.
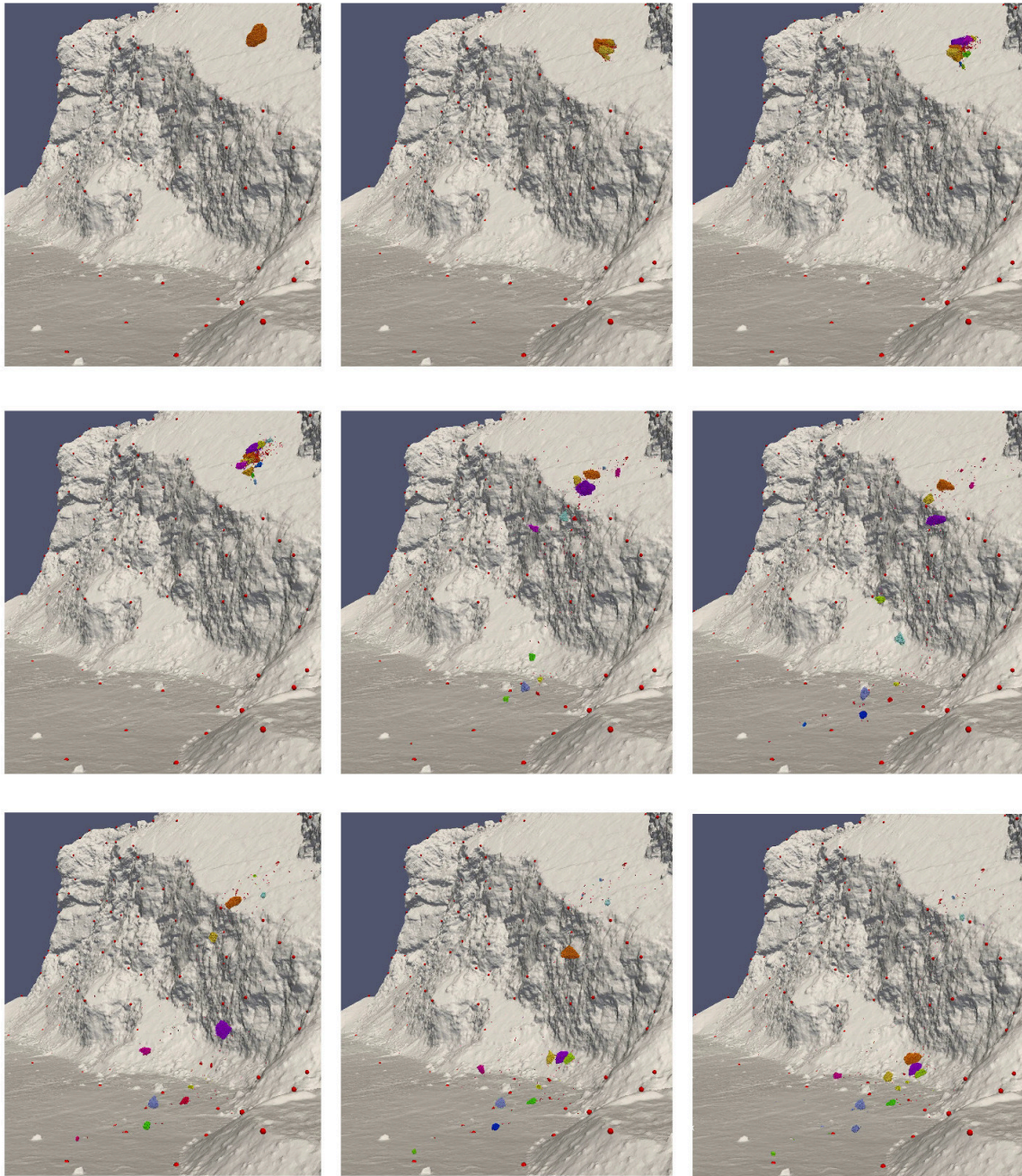
**Figure 3.41:** Simulation of block #8 on the real slope with a packing spheres radius of 2 cm, an impacting velocity of 9 m/s and a rotational velocity of 0.7 rad/s.

As final remarks, DEM has shown to be a very promising technique and can help understanding a highly stochastic phenomena like rockfall fragmentation. The model built in Yade during the research stay in IRSTEA, is capable of reproducing the phenomena, but it should go through an entire calibration process in order to be absolutely functional. All tools needed for the specific analysis of the fragmentation process in Yade have been developed and are ready for this future line of research, including specific fragment segmentation algorithms which also computes fragment state variables like linear and angular velocities and an algorithm to impose initial kinematic conditions on a block formed by several spheres to match field test initial conditions.

# Chapter 4

# Methodology: Development of RockGIS code

The new acquired knowledge on fragmentation process in rockfalls during the development of this thesis (Chapter 3) was used to develop a new rockfall simulation model that accounts for fragmentation. This new model was named RockGIS (Matas et al., 2017; Matas et al., 2020b). It implements state of the art of rockfall propagation methodologies while adapting them for the consideration of fragmentation. It works with a lumped mass approach, which means blocks are simulated in the space as non dimensional points and all their mass is concentrated in these points. The name of the code includes the acronym GIS for the close relationship with Geographic Information Systems, since RockGIS takes the spatial information from digital terrain models in GIS raster format, and therefore, uses GIS tools to manage input and output data. However, the simulations run on a 3D space defined by a raster digital elevation model (DEM in this chapter refers to Digital Elevation Model and not to Discrete Element Method as in the previous chapter). Using this raster model has some spatial limitations as, for instance, not being able to consider detachment points from overhangs, but it allows for a better performance in terms of contact detection between the rock block and the slope surface, and thus a better computational efficiency.

To run the model, first the DEM and the initial block conditions (release points and kinematics) have to be defined. Then from these points, the kinematic propagation of each one of the blocks is computed considering its interaction with the ground surface and the possibility of breakage during this interaction. In case of a block breakage, each one of the fragments is simulated as a new block with its initial kinematic conditions and volume coming from the fragmentation model. In the following sections, first, the required input data for running RockGIS are explained. Then, the internal functioning of RockGIS and all its components are described.

## 4.1   Input data

To run a simulation three main inputs are required: the digital elevation model (DEM) representing the terrain where the propagation occurs, the blocks initial conditions and a file containing the set of parameters controlling the model (some of them geographically

distributed along the digital elevation model). Following subsections describe in detail the topographic model and initial block kinematics. The required parameters contained in the parameters file are described later.

### 4.1.1 Blocks initial conditions

A block is simulated in RockGIS as an object with state variables. Each block object stores the position, linear velocity, angular velocity and its volume (related to the mass by its density). To start a simulation, it is required to impose initial values for all of the state variables. The position must be above the ground surface, otherwise the block will fall to the infinity since no contact would be detected with the ground surface. Both linear and angular velocities are initiated with low values considering the initial propagation direction of the block. Common values are 0.5-1 m/s for liniar velocity and 0.5-1 rad/s depending on the expected failure mechanism.

In rockfall hazard analysis, usually more than one single block is simulated for statistical representativeness. Then the initial imposed conditions can be slightly modified using Monte Carlo method to obtain different possible results considering very similar initial conditions. In this case, a specific subroutine is used to generate these statistically disturbed initial conditions. When considering a fragmental rockfall in which a IBSD is expected to detach, the list of all blocks forming it has to be introduced in the code and individually simulated. This is how RockGIS deals with the initial disaggregation of a fractured rock mass when detached. This approach was successfully used in Matas et al. (2017) and Matas et al. (2020b).

### 4.1.2 Topographic model

To represent virtually the terrain in the simulations of the RockGIS code, a high-resolution digital elevation model is used. It consists of a raster grid containing information on the height of the surface in each squared cell. Depending on the study site, models from 1x1 m to 0.1x0.1 m spatial resolution of cellsize were used in this work, mostly derivated from 3D point clouds obtained from UAV photogrammetry or airbone lidar system (ALS). Although other approaches can be taken to represent the terrain, like 3D point clouds (Noël et al., 2018b), the raster approach is computationally very efficient. This is one of the main raisons why raster DEM was chosen for the simulation of fragmental rockfalls, where several number of fragments could be generated from a single falling block, what significantly increases the number of interactions with the terrain.

The contact detection algorithm to determine when the block impacts the ground requires the knowledge of the height of the block with respect to the surface. The Z-value of the terrain at certain X,Y coordinates is calculated using a bilinear interpolation between the four nearest neighboring cells. Each cell contains a single elevation value which is used to place a point in the center of the cell with its corresponding elevation. Then the four neightbouring points are used for the interpolation (Figure 4.1). This approach gives a continuous interpolation of the surface based on the digital elevation model cells. In the code, a function called "height to ground" (H2G) gives the height of the block with respect to the slope surface. In Figure 4.1 the block is represented by the red dot,

the green dotted line is the H2G value. The contact detection algorithm, explained in following subsections, uses recursively this H2G function to detect the exact contact point between the block and the interpolated surface.
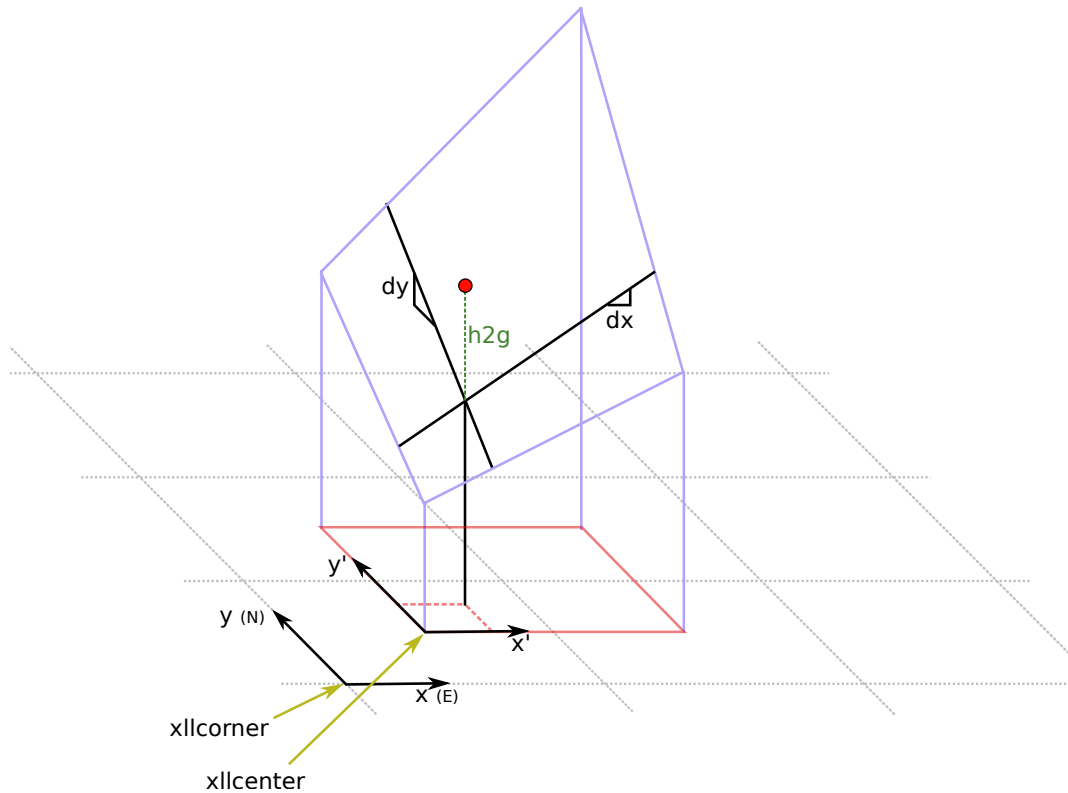


**Figure 4.1:** Scheme of the bilinear interpolation approach to compute the height of the simulated blocks from the ground surface. The grid in the bottom corresponds to the raster digital elevation cells. In the center of each cell, the corresponding height is used for the surface interpolation. The red dot represents a block and h2g is the height with respect the interpolated surface.

## 4.2   Simulation of fragmental rockfalls

As explained in the introduction of this chapter, the knowledge acquired regarding the fragmentation in rockfalls was used to build RockGIS. The propagation of rockfalls in RockGIS is based on existing methodologies and was reformulated to allow the consideration of fragmentation. The fragmentation module was developed using data obtained in the field inventories and real scale experiments described in Chapter 3.

Once all the input data required are provided to RockGIS, from the chosen release points and considering initial velocity conditions, the trajectories of the blocks are computed by integrating movement equations that result in ballistic trajectories as described in Gischig et al. (2015). This approach also accounts for rotational velocity of the blocks during propagation. A contact algorithm is used to determine when the flying blocks impact on the ground surface. This algorithm uses a bisection approach once the trajectory has intersected the ground surface to determinethe impact point accurately. When an impact

is detected, the rebound conditions are evaluated using a rebound model (Wyllie, 2014). Then, the fragmentation model checks whether fragmentation occurs or not at certain impact. In case it does not, the block continues its propagation considering the reflected velocity provided by the rebound model. In case of fragmentation, the impacting rock mass is distributed among the newly created fragments. Nowadays, RockGIS considers the fractal theory described in Ruiz-Carulla and Corominas (2019). All generated fragments are treated and simulated as new blocks with their own initial kinematic conditions. The initial release position of each new generated fragment is the impacting point, and its velocity is computed within an ejection cone using a stochastic process (Matas et al., 2020b). This process keeps going on iteratively until no more fragments are generated during the impacts and all of them stop. The stoppage criteria accounted in the model considers a threshold velocity at which the block is assumed to be effectively stoped. Figure 4.2 shows the basic flowchart for the propagation simulation of a single block. Following subsections develop each part of the simulation process in detail.
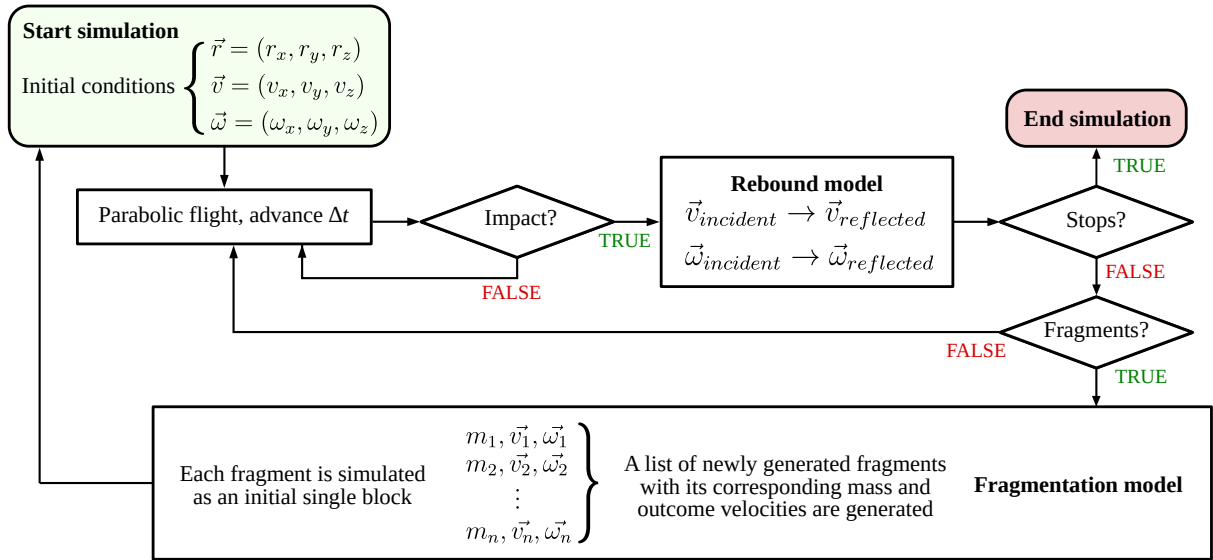


**Figure 4.2:** RockGIS flowchart for the simulation of the propagation of an individual block.

## 4.2.1 Block kinematics

Blocks are considered as points in space with all the mass concentrated (lumped mass approach) and they have, as state variables, a position $\vec{r} = (x, y, z)$, linear velocity $\vec{v} = (v_x, v_y, v_z)$, rotational velocity $\vec{\omega} = (\omega_x, \omega_y, \omega_z)$ and volume. This approach does not explicitly account for the shape of the blocks except for the rebound model in which the blocks are assumed to be spheres (hybrid approach). Due to this simplification, some kinematic behaviors conditioned by the shape of the blocks may not be represented in a fully accurate way and may affect the results of the simulations. This deficiency is overcame by a thorough calibration process. Other variables, such as information regarding the parent fragment or the current motion state in the simulation algorithm are stored for numerical purposes. Blocks are subject to the gravity acceleration $\vec{a} = (0, 0, -g)$ and by integrating the movement equations with a certain time discretization,

$\triangle t$, the parabolic trajectories are obtained as shown in Figure 4.3. Considering an initial position, the linear and rotational velocities of a block in each time step of the simulation keep producing a parabolic flight until the contact with the terrain, mitigation structures, or virtual control sections is detected. During the interaction whith the terrain, the rebound and fragmentation modules are applied and the resulting fragments and their reflected velocities are determined. Then, each fragment is treated as a new individual block and the flying phase is restarted. The internals of the fragmentation process in RockGIS are detailed in following subsections.
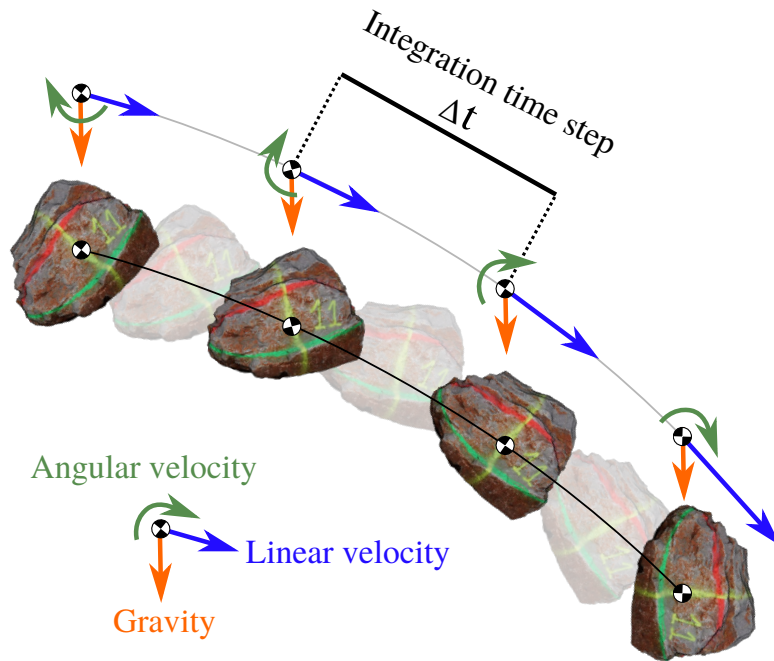


**Figure 4.3:** Kinematic integration scheme considering incremental time steps which produce parabolic flights until blocks impact with the ground surface or any other considered object during the simulation.

## 4.2.2 Rebound model

The contact detection between blocks and the terrain is computed by the bisection method (Sheng, 2005), which is frequently used in photogrammetry. At every time step, the block moves according to its velocity and the value of H2G is checked. If the value is less than zero, it means that the block is located under the ground surface. Then, an iterative process, using the bisection method, determines the exact time step that makes the block intersect with the slope surface with a certain tolerance. This tolerance is always on the positive side of H2G to ensure that the block numerically never penetrates the ground. A common value used for this tolerance is 0.1-1 cm. This contact detection algorithm leads to the block positioned over the surface and ready to apply the rebound model.

Once impact with the terrain is detected, a rebound algorithm is applied to compute the reflected velocity of the block. The aim of a rebound model is to determine the reflected linear and angular velocities (after impact) considering the incidence velocities (before impact) and the impact geometry. The last version of RockGIS implements the rebound

approach proposed by Gischig et al. (2015). The first step required to apply a rebound model is to determine the local coordinate system $\overrightarrow{e_L}, \overrightarrow{e_T}, \overrightarrow{e_N}$ on the impact point to be used for the computations. In this right-handed system $\overrightarrow{e_N}$ is the normal unitary vector to the surface at the impacting point while $\overrightarrow{e_L}$ and $\overrightarrow{e_T}$ are contained in the impacting plane being parallel and transverse to the projected linear incident velocity respectively. For the consideration of local roughness and the addition of stochasticity to the process this local reference system is slightly rotated at each impact twice: first in the longitudinal direction (parallel with the incident vector) and then in the transverse direction. All formulation for this process is extensively explained in Gischig et al. (2015).

Once the local reference system is computed, the incident linear and angular velocities must be converted from the global reference system to the local reference system using the corresponding transformation matrix obtained from the relation between the new local reference system and the global reference system. This matrix is obtained by projecting one of the reference systems to the other reference system. Equation 4.1 shows $T_{l \to g}$ which is the transformation matrix to convert a vector in the local reference system to the global reference system $(\overrightarrow{e_x}, \overrightarrow{e_y}, \overrightarrow{e_z})$.

$$
T_{l \to g} = \begin{bmatrix} \overrightarrow{e_x} \cdot \overrightarrow{e_L} & \overrightarrow{e_x} \cdot \overrightarrow{e_T} & \overrightarrow{e_x} \cdot \overrightarrow{e_N} \\ \overrightarrow{e_y} \cdot \overrightarrow{e_L} & \overrightarrow{e_y} \cdot \overrightarrow{e_T} & \overrightarrow{e_y} \cdot \overrightarrow{e_N} \\ \overrightarrow{e_z} \cdot \overrightarrow{e_L} & \overrightarrow{e_z} \cdot \overrightarrow{e_T} & \overrightarrow{e_z} \cdot \overrightarrow{e_N} \end{bmatrix} = \begin{bmatrix} e_{L_x} & e_{T_x} & e_{N_x} \\ e_{L_y} & e_{T_y} & e_{N_y} \\ e_{L_z} & e_{T_z} & e_{N_z} \end{bmatrix} \tag{4.1}
$$

To perform the reverse operation and convert a vector expressed in the global reference system to the local reference system the matrix $T_{g \to l}$ can be computed as the inverse matrix of $T_{g \to l} = T_{l \to g}^{-1}$. Equation 4.2 and 4.3 show how the block velocities expressed in the global reference system are converted to the local reference system. In all equations in this section the super index $i$ means incident while the later used super index $r$ means reflected.

$$
\overrightarrow{v_{local}^i} = T_{g \to l} \cdot \overrightarrow{v_{global}^i} = \left( v_L^i, v_T^i, v_N^i \right) \tag{4.2}
$$

$$
\overrightarrow{\omega_{local}^i} = T_{g \to l} \cdot \overrightarrow{\omega_{global}^i} = \left( \omega_L^i, \omega_T^i, \omega_N^i \right) \tag{4.3}
$$

At this point, the W. Goldsmith (1960) model is adopted considering nonslip impacts. This model was derived for the impact and rebound of a spherical body with a planar surface. It considers that the normal impulse of a block is modified by a normal restitution factor $K_n$. As in Gischig et al. (2015), in RockGIS the tangential impulse is also assumed to be reduced by a second restitution factor $K_t$. This second factor aims at accounting for nonfrictional momentum losses in the longitudinal direction. In the following equations, $R$ is the equivalent radius of the block. Equations 4.4 and 4.5 show the computation for the transversal and longitudinal directions respectively.

$$
\begin{pmatrix} v_T^r \\ R\omega_L^r \end{pmatrix} = \begin{pmatrix} \frac{5}{7}K_t & -\frac{2}{7}K_t \\ -\frac{5}{7}K_t & \frac{2}{7}K_t \end{pmatrix} \cdot \begin{pmatrix} v_T^i \\ R\omega_L^i \end{pmatrix} \tag{4.4}
$$

$$
\begin{pmatrix} v_L^r \\ R\omega_T^r \end{pmatrix} = \begin{pmatrix} \frac{5}{7}K_t & -\frac{2}{7}K_t \\ -\frac{5}{7}K_t & \frac{2}{7}K_t \end{pmatrix} \cdot \begin{pmatrix} v_L^i \\ R\omega_T^i \end{pmatrix} \tag{4.5}
$$

In the normal direction the income normal velocity is scaled by the normal restitution factor $K_n$ and the direction of the movement is inverted by changing the sign as shown in Equation 4.6.

$$v_N^r = -K_N \cdot v_n^i \tag{4.6}$$

And the final local reflected velocities would be as shown in Equations 4.7 and 4.8.

$$\overrightarrow{v_{local}^r} = (v_L^r, v_T^r, v_N^r) \tag{4.7}$$

$$\overrightarrow{\omega_{local}^r} = (\omega_L^r, \omega_T^r, 0) \tag{4.8}$$

These local reflected velocities have to be converted back to the global reference system in order to continue the block propagation. To do so, the transformation matrix from the local to the global reference system is used in Equations 4.9 and 4.10.

$$\overrightarrow{v_{global}^r} = T_{l \to g} \cdot \overrightarrow{v_{local}^r} \tag{4.9}$$

$$\overrightarrow{\omega_{global}^r} = T_{l \to g} \cdot \overrightarrow{\omega_{local}^r} \tag{4.10}$$

This velocity vectors are imposed to the block and the propagation algorithm continues. The restitution coefficients $K_n$ and $K_n$ can be estimated using different approaches. In RockGIS, this coefficients are computed at each impact using Wyllie (2014) and Gischig et al. (2015) equations, respectively. The normal restitution coefficient is computed as shown in Equation 4.11.

$$K_n = K_{na} \cdot \theta_i^{K_{nb}} \tag{4.11}$$

Where $K_{na}$ was estimated by Wyllie (2014) in 19.5 and $K_{nb}$ in -1.03 from a set of field tests and $\theta_i$ is the incidence angle, different for each impact. In RockGIS both $K_{na}$ and $K_{nb}$ are adjusted around these proposed values to match each testing site conditions. The tangential restitution coefficient follows a hyperbolic formulation expressed in Equation 4.12.

$$K_t = \frac{E_{t0.5}}{E_d^i + E_{t0.5}} \tag{4.12}$$

Where $E_{t0.5}$ is a reference deformation energy value the value at which $K_t$ equals to 0.5 and $E_d^i$ is the deformation energy proportional to the particle mass and the square of incident normal velocity as per Equation 4.13, where $R$ is the equivalent radius of the block and is the normal incident velocity to the local reference system.

$$E_d^i = R \cdot v_N^i{}^2 \tag{4.13}$$

The value of $E_{t0.5}$ has to be adjusted to each study site. In RockGIS both $K_n$ and $K_t$ can be computed using different approaches since the module is prepared to be easily upgradable. However, during the development of this research the combination of both of theses approaches to compute the restitution factors has shown the best results in the studied cases.

### 4.2.3 The fragmentation model

RockGIS can be used to consider both the disaggregation of the initial rock mass and the breakage of the blocks during propagation. The disaggregation of the IBSD is assumed in all cases and the trajectory of each of the involved block is modeled individually. A specific module is called every time a block hits the ground, to check for the breakage criterion. This module decides whether the block remains intact or breaks. In the case of breakage, the module generates the new fragment size distribution based on the Rockfall Fractal Fragmentation Model (Ruiz-Carulla and Corominas, 2019) as shown in Figure 4.4.
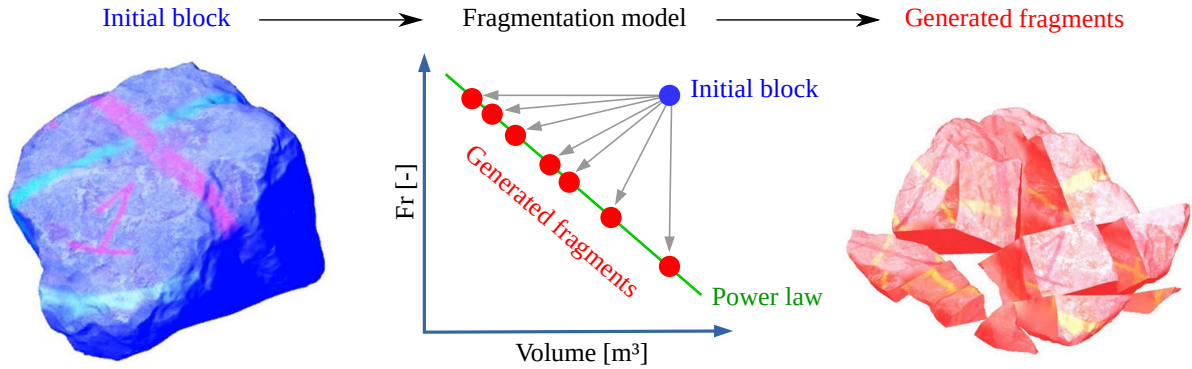


**Figure 4.4:** Scheme of the fragmentation process using fractal theory during an impact. The image has been adapted from Ruiz-Carulla and Corominas (2019).

In the first versions of the code (Matas et al., 2017), the power law parameters at each impact remained unchanged throughout the entire simulation. This means that every time fragmentation occurred the same power law was applied to distribute the initial mass among the new generated fragments. Although this approach was able to satisfactorily simulate fragmentation in large real rockfalls, it was limited when comparing the results of different impacting conditions since the parameters controlling the fragmentation model where always fixed. To overcome these limitations in the final version of the code, the power law parameters controlling fragmentation depend on the impacting conditions. This means that at each impact, these parameters are computed according to the incident velocities and block volume. In this case, the power law used for the fragment generation is unique and specific for the considered impact conditions.

The fragment volume distribution after breakage is generated by Equation 4.14. This equation gives the volume of the $nth$ generated fragment considering the specific impacting conditions of a block. The impacting conditions will determine the fractal dimension $D_f$. This iterative process builds the resultant fragment distribution as shown in Figure 4.4. The fragment generation process ends when one of these two conditions are satisfied:

1. The last generated fragment is smaller than a user-defined minimum volume. In this study, this value was set to the minimum fragment volume measured in the field. This criterion avoids a mathematically infinite loop reaching senselessly small fragment sizes.

2. The sum of all generated fragments reaches the initial block volume. In this case, the last fragment is the difference between the sum of all previous generated fragments and the initial block volume.

$$V_n = V_0 \cdot L_{max} \cdot n^{\frac{-1}{D_f}} \tag{4.14}$$

where:

$V_n$ volume of the fragment "n";
$V_0$ initial block volume;
$n$ number of fragments, running from 1 to infinite;
$L_{max}$ largest generated fragment;
$D_f$ the fractal dimension which controls the shape of the fragment distribution.

Both $L_{max}$ and the $D_f$ depend on the model parameters $b$ and $q$, as defined in Equations 4.15 and 4.16 (Perfect, 1997).

$$L_{max} = q \cdot b^n \tag{4.15}$$

$$D_f = 3 + \frac{log(1-q)}{log(b)} \tag{4.16}$$

where:

$b$ the proportion between the fragment size generated and the initial volume;
$q$ the probability of survival, expressed as the proportion of the block that breaks to create new fragments.

These two model parameters, $b$ and $q$, vary at each impact depending on the kinematic conditions. At each impact, the new surface area generated by breakage is estimated as a function of the normal impacting kinetic energy (Equation 4.17).

$$N_a = 1_1 \cdot Ek_n^{a_2} \tag{4.17}$$

where:

$N_a$ new generated surface area [m2];
$Ek_n$ kinetic energy in normal impact direction [J];
$a_1, a_2$ model parameters to calibrate.

This equation involves the impacting angle and block dimensions. The parameters $a_1, a_2$ can be estimated from the potential energy of first impacts of the inventoried rockfall. Ruiz-Carulla and Corominas (2019) found a relation between the new generated surface area and the initial area for each impact (Equation 4.18), which can be related to the

power law parameters ($b$ and $q$) that control fragment distribution (Equations 4.19 and 4.20).

$$\frac{Na}{Ta} = \frac{Na}{Ia + Na} \tag{4.18}$$

$$b = b_1 \frac{Na}{Ta} + b_2 \tag{4.19}$$

$$q = q_1 \frac{Na}{Ta} + q_2 \tag{4.20}$$

where:

$Na$ new generated surface area $[m^2]$;
$Ta$ total surface area $[m^2]$;
$Ia$ initial surface area $[m^2]$;
$b1, b2$ linear model parameters controlling $b$; must be calibrated;
$q1, q2$ linear model parameters controlling $q$; must be calibrated.

### 4.2.4  Energy transfered to the fragments

Finally, by adding a certain degree of stochasticity, the simulator defines the trajectories of the new fragments that are generated. The fragments are distributed within a cone of a given angle around the expected reflected trajectory of an intact (unfragmented) block as shown in Figure 4.5. This approach is based on field evidences observed during the realization of real scale tests described in Chapter 3.
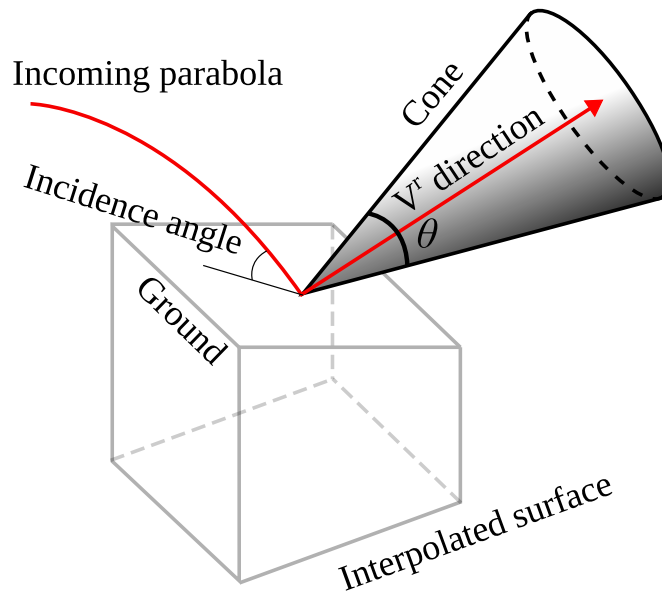


**Figure 4.5:** Cone shaped envelope of all the possible trajectories of each rock fragment after a fragmentary impact. The revolution axis follows the direction of the computed velocity after the impact $\overrightarrow{v^r}$

Once the list of generated fragments is computed, linear and rotational velocities must be assigned to each fragment. The values estimated for energy loss during the fragmentation process in Giacomini et al. (2009) are used. The knowledge on energy transferred between fragments is still in its early stages and for simplicity, it is assumed that the energy is distributed throughout fragments proportionally to their mass, which leads to the equal post-fragmentation velocity modulus of all fragments. These velocities are assumed to remain within a cone whose revolution axis is on the outcome velocity computed by the rebound model. The aperture of the cone is defined by the angle $\theta$ (Figure 4.5). Normal unitary vectors are randomly computed inside the cone following Hall (2017) method. These unitary vectors are multiplied by the outcome velocity and assigned to each of the generated fragments. For the reflected rotational velocity, a reduction factor is applied to the velocity computed by the rebound model in order to reproduce energy loss during fragmentation. From this point, each fragment is treated as a new block with its own state variables.

Figure 4.6 shows an example of the simulation of the release of a single block in the testing site #4 as described in section 3.2. This figure shows the difference in trajectories for the normal case with the fragmentation module activated and another for a synthetic case in which this module has been disabled (purple line). In the first impact, when the fragmentation module is active, the block breaks and all new fragments are ejected inside a cone following the methodology described in this section. Note that some fragments are able to break again when impacting against the base of the slope producing second fragmentations.
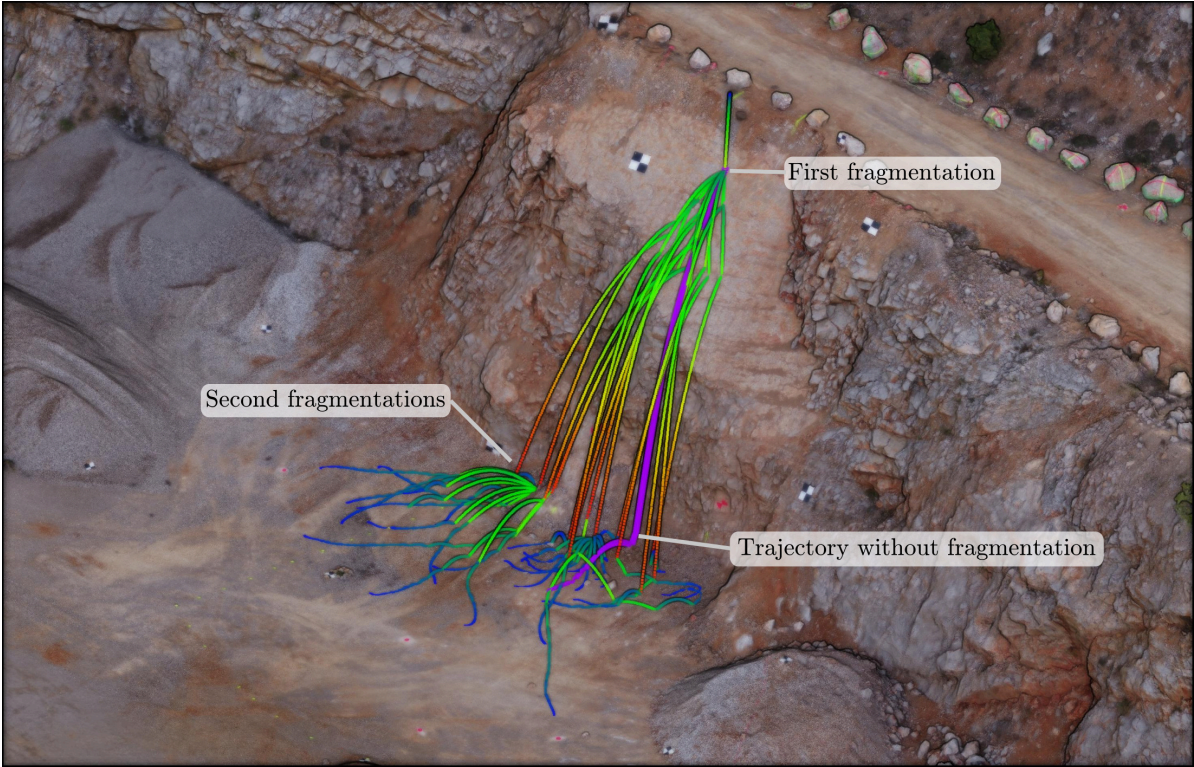


**Figure 4.6:** Example of a real scale test simulation of a single block with and without (purple line) activating the fragmentation module.

## 4.3 Calibration procedure

The calibration of RockGIS code in each study site was very challenging since several parameters concerning the rebound and fragmentation models had to be adjusted to make the results match the field observations. During the development of the code and its testing on different real case scenarios the calibration criteria have evolved from the first studies in Matas et al. (2017) and Corominas et al. (2019) to the last calibration in Matas et al. (2020b). The available data vary significantly depending on the site -from very controlled scenarios like real scale test to almost no previous information of a real scale event-, and conditions the calibration criteria to use. Thus, in each case different selected goodness of fit indicators where considered. The following list summarizes all possible goodness of fit indicators used in the different calibrations performed (Matas et al., 2017; Corominas et al., 2019; Matas et al., 2020b):

1. Similarities between the RBSD resultant from the simulations and the RBSD measured in the field.

2. Similarities between the runout distribution resultant from the simulations and the runout distribution measured in the field.

3. The cumulative spatial distribution of the volume of the fragments as a function of distance from the release point.

4. Comparison between the position of the center of gravity of the whole deposited block fragment distribution.

5. Bounding polygon of the young debris cover (YDC) over the slope surface.

6. Correlation between lateral scattering of the simulated trajectories and the observed ones

7. Total number of generated fragments.

8. Cumulative passing frequency and cumulative volume crossing a reference line (like forest roads, hiking paths, or dynamic barriers).

When the feasible goodness of fit indicators for each site where determined, the calibration process consisted of a trial and error iterative process trying to match field data by minimizing the error between simulations and observations. For the sake of brevity, in this section the more recent and complex calibration performed using RockGIS in Matas et al. (2020b) is used as example. In this study, RockGIS was used to calibrate the results of a real scale fragmentation test performed in a quarry and described in section 3.2. For the release point, just one seeder was considered in the average position of the release position of the blocks during the experiments. A horizontal velocity of 0.2 m/s was imposed to consider the initial momentum given to the blocks due to the movement of the backhoe shovel during the release. The digital elevation model used in this study was obtained from a UAV flight prior to the execution of the tests performed on the slope with a resolution of 0.2 x 0.2 meters. Just one material was considered on the entire slope, since the fine layer over the bedrock at the base of the slope, which was used to

**Table 4.1:** List of parameters considered for the model calibration.

| Parameter | Description |
| --- | --- |
| $K_{na}$ | Multiplier of the power law relating the normal impact velocity with the normal restitution coefficient (Equation 4.11). |
| $K_{nb}$ | Exponent of the power law relating the normal impact velocity with the normal restitution coefficient (Equation 4.11). |
| $E_{t0.5}$ | Parameter that controls the hyperbolic curve of the tangential restitution coefficient with the tangential impact velocity (Equation 4.12). |
| $a_1$ | Multiplier of the power law relating the normal impact remaining energy and the new area (Equation 4.17). |
| $a_2$ | Multiplier of the power law relating the normal impact remaining energy and the new area (Equation 4.17). |
| $b_1$ | Multiplier of the power law relating the fractal dimension and the new area (Equation 4.19). |
| $b_2$ | Exponent of the power law relating the fractal dimension and the new area (Equation 4.19). |
| $q_1$ | Multiplier of the power law relating the probability of survival with the new area (Equation 4.20). |
| $q_2$ | Multiplier of the power law relating the probability of survival with the new area (Equation 4.20). |
| $\theta$ | Angle defining the cone in which fragments may propagate after breakage (in degrees) |

make the surface even, was estimated to be around 2–5-cm thick. One simulation event consists of the release of the 21 tested blocks along with their respective fragment volumes measured in place. Note that, in the simulation, the rock fragments do not interact during propagation. Having set these initial conditions, the calibration procedure could begin.

First, a list of parameter combinations was generated using combinatorics. To achieve this, testing value ranges obtained from an iterative heuristic trial and error process were imposed for each parameter. The combination of all possible parameter values gives a total $N = \prod^i n_i$ cases to be tested, where $n_i$ is the number of intervals of each parameter and $i$ is the number of considered parameters. The ten parameters that affect the most the propagation and fragmentation process are described in Table 4.1. To determine the cases to be simulated, a certain number intervals for each parameter has to be imposed between the optimization ranges. In Matas et al. (2020b), for example, 20 intervals were used leading to a total of $2.56 \cdot 10^{10}$ simulation cases.

For each set of parameters, a certain number of rockfall propagation simulations were run varying the stochastic seed for statistical representativeness. The number of repetitive simulations performed could be increased as the code became more performant, and the value used in the final version for statistical representativeness was established around 1000 simulations. The initial seed determines the random numbers used during the stochastic processes in the simulation and may change the results of a single simulation if modified. The results of the simulations are averaged to obtain a mean behavior representative of the parameter set that is independent of the initial randomness seed. If just one simulation is performed, the calibration would only be meaningful for a specific

seed. Once averaged, the resultant distributions were compared against the experimental data.

The goodness of the optimization for each one of the numerically comparable criteria (1, 2, and 3) is evaluated as a function of the residuals. The statistic $\epsilon$ (Equation 4.21) computes a mean error between two discrete distributions by considering the squared distance between simulation and measurement results and dividing by the total number of checkpoints.

$$\epsilon = \frac{1}{n} \sum^{n} \frac{(O_i - E_i)^2}{E_i} \qquad (4.21)$$

where:

$n$ total number of checkpoints;
$E_i$ expected value on the checkpoint (field data);
$O_i$ observed value on the checkpoint (simulation result).

To evaluate the experimental and simulated distributions at the same points, $n = 1000$ samples were examined between the maximum and minimum range of the distributions using linear interpolation between points.

The optimization of the calibration consists of finding the combination of parameters that minimizes the value of $\epsilon$ for the three considered criteria. To achieve this, both the product and the sum of the resulting $\epsilon$ were compared between parameter sets, and the set giving the lowest value was selected. Figure 4.7 shows the workflow for the entire calibration process.

To perform the huge amount of simulations, a parallelization script was written so that a full simulation can be run in the RockGIS program for the 21 blocks, considering a specific parameter set in multiple CPU cores at a time. Each thread stored the $\epsilon$ values and, when all sets were tested, the best fitting ones were chosen. This entire process ran on an HPC using 24 cores. It took about 24 hours.
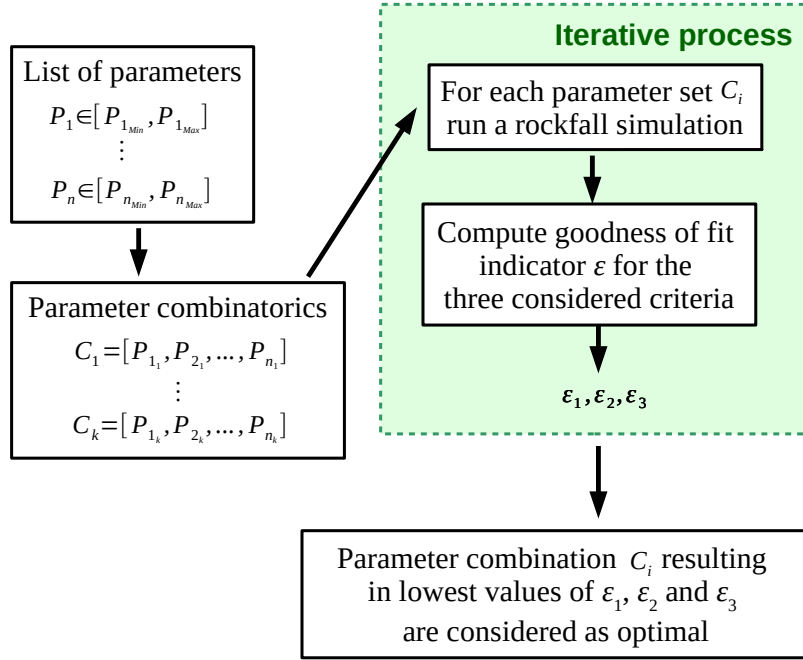
**Figure 4.7:** Workflow of the calibration process used to adjust the volume, runout and cumulative volume distributions of the field tests.

## 4.4 Quantitative risk assessment considering fragmentation

Risk is estimated as the product of the annual probability of a block reaching a reference location, the spatio-temporal probability of the exposed element and the vulnerability of the element for a certain intensity level (Corominas et al., 2014). When considering fragmentation, the established procedure to estimate the runout probability by computer simulations has to be adapted. When not considering fragmentation some blocks are released from expected sources, then the runout probability at each reference location is computed by dividing total number of blocks reaching the site by total simulated blocks. However, when considering fragmentation one single rockfall may lead to multiple fragments reaching the location and thus obtaining runout probabilities mathematically higher than one. For the estimation of exposure, fragmentation will also have a significant effect since one single rockfall may produce a number of fragments with divergent trajectories, thus increasing the width of the area affected by the rockfall. Consequently, the probability of any trajectory intersecting the exposed element will increase as shown in Figure 4.8 In this scheme a single block falling produces three impacts on the exposed element and would just be possible to have one impact in case of not considering fragmentation. Note that despite the impact probability may increase depending on the topographic conditions, the impacting kinetic energy may decrease due to the reduction of the fragments sizes.
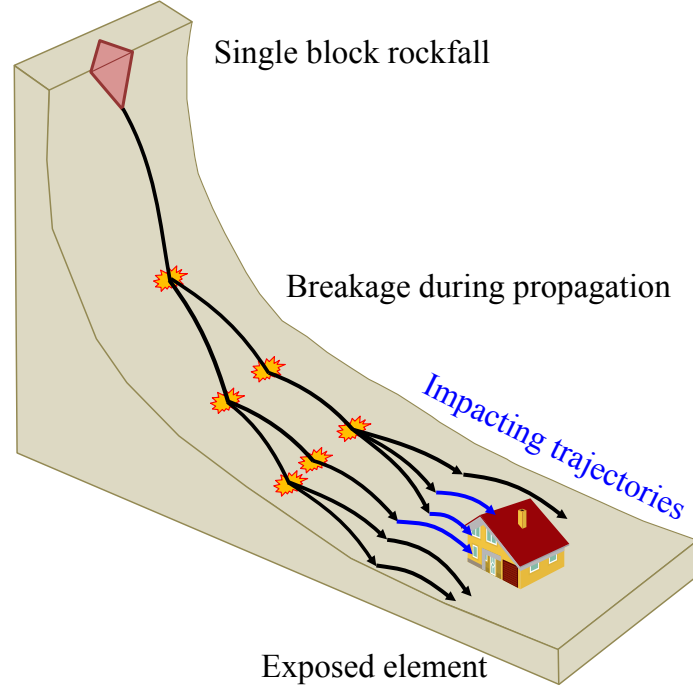
**Figure 4.8:** Example of a single block falling and producing more than one impact on an exposed element. The same example would apply to linear infrastructures like roads or hiking paths.

To integrate fragmentation in QRA analysis we have modified the formulation presented by Agliardi et al. (2009). We calculate the probability that a certain number of fragments $f$ produced during an event of magnitude $i$, that could reach the exposed element $j$ and then, integrate it for all number of possible fragments reaching the element. Thus, instead of having a single runout probability for each event magnitude we have a probability distribution that a certain number of fragments could reach the element. Equation 4.22 shows the modified expression to estimate the risk R, due to the occurrence of a rock fall of magnitude (volume) $i$ that produces $f$ fragments during its propagation on an exposed element $j$ located at a reference distance $X$ from the source;

$$R = \sum_{j=1}^{J} \sum_{i=1}^{I} \sum_{f=1}^{F} N_i \cdot P_f(X/D)_i \cdot P_f(T/X)_j \cdot V_{ijf} \tag{4.22}$$

where:

$N_i$ : the annual frequency of rockfalls of volume class $i$; .
$P_f(X/D)_i$ : the probability that $f$ fragments generated by the detached rock mass of the size class $i$ reach a point located at a distance $X$ from the source;
$P_f(T/X)_j$ : the exposure or the probability that an element $j$ be in the trajectory of the $f$ fragments generated by the rock fall at the distance $X$, at the timing of the event;
$V_{ijf}$ : the vulnerability of a exposed element $j$ in the case of being impacted by $f$ fragments generated by the $i$ magnitude block.

In the study case of *Monasterio de Piedra*, (Spain) (Corominas et al., 2019) the exposed elements are visitors walking through a hiking path around a touristic lake. In this

situation, fragmentation also modifies the exposure of the elements, since the affected width of the linear path may increase when more fragments reach the path. Equation 4.23 shows the expression considered for the exposure (modified from Nicolet et al. (2016)).

$$P_f(T/X) = \frac{f_p \cdot (W_f + l_p)}{24 \cdot 1000 \cdot v_p} \tag{4.23}$$

Where:

$f_p$ is the flow of visitors (persons/day);
$W_f$ is the width of the rockfall debris front depending on number of impacting fragments $f$ computed in the simulation (m);
$l_p$ is the width of the person (m);
$v_p$ is the mean velocity of persons (km/h).

This approach was applied to Monasterio de Piedra study case and was published in Corominas et al. (2019). For more details, the paper can be found in the annex and obtained results will be shown and discussed in the following chapter.

# Chapter 5

# Results: RockGIS performance and applications

Although this thesis focuses on the development of a numerical tool to simulate fragmental rockfalls, an extensive experimental research was also carried out in order to increase the knowledge of the phenomenon and design improved modelling approaches. The Experimental methodologies and examples of the obtained results can be found in Chapter 2 and all experimental results are published and can be consulted in the recent publications in which the author of this thesis was involved (Gili et al., 2016; Matas et al., 2020b; Matas et al., 2020a; Gili et al., 2020). In this chapterthe results regarding the numerical part and the use of RockGIS code are presented.

The developed methodology for the simulation of fragmentation in rockfalls and its numerical materialization into RockGIS was used for the representation of the phenomenon in several study cases and different scenarios. In each case, the parameters controlling both the propagation and the fragmentation processes had to be adjusted and calibrated. Especially the ones controlling fragmentation since the knowledge on the range of values of these parameters is still in its early stage. Moreover, during the development of this thesis the model has evolved, and different approaches for the consideration of fragmentation have been considered (Moya et al., 2013; Ruiz-Carulla et al., 2017; Ruiz-Carulla and Corominas, 2019), thus not allowing direct comparison of the model parameters. In this section the results obtained in all tested scenarios are shown and discussed, including the comparison of the fragment distribution curves and the runout distributions. The scenarios where RockGIS has been tested will be referred as per the following list:

1. **Vilanova de Benat rockfall:** A 10,000 $m^3$ rockfall occurred on a limestone cliff in the Cadí Sierra, Eastern Pyrenees near Vilanova de Banat village in November 2011. A reconstruction of the event considering fragmentation was done and published in Matas et al. (2017).

2. **Monasterio de Piedra rockfall:** After a 800 $m^3$ rockfall on February 2017 in a touristic path in the Monasterio de Piedra natural space, a full risk assesment of the hiking path was performed. To do so, RockGIS was first calibrated using the known rockfalls and the 2017 event. When the model was calibrated a full set of simulations considering different block volumes, fragmentation degrees and the presence of protections structures were computed. Results allowed the quantification

of the hazard in the hiking path, and a quantitative risk asessment of the different alternative routes. The inventorying process of the 2017 event can be found on section 3.1 and results of this study were published in Corominas et al. (2019).

3. **Mallorca Ma-10 road rockfall:** The Ma-10 road has some sections which are placed just under the cliffs of the Serra de Tramuntana massif. The road is equiped with several protection structutres like concrete galleries and rockfall fences. However, local authorities have reported some rockfalls which destroyed the protections and reached the road. A 10 $m^3$ rockfall occurred in 2017 was used to calibrate the model in that scenario and preliminary tests were done to design the methodology to develop a quantitative risk assessment in the road so as to have a prioritization criteria for road maintenance. The process and results of this preliminary study were published in Ruiz-Carulla et al. (2020).

4. **Real scale test in Foj quarry:** In the last real scale test performed in a quarry and described in section 3.2, the field data collected allowed a precise calibration of RockGIS in order to reproduce the observed fragments distributions and runout distributions. This test gave large amount of information regarding the fragmentation process of a single block, which can not be observed in a natural event concerning several cubic meters. The methodology and the obtained results were published in Matas et al. (2020b).

## 5.1  Rockfall block size distributions

For a proper representation of a fragmental rockfall in a simulation, the resultant fragment size distribution (or RBSD) has to match with the observed in the field. In RockGIS, from a starting in situ block size distribution (IBSD) the program computes the trajectory of each block and all fragments that may generate after breakage during its propagation. The in situ block size distributions for the study cases 1 and 2 was estimated using 3D reconstructions of the mass previously to the failure considering the corresponding fracture network. In study case 3 the IBSD was an individual 10 $m^3$ block. In the study case 4, the IBSD was the aggregation of all single simulated blocks, which where measured by different techniques such as manual tape and 3D reconstruction using photogrammetry from UAV.

The RBSD can be measured using different techniques explained in section 3.1 (manual tape measurement in the field, 2D post processing of orthophotos taken from UAV both manually or semi-automatic, or 3D measurement from point clouds). In all 4 study cases the RBSD was estimated with different levels of accuracy. In a very controlled scenario like the real scale test performed in the study case 4 this distribution could be measured with more accuracy than events involving several cubic meters like in cases 1 and 2. In the study case 3 the deposited fragments measurements were provided by the Mallorca Government and where hand measured by tape.

In Figure 5.1 the results of the simulated RBSD in each study case compared to the field RBSD are shown. These figures also show the IBSD used as an input for the simulations except in Figure 5.1c, corresponding to Mallorca case, where no IBSD is shown since this case was a single block.
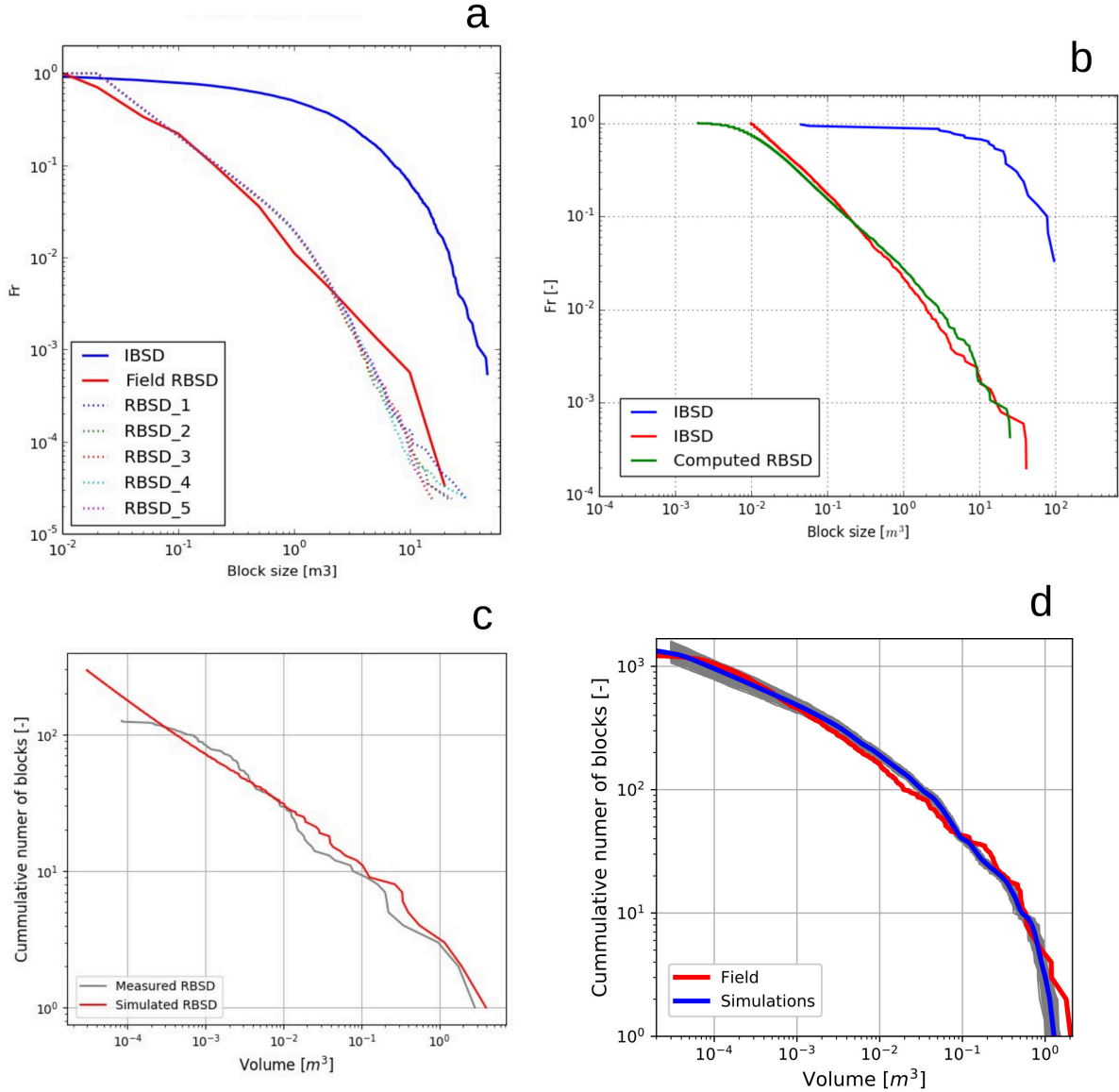
**Figure 5.1:** Comparison between the RBSD measured in the field with the simulations in the four main study cases (a) Vilanova de Benat; (b) Monasterio de Piedra; (c) Mallorca Ma-10 and (d) Real scale test in Foj quarry.

## 5.2 Runout and maximum reach

The maximum expected reach of a potential rockfall is a key parameter for assessing hazard and thus the risk. In the studied cases, the parameters where calibrated in order to make the runouts match the ones observed. Different accuracy levels where achieved when measuring the runouts in the different cases. As explained in the last section, in a more controlled scenarios the quality of the data was higher. In testing site 4 both the final position and volume could be measured for each deposited fragment. This allowed a precise reconstruction of the runout distribution. In study case 1, an approach based on field interpolation considering sampling plots was done. In the latter study, the runout validation criteria used are described in the following list:

1. Position of the center of gravity of the final distribution: A mean error of 2.92 m was measured in 5 simulations. This represents a 1,08% of relative error with respect to the runout of the center of gravity of the whole deposit, which reached 268m.

2. Comparison of the number of blocks reaching a certain travel distance. Figure 5.2a shows the comparison between the field estimation and the simulation results of 5 different runs. Note that in this graph, a few large scattered blocks which reached longer runouts cannot be appreciated since the total number is relatively small (they can be appreciated in Figure 5.2c). This figure shows how most of the simulated block reached a runout between 200 and 250 meters, similar to the ones observed in the field. However, the simulation show a tail of fragments reaching larger distances. This can be due to some unmeasured blocks in the field, as discussed in Matas et al. (2017).

3. The number of blocks passing a reference line: The number of blocks crossing the forest road used for validation was slightly overestimated in the simulations, but the total volume of the blocks crossing the forest road was similar to the field data (-10% to +21%). This overestimation may be explained by the incompleteness of the inventory as the smallest blocks outside the YDC were not measured. Figure 5.2b shows the longest runout fragments of the five simulations crossing the reference line (the ones inside the orange polygon).

4. Dispersion of the young debris cover (YDC): It is observed that the YDC perimeter is quite similar to the contour of the polygon containing 80% of the simulated blocks (Figure 5.2c). Moreover, most of the large scattered blocks remain inside the 99% polygon. In this density analysis, the simulated blocks with the largest runout cannot be observed as they are not quantitatively representative relative to the total amount of simulated blocks (less than 1%).

In both study cases 2 and 3 the runouts were measured qualitatively. In Monasterio de Piedra, case 2, the deposit produced by the simulation was superposed to the ortophoto of the real deposit and the simulation parameters where adjusted until they qualitatively matched (Figure 5.3a). The fragments reaching maximum runout were also considered, and their volumes were coherent with the ones observed on the field. Figure 5.3b shows the resultant trajectories of a simulation in this case. In the study case 3, in Mallorca, the author could not have direct access to the final deposit since the blocks affecting the road where rapidly removed in order to reestablish the road traffic. However, data provided by the road authority allowed for a qualitative approach considering how many blocks reached the road. The simulation was, like in the previous case, adjusted until the results matched the observations explained in their reports (Figure 5.4).
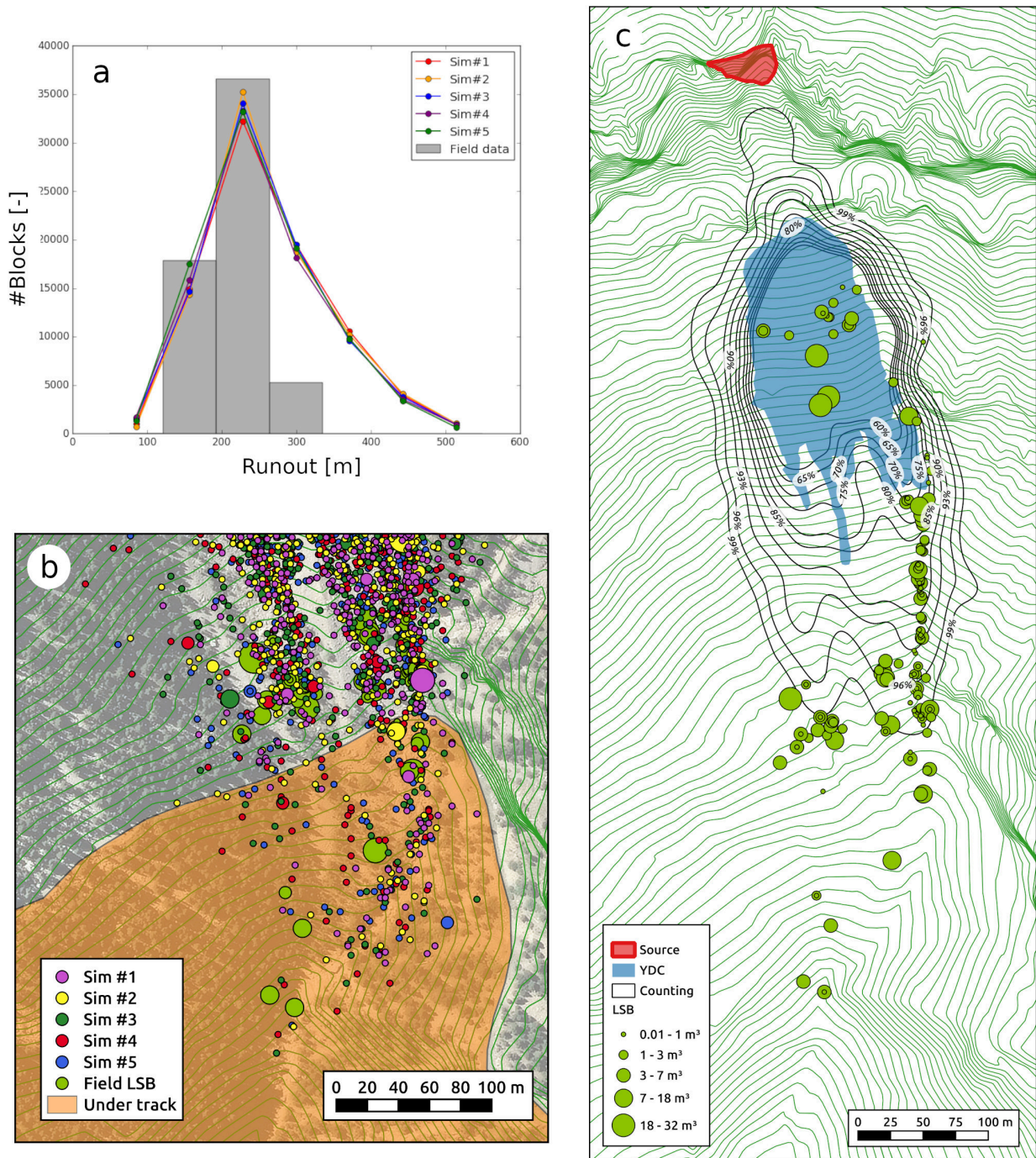
**Figure 5.2:** Runout results in the Vilanova de Benat case. (a) Comparison between the number of blocks reaching a certain runout in the simulations with the field measurements. (b) Maximum runout comparison considering a reference line. (c) Comparison of the extent of the measured deposit with the simulation results. Isolines containing a certain percentage of blocks are shown.
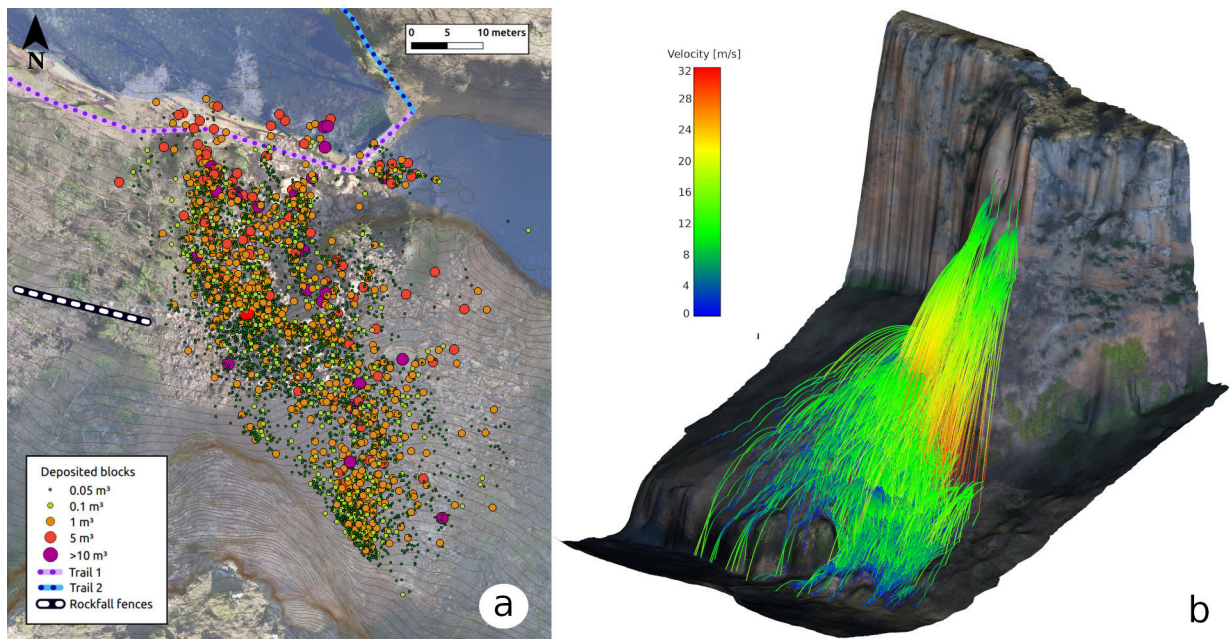
**Figure 5.3:** (a) Final deposit of the simulated blocks superposed to the deposit of the 2017 event in Monasterio de Piedra. The runout calibration was performed qualitatively taking into account the maximum runout reached by the fragments impacting into the train and the lake. (b) Resultant trajectories of the simulation of the 2017 event.



**Figure 5.4:** Reconstruction of the 10 $m^3$ rockfall in Ma-10 Road in Mallorca. The runout calibration was done qualitatively considering the final position of the fragments reaching the road.

In the study case 4, a real-scale test in a quarry, all fragments were georreferenced and their volume estimated. This information allowed a quantitative calibration considering both distributions. Calibration criteria used in this scenario (rockfall block size distribution in Figure 5.1d, runout distribution in Figure 5.5a and runout vs cumulative volume in

Figure 5.5b) gave values of $\epsilon$ of 0.028, 0.0015 and 0.4 respectively following Equation 4.21. The values of the parameters resulting from the calibration were: $na_1 = 0.0031$, $na_2 = 0.7562$, $b_1 = -1.6125$, $b_2 = 2.4875$, $q_1 = -0.5125$, $q_2 = 1.0$, $Kn_a = 19.54$, $Kn_b = -1.03$, $Kt_a = 22.6$ and $\theta = 83°$. The average runout distribution among 1000 simulations matched the field measured distribution well, although the maximum runout was slightly overestimated (Figure 5.5a). In the tests, the maximum measured runout distance was 35.2 m, while the average obtained in the simulations was 38.9 m. This distribution is very sensitive to the seed (the number used to generate a sequence of random numbers) as shown in Figure 5.5a, where simulations resulted in distributions that differed from the average curve. The variability of ejecting velocities after fragmentation, which were randomly assigned inside a cone, made some blocks follow high parabolic trajectories, while others were ejected almost tangentially to the surface. This variability explains why, in some simulations, the blocks may travel significantly long distances.

The cumulative volume curve (Figure 5.5b) shows that the model tends to accumulate more volume at the bottom of the slope than observed in the tests. Furthermore, some big blocks traveled longer distances than in the simulations. After analyzing in depth the videos of all fragments greater than 0.3 $m^3$ that traveled a runout distance of more than 20 m, we qualitatively observed that they acquired high rotational velocities and ended their propagation by a rolling motion. Although our model accounts for rolling in a simplified way by small jumps, and considering its rotational motion on the rebound algorithm, the shape effect seems to allow some of the blocks to travel a few more meters.

In this case 4 the extend of the deposit was also checked with the polygons containing a specific number of fragments as shown in Figure 5.6. As in the cumulative volume curve, the simulation tended to accumulate more fragments in the base of the slope, but the overall shape of the curves was qualitatively similar. Note that test results show more scattering, for example on contours of 60%, where the width of the test polygon is 50% greater than the simulation width. This higher dispersion may be explained by the variability of the backhoe when blocks were released, since there was between 1–2 m of variability in the release operation.

Finally, as a last check for the goodness of the results, all measured fragments in the field are shown classified by volumes in Figure 5.7. The contours containing a defined percentage of total cumulative volume are also plotted. Note that a large fragment traveled a very long distance (the blue block shown on the left of Figure 5.7). This corresponds to an initial released block of 1.8 $m^3$ that, after fragmenting on the first impact, projected the 0.9 $m^3$ fragment at an almost horizontal angle and with significant rotational velocity. This fragment travelled the last 6–8 m of its trajectory by rolling. However, most of the fragments remained within the 95% volume contour.
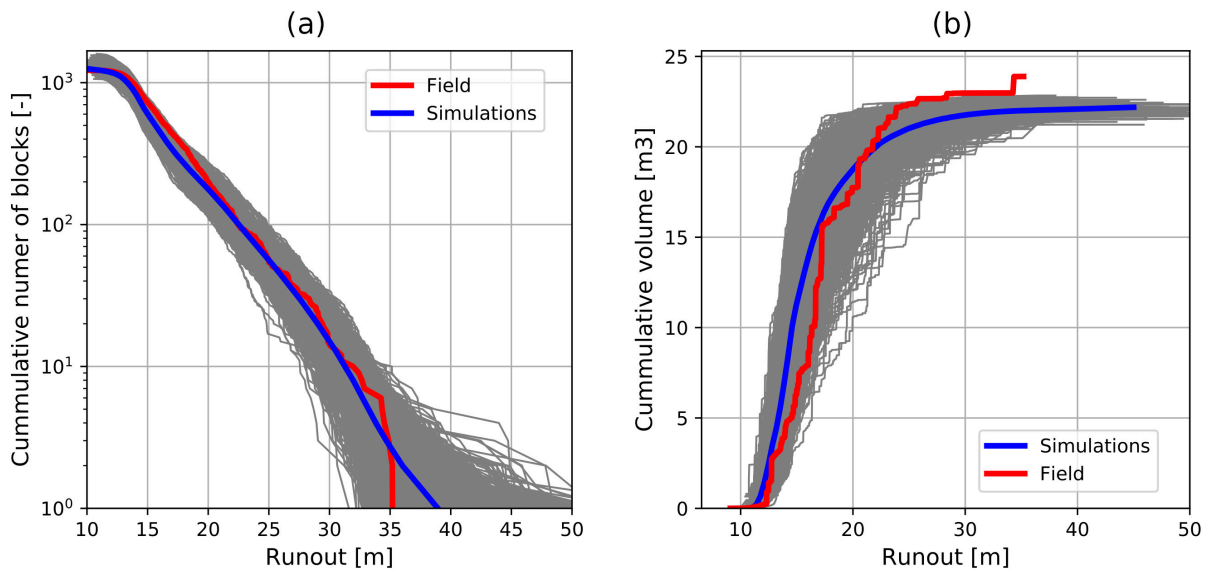
**Figure 5.5:** Runout calibration results of the study case 4, a real scale test in a quarry. (a) Comparison of rockfall runout distribution measured in real-scale tests with the average of the simulation results. Results of each individual simulation are shown in gray, while the average behavior is in blue; (b) Deposited cumulative volume as a function of the runout distance from the release point. The results of each individual simulation are shown in gray, while the average behavior is in blue.
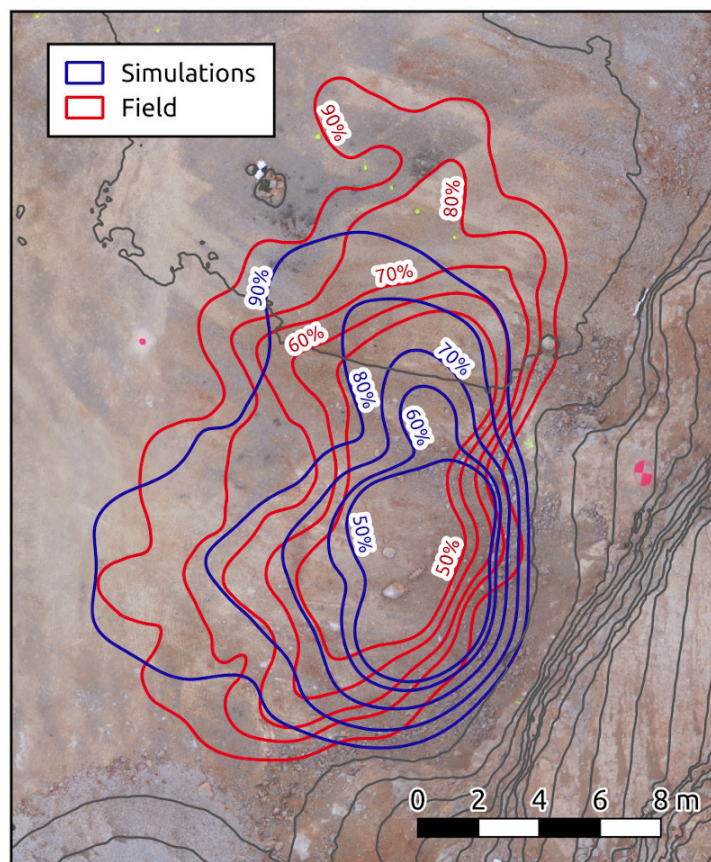


**Figure 5.6:** Isolines containing a certain percentage of stopped fragments for both field measurements and simulation results in the study case 4. (Matas et al., 2020b)
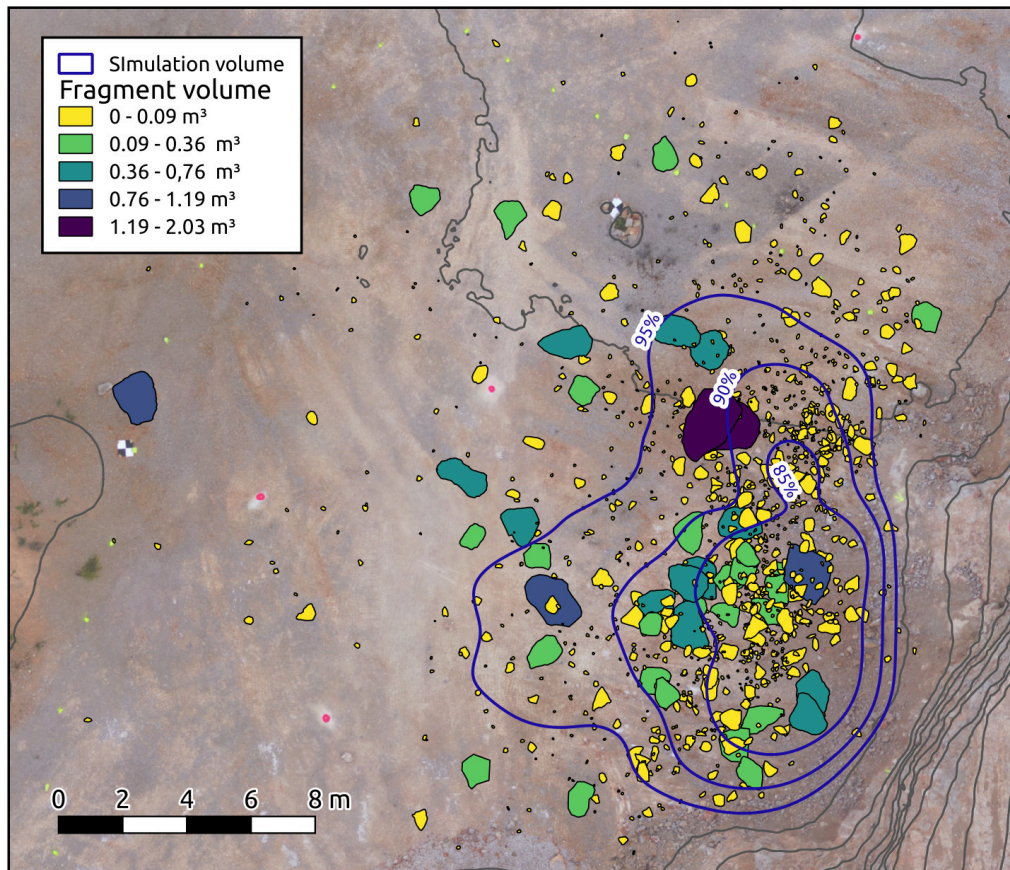
**Figure 5.7:** Isolines containing a certain percentage of deposited volume and measured fragments on the orthophoto obtained from the simulation in the study case 4. (Matas et al., 2020b)

## 5.2.1 Protection structures

RockGIS is able to simulate the effect of risk mitigation structures during the simulations. Every time a fragment hits a protection structure a special subroutine is called which decide how to proceed. In case of dynamic barriers, a simple comparison between the actual kinetic energy of the block and the design energy of the barrier determines if the block can be stopped or not. In case it is not, the absorbed energy by the fence is subtracted from the kinetic energy of the block and it continues its propagation assuming it broke the fence. This approach allows to easily check the performance of existing rockfall mitigation structures or improve its design in the planning phase. In the study case 2, a full quantitative risk assessment (QRA) was performed considering different scenarios with or without fragmentation and with or without the dynamic barriers that were actually present in the site. Figure 5.10 shows the trajectory results of the simulation of a 5 $m^3$ block both considering and not considering the effect of the dynamic barriers. During the performance of a QRA several block sizes are checked, and Figure 5.8 shows the mitigation effect of the dynamic barrier by reducing the number of blocks that are able to reach the trail. In case of small blocks from 0.05 to 1 $m^3$ the reduction is significant going from 60% reach to 14% in the case of 1 $m^3$. For bigger blocks the reduction is slight since the developed kinetic energies during the propagation allow the blocks to break the fences. The reduction for the 5 $m^3$ is a 13% while just 3% for the 10 $m^3$ blocks.

77

In the study case 3, the 10 $m^3$ block fragmented and some of the fragments where stopped by a dynamic barrier. For the qualitative calibration of the runout the barrier was considered, but the expected trajectories in case the barrier had not been present can be estimated. Figure 5.9 shows the comparison between considering or not the effect of the barrier. Without the barrier several more fragments would have reached the road.
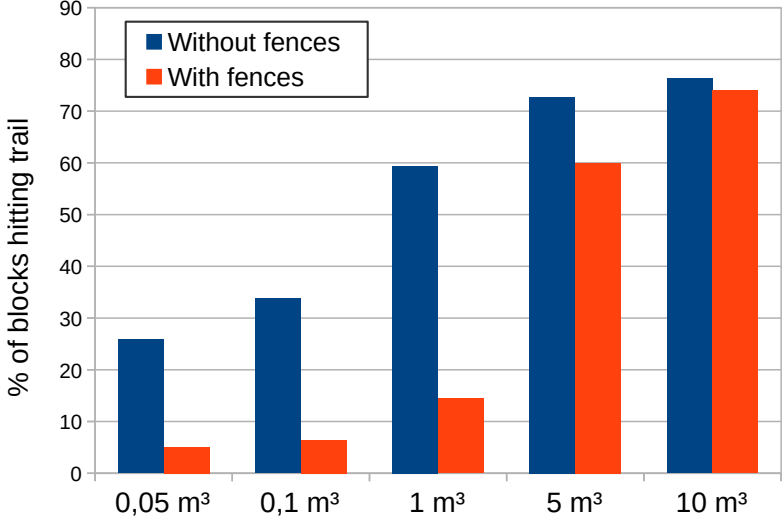


**Figure 5.8:** Comparison of the percentage of blocks reaching the hiking path when considering or not the dynamic barriers or fences for different block volumes.



**Figure 5.9:** Simulation of the 10 $m^3$ event in Ma-10 (case study 3) without considering the effect of the dynamic barrier (left) and considering it (right).

**Figure 5.10:** Simulation results of 5 $m^3$ block released from multiple initial sources in the Monasterio de Piedra study case. In (a) dynamic barriers are not accounted for while they are in in (b).

## 5.3 Quantitative risk assessment

A full QRA was performed on Monasterio de Piedra study case. The aim was assessing the risk of different hiking trail alternatives to see which opti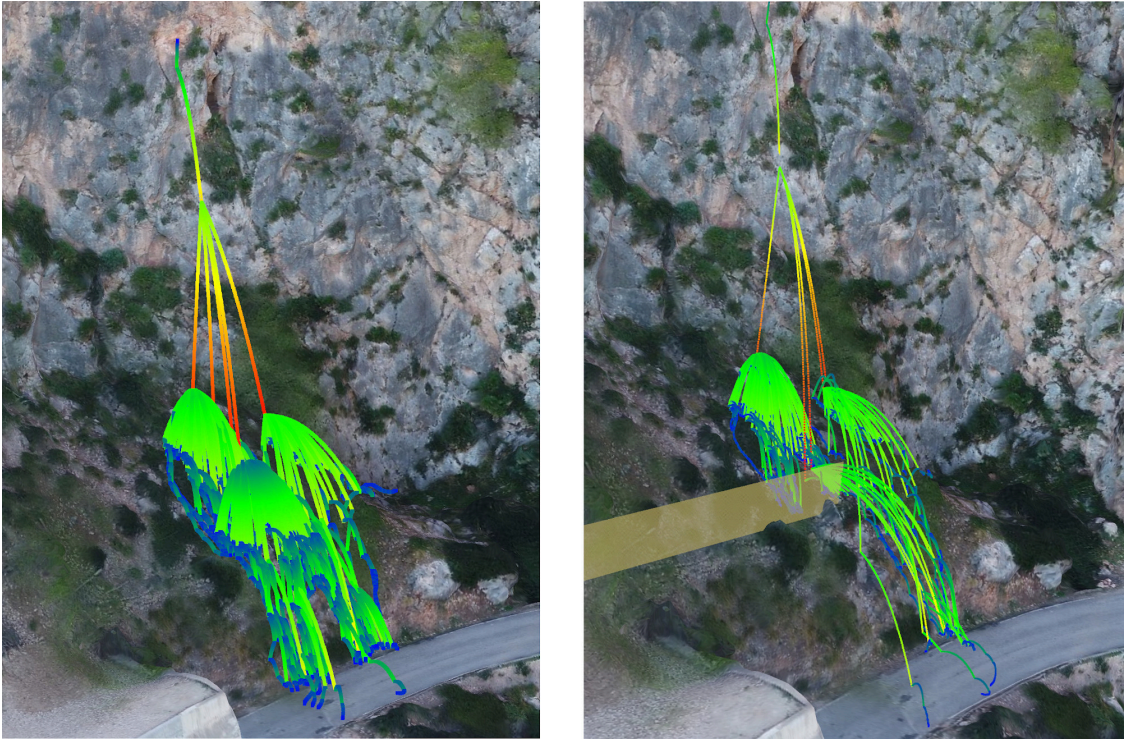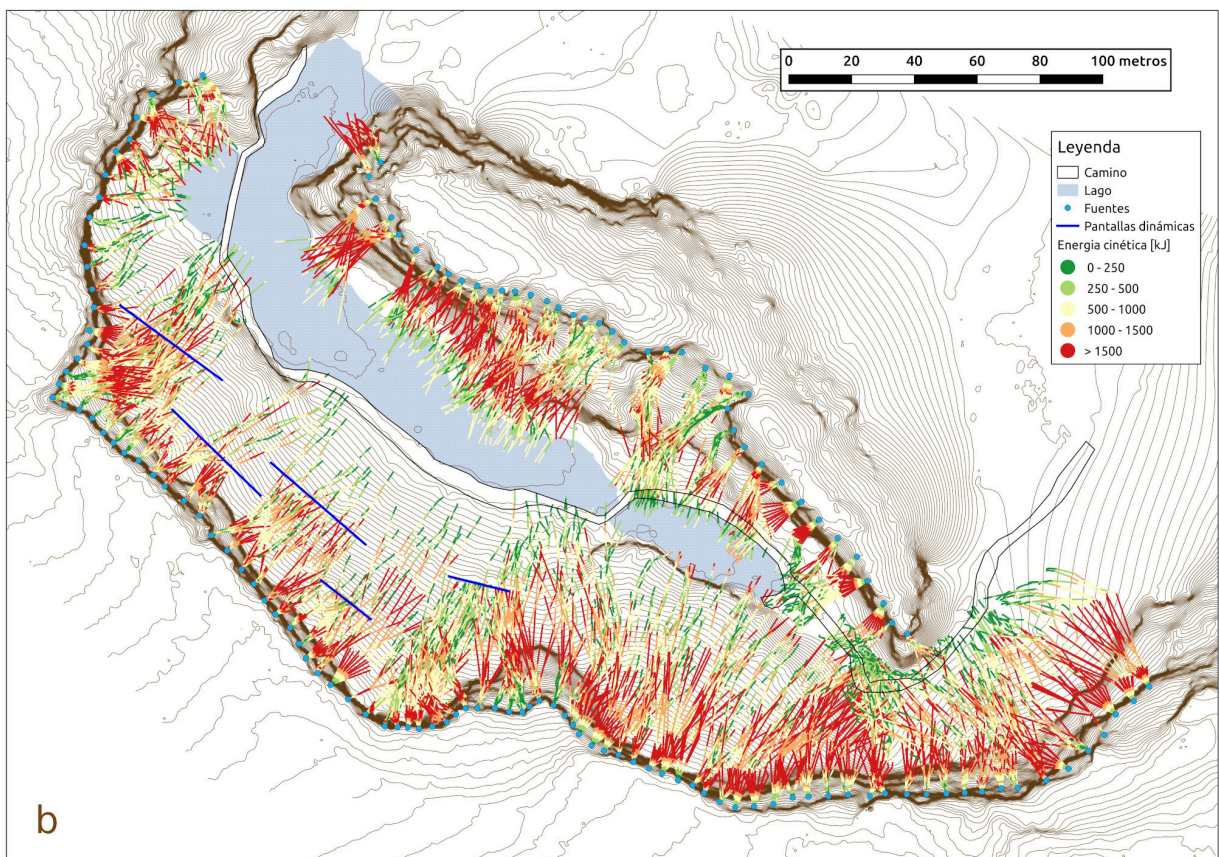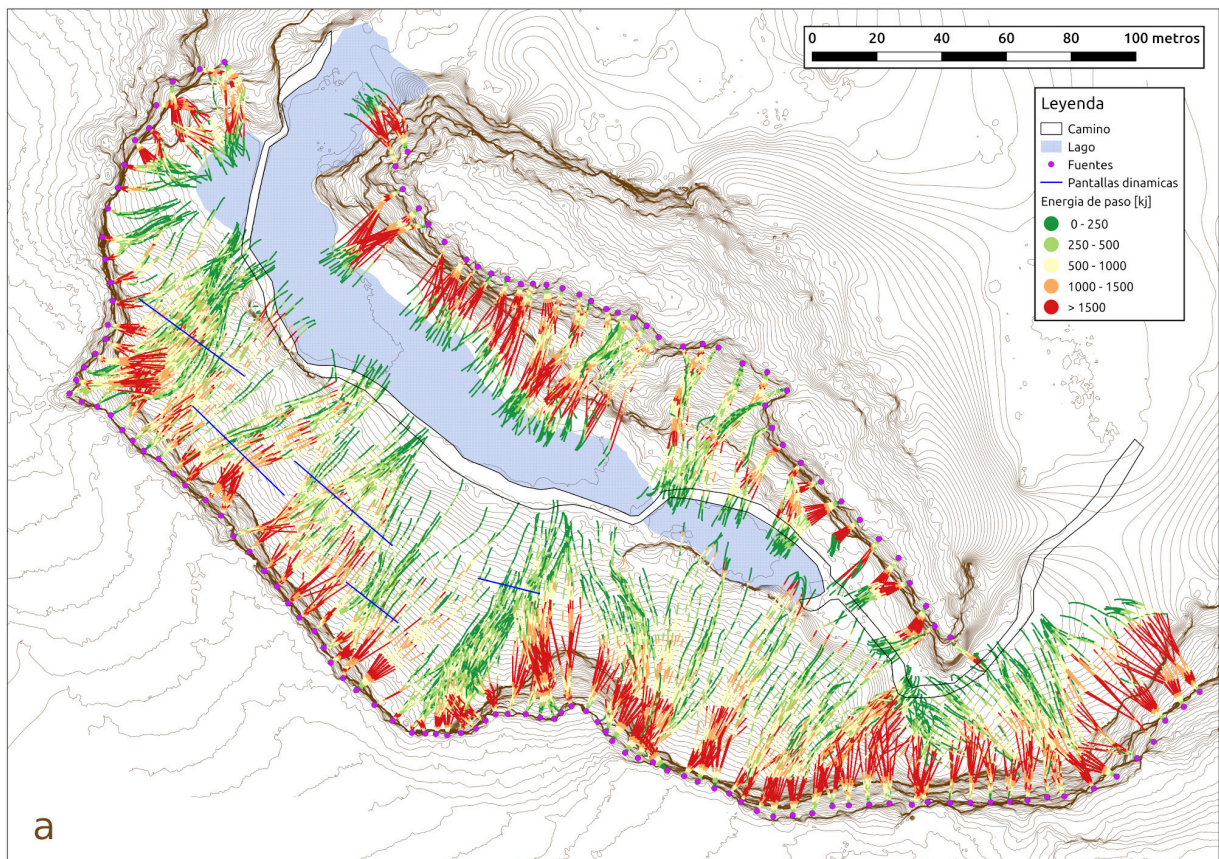on was the safest. The hiking trail studied was divided into different sections, and risk was assessed section by section. In this section the results of the trail section affected by the 2017 rockfall, and published in Corominas et al. (2019) are shown. Figure 5.11 shows the scenario, with two possible paths to cross from one side of the lake to the other, the deposit of the 2017 rockfall and the cliffs whose blocks may reach the corresponding paths.
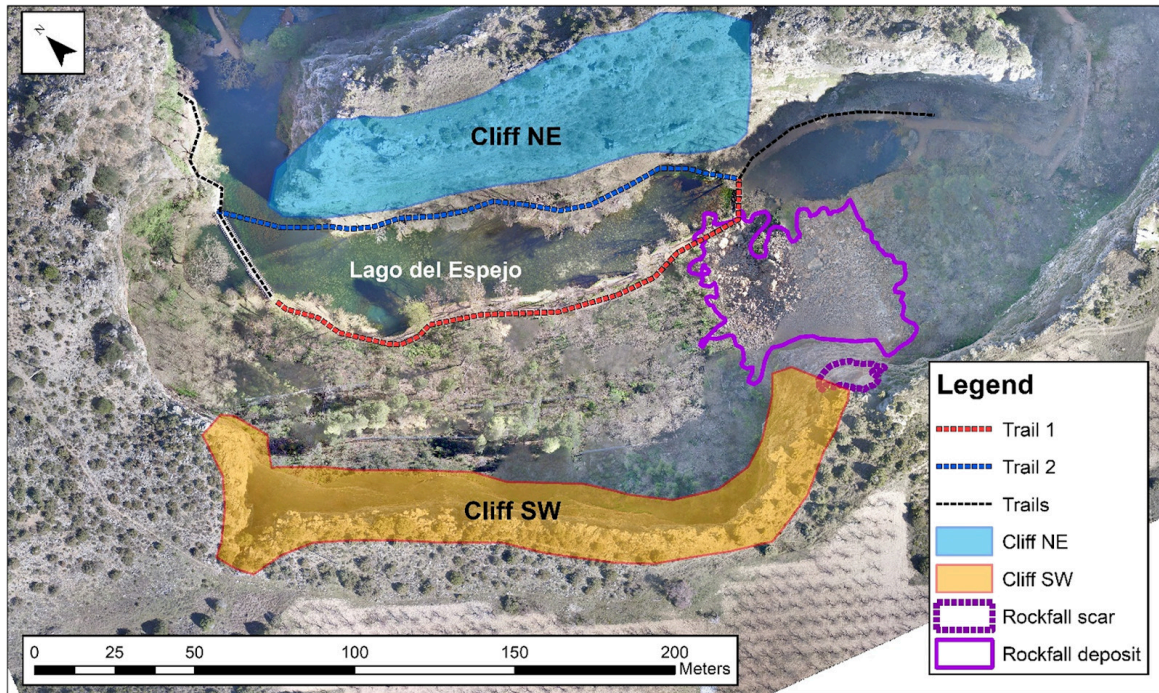


**Figure 5.11:** Scheme of the Monasterio de Piedra scenario with the scar and deposit of the 2017 event and the affected trail (Corominas et al., 2019).

As explained in previous sections, for a quantitative assessment of risk several terms forming the risk equation must be estimated. First, the frequency of the rockfall events was estimated using two information sources: (i) the count of rock blocks intercepted by the barriers installed 15 years ago (in 2002), and (ii) the inventory of three large events ($>400$ $m^3$ ), two historical (1986 and 2017) and the third of unknown age. A total of 209 rock blocks were measured in four barriers. These barriers where built 10 years before the analysis, which gave a time span for the frequency estimation. With this information a magnitude frequency table could be estimated (Table 5.1).

**Table 5.1:** Frequency of rockfall events estimated for Monasteio de Piedra study case.

| Volume class ($m^3$) | Events/yr | Volume/ka ($m^3$) |
|:---:|:---:|:---:|
| $\leqslant 0.005$ | 45.1463 | 226 |
| $0.005 < x \leqslant 0,05$ | 5.9514 | 523 |
| $0.05 < x \leqslant 0.5$ | 0.7846 | 916 |
| $0.5 < x \leqslant 5$ | 0.1034 | 1433 |
| $5 < x \leqslant 50$ | 0.0136 | 2114 |
| $50 < x \leqslant 500$ | 0.0018 | 3013 |
| $> 500$ | 0.0002 | 4198 |

The next component is the probability of reach, which was estimated using RockGIS. Once the model was calibrated considering the 2017 event and some maximum reach points measured during cleaning works in the cliff, a set of simulations with different configurations was performed. These simulations considered different magnitude events, different fragmentation scenarios and the presence or not of the dynamic barriers. In Figure 5.12 an example of the obtained results is shown for the cases of 1 $m^3$ and 10 $m^3$, without considering the effect of the barriers nor fragmentation. After performing the combination of all possible scenarios, the total number of blocks reaching the path were collected and results are shown on Table 5.2.

**Table 5.2:** Proportion of rockfall trajectories reaching the trail section for both unfragmented (U) and fragmented (F) rockfalls.

| Rockfall volume | Natural State | | Flexible fences | |
|:---:|:---:|:---:|:---:|:---:|
| | U | F | U | F |
| $< 0.05$ | 0.1194 | 0 | 0.0220 | 0 |
| $0.05 < x \leqslant 0.5$ | 0.3280 | 0 | 0.0647 | 0 |
| $0.5 < x \leqslant 5$ | 0.5896 | 0.0425 | 0.1455 | 0.0124 |
| $5 < x \leqslant 50$ | 0.7647 | 0.2327 | 0.7361 | 0.1310 |
| $50 < x \leqslant 500$ | 0.8320 | 0.6309 | 0.8312 | 0.5135 |
| $> 500$ | 0.8735 | 0.7996 | 0.8736 | 0.7574 |

When considering fragmentation, as detailed in section 4.4, the width of the rockfall affecting the exposed element has to be considered since the exposure is affected by this width (Matas et al., 2018). Simulations considering different magnitudes were performed to estimate the affected with in different sections of the path as shown in Figure 5.13. The average results for different rockfall magnitudes are shown in Table 5.3.
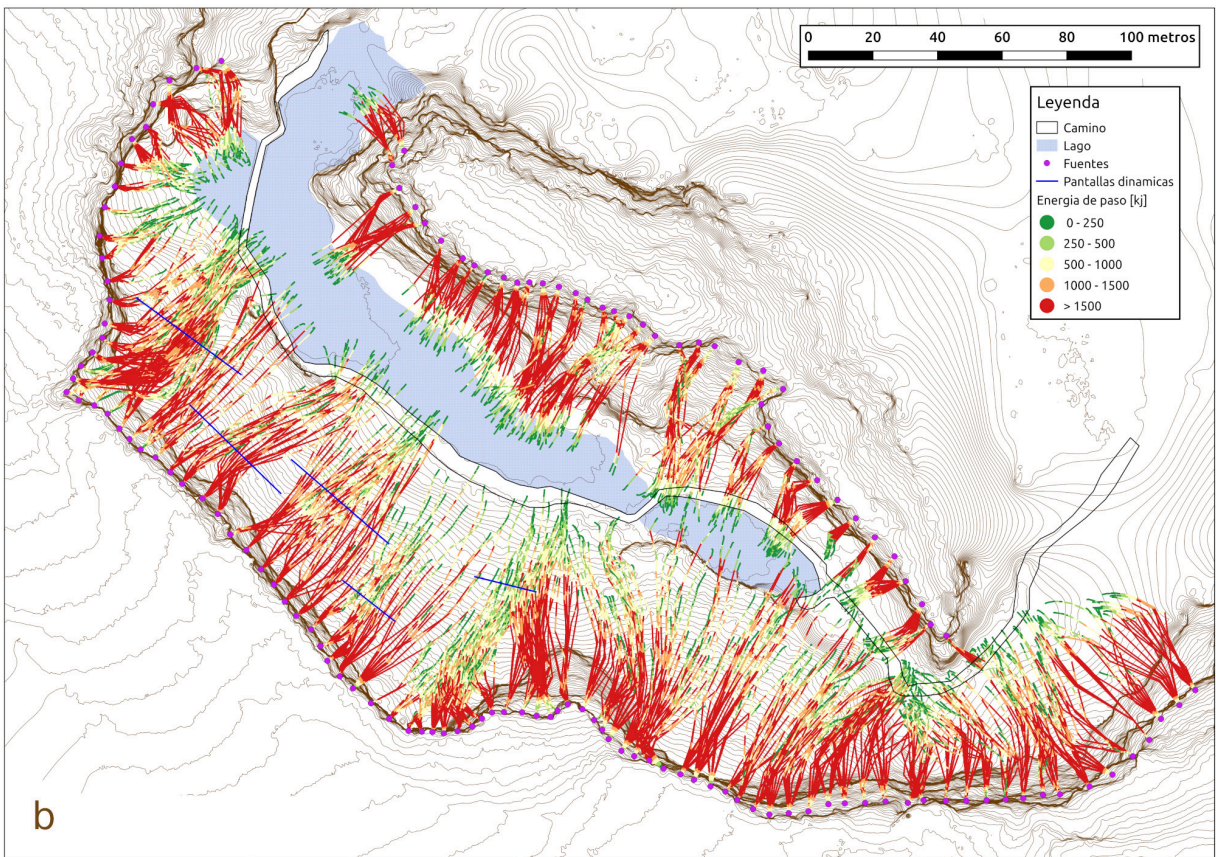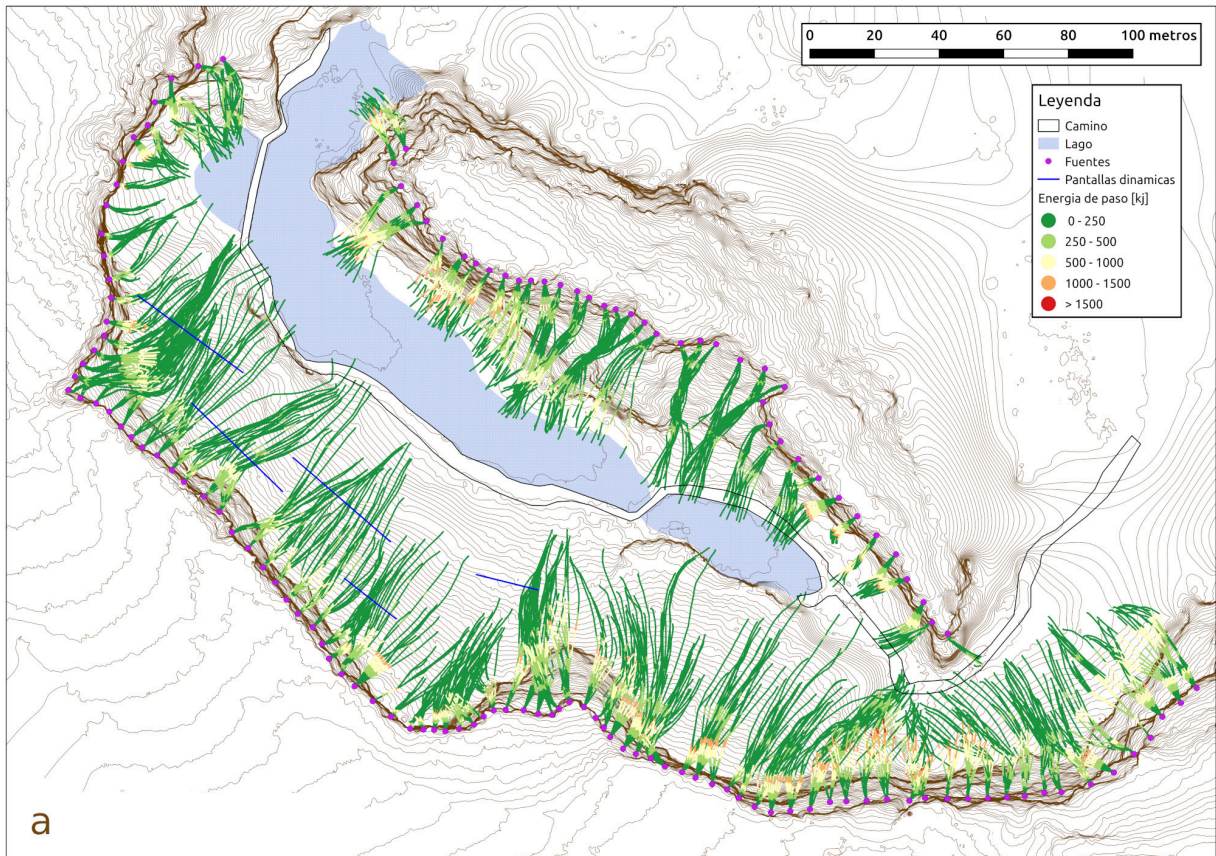
**Figure 5.12:** Simulation results used in the QRA in Monasterio de Piedra case without considering the effect of the dynamic barriers for 1 $m^3$ blocks (above) and for 10 $m^3$ blocks (below). Color scale shows the developed energies during propagation in kJ.
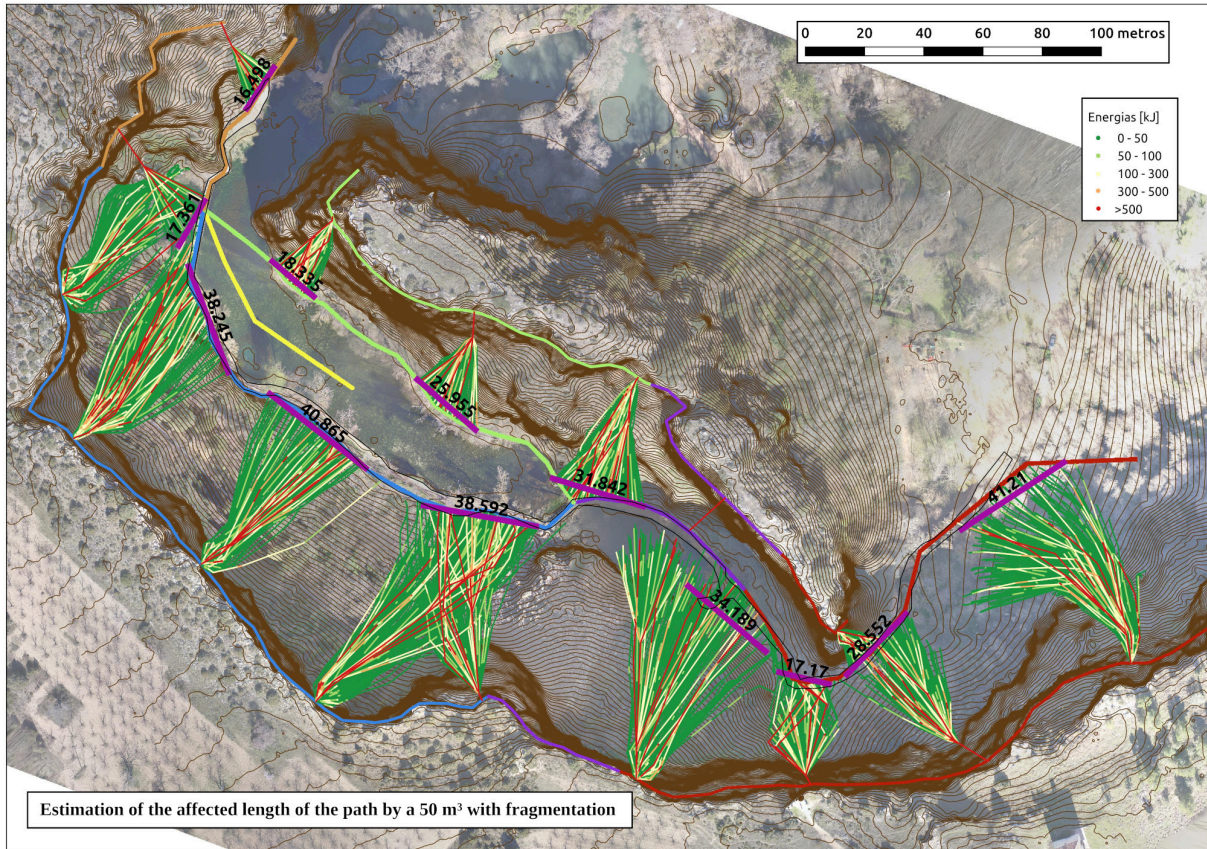
**Figure 5.13:** Estimation of the affected length of the hiking path for a 50 $m^3$ event considering fragmentation.

**Table 5.3:** Values of the affected width W in the trail for different fragmental rockfall volumes, calculated with the RockGIS code.

| Volume class (m3) | Unfragmented rockfalls | Fragmental rockfalls |
|---|---|---|
| x <0.05 | 0.2 | None reaching |
| 0.05<x <0.5 | 0.8 | None reaching |
| 0.5 <x <5 | 1.5 | 17.5 |
| 5 <x <50 | 3.5 | 20 |
| 50 <x <500 | 8 | 40 |
| 500 <x | 10 | 55 |

The last term of the equation is the vulnerability. In this study case, the exposed elements where the humans walking trough the paths, and vulnerability was set to 1 for the events involving blocks bigger than 0.5 $m^3$. This means that all blocks exceeding this dimension would kill an impacted person. This is a conservative hypothesis, but the only option since as far as the author knows, no vulnerability curves have been documented for humans. For smaller blocks, the vulnerability was reduced considering that the probabilities of impact in a critical body part were also reduced by the size reduction of the blocks.

Finally, with all this information the risk could be estimated for the different scenarios. Table 5.4 summarizes the results in the case of fragmental and unfragmented rockfalls both considering or not the presence of the fences.

In the case of not considering the dynamic barriers, some contrasting results of the rockfall fragmentation must be highlighted. On one side, fragmentation reduces the risk totally for rockfall volumes of less than 0.5 $m^3$. This is because fragmentation prevents the rock fragments from reaching the trail section that is, reaching probability equals to zero. On the opposite side, for rockfall volumes larger than 50 $m^3$, fragmentation raises the risk to the visitors. The reason is that the generation of the cone of fragments increases substantially the impacting probability, particularly for large rockfall events whose fragments virtually occupy the whole cone width (Matas et al., 2018). In contrast, for rockfall volumes ranging between 0.5 and 50 $m^3$, the bigger of exposure is compensated by the reduction of the run-out. These effects have a direct consequence on the overall risk value as most of the risk originates from the high-frequency small-magnitude rockfall events, whose runout is strongly affected by the fragmentation. The annual probability of loss of life for individual visitors is reduced from $1.2 \cdot 10^{-2}$ to $3.5 \cdot 10^{-4}$, which is almost two orders of magnitude.

**Table 5.4:** Individual risk (annual probability of loss of life) for intact and fragmental rockfalls considering initial situation (top) and the presence of flexible rockfall protection fences (bottom).

| Initial | | | Unfragmented rockfalls | | | Fragmental rockfalls | | |
|---|---|---|---|---|---|---|---|---|
| Mi (m3) | Ni | V | P(X:D) | P(T:X) | Risk | P(X:D) | P(T:X) | Risk |
| $\leqslant 0{,}05$ | 16.32 | 0.5 | 0.119 | 0.010 | $9.9 \cdot 10^{-3}$ | 0.000 | 0.000 | 0.000 |
| $0{,}05 \leqslant 0{,}5$ | 0.25 | 0.9 | 0.328 | 0.019 | $1.4 \cdot 10^{-3}$ | 0.000 | 0.000 | 0.000 |
| $0{,}5 \leqslant 5$ | $3.3 \cdot 10^{-2}$ | 1.0 | 0.590 | 0.022 | $4.3 \cdot 10^{-4}$ | 0.042 | 0.034 | $4.7 \cdot 10^{-5}$ |
| $5 \leqslant 50$ | $4.3 \cdot 10^{-3}$ | 1.0 | 0.765 | 0.066 | $2.2 \cdot 10^{-4}$ | 0.233 | 0.120 | $1.2 \cdot 10^{-4}$ |
| $50 \leqslant 500$ | $5.7 \cdot 10^{-4}$ | 1.0 | 0.832 | 0.124 | $5.9 \cdot 10^{-5}$ | 0.631 | 0.374 | $1.4 \cdot 10^{-4}$ |
| $>500$ | $8.0 \cdot 10^{-5}$ | 1.0 | 0.873 | 0.153 | $1.0 \cdot 10^{-5}$ | 0.800 | 0.678 | $4.2 \cdot 10^{-5}$ |
| Annual probability of loss of life | | | | | 0,012 | | | $3.5 \cdot 10^{-4}$ |
| **Fences** | Ni | V | P(X:D) | P(T:X) | Risk | P(X:D) | P(T:X) | Risk |
| $\leqslant 0{,}05$ | 16.32 | 0.5 | 0.022 | 0.0102 | $1.8 \cdot 10^{-3}$ | 0.000 | 0.000 | 0.000 |
| $0{,}05 \leqslant 0{,}5$ | 0.25 | 0.9 | 0.065 | 0.0189 | $2.8 \cdot 10^{-4}$ | 0.000 | 0.000 | 0.000 |
| $0{,}5 \leqslant 5$ | $3.3 \cdot 10^{-2}$ | 1.0 | 0.145 | 0.0219 | $1.1 \cdot 10^{-4}$ | 0.012 | 0.037 | $1.5 \cdot 10^{-5}$ |
| $5 \leqslant 50$ | $4.3 \cdot 10^{-3}$ | 1.0 | 0.736 | 0.0656 | $2.1 \cdot 10^{-4}$ | 0.131 | 0.122 | $6.9 \cdot 10^{-5}$ |
| $50 \leqslant 500$ | $5.7 \cdot 10^{-4}$ | 1.0 | 0.831 | 0.1239 | $5.9 \cdot 10^{-5}$ | 0.513 | 0.359 | $1.1 \cdot 10^{-4}$ |
| $>500$ | $8.0 \cdot 10^{-5}$ | 1.0 | 0.874 | 0.1531 | $1.0 \cdot 10^{-5}$ | 0.757 | 0.650 | $3.8 \cdot 10^{-5}$ |
| Annual probability of loss of life | | | | | $2.5 \cdot 10^{-3}$ | | | $2.3 \cdot 10^{-4}$ |

When considering the dynamic barriers, the effects observed in the natural conditions, such as the runout reduction and the increase of exposure are found here as well. However, the efficacy of the flexible rockfall fences in stopping the falling blocks and the subsequent risk reduction is better observed in the analysis of unfragmented rockfalls. There is a reduction of 80% of the annual risk for visitors. Most of the reduction is due to the trapping of small-size rockfall events. The reduction of risk for fragmental rockfall is less significant. The annual risk is reduced around 35% only. The reason is that most of the mid and large-size fragmental rockfalls cannot be stopped by the fences. There exist however an additional cause for this particular example. The probability of reach for fragmental rockfalls in the volume range of 0.5 to 5 $m^3$, has been reduced from 0.04 to 0.01 only. This contrast with the significant reduction observed for the non-fragmented events which is from 0.59 to 0.15. This is because a small percentage of modelled trajectories

are not intercepted by the fences while some rebounds are higher than the height of the fences. This percentage cannot be reduced unless further protection works are carried out. A significant percentage (over 50%) of the large rockfalls for both unfragmented and fragmental rockfalls reach the trail. The existing protection fences are not capable to intercept their trajectories. It is worth noticing however, that for the range of fragmental rockfall volumes between 5 and 50 $m^3$, the reach probability is reduced up to 0.13.

## 5.4 Sensitivity to parameters

The sensitivity analysis of the model to the controlling parameters was checked in two of the study cases. In the case of Vilanova de Benat rockfall, simulations varying the angle of the cone $\theta$ and parameter $b$ controlling the fragmentation law (Ruiz-Carulla et al., 2017) where performed, keeping constant all the parameters obtained with the calibration process. For the cone, 10°, 20°, 40° and 60° apertures were chosen. The location of the center of gravity and the line defining the area containing 80% of the deposited blocks for each case are shown in Figure 5.14a. This figure shows how in this scenario fragmentation reduces the runout of the gravity center of the whole distribution, reduces also the maximum runout and increases the lateral dispersion of the fragments. To appreciate the influence of parameter $b$, five simulations were performed considering values 0.5, 0.75, 1.0, 1.25 and 1.5. Figure 5.14b shows the cumulative number of blocks of each obtained RBSD. An inflexion point can be observed due to the slope variation of the power law. In this figure, the limitation of the model to generate a maximum volume of fragments each time breakage occurs depends on parameter $b$. Note that the results with $b$ equal to 0.75 seem to fit the field RBSD better, but the total number of blocks generated in this case was more than double the estimated number of blocks in the field. Additionally, during the calibration phase with $b$ equal to 0.75, the other calibration criteria gave unsatisfactory results.

The sensitivity was also check in study case 4, the real scale fragmentation test performed in a quarry (Matas et al., 2020b). In this case the parameter set considered as a reference was the result of the calibration process. Each plot in Figure 5.15a–j shows the values of the three $\epsilon$ statistics of each one of the calibration criteria, as a function of the tested parameter. The simulations showed high sensitivity to the pairs of parameters controlling fragmentation: $na_1$, $na_2$; $b_1$, $b_2$; and $q_1$, $q_2$ (Figures 5.15a–f). Each pair displayed similar behavior within the testing range, as expected. Slight variations in the shape of these pairs of curves was due to discretization of the evaluation interval in each case. Note that $b_1$, $b_2$ and $q_1$, $q_2$ define a line, so the shape of the distributions must be very similar regardless of the parameter that varies (but with its corresponding value interval). In the case of $b$, with a focus on runout only, two minimums could be found in the optimization curve but the volume curve showed a clear minimum around $b_1 = $ -1.6 and $b_2 = 2.49$. The same occurred with $q$ where the optimum value was found to be around $q_1 = $ -0.54 and $q_2 = 1$. A zoom on the interval of values that gives, for example, a value of the indicator $\epsilon$ smaller than one in the case of runouts reveals that the range of acceptance of $na_1$, $b_1$ and $q_1$ represents respectively 29%, 8% and 7% variation with respect to the optimum value, while for parameters $na_2$, $b_2$ and $q_2$, the values are, respectively, 5%, 2% and 1.3%. As expected, slight changes in the exponent of the potential function controlling the new generated area and the slopes of the lines controlling $b$ and $q$ were found to have more

influence on the final result (Matas et al., 2020b).
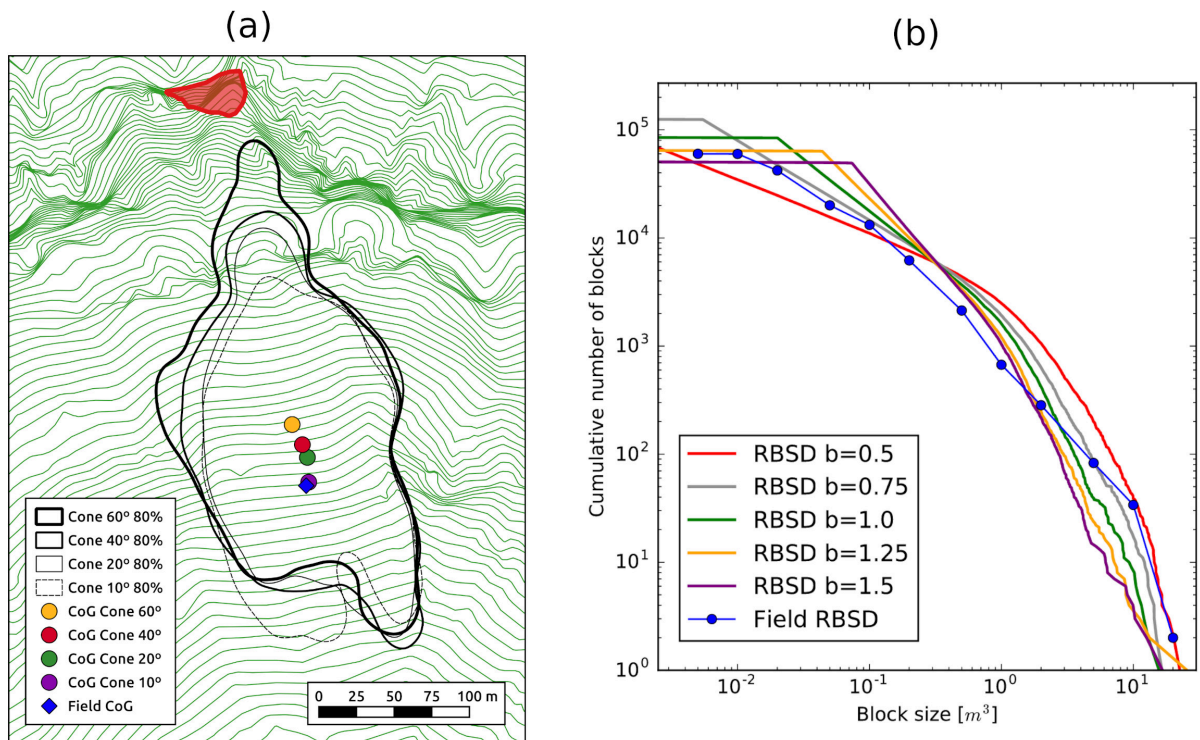


**Figure 5.14:** Results of the parameter sensibility analysis in Vilanova de Benat study case: (a) Density map of the accumulated blocks of four simulations varying the angle of the cone $\theta$ and their centre of gravity. Isolines represent the percentage of the blocks that came to a stop within the corresponding polygon; (b) Cumulative number of blocks of the five simulations performed keeping all the parameters constant except the slope of the power law.
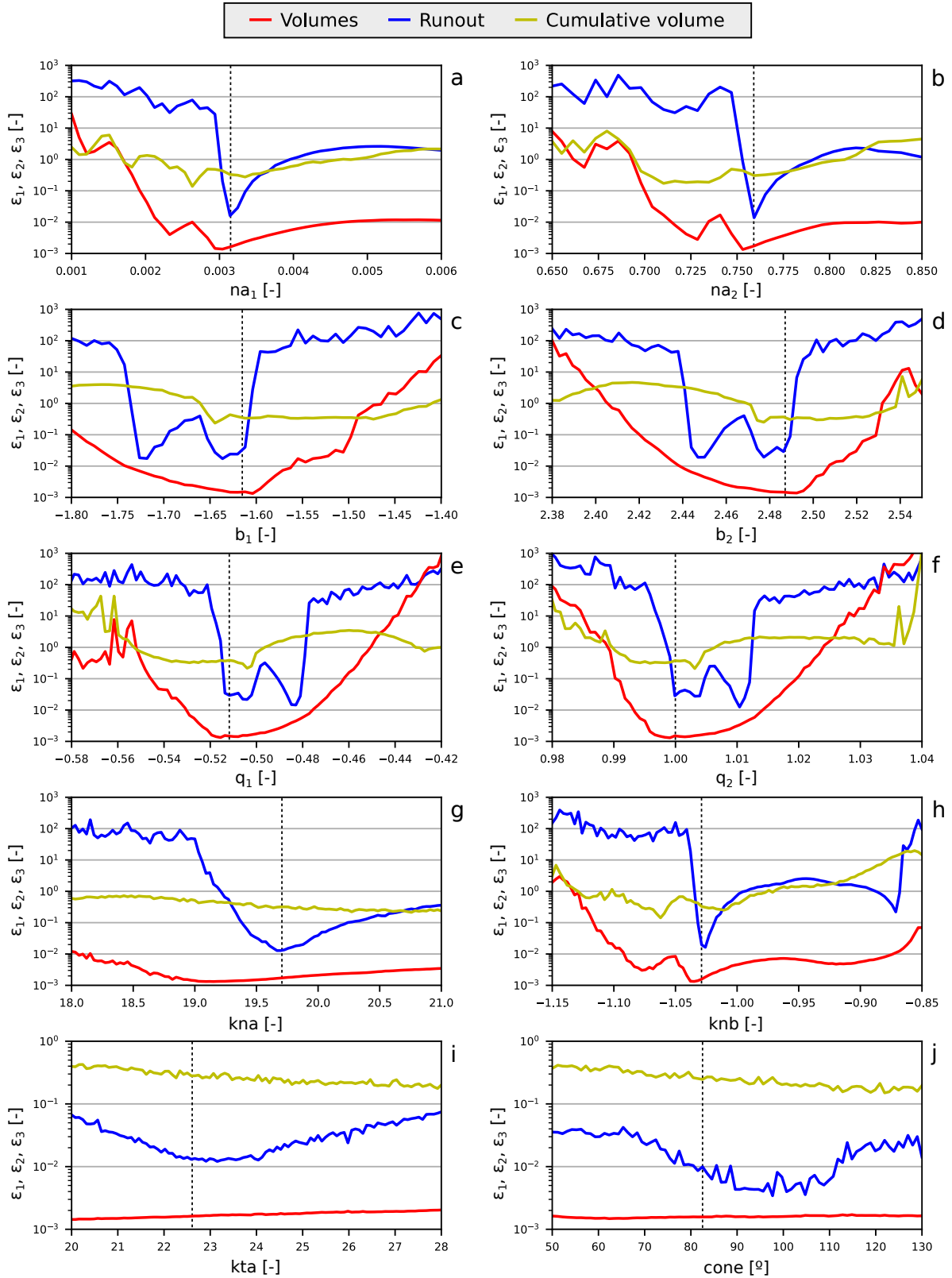
**Figure 5.15:** Results of the sensitivity analysis in the study case 4, a real scale rockfall fragmentation test performed in a quarry. Each plot shows the evolution of the three calibration criteria (volumes, runout and cumulative volume versus runout) within the testing range for each one of the tested parameters. The dashed vertical lines mark the optimal value of the parameter. (a-f): fragmentation law parameters; (g-h): parameters controlling normal restitution coefficients; (i): tangential restitution coefficient parameter and (j) cone aperture when fragmentation occurs. (Matas et al., 2020b)

## 5.5 The effect of fragmentation

In all the test sites, the effect of considering or not the fragmentation phenomenon was checked. One of the most important effects of fragmentation is on the rockfall runout. Fragmentation may significantly reduce the rockfall propagation if the slope is sufficiently gentle and long. This is clearly illustrated in the analysis of the trail section affected by the 2017 rockfall in the Monasterio de Piedra study case (Figure 5.16). None of the rock fragments of the small size (less than $0.5m^3$) fragmented rock masses reaches the trail section (Corominas et al., 2019). This is the reason for the substantial reduction (more than one order of magnitude) of the risk compared to the value of risk for intact blocks for this magnitude range. However, the favorable effect of fragmentation disappears when rockfalls propagate along steep slopes. The blocks cannot stop and the generated cone of fragments increases the exposure, as shown in the trail in the opposite side of the lake.

In the study case 4, fragmentation also increased the runout of the blocks since the ejection of the fragments following tangential trajectories to the ground or big parabolic flights allowed the fragments to reach longer runout distances (Figure 5.17). The ejection of the fragments due to fragmentation increases the total runout in this scenario, but reduces the kinetic energy of each individual fragment compared to the initial block.
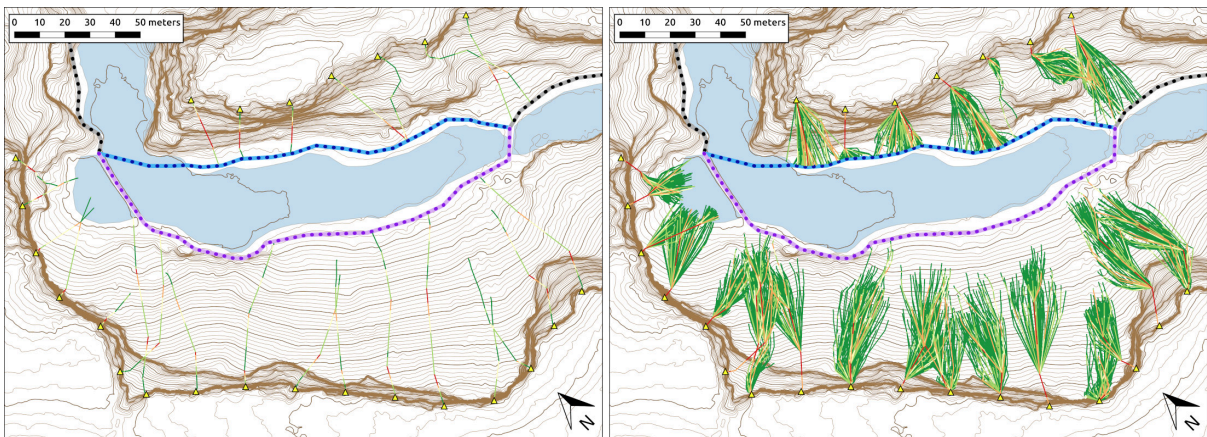


**Figure 5.16:** Trajectories of a 10 $m^3$ block in Monasterio de Piedra study case. Fragmentation is not considered in the image on the left while it is on the image on the right.
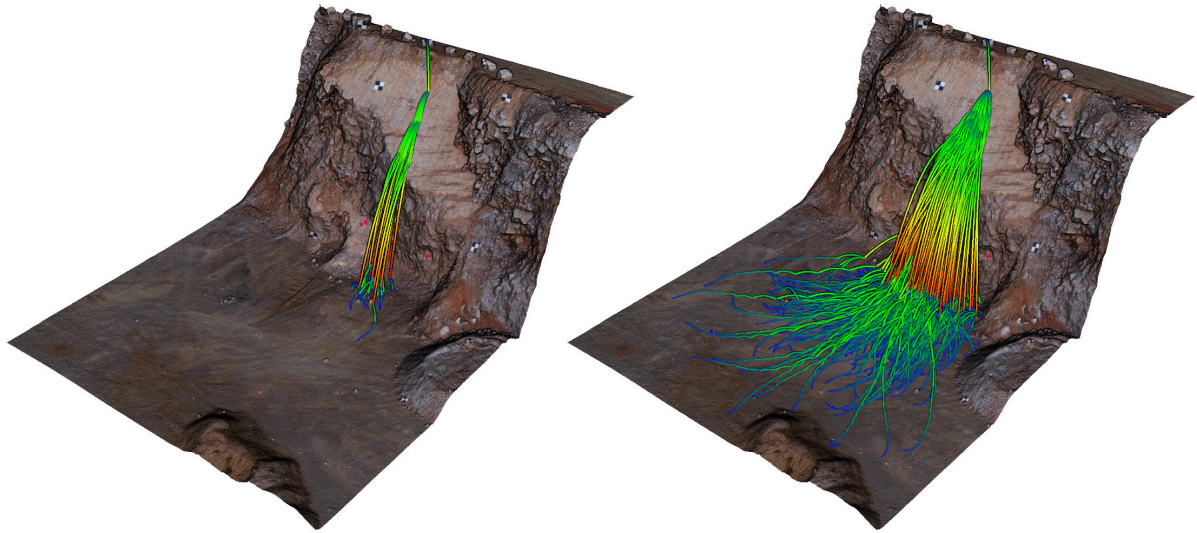
**Figure 5.17:** 3D trajectories of all blocks simulated in the real scale tests scenario 4: Without considering fragmentation (left) and considering fragmentation (right).

# Chapter 6

# Conclusions and future perspectives

The main research question of this thesis, as stated in the first chapter, is "How does the fragmentation influence rockfall propagation?". To answer this question, we carried out a set of real scale tests and the inventory of several natural rockfall events. The analysis of the empirical data acquired provided the bases for better understanding the mechanism of fragmentation and, in particular, the fragmentation laws, the kinematics of the fragments, their trajectories and runout. All this knowledge allowed designing a methodology to consider fragmentation in rockfall propagation codes. The RockGIS code was built from scratch implementing the new observations and findings. Once the model was fully functional, it was used to reproduce fragmental rockfalls in different scenarios. The results after the calibration process considering different fragmentation scenarios showed that the model is capable of reproducing satisfactorily the observations. Moreover, the code has proven to be a powerful tool for the analysis of the consequences of fragmentation phenomenon in rockfalls and in the assessment of hazard and risk. Finally, the code can be used to assess the performance of the rockfall protective works. The conclusions of this thesis are presented here by subjects as follows:

**DATA ACQUISITION**

Few experimental data about fragmentation in rockfalls existed before this thesis. The developed methodologies used to gather information of both natural events and real scale tests gave high quality data for a better understanding of the phenomenon. The new technological advances in image capturing from UAV and the improvement on the recording frame rate of the video cameras played an indispensable role in this acquisition. The minimum fragment size measured using different methods was $10^{-3}$ $m^3$ for natural big events and reached $10^{-5}$ $m^3$ in the case of real scale controlled tests. The precise measurement of the outgoing fragment trajectories after impact in the real scale tests performed allowed the development of the methodology to consider fragmentation upon impact.

Data acquired during this thesis suggest that (i) fragment distributions can be characterized by fractal laws which are easy to implement into a rockfall propagation code; (ii) fragmentation does not depend exclusively on the impact energy, the relationship between the stiffness of the block and that of the ground as well as the geometry of the impact are relevant factors. The fragmentation model considers different fragmentation parameters

as a function of the impacting conditions and can be adjusted depending on the slope material; (iii) the energy transmission to the fragments after breakage is a key point on reproducing fragmentation and preliminary data (still being processed) showed that in the testing conditions of a 41º impacting slope the momentum boost of the fragments was not significant and the reflected velocities of the fragments where similar. Thus, the simplification of considering an energy distribution proportional to the mass in the model, which leads to equal reflected velocities, showed satisfactory results; (iv) the reflected fragments trajectories after breakage were observed to stay within a cone. The values of the cone aperture ranged between 25º and 145º with an average value of 75º; (v) the ejected velocities after fragmentation made some fragments follow high parabolic trajectories while others were ejected almost tangentially to the slope surface. This effect allowed some fragments to reach higher runouts compared to unfragmented blocks; (vi) restitution factors are strongly affected by the impacting velocity and fragmentation can also affect its value since part of the energy is dissipated by the generation of new fractures; (vii) the fragmentation process is an extremely stochastic phenomena and blocks with very similar sizes, materials and impacting conditions gave different fragmentation patterns depending on the geometry of the block during the impact and the stiffness of the impacting surface.

## MODELLING FRAGMENTATION IN ROCKFALLS

A stochastic modelling approach for considering fragmentation in rockfalls has been developed and implemented in the rockfall simulation code RockGIS. The code is implemented using C++, a compiled programming language known for its performance since it has a low abstraction level. This code is planned to be open sourced after the defence of this thesis so as the scientific community and professionals can review, reuse and improve it with its contributions.

In the code the propagation of the blocks is simulated using a lumped mass approach in the space defined by a raster digital elevation model and performs the rebound calculations using restitution factors according to the land cover. The trajectory of the blocks is computed by integrating movement equations that result in ballistic trajectories. A contact algorithm is used to determine when the flying particles impact the ground surface. This algorithm uses a bisection approach once the trajectory has intersected the ground surface to determine with accuracy the impact point. The lumped mass approach allows an easy detection of the contact compared to rockfall propagation models explicitly considering the shape of the block since several more possible contacts have to be checked at each time step. When the impact is detected, the rebound conditions are evaluated, and the new trajectory is defined using the restitution. Then, a fragmentation module is triggered and depending on the impacting conditions determines the parameters describing the fragmentation law to use. If the fragmentation law does not produce more than one fragment, the block remains unbroken and keeps its propagation following the initially computed trajectory. In case the computed parameters produce the breakage of the block, the mass is then distributed according to the either scale invariant or variant potential law that they define. After breakage, the hypothesis that fragment trajectories stay within a cone-shaped envelope has proven to be a simple yet effective way to represent the phenomenon.

The implementation of the code was done modularly to allow the modification of each of its parts. Thus, it is possible to modify the functions that determine the restitution factors, the laws of fragmentation to distribute the mass as well as the distribution of the energy between the different fragments after breakage.

The implementation of these procedures in RockGIS has shown good results in different scenarios from big natural events of 10-10,000 $m^3$ of initially detached rock mass to real scale tests with blocks ranging 0.3 to 2 $m^3$. The calibration process considering fragmentation was very challenging since in addition to the usual parameters in propagation models that do not consider fragmentation, it was necessary to simultaneously calibrate the parameters that control the breakage of the blocks. Moreover, it was necessary to define novel goodness of fit indicators to evaluate the performance of the model when considering fragmentation in terms of (i) the fragment size distribution of the final deposit; (ii) the lateral scattering of the fragments; (iii) the cumulative spatial distribution of the volume of the fragments as a function of distance from the release point; (iv) the runout distribution of the fragments. The simulations were able to reproduce, in all the studied scenarios, the considered goodness of fit indicators. The calibration criteria for fragmental rockfall simulations proposed in this thesis establish a solid base for future studies.

## QUANTITATIVE RISK ASSESSMENT

The quantitative risk analysis of fragmental rockfall has to overcome several challenges related to the evaluation of the occurrence probability or frequency of the events, the runout modeling and the behavior of the falling mass. It must also account for the uncertainties due to inherently complex physical processes involved and the stochastic variability of all the relevant parameters. To the author's knowledge, this thesis includes the first attempt to address the quantitative risk assessment of fragmental rockfalls. It has been carried out with simulations using the RockGIS code and considering a fragmentation law for the falling rock masses.

Fragmentation has forced us to rethink the concept of exposure since it can increase the affected area due to the increment of the number of moving fragments and the scattering of their trajectories. The classical risk equation had to be slightly modified to consider the possible scattering of fragments and thus the increment on the affection area in the case of linear structures. Differences of up two orders of magnitude in the estimation of the annual probability of loss of life were obtained between considering or not fragmentation.

We should keep in mind that rockfalls, as well as fragmentation, are stochastic phenomena. To use the proposed approach for risk analysis and the design of protective measures, a precise calibration is required to ensure the parameters are appropriate for the case study considered.

## EFFECTS OF FRAGMENTATION

The answer to the main research question is that fragmentation in rockfalls has both a significant and contrasting effect on the calculation of risk and should not be obviated in risk analysis. Risk is significantly reduced if the slope where blocks propagate is sufficiently

long and gentle. In this case, the new fragments generated mobilize less energy and can be trapped by the topographic irregularities, obstacles and the protection measures. Conversely, a wide range of block sizes are able to reach exposed elements below steep slopes. In such a situation, fragmentation increases notably the divergence of the block trajectories, which increases the impacting probabilities on exposed elements.

## FUTURE WORKS

The RockGIS code has the ability to do forward analysis. Based on the work of Ruiz-Carulla and Corominas (2019), the final fragment size distribution can be estimated. To do so, it is necessary to determine both the in situ block size distribution of the unstable rock mass and the estimated potential energy of the firsts impacts. Then, this estimation could be used as a reference to calibrate the internal parameters or the fragmentation module in RockGIS code.

There is room for improvement on the consideration of the rebound depending on the size of the impacting fragment. It is common to use different sets of restitution coefficients for different block sizes, but when considering fragmentation the model has to be able to reproduce this different behaviour depending on the size. Terrain roughness plays a significant role in this effect, and some authors are currently working on approaches to improve its consideration into propagation codes. Real scale tests showed that the impacting position of the block (face, edge or a vertex with respect to the surface), the relative orientation between the maximum impact force direction and the main weakness anisotropy and the stiffness of the impacting surface may control the fragmentation pattern. One of the limitations of considering a lumped mass approach when simulating the breakage of a block is that its relative position when impacting with the slope is unknown since the geometry is not explicitly accounted for. This limitation may be overcome by considering a stochastic approach to determine how probable is that the block impacts with a face, an edge or a vertex.

Future work should include testing the model on other real rockfall events and performing more real scale tests to improve the mass and energy distribution algorithms used in the fragmentation model. These improvements will allow an approximate guess of the parameters that have to be used in the fragmentation model depending on the variables that affect the process, such as the rock material and the coverage.

The comminution in large rockfalls has shown to significantly modify the fragmentation pattern of the blocks placed at the bottom of the detached mass when impacting with the slope. The experimental results regarding the laboratory test carried out during this research may allow a first approach to considering different fragmentation parameters on the blocks placed at the bottom of the unstable rock mass. However, this subject is still in its early stages and more research is required for a better understanding of the comminution mechanism. Some authors have started to use the discrete element approach to simulate this behaviour, and the results are promising. With a good calibration, this method allows to test several initial configurations with slight changes on the input parameters, which is very adequate when dealing with such stochastic phenomena like fragmental rockfalls.

In this work, a simplistic approach has been adopted for the consideration of the protection

structures since the focus was on the fragmentation process. However, recent authors have proposed more sophisticated approaches using discrete elements simulations to build meta models into propagation codes. In these studies, they build virtual physical models of dynamic fences, concrete galleries and embankments and simulate different impacting conditions. Then, a mathematical model is adjusted to reproduce the effect of the different impacting scenarios with the structure. The same applies to the consideration of the forest, considered as a natural rockfall protection. This kind of metamodels could be implemented into RockGIS code to improve the accuracy when evaluating the performance of protection structures and the effect of vegetation.

# Bibliography

Abbruzzese, J. M., Sauthier, C., and Labiouse, V. (2009). "Considerations on Swiss methodologies for rock fall hazard mapping based on trajectory modelling". In: *Natural Hazards and Earth System Science* 9.4, pp. 1095–1109. ISSN: 16849981. DOI: 10.5194/nhess-9-1095-2009.

Agliardi, F. and Crosta, G. B. (2003). "High resolution three-dimensional numerical modelling of rock-falls". In: *International Journal of Rock Mechanics and Mining Sciences* 40.4, pp. 455–471. ISSN: 13651609. DOI: 10.1016/S1365-1609(03)00021-2.

Agliardi, F., Crosta, G. B., and Frattini, P. (2009). "Integrating rockfall risk assessment and countermeasure design by 3D modelling techniques". In: *Natural Hazards and Earth System Science* 9.4, pp. 1059–1073. ISSN: 16849981. DOI: 10.5194/nhess-9-1059-2009.

Asteriou, P., Saroglou, H., and Tsiambaos, G. (2012). "Geotechnical and kinematic parameters affecting the coefficients of restitution for rock fall analysis". In: *International Journal of Rock Mechanics and Mining Sciences* 54.0, pp. 103–113. ISSN: 13651609. DOI: 10.1016/j.ijrmms.2012.05.029.

Asteriou, P. and Tsiambaos, G. (2016). "Empirical Model for Predicting Rockfall Trajectory Direction". In: *Rock Mechanics and Rock Engineering* 49.3, pp. 927–941. ISSN: 07232632. DOI: 10.1007/s00603-015-0798-7.

– (2018). "Effect of impact velocity, block mass and hardness on the coefficients of restitution for rockfall analysis". In: *International Journal of Rock Mechanics and Mining Sciences* 106, pp. 41–50. ISSN: 13651609. DOI: 10.1016/j.ijrmms.2018.04.001.

Ayala-Carcedo, F. J., Cubillo-Nielsen, S., Alvarez, A., Domínguez, M. J., Laín, L., Laín, R., and Ortiz, G. (2003). "Large scale rockfall reach susceptibility maps in La Cabrera Sierra (Madrid) performed with GIS and dynamic analysis at 1:5,000". In: *Natural Hazards* 30.3, pp. 325–340. ISSN: 0921030X. DOI: 10.1023/B:NHAZ.0000007095.12516.90.

Azzoni, A., Rossi, P. P., Drigo, E., Giani, G. P., and Zaninetti, A. (1992). "In situ observation of rockfall analysis parameters". In: *Sixth International Symposium of Landslides*. Rotterdam, The Netherlands, pp. 307–314.

Blasio, F. and Crosta, G. (2015). "Fragmentation and boosting of rock falls and rock avalanches". In: *Geophysical Research Letters* 42.20, pp. 8463–8470. DOI: 10.1002/2015GL064723.

Blasio, F., Dattola, G., and Crosta, G. (2018). "Extremely Energetic Rockfalls". In: *Journal of Geophysical Research: Earth Surface*. DOI: 10.1029/2017JF004327.

Bonneau, D. A., Hutchinson, D. J., DiFrancesco, P.-M., Coombs, M., and Sala, Z. (2019). "Three-dimensional rockfall shape back analysis: methods and implications". In: *Natural Hazards and Earth System Sciences* 19.12, pp. 2745–2765. DOI: 10.5194/nhess-19-2745-2019.

Bourrier, F., Dorren, L., Nicot, F., Berger, F., and Darve, F. (2009). "Toward objective rockfall trajectory simulation using a stochastic impact model". In: *Geomorphology* 110.3-4, pp. 68–79. ISSN: 0169555X. DOI: 10.1016/j.geomorph.2009.03.017.

Bourrier, F., Berger, F., Tardif, P., Dorren, L., and Hungr, O. (2012). "Rockfall rebound: comparison of detailed field experiments and alternative modelling approaches". In: *Earth Surface Processes and Landforms* 37.6, pp. 656–665. ISSN: 1096-9837. DOI: 10.1002/esp.3202.

Bourrier, F. and Hungr, O. (2013a). "Rockfall Dynamics: A Critical Review of Collision and Rebound Models". In: *Rockfall Engineering*. John Wiley & Sons, Inc., pp. 175–209. ISBN: 9781118601532. DOI: `10.1002/9781118601532.ch6`.

– (2013b). "Rockfall Dynamics: A Critical Review of Collision and Rebound Models". In: *Rockfall Engineering*. John Wiley & Sons, Inc., pp. 175–209. ISBN: 9781118601532. DOI: `10.1002/9781118601532.ch6`.

Bozzolo, D., Pamini, R., and Hutter, K. (1988). "Rockfall analysis – A mathematical model and its test with field data". In: *5th International Symposium on Landslides*. Balkema, Rotterdamm, Lausanne, Switzerland, pp. 555–563.

Budetta, P., De Luca, C., and Nappi, M. (2016). "Quantitative rockfall risk assessment for an important road by means of the rockfall risk management (RO.MA.) method". In: *Bulletin of Engineering Geology and the Environment* 75.4, pp. 1377–1397. ISSN: 1435-9537. DOI: `10.1007/s10064-015-0798-6`.

Budetta, P. and Santo, A. (1994). "Morphostructural evolution and related kinematics of rockfalls in Campania (southern Italy): A case study". In: *Engineering Geology* 36.3-4, pp. 197–210. ISSN: 00137952. DOI: `10.1016/0013-7952(94)90004-3`.

Caviezel, A., Demmel, S. E., Ringenbach, A., Bühler, Y., Lu, G., Christen, M., Dinneen, C. E., Eberhard, L. A., Von Rickenbach, D., and Bartelt, P. (2019). "Reconstruction of four-dimensional rockfall trajectories using remote sensing and rock-based accelerometers and gyroscopes". In: *Earth Surface Dynamics* 7.1, pp. 199–210. ISSN: 2196632X. DOI: `10.5194/esurf-7-199-2019`.

Chau, K. T., Chan, L. C. P., Wu, J. J., Liu, J., Wong, R. H. C., and Lee, C. F. (1998). "Experimental studies on rockfall and debris flow". In: *One Day Seminar on Planning, Design and Implementation of Debris Flow and Rockfall Hazards Mitigation Measures*. Hongkong, China, pp. 115–128.

Chau, K. T., Wong, R. H., and Wu, J. J. (2002). "Coefficient of restitution and rotational motions of rockfall impacts". In: *International Journal of Rock Mechanics and Mining Sciences* 39.1, pp. 69–77. ISSN: 13651609. DOI: `10.1016/S1365-1609(02)00016-3`.

Chau, K. T., Wong, R. H., Liu, J., and Lee, C. F. (2003). "Rockfall Hazard Analysis for Hong Kong Based on Rockfall Inventory". In: *Rock Mechanics and Rock Engineering* 36.5, pp. 383–408. ISSN: 07232632. DOI: `10.1007/s00603-002-0035-z`.

Copons, R., Vilaplana, J. M., and Linares, R. (2009). "Rockfall travel distance analysis by using empirical models (Solà d'Andorra la Vella, Central Pyrenees)". In: *Natural Hazards and Earth System Science* 9.6, pp. 2107–2118. ISSN: 16849981. DOI: `10.5194/nhess-9-2107-2009`.

Corominas, J., Westen, C. van, Frattini, P., Cascini, L., Malet, J. P., Fotopoulou, S., Catani, F., Van Den Eeckhaut, M., Mavrouli, O., Agliardi, F., Pitilakis, K., Winter, M. G., Pastor, M., Ferlisi, S., Tofani, V., Hervás, J., and Smith, J. T. (2014). "Recommendations for the quantitative analysis of landslide risk". In: *Bulletin of Engineering Geology and the Environment* 73.2, pp. 209–263. ISSN: 14359529. DOI: `10.1007/s10064-013-0538-8`.

Corominas, J. (1996). "The angle of reach as a mobility index for small and large landslides". In: *Canadian Geotechnical Journal* 33.2, pp. 260–271. ISSN: 00083674. DOI: `10.1139/t96-005`.

Corominas, J., Copons, R., Vilaplana, J. M., Altimir, J., and Amigó, J. (2003). "Integrated landslide susceptibility analysis and hazard assessment in the principality of Andorra". In: *Natural Hazards* 30.3, pp. 421–435. ISSN: 0921030X. DOI: `10.1023/B:NHAZ.0000007094.74878.d3`.

Corominas, J., Coros, J., and Mavrouli, O. (2012). "Simplified approach for obtaining the block volume distribution of fragmental rockfalls". In: 2. Ed. by E. Eberhardt, C. Froese, and A. Turner, pp. 1159–1164.

Corominas, J. (2013). "Avoidance and Protection Measures". In: *Treatise on Geomorphology*, pp. 259–272. ISBN: 9780080885223. DOI: `10.1016/B978-0-12-374739-6.00176-7`.

Corominas, J., Mavrouli, O., and Ruiz-Carulla, R. (2017). "Rockfall Occurrence and Fragmentation". In: *Advancing Culture of Living with Landslides*. Ed. by K. Sassa, M. Mikoš, and Y. Yin. Cham: Springer International Publishing, pp. 75–97. ISBN: 978-3-319-59469-9. DOI: `10.1007/978-3-319-59469-9_4`.

Corominas, J., Matas, G., and Ruiz-Carulla, R. (2019). "Quantitative analysis of risk from fragmental rockfalls". In: *Landslides* 16.1, pp. 5–21. ISSN: 16125118. DOI: 10.1007/s10346-018-1087-9.

Coulibaly, J., Chanut, M.-A., Lambert, S., and Nicot, F. (May 2019). "Toward a Generic Computational Approach for Flexible Rockfall Barrier Modeling". In: *Rock Mechanics and Rock Engineering*. DOI: 10.1007/s00603-019-01878-6.

Crosta, G. B. and Agliardi, F. (2003). "A methodology for physically based rockfall hazard assessment". In: *Natural Hazards and Earth System Science* 3.5, pp. 407–422. ISSN: 15618633. DOI: 10.5194/nhess-3-407-2003.

Crosta, G. B., Agliardi, F., Frattini, P., and Lari, S. (2015). "Key issues in rock fall modeling, hazard and risk assessment for rockfall protection". In: *Engineering Geology for Society and Territory - Volume 2: Landslide Processes*. Ed. by G. Lollino, D. Giordan, G. B. Crosta, J. Corominas, R. Azzam, J. Wasowski, and N. Sciarra. Cham: Springer International Publishing, pp. 43–58. ISBN: 9783319090573. DOI: 10.1007/978-3-319-09057-3_4.

Cruden, D. and Fell, R. (1997). *Landslide Risk Assessment*. CRC Press. ISBN: 9789054109143.

Cuervo, S., Daudon, D., Richefeu, V., Villard, P., and Lorentz, J. (2015). "Discrete element modeling of a rockfall in the south of the "Massif Central", France". In: *Engineering Geology for Society and Territory - Volume 2: Landslide Processes*. ISBN: 9783319090573. DOI: 10.1007/978-3-319-09057-3_294.

Cui, S. hua, Pei, X. jun, and Huang, R. qiu (2017). "Rolling motion behavior of rockfall on gentle slope: an experimental approach". In: *Journal of Mountain Science* 14.8, pp. 1550–1562. ISSN: 16726316. DOI: 10.1007/s11629-016-4144-7.

Davies, T. R., McSaveney, M. J., and Hodgson, K. A. (1999). "A fragmentation-spreading model for long-runout rock avalanches". In: *Canadian Geotechnical Journal* 36.6, pp. 1096–1110. ISSN: 00083674. DOI: 10.1139/t99-067.

Davies, T. R. and McSaveney, M. J. (2002). "Dynamic simulation of the motion of fragmenting rock avalanches". In: *Canadian Geotechnical Journal* 39.4, pp. 789–798. ISSN: 00083674. DOI: 10.1139/t02-035.

Dorren, L. K. A., Berger, F., and Putters, U. S. (2006). "Real-size experiments and 3-D simulation of rockfall on forested and non-forested slopes". In: *Natural Hazards and Earth System Science* 6.1, pp. 145–153. DOI: 10.5194/nhess-6-145-2006.

Dorren, L., Berger, F., le Hir, C., Mermin, E., and Tardif, P. (2005). "Mechanisms, effects and management implications of rockfall in forests". In: *Forest Ecology and Management* 215.1, pp. 183–195. ISSN: 0378-1127. DOI: https://doi.org/10.1016/j.foreco.2005.05.012.

Dorren, L. K. and Seijmonsbergen, A. C. (2003a). "Comparison of three GIS-based models for predicting rockfall runout zones at a regional scale". In: *Geomorphology* 56.12, pp. 49–64. ISSN: 0169-555X. DOI: http://dx.doi.org/10.1016/S0169-555X(03)00045-X.

Dorren, L. K. and Seijmonsbergen, A. C. (2003b). "Comparison of three GIS-based models for predicting rockfall runout zones at a regional scale". In: *Geomorphology* 56.1-2, pp. 49–64. ISSN: 0169555X. DOI: 10.1016/S0169-555X(03)00045-X.

Dupire, S., Bourrier, F., Monnet, J. M., Bigot, S., Borgniet, L., Berger, F., and Curt, T. (2016). "Novel quantitative indicators to characterize the protective effect of mountain forests against rockfall". In: *Ecological Indicators* 67, pp. 98–107. ISSN: 1470160X. DOI: 10.1016/j.ecolind.2016.02.023.

Dussauge-Peisser, C., Helmstetter, A., Grasso, J. R., Hantz, D., Desvarreux, P., Jeannin, M., and Giraud, A. (2002). "Probabilistic approach to rock fall hazard assessment: Potential of historical data analysis". In: *Natural Hazards and Earth System Sciences* 2.1-2, pp. 15–26. ISSN: 15618633. DOI: 10.5194/nhess-2-15-2002.

Effeindzourou, A., Thoeni, K., Giacomini, A., and Wendeler, C. (2017). "Efficient discrete modelling of composite structures for rockfall protection". In: *Computers and Geotechnics* 87, pp. 99–114. ISSN: 0266-352X. DOI: https://doi.org/10.1016/j.compgeo.2017.02.005.

Einstein, H. (1988). "Landslide risk assessment procedure". In: *Proceedings of the Fifth International Symposium on Landslides*. Ed. by C. Bonnard. Vol. 2. ISBN 9061918391. Lausanne, Switzerland: Balkema, Rotterdam, pp. 1075–1090.

Elmouttie, M. K. and Poropat, G. V. (2012). "A Method to Estimate In Situ Block Size Distribution". In: *Rock Mechanics and Rock Engineering* 45.3, pp. 401–407. ISSN: 1434-453X. DOI: 10.1007/s00603-011-0175-0.

Evans, S. G. and Hungr, O. (1993). "The assessment of rockfall hazard at the base of talus slopes". In: *Canadian Geotechnical Journal* 30.4, pp. 620–636. ISSN: 0008-3674. DOI: 10.1139/t93-054.

Fell, R., Ho, K. K. S., Lacasse, S., and Leroi, E. (2005). "A framework for landslide risk assessment and management". In: *International Conference on Landslide Risk Management, Vancouver, Canada*. Vol. 31.

Fell, R., Corominas, J., Bonnard, C., Cascini, L., Leroi, E., and Savage, W. Z. (2008). "Guidelines for landslide susceptibility, hazard and risk zoning for land use planning". In: *Engineering Geology* 102.3-4, pp. 85–98. ISSN: 00137952. DOI: 10.1016/j.enggeo.2008.03.022.

Feng, L., Pazzi, V., Intrieri, E., Gracchi, T., and Gigli, G. (2019). "Rockfall seismic features analysis based on in situ tests: frequency, amplitude, and duration". In: *Journal of Mountain Science* 16.5, pp. 955–970. ISSN: 19930321. DOI: 10.1007/s11629-018-5286-6.

Ferlisi, S., Cascini, L., Corominas, J., and Matano, F. (2012). "Rockfall risk assessment to persons travelling in vehicles along a road: The case study of the Amalfi coastal road (southern Italy)". In: *Natural Hazards* 62.2, pp. 691–721. ISSN: 0921030X. DOI: 10.1007/s11069-012-0102-z.

Ferrari, F., Giacomini, A., and Thoeni, K. (2016). "Qualitative Rockfall Hazard Assessment: A Comprehensive Review of Current Practices". In: *Rock Mechanics and Rock Engineering* 49.7, pp. 2865–2922. ISSN: 1434-453X. DOI: 10.1007/s00603-016-0918-z.

Finlay, P. J., Mostyn, G. R., and Fell, R. (1999). "Landslide risk assessment: Prediction of travel distance". In: *Canadian Geotechnical Journal* 36.3, pp. 556–562. ISSN: 00083674. DOI: 10.1139/t99-012.

Fornaro, M., Peila, D., and Nebbia, M. (1990). "Block falls on rock slopes - application of a numerical simulator program to some real cases: Fornaro, M; Peila, D; Nebbia, M Proc 6th International Congress International Association of Engineering Geology, Amsterdam, 6–10 August 1990V3, P2173–2180. Publ". In: *International Journal of Rock Mechanics and Mining Sciences & Geomechanics Abstracts* 29.4, p. 257. ISSN: 0148-9062. DOI: https://doi.org/10.1016/0148-9062(92)90920-U.

Francioni, M., Antonaci, F., Sciarra, N., Robiati, C., Coggan, J., Stead, D., and Calamita, F. (2020). "Application of Unmanned Aerial Vehicle Data and Discrete Fracture Network Models for Improved Rockfall Simulations". In: *Remote Sensing* 12, p. 2053. DOI: 10.3390/rs12122053.

Giacomini, A., Buzzi, O., Renard, B., and Giani, G. P. (2009). "Experimental studies on fragmentation of rock falls on impact with rock surfaces". In: *International Journal of Rock Mechanics and Mining Sciences* 46.4, pp. 708–715. ISSN: 13651609. DOI: 10.1016/j.ijrmms.2008.09.007.

Giacomini, A., Thoeni, K., Lambert, C., Booth, S., and Sloan, S. W. (2012). "Experimental study on rockfall drapery systems for open pit highwalls". In: *International Journal of Rock Mechanics and Mining Sciences* 56.0, pp. 171–181. ISSN: 13651609. DOI: 10.1016/j.ijrmms.2012.07.030.

Giani, G. P., Giacomini, A., Migliazza, M., and Segalini, A. (2004). "Experimental and theoretical studies to improve rock fall analysis and protection work design". In: *Rock Mechanics and Rock Engineering* 37.5, pp. 369–389. ISSN: 07232632. DOI: 10.1007/s00603-004-0027-2.

Giani, G. (1992). *Rock Slope Stability Analysis*. Taylor & Francis.

Gili, J. A., Ruiz, R., Matas, G., Corominas, J., Lantada, N., Núñez, M. A., Mavrouli, O., Buill, F., Moya, J., Prades, A., and Moreno, S. (2016). "Experimental study on rockfall fragmentation: In situ test design and first results". In: *Landslides and Engineered Slopes. Experience, Theory and Practice*. Ed. by S. Aversa, L. Cascini, L. Picarelli, and C. Scavia. Vol. 2. ISL Proceedings, pp. 983–990. ISBN: 9781138029880. DOI: 10.1201/b21520-116.

Gili, J. A., Ruiz-Carulla, R., Matas, G., Moya, J., Prades, A., Corominas, J., Lantada, N., Nuñez-Andrés, M. A., Buill, F., Puig, C., Martínez-Bofill, J., Saló, L., and Mavrouli, O. (2020). "Rockfalls: analysis of the block fragmentation through field experiments". In: *Landslides* Submitted.

Gischig, V. S., Hungr, O., Mitchell, A., and Bourrier, F. (2015). "Pierre3D: a 3D stochastic rockfall simulator based on random ground roughness and hyperbolic restitution factors". In: *Canadian Geotechnical Journal* 52.9, pp. 1360–1373. ISSN: 0008-3674. DOI: 10.1139/cgj-2014-0312.

Grady, D. and Kipp, M. (1987). "Dynamic Rock Fragmentation". In: *Fracture Mechanics of Rock*, pp. 429–475. DOI: 10.1016/b978-0-12-066266-1.50015-6.

Guccione, D., Thoeni, K., Giacomini, A., Buzzi, O., and Fityus, S. (2020). "Efficient multi-view 3d tracking of arbitrary rock fragments upon impact". In: *ISPRS - International Archives of the Photogrammetry, Remote Sensing and Spatial Information Sciences* XLIII-B2-2020, pp. 589–596. DOI: 10.5194/isprs-archives-XLIII-B2-2020-589-2020.

Guo, J., Liu, Y., Wu, L., Liu, S., Yang, T., Zhu, W., and Zhang, Z. (2019). "A geometry- and texture-based automatic discontinuity trace extraction method for rock mass point cloud". In: *International Journal of Rock Mechanics and Mining Sciences* 124, p. 104132. ISSN: 1365-1609. DOI: https://doi.org/10.1016/j.ijrmms.2019.104132.

Guzzetti, F., Reichenbach, P., and Wieczorek, G. F. (2003). "Rockfall hazard and risk assessment in the Yosemite Valley, California, USA". In: *Natural Hazards and Earth System Science* 3.6, pp. 491–503. ISSN: 15618633. DOI: 10.5194/nhess-3-491-2003.

Guzzetti, F., Crosta, G., Detti, R., and Agliardi, F. (2002). "STONE: A computer program for the three-dimensional simulation of rock-falls". In: *Computers and Geosciences* 28.9, pp. 1079–1093. ISSN: 00983004. DOI: 10.1016/S0098-3004(02)00025-0.

Guzzetti, F., Ardizzone, F., Cardinali, M., Rossi, M., and Valigi, D. (2009). "Landslide volumes and landslide mobilization rates in Umbria, central Italy". In: *Earth and Planetary Science Letters* 279.3, pp. 222–229. ISSN: 0012-821X. DOI: https://doi.org/10.1016/j.epsl.2009.01.005.

Hall, D. C. (2017). "Sampling random directions within an elliptical cone". In: *Computer Physics Communications* 219, pp. 87–90. ISSN: 00104655. DOI: 10.1016/j.cpc.2017.05.010.

Hantz, D. (2011). "Quantitative assessment of diffuse rock fall hazard along a cliff foot". In: *Natural Hazards and Earth System Science* 11.5, pp. 1303–1309. ISSN: 15618633. DOI: 10.5194/nhess-11-1303-2011.

Heim, Albert (1932). "Bergsturz und Menschenleben". In: *Naturforschenden Gesellschaft in Zürich* 77, p. 218.

Ho, K., Leroi, E., and Roberds, B. (2000). "Quantitative risk assessment: Application, myths and future direction". In: *ISRM International Symposium 2000 GeoEng2000*. Melbourne, pp. 269–312.

Hoek, E. (1987). "Rockfall: a computer program for prediction rockfall trajectories". In: *ISRM News J.* 2, pp. 4–16.

Hoek, E. (2000). "Analysis of rockfall hazards". In: *Practical rock engineering*. Ed. by E. Hoek. Chap. Analysis o, pp. 141–165.

Hsü, K. J. (1975). "Catastrophic debris streams (sturzstroms) generated by rockfalls". In: *Bulletin of the Geological Society of America*. ISSN: 19432674. DOI: 10.1130/0016-7606(1975)86<129:CDSSGB>2.0.CO;2.

Hu, J., Li, S., Shi, S., Li, L., Zhang, Q., Liu, H., and He, P. (2018). *Experimental Study on Parameters Affecting the Runout Range of Rockfall*. DOI: 10.1155/2018/4739092.

Hudaverdi, T., Kuzu, C., and Fisne, A. (2012). "Investigation of the blast fragmentation using the mean fragment size and fragmentation index". In: *International Journal of Rock Mechanics and Mining Sciences* 56, pp. 136–145. DOI: 10.1016/j.ijrmms.2012.07.028.

Hungr, O. and Evans, S. G. (1988). "Engineering evaluation of fragmental rockfall hazards". In: *Landslides. Proc. 5th symposium, Lausanne, 1988. Vol. 1*, pp. 685–690.

Hungr, O., Evans, S. G., and Hazzard, J. (1999). "Magnitude and frequency of rock falls and rock slides along the main transportation corridors of southwestern British Columbia". In: *Canadian Geotechnical Journal* 36.2, pp. 224–238. ISSN: 00083674. DOI: 10.1139/t98-106.

Hungr, O., Corominas, J., and Eberhardt, E. (2005). "Estimating landslide motion mechanism, travel distance and velocity". In: *Landslide Risk Management*, pp. 99–128.

Hungr, O., Leroueil, S., and Picarelli, L. (2014). "The Varnes classification of landslide types, an update". In: *Landslides* 11, pp. 167–194. ISSN: 16125118. DOI: 10.1007/s10346-013-0436-y.

Imre, B., Räbsamen, S., and Springman, S. M. (2008). "A coefficient of restitution of rock materials". In: *Computers and Geosciences* 34.4, pp. 339–350. ISSN: 00983004. DOI: 10.1016/j.cageo.2007.04.004.

IUGS (1997). "Quantitative risk assessment for slopes and landslides - The state of the art". In: *Landslide Risk Assessment*. Ed. by D. Cruden and R. Fell. Balkema, Rotterdam, pp. 3–12.

Jaboyedoff, M., Dudt, J. P., and Labiouse, V. (2005). "An attempt to refine rockfall hazard zoning based on the kinetic energy, frequency and fragmentation degree". In: *Natural Hazards and Earth System Science* 5.5, pp. 621–632. DOI: 10.5194/nhess-5-621-2005.

Jaboyedoff, M. and Labiouse, V. (2011). "Technical note: Preliminary estimation of rockfall runout zones". In: *Natural Hazards and Earth System Science* 11.3, pp. 819–828. ISSN: 15618633. DOI: 10.5194/nhess-11-819-2011.

Ji, Z. M., Chen, Z. J., Niu, Q. H., Wang, T. J., Song, H., and Wang, T. H. (2019). "Laboratory study on the influencing factors and their control for the coefficient of restitution during rockfall impacts". In: *Landslides* 16.10, pp. 1939–1963. ISSN: 16125118. DOI: 10.1007/s10346-019-01183-x.

Kitahra, I., Atsumi, S., Degawa, R., Kawamura, Y., Jang, H., and Ohta, Y. (2016). "3D Model Reconstruction of Rocks on a Slope for Simulating a Rock Fall". In: *Geo-Chicago 2016*. Geo-Chicago Proceedings, pp. 508–517. DOI: 10.1061/9780784480120.052.

Labiouse, V. and Heidenreich, B. (2009). "Half-scale experimental study of rockfall impacts on sandy slopes". In: *Natural Hazards and Earth System Sciences* 9.6, pp. 1981–1993. DOI: 10.5194/nhess-9-1981-2009.

Lambert, S., Bourrier, F., and Toe, D. (2013). "Improving three-dimensional rockfall trajectory simulation codes for assessing the efficiency of protective embankments". In: *International Journal of Rock Mechanics and Mining Sciences* 60, pp. 26–36. ISSN: 13651609. DOI: 10.1016/j.ijrmms.2012.12.029.

Lambert, S., Bourrier, F., Gotteland, P., and Nicot, F. (Oct. 2019). "An experimental investigation of the response of slender protective structures to rockfall impacts". In: *Canadian Geotechnical Journal*. DOI: 10.1139/cgj-2019-0147.

Lan, H., Derek Martin, C., and Lim, C. H. (2007). "RockFall analyst: A GIS extension for three-dimensional and spatially distributed rockfall hazard modeling". In: *Computers and Geosciences* 33.2, pp. 262–279. ISSN: 00983004. DOI: 10.1016/j.cageo.2006.05.013.

Lee, E. M. and Jones, D. K. . (2006). "Landslide Risk Assessment". In: *Quarterly Journal of Engineering Geology and Hydrogeology* 39.4, pp. 402–402. ISSN: 1470-9236. DOI: 10.1144/1470-9236/05-102.

Leine, R. I., Schweizer, A., Christen, M., Glover, J., Bartelt, P., and Gerber, W. (2014). "Simulation of rockfall trajectories with consideration of rock shape". In: *Multibody System Dynamics* 32.2, pp. 241–271. ISSN: 13845640. DOI: 10.1007/s11044-013-9393-4.

Li, Tianchi (1983). "A mathematical model for predicting the extent of a major rockfall." In: *Zeitschrift fur Geomorphologie* 24, pp. 473–482. ISSN: 03728854.

Li, L. and Lan, H. (2015). "Probabilistic modeling of rockfall trajectories: a review". In: *Bulletin of Engineering Geology and the Environment* 74.4, pp. 1163–1176. ISSN: 14359529. DOI: 10.1007/s10064-015-0718-9.

Lied, K. (1977). "Rockfall problems in Norway". In: *Rockfall dynamics and protective work effectiveness* 90, pp. 51–53.

Lilly, P. (1986). "An Empirical Method pf Assessing Rockmass blastability". In: *Large Open Pit Mine Conference*, pp. 89–92.

Lu, G., Caviezel, A., Christen, M., Demmel, S. E., Ringenbach, A., Bühler, Y., Dinneen, C. E., Gerber, W., and Bartelt, P. (2019). "Modelling rockfall impact with scarring in compactable soils". In: *Landslides* 16.12, pp. 2353–2367. ISSN: 16125118. DOI: `10.1007/s10346-019-01238-z`.

Lu, P. and Latham, J.-P. (1999). "Developments in the Assessment of In-situ Block Size Distributions of Rock Masses". In: *Rock Mechanics and Rock Engineering* 32.1, pp. 29–49. ISSN: 1434-453X. DOI: `10.1007/s006030050042`.

Luo, G., Xiewen, H., Yingjin, D., Jiankang, F., and Xuefeng, M. (2019). "A collision fragmentation model for predicting the distal reach of brittle fragmentable rock initiated from a cliff". In: *Bulletin of Engineering Geology and the Environment* 78.1, pp. 579–592. ISSN: 14359529. DOI: `10.1007/s10064-018-1286-6`.

Macciotta, R., Martin, C. D., Morgenstern, N. R., and Cruden, D. M. (2016). "Quantitative risk assessment of slope hazards along a section of railway in the Canadian Cordillera—a methodology considering the uncertainty in the results". In: *Landslides* 13.1, pp. 115–127. ISSN: 16125118. DOI: `10.1007/s10346-014-0551-4`.

Mandelbrot, B. B. (1982). *The fractal geometry of nature*. W. H. Freeman.

Marchelli, M. and De Biagi, V. (2019). "Optimization methods for the evaluation of the parameters of a rockfall fractal fragmentation model". In: *Landslides* 16.7, pp. 1385–1396. ISSN: 16125118. DOI: `10.1007/s10346-019-01182-y`.

Matas, G., Corominas, J., and Lantada, N. (2018). "Effect of rockfall fragmentation on exposure and subsequent risk analysis". In: *International Symposium Rock Slope Stability*, pp. 99–100.

Matas, G., Lantada, N., Corominas, J., Gili, J. A., Ruiz-Carulla, R., and Prades, A. (2017). "RockGIS: a GIS-based model for the analysis of fragmentation in rockfalls". In: *Landslides* 14.5, pp. 1565–1578. ISSN: 16125118. DOI: `10.1007/s10346-017-0818-7`.

Matas, G., Parras, E., Lantada, N., Gili, J., Ruiz-Carulla, R., Corominas, J., Moya, J., Prades, A., Buil, F., Nuñez-Andres, M., and Puig, C. (2020a). "Laboratory test to study the effect of comminution in rockfalls". In: *XIII International Symposium on Landslides*. Cartagena de Indias, Colombia.

Matas, G., Lantada, N., Corominas, J., Gili, J., Ruiz-Carulla, R., and Prades, A. (2020b). "Simulation of full-scale rockfall tests with a fragmentation model". In: *Geosciences (Switzerland)* 10.5. ISSN: 20763263. DOI: `10.3390/geosciences10050168`.

Mavrouli, O. and Corominas, J. (2010). "Rockfall vulnerability assessment for reinforced concrete buildings". In: *Natural Hazards and Earth System Science* 10.10, pp. 2055–2066. ISSN: 15618633. DOI: `10.5194/nhess-10-2055-2010`.

Mavrouli, O. and Corominas, J. (2017). "Comparing rockfall scar volumes and kinematically detachable rock masses". In: *Engineering Geology* 219, pp. 64–73. ISSN: 00137952. DOI: `10.1016/j.enggeo.2016.08.013`.

Mavrouli, O., Corominas, J., Ibarbia, I., Alonso, N., Jugo, I., Ruiz, J., Luzuriaga, S., and Navarro, J. A. (2019). "Integrated risk assessment due to slope instabilities in the roadway network of Gipuzkoa, Basque Country". In: *Natural Hazards and Earth System Sciences* 19.2, pp. 399–419. ISSN: 16849981. DOI: `10.5194/nhess-19-399-2019`.

Meissl, G. (1998). "Modellierung der Reichweite von Felsstüurzen: Fallbeispiele zur GIS-gestützten Gefahrenbeurteilung". PhD thesis. Institut fur Geographie Univ. Innsbruck.

Mentani, A., Govoni, L., Gottardi, G., Lambert, S., Bourrier, F., and Toe, D. (2016). "A New Approach to Evaluate the Effectiveness of Rockfall Barriers". In: *Procedia Engineering* 158, pp. 398–403. ISSN: 18777058. DOI: `10.1016/j.proeng.2016.08.462`.

Mitchell, A. and Hungr, O. (2017). "Theory and calibration of the pierre 2 stochastic rock fall dynamics simulation program". In: *Canadian Geotechnical Journal* 54.1, pp. 18–30. ISSN: 12086010. DOI: 10.1139/cgj-2016-0039.

Moos, C., Fehlmann, M., Trappmann, D., Stoffel, M., and Dorren, L. (2018). "Integrating the mitigating effect of forests into quantitative rockfall risk analysis - Two case studies in Switzerland". In: *International Journal of Disaster Risk Reduction* 32. Advancing Ecosystems and Disaster Risk Reduction in Policy, Planning, Implementation, and Management, pp. 55–74. ISSN: 2212-4209. DOI: https://doi.org/10.1016/j.ijdrr.2017.09.036.

Moya, J., Corominas, J., and Mavrouli, O. (2013). "A geomorphologic and probabilistic approach to the number and size of blocks of fragmental rockfalls". In: *International Conference on Geomorphology*, p. 1.

Nicolet, P., Jaboyedoff, M., Cloutier, C., Crosta, G. B., and Lévy, S. (2016). "Brief communication: On direct impact probability of landslides on vehicles". In: *Natural Hazards and Earth System Sciences* 16.4, pp. 995–1004. ISSN: 16849981. DOI: 10.5194/nhess-16-995-2016.

Noël, F., Wyser, E., Jaboyedoff, M., Derron, M.-H., Cloutier, C., Turmel, D., and Locat, J. (2018a). "Real-size rockfall experiment: How different rockfall simulation impact models perform when confronted with reality?" In: *Geohazards Proceedings*.

Noël, F., Cloutier, C., Turmel, D., and Locat, J. (Apr. 2018b). "Using point clouds as topography input for 3D rockfall modeling". In: ISL Proceedings. Chap. Rockfalls, pp. 1531–1535. ISBN: 9781315375007. DOI: 10.1201/9781315375007-178.

Paluszny, A., Tang, X., Nejati, M., and Zimmerman, R. W. (2016). "A direct fragmentation method with Weibull function distribution of sizes based on finite- and discrete element simulations". In: *International Journal of Solids and Structures* 80, pp. 38–51. ISSN: 00207683. DOI: 10.1016/j.ijsolstr.2015.10.019.

Peng, B. (2000). "Rockfall Trajectory Analysis : Parameter Determination and Application". MA thesis. University of Canterbury. Geological Science.

Perfect, E. (1997). "Fractal models for the fragmentation of rocks and soils: a review". In: *Engineering Geology* 48.3. Fractals in Engineering Geology, pp. 185–198. ISSN: 0013-7952. DOI: https://doi.org/10.1016/S0013-7952(97)00040-9.

Pfeiffer, T. J. and Bowen, T. D. (1989). "Computer simulation of rockfalls". In: *Bulletin - Association of Engineering Geologists* 26.1, pp. 135–146. ISSN: 1078-7275. DOI: 10.2113/gseegeosci.xxvi.1.135.

Piteau, D. and Clayton, R. (1977). "Computerized design of rock slopes using interactive graphics for the input and output of geometrical data". In: *Proceedings of the 16th Symposium on Rock Mechanics*, pp. 62–63.

Prades, A., Matas, G., Núñez-Andrés, A., Buill, F., Nieves, N., and Corominas, J. (2017). "Determinación de trayectorias de bloques rocosos en ensayos mediante videogrametría". In: *Primer Congreso en Ingeniería Geomática*, pp. 34–40. DOI: 10.4995/cigeo2017.2017.6617.

Richards, L., Peng, B., and Bell, D. (2001). "Laboratory and field evaluation of the normal coefficient of restitution for rocks". In: *Proceedings of Eurock*, pp. 149–156.

Ritchie, A. M. (1963). "Evaluation of Rockfall and Its Control". In: *In Highway Research Record 17, Stability of Rock Slopes, Highway Research Board, National Research Council, Washington, D.C.* 17, pp. 13–28.

Robotham, M. E., Wang, H., and Walton, G. (1995). "Assessment of risk from rockfall from active and abandoned quarry slopes". In: *Transactions - Institution of Mining & Metallurgy, Section A* 104.Jan-April. ISSN: 01489062. DOI: 10.1016/0148-9062(95)93408-h.

Ruiz-Carulla, R., Corominas, J., and Mavrouli, O. (2016). "Comparison of block size distribution in rockfalls". In: *Landslides and Engineered Slopes. Experience, Theory and Practice*. Vol. 3. Unknown, pp. 1767–1774. ISBN: 9781138029880. DOI: 10.1201/b21520-220.

Ruiz-Carulla, R. and Corominas, J. (2019). "Analysis of Rockfalls by Means of a Fractal Fragmentation Model". In: *Rock Mechanics and Rock Engineering*. ISSN: 1434-453X. DOI: 10.1007/s00603-019-01987-2.

Ruiz-Carulla, R., Corominas, J., and Mavrouli, O. (2015). "A methodology to obtain the block size distribution of fragmental rockfall deposits". In: *Landslides* 12.4, pp. 815–825. ISSN: 16125118. DOI: 10.1007/s10346-015-0600-7.

– (2017). "A fractal fragmentation model for rockfalls". In: *Landslides* 14.3, pp. 875–889. ISSN: 16125118. DOI: 10.1007/s10346-016-0773-8.

Ruiz-Carulla, R., Corominas, J., Gili, J. A., Matas, G., Lantada, N., Moya, J., Prades, A., Núñez-Andrés, M. A., Buil, F., and Puig, C. (2020). "Analysis of Fragmentation of Rock Blocks from Real-Scale Tests". In: *Geosciences* 10.8, p. 308. DOI: 10.3390/geosciences10080308.

Sabatakakis, N., Depountis, N., and Vagenas, N. (2015). "Evaluation of rockfall restitution coefficients". In: *Engineering Geology for Society and Territory - Volume 2: Landslide Processes*. Ed. by G. Lollino, D. Giordan, G. B. Crosta, J. Corominas, R. Azzam, J. Wasowski, and N. Sciarra. Cham: Springer International Publishing, pp. 2023–2026. ISBN: 9783319090573. DOI: 10.1007/978-3-319-09057-3_359.

Sala, Z., Jean Hutchinson, D., and Harrap, R. (2019). "Simulation of fragmental rockfalls detected using terrestrial laser scans from rock slopes in south-central British Columbia, Canada". In: *Natural Hazards and Earth System Sciences* 19.11, pp. 2385–2404. ISSN: 16849981. DOI: 10.5194/nhess-19-2385-2019.

Sass, O. and Oberlechner, M. (2012). "Is climate change causing increased rockfall frequency in Austria?" In: *Natural Hazards and Earth System Sciences* 12, pp. 3209–3216. DOI: 10.5194/nhess-12-3209-2012.

Scheidegger, A. E. (1973). "On the prediction of the reach and velocity of catastrophic landslides". In: *Rock Mechanics Felsmechanik Mécanique des Roches* 5, pp. 231–236. ISSN: 00357448. DOI: 10.1007/BF01301796.

Scholtès, L. and Donzé, F.-V. (2012). "Modelling progressive failure in fractured rock masses using a 3D discrete element method". In: *International Journal of Rock Mechanics and Mining Sciences* 52, pp. 18–30. ISSN: 1365-1609. DOI: https://doi.org/10.1016/j.ijrmms.2012.02.009.

– (2013). "A DEM model for soft and hard rocks: Role of grain interlocking on strength". In: *Journal of the Mechanics and Physics of Solids* 61.2, pp. 352–369. ISSN: 0022-5096. DOI: https://doi.org/10.1016/j.jmps.2012.10.005.

Sheng, Y. (2005). "Theoretical analysis of the iterative photogrammetric method to determining ground coordinates from photo coordinates and a DEM". In: *Photogrammetric Engineering and Remote Sensing* 71.7, pp. 863–871. ISSN: 00991112. DOI: 10.14358/PERS.71.7.863.

Šmilauer, V. and Chareyre, B. (2015). *Dem formulation. In Yade Documentation 2nd ed.* The Yade Project. doi: 0.5281/zenodo.34044.

Spadari, M., Giacomini, A., Buzzi, O., Fityus, S., and Giani, G. P. (2012). "In situ rockfall testing in New South Wales, Australia". In: *International Journal of Rock Mechanics and Mining Sciences* 49.0, pp. 84–93. ISSN: 13651609. DOI: 10.1016/j.ijrmms.2011.11.013.

Straub, D. and Schubert, M. (2008). "Modeling and managing uncertainties in rockfall hazards". In: *Georisk: Assessment and Management of Risk for Engineered Systems and Geohazards* 2, pp. 1–15. DOI: 10.1080/17499510701835696.

Stronge, W. J. (2000). *Impact Mechanics.* Cambridge University Press. DOI: 10.1017/CBO9780511626432.

Thoeni, K., Giacomini, A., Lambert, C., Sloan, S. W., and Carter, J. P. (2014). "A 3D discrete element modelling approach for rockfall analysis with drapery systems". In: *International Journal of Rock Mechanics and Mining Sciences* 68, pp. 107–119. ISSN: 13651609. DOI: 10.1016/j.ijrmms.2014.02.008.

Toe, D., Bourrier, F., Dorren, L., and Berger, F. (2018). "A Novel DEM Approach to Simulate Block Propagation on Forested Slopes". In: *Rock Mechanics and Rock Engineering* 51.3, pp. 811–825. ISSN: 07232632. DOI: 10.1007/s00603-017-1348-2.

Turcotte, D. L. (1986). "Fractals and fragmentation." In: *Journal of Geophysical Research* 91.B2, pp. 1921–1926. ISSN: 01480227. DOI: 10.1029/JB091iB02p01921.

Turner, A. and Duffy, J. (2012). "Modelling and prediction of rockfall". In: *Transportation Research Board*. Ed. by E. Eberhardt, C. Froese, and A. Turner. Washington D.C, pp. 334–406.

Vallero, G., De Biagi, V., Barbero, M., Castelli, M., and Napoli, M. L. (2020). "A method to quantitatively assess the vulnerability of masonry structures subjected to rockfalls". In: *Natural Hazards* 103.1, pp. 1307–1325. ISSN: 15730840. DOI: 10.1007/s11069-020-04036-2.

Van Dijkem, J. and van Westen, C. (1990). "Rockfall hazard: a geomorphological application of neighbourhood analysis with ILWIS". In: *ITC Journal* 1, pp. 40–44.

van Westen, C. J., Asch, T. W. van, and Soeters, R. (2006). "Landslide hazard and risk zonation - Why is it still so difficult?" In: *Bulletin of Engineering Geology and the Environment* 65.2, pp. 167–184. ISSN: 14359529. DOI: 10.1007/s10064-005-0023-0.

Varnes, D. (1978). "Slope movement types and processes". In: *Landslides, Analysis and Control*. Ed. by R. Schuster, R.L. and Krizek. Transportation Research Board, Special Report No. 176, National Academy of Sciences, chap. 176, pp. 11–33.

Volkwein, A., Schellenberg, K., Labiouse, V., Agliardi, F., Berger, F., Bourrier, F., Dorren, L. K., Gerber, W., and Jaboyedoff, M. (2011). "Rockfall characterisation and structural protection - A review". In: *Natural Hazards and Earth System Science* 11.9, pp. 2617–2651. ISSN: 15618633. DOI: 10.5194/nhess-11-2617-2011.

Volkwein, A. and Klette, J. (2014). "Semi-Automatic Determination of Rockfall Trajectories". In: *Sensors (Basel, Switzerland)* 14.10, pp. 18187–18210. ISSN: 1424-8220. DOI: 10.3390/s141018187.

W. Goldsmith (1960). *Impact—The Theory and Physical Behaviour of Colliding Solids*. DOI: 10.1007/BF02472016.

Wang, Y., Jiang, W., Cheng, S., Song, P., and Mao, C. (2018). "Effects of the impact angle on the coefficient of restitution in rockfall analysis based on a medium-scale laboratory test". In: *Natural Hazards and Earth System Sciences* 18.11, pp. 3045–3061. ISSN: 16849981. DOI: 10.5194/nhess-18-3045-2018.

Wang, Y. and Tonon, F. (2011). "Discrete element modeling of rock fragmentation upon impact in rock fall analysis". In: *Rock Mechanics and Rock Engineering* 44.1, pp. 23–35. ISSN: 07232632. DOI: 10.1007/s00603-010-0110-9.

Wyllie, D. C. (2014). "Calibration of rock fall modeling parameters". In: *International Journal of Rock Mechanics and Mining Sciences* 67.0, pp. 170–180. ISSN: 13651609. DOI: 10.1016/j.ijrmms.2013.10.002.

Yan, Y., Li, T., Liu, J., Wang, W., and Su, Q. (2019). "Monitoring and early warning method for a rockfall along railways based on vibration signal characteristics". In: *Scientific Reports* 9.1, p. 6606. ISSN: 20452322. DOI: 10.1038/s41598-019-43146-1.

Ye, Y., Zeng, Y., Thoeni, K., and Giacomini, A. (2019a). "An Experimental and Theoretical Study of the Normal Coefficient of Restitution for Marble Spheres". In: *Rock Mechanics and Rock Engineering* 52.6, pp. 1705–1722. ISSN: 1434453X. DOI: 10.1007/s00603-018-1709-5.

Ye, Y., Thoeni, K., Zeng, Y., Buzzi, O., and Giacomini, A. (2019b). "Numerical Investigation of the Fragmentation Process in Marble Spheres Upon Dynamic Impact". In: *Rock Mechanics and Rock Engineering*. ISSN: 1434-453X. DOI: 10.1007/s00603-019-01972-9.

Zhang, Z. X., Kou, S. Q., Jiang, L. G., and Lindqvist, P. A. (2000). "Effects of loading rate on rock fracture: Fracture characteristics and energy partitioning". In: *International Journal of Rock Mechanics and Mining Sciences* 37.5, pp. 745–762. ISSN: 01489062. DOI: 10.1016/s1365-1609(00)00008-3.

Zhao, T., Crosta, G. B., Utili, S., and De Blasio, F. V. (2017). "Investigation of rock fragmentation during rockfalls and rock avalanches via 3-D discrete element analyses". In: *Journal of Geophysical Research: Earth Surface* 122.3, pp. 678–695. ISSN: 21699011. DOI: 10.1002/2016JF004060.

Zhao, T., Crosta, G. B., Dattola, G., and Utili, S. (2018). "Dynamic Fragmentation of Jointed Rock Blocks During Rockslide-Avalanches: Insights From Discrete Element Analyses". In: *Journal of Geophysical Research: Solid Earth* 123.4, pp. 3250–3269. ISSN: 21699356. DOI: 10.1002/2017JB015210.

# Appendix

#1 List of scientific publications

#2 Compendium articles

        Article A

        Article B

        Article C

# Appendix #1: List of scientific publications

This appendix collects all the papers published in journals and conferences during the realization of this doctoral thesis

**Journals:**

Gili JA, Ruiz-Carulla R, **Matas G**, Moya J, Prades A, Corominas J, Lantada N, Nuñez-Andrés, MA, Buill F, Puig C, Martínez-Bofill J, Saló L, and Mavrouli O (2020). *Rockfalls: analysis of the block fragmentation through field experiments.* In: Landslides, Submitted.

Ruiz-Carulla R, Corominas J, Gili JA, **Matas G**, Lantada N, Moya J, Prades A, Núñez-Andrés MA, Buill F and Puig C (2020) *Analysis of fragmentation of rock blocks from real-scale tests.* Geosciences, Geosciences (Switzerland) 10 (8), 308. doi: 10.3390/geosciences10080308

**Matas G,**, Lantada N, Corominas J, Gili J, Ruiz-Carulla R, and Prades A (2020). *Simulation of full-scale rockfall tests with a fragmentation model.* Geosciences (Switzerland) 10 (5). doi: 10.3390/geosciences10050168.

Corominas J, **Matas G**, Ruiz-Carulla R (2019). *Quantitative analysis of risk from fragmental rockfalls.* Landslides. Doi: 10.1007/s10346-018-1087-9

Saló L, Corominas J, Lantada N, **Matas G**, Prades A, Ruiz-Carulla R (2018). *Seismic energy analysis as generated by impact and fragmentation of single-block experimental rockfalls.* JGR-Earth Surface. doi: 10.1029/2017JF004374

**Matas G**, Lantada N, Corominas J, Gili JA, Ruiz-Carulla R and Prades A (2017). *RockGIS: A GIS-based model for the analysis of fragmentation in rockfalls.* Landslides. doi: 10.1007/s10346-017-0818-7

**Peer-reviewed conferences:**

Ruiz-Carulla R, Corominas J, **Matas G**. and Lantada N. (2020) *3D analysis of a fragmental rockfall.* 5th World Landslide forum, (Kyoto, Japan, 2nd-6th November 2020, 2021)

**Matas G**, Parras E, Lantada N, Gili J, Ruiz-Carulla R, Corominas J, Moya J, Prades A, Buil F, Nuñez-Andres MA, Puig C. (2020) *Laboratory test to study the effect of comminution in rockfalls.* XIII International Symposium on Landslides (Cartagena de Indias, Colombia, February 22-26 of 2021)

**Matas G**, Lantada N, Corominas J, Ruiz-Carulla R, Prades A, Gili JA (2020). *Calibration of a rockfall simulator with a fragmentation model in a real scale test,* in

PM Dight (ed.), Proceedings of the 2020 International Symposium on Slope Stability in Open Pit Mining and Civil Engineering, Australian Centre for Geomechanics, Perth, pp.1141-1148

**Matas G**, Corominas J, Lantada N, (2018). *Effect of rockfall fragmentation on exporsure and subsequent risk analysis.* IV Symposium Rock Slope Stability (RSS2018) 13-15 de noviembre, Manège de Chambéry (France)

Corominas J, **Matas G**, Ruiz-Carulla R, (2018). *The fragmentation of rockfalls and the analysis of risk.* Keynote lecture. Engineering Resiliency in a Changing Climate, Geohazards 7, Canmore, Canada.

Lantada N, Corominas J, Gili JA, Ruiz-Carulla R, **Matas G**, Mavrouli A, Núñez-Andrés MA, Moya J, Buill F, Abellan A, Puig C, Prades A, Martinez-Bofill J, Saló Ll (2017). *Le projet ROCKRISK: quantification et prévention des risques de chutes de blocs.* JAG 2017 - 5èmes Journées Aléas Gravitaires, Besançon, France.

**Matas G**, Lantada N, Corominas J, Gili JA, Ruiz-Carulla R and Prades A (2017). *Modelización de desprendimientos rocosos considerando la fragmentación.* Simposio Nacional sobre Taludes y Laderas Inestables, Santander, Spain.

Gili J, **Matas G**, Corominas J, Núñez-Andrés MA, Lantada N, Ruiz R, Mavrouli O, Buill F, Moya J, Prades A, Puig-Polo C, Martinez-Bofill J, Salo Ll. (2017). *Diseño y primeros resultados de tres ensayos de lanzamiento de bloques de roca para el estudio de la fragmentación.* Simposio Nacional sobre Taludes y Laderas Inestables, Santander, Spain.

Prades A, **Matas G**, Núñez-Andrés MA, Buill F, Lantada N, Corominas J (2017). *Determinación de trayectorias de bloques rocosos en ensayos mediante videogrametría.* CIGeo, Primer Congreso en Ingeniería Geomática. Valencia, Spain.

Corominas J, Lantada N, Gili JA, Ruiz-Carulla R, **Matas G**, Mavrouli A, Núñez-Andrés MA, Moya J, Buill F, Abellan A, Puig C, Prades A, Martinez-Bofill J, Saló Ll (2017). *The RockRisk Project: Rockfall risk quantification and prevention.* 6th Interdisciplinary Workshop on Rockfall Protection (Rocexs2017), Barcelona, Spain.

**Matas G**, Lantada N, Corominas J, Gili JA, Ruiz-Carulla R and Prades A (2017). *Rockfall fragmentation analysis: Vilanova de Banat case study.* 6th interdisciplinary workshop on rockfall protection (Rocexs2017), Barcelona, Spain.

Gili JA, Ruiz-Carulla R, **Matas G**, Corominas J, Lantada N, Núñez, MA, Mavrouli O, Buill F, Moya J, Prades A, Moreno S. (2016). *Experimental study on rockfall fragmentation: in situ test design and firsts results.* International Symposium Landslides 2016 (ISL2016), Napoli (Italia). doi: 10.1201/b21520-116

**Matas G**, Lantada N, Gili JA and Corominas J (2016). *Simulation of rockfall fragmentation mechanism in a GIS-based tool. In: ISRM International Symposium.* ”Rock Mechanics and Rock Engineering: From the Past to the Future”. Cappadocia: CRC Press, p. 671-675.

Ruiz-Carulla R, **Matas G**, Prades A, Gili JA, Corominas J, Lantada N, Buil F, Mavrouli O, Núñez-Andrés MA, Moya J (2016). *Analysis of rock block fragmenta-*

*tion by means of real-scale tests.* 3rd RSS Rock Slope Stability conference. Lyon (France).

**Other conferences:**

Lantada N, Corominas J, Gili JA, **Matas G**, Ruiz-Carulla R, Prades A, Puig-Polo C, Núñez-Andrés MA, Moya J, Buill F, Mavrouli O (2020) *The RockModels project: Rockfalls characterization and modelling.* EGU2020, European Geosciences Union (Viena, Austria 3rd-8th May 2020). Abstract id. EGU2020-20353 .

**Matas G**, Lantada N, Corominas J, Gili JA, Ruiz-Carulla R, Prades A (2020) *Rockfall fragmentation simulations of real scale tests.* EGU2020, European Geosciences Union (Viena, Austria 3rd-8th May 2020). Abstract id. EGU2020-19352

**Matas G**, Lantada N, Corominas J, Gili JA, Ruiz-Carulla R and Prades A (2017). *Procedure for assessing the performance of a rockfall fragmentation model.* In: EGU General Assembly 2017. Geophysical Research Abstracts, Vol. 19, EGU2017-17709.

**Matas G**, Lantada N, Gili JA and Corominas J (2015). *An open source GIS-based tool to integrate the fragmentation mechanism in rockfall propagation.* In: EGU General Assembly 2015. Geophysical Research Abstracts, Vol. 17, EGU2015-13660-1, Vienna (Austria).

# Appendix #2: Article A

Matas, G., Lantada, N., Corominas, J., Gili, J. A., Ruiz-Carulla, R., and Prades, A. (2017). "RockGIS:a GIS-based model for the analysis of fragmentation in rockfalls". In: Landslides 14.5, pp. 1565–1578. doi: 10.1007/s10346-017-0818-7

# Appendix #2: Article B

Corominas, J., Matas, G., and Ruiz-Carulla, R. (2019). "Quantitative analysis of risk from fragmental rockfalls". In: Landslides 16.1, pp. 5–21. doi: 10.1007/s10346-018-1087-9.

**ATTENTION¡¡**

Pages 127 to 144 of the thesis, containing the article mentioned above, are available at the editor's web:

https://link.springer.com/article/10.1007/s10346-018-1087-9

# Appendix #2: Article C

**Matas, G.**, Lantada, N., Corominas, J., Gili, J., Ruiz-Carulla, R., and Prades, A. (2020). "Simulation of full-scale rockfall tests with a fragmentation model". In: Geosciences (Switzerland) 10.5. doi: 10.3390/geosciences10050168.

# Simulation of Full-Scale Rockfall Tests with a Fragmentation Model

**Gerard Matas** [1],*[ID], **Nieves Lantada** [1][ID], **Jordi Corominas** [1], **Josep Gili** [1][ID], **Roger Ruiz-Carulla** [1] and **Albert Prades** [2]

[1] Division of Geotechnical Engineering and Geosciences, Universitat Politècnica de Catalunya. C. Jordi Girona 1-3, 08034 Barcelona, Spain; nieves.lantada@upc.edu (N.L.); jordi.corominas@upc.edu (J.C.); j.gili@upc.edu (J.G.); roger.ruiz@upc.edu (R.R.-C.)

[2] Division of Geotechnical Engineering and Geosciences, Universitat Politècnica de Catalunya. Dr. Marañón 44-50, 08028 Barcelona, Spain; alberto.prades.i@upc.edu

* Correspondence: gerard.matas@upc.edu; Tel.: +34-93-401-69-25

**Abstract:** In this paper, we present the upgraded version of RockGIS, a stochastic program for the numerical simulation of rockfalls and their fragmentation, based on a fractal model. The code has been improved to account for a range of fragmentation scenarios, depending on the impact conditions. In the simulation, the parameters of the fractal fragmentation model that define the sizes of the generated fragments were computed at each impact according to the kinematic conditions. The performance of the upgraded code was verified and validated by real-scale rockfall tests performed in a quarry. The tests consisted of the release of 21 limestone blocks. For each release, the size and spatial distribution of the fragments generated by the impacts were measured by hand and from orthophotos taken via drone flights. The trajectories of the blocks and the resulting fragments were simulated with the code and calibrated with both the volume distribution and the runout distances of the fragments. Finally, as all the relevant rockfall parameters involved were affected by strong uncertainty and spatial variability, a parametric analysis was carried out and is discussed.

## 1. Introduction

A rockfall is a rapid mass movement generated by the detachment of a rock volume from a slope that falls, bounces, and rolls during its propagation downhill [1,2]. Rockfalls often threaten civil infrastructures, buildings and transportation networks in mountainous regions [3–10]. These phenomena have great destructive potential due to the high speed and, consequently, the high kinetic energy the rockfall can reach during its propagation [11].

In a rockfall, the initial mobilized mass can be either a single massive block or a set of blocks defined by the joint system in the massif. The concept of in situ block size distribution (IBSD) was introduced to describe the initial distribution of block sizes within the rock mass [12–14]. During propagation, the block or blocks that originally form the IBSD may break on collision with the ground to produce fragments that are smaller than the original ones. The term fragmental rockfall is used to refer to this phenomenon [15,16] and the final distribution of the fragments is called the rockfall block size distribution (RBSD).

In recent years, significant improvements have been made in rockfall risk analysis methodologies [17,18], particularly for transportation infrastructures [19–22] and urban areas [23–25]. The design and implementation of risk mitigation structures such as dynamic barriers, embankments and galleries has also been improved by increasing the energy absorption and

the diversion capacity [26–28]. Knowledge of the expected kinematic conditions of a rockfall at a certain point, such as the impact energy and bouncing height, is required for risk assessment and the proper design of risk mitigation structures. The impact energy depends on many variables like the initial volume, release height, path topography, and the geomechanical properties of the slope. Rockfall propagation models have been developed to determine the trajectories, the potential runout, and impact energies. Some of these models are based on empirical observations [29,30] and others are processes that are based on and simulate the physics of the phenomenon with approaches of varying detail [31–38]. However, fragmentation is rarely considered in these analyses [39,40].

Real-scale tests [5,33,35,38,41–46] and laboratory tests [47,48] have been performed for a better understanding of the rockfall phenomenon and proper calibration of the existing rockfall simulation models. Some of these tests focused on calibrating the rock–slope interaction models (rebound) to match different criteria: maximum runout, runout distribution, divergence trajectories, passing height and passing velocity in control points. Only a few of the cited studies focused on the analysis of fragmentation [5,46]. The latter is critical to determine trajectories and impact energy and has a significant effect on the resulting risk [49].

The mining industry has historically been the most interested in fragmentation to assess the efficiency of blasting operations [50,51]. However, many researchers have paid attention to fragmentation recently, as an important factor in the study of rockfalls [37,52–55] and rock avalanches [56–60]. In rockfall events, three main consequences are observed when a block fragments:

1. **Reduction in the initial block size**. This can range from six to nine orders of magnitude in single isolated blocks from 1 to 2 m$^3$ [46], and 15 to 18 orders of magnitude in events that mobilize over 20,000 m$^3$ [61]. Macciotta et al [62] showed the influence of the structure of the rock mass at the detachment location on the block size reduction. To study the block size distributions, Ruiz-Carulla et al. [14] proposed a fractal approach in which a finite number of iterations was adopted, based on Mandelbrot [63] and Turcotte [64], who had already developed fractal theory to deal with complex natural phenomena. This type of approach has been used to derive the RBSD from the ISBD of past rockfall events [14,65]. Recently, a continuous approach using fractal theory and the scale-variant fractal probability model has been proposed for rockfalls [66];

2. **Divergence of trajectories**. After breakage, fragments adopt fan-like diverging trajectories from the collision point [56,61,67–69]. Few studies have targeted the evaluation of trajectory divergence after fragmentation in rockfalls, including numerical modeling [70] and field experiments [5,46];

3. **Momentum boost effect**. After fragmentation, small fragments may reach velocities higher than big ones [61,70–72]. The distribution of energy after breakage is still unknown and, in some numerical investigations, no correlation has been found between the fragment size and fragment kinetic energy for a given impact velocity [72]. To our knowledge, only a few studies have attempted to measure the energy distribution after fragmentation in rockfalls [69], which, under the current state of the knowledge, is still highly uncertain.

The combination of these three effects can produce a range of scenarios. Although the fragment size is reduced, the potential increment in velocity due to the momentum boost effect may lead to high energies concentrated in a small area. It has been observed that in this scenario blocks with significantly less energy than the design value can punch out dynamic rockfall barriers [44]. This is called the "bullet effect". Moreover, trajectory divergence, combined with size reduction, may have opposite effects depending on the topography. In scenarios where propagation takes place on gentle slopes, the overall runout of the fragments may decrease when compared to the unbroken blocks. This effect disappears on steep slopes [49].

This paper presents the performance of the RockGIS code for simulating fragmentation in rockfalls [40], which has been upgraded for this study. The code was calibrated and validated with a set of full-scale rockfall tests, performed in a quarry to provide quality and reliable data. The results of the experiments were used to calibrate the model focusing on the volume distribution of the

fragments after breakage, the distances traveled, and the trajectories. The paper is organized as follows. Firstly, we present the RockGIS code that accounts for fragmentation in the stochastic simulation of rockfalls. The model has been upgraded by adding scale-variant laws and adaptable model parameters for the analysis of fragmentation [66]. Secondly, we describe the experimental setup of the quarry, the test equipment, and the data gathering procedures of the real-scale tests. These tests were carried out in the framework of the national research project RockModels, an important part of which has been dedicated to determining the fragmentation of rock masses and its application in fragmentation and propagation models. Thirdly, we calibrate the model and discuss the results of the simulations. Finally, we describe the parametric analysis.

## 2. Code Description

The rockfall code used for this study is RockGIS [40], which takes a lumped-mass approach and allows for the fragmentation of blocks during their propagation. The code requires the following input data: the digital elevation model (DEM) of the study area, the land use map to define the spatially distributed parameters involved in the impact and the rebound parameter, the location of the source of detachable blocks, their volumes, and their initial kinematic conditions. The trajectory of the blocks is computed by integrating movement equations that result in ballistic trajectories. A contact algorithm is used to determine when the flying particles impact the ground surface. This algorithm uses a bisection approach once the trajectory has intersected the ground surface to determine, with accuracy, the impact point. When the impact is detected, the rebound conditions are evaluated, and the new trajectory is defined. In case of fragmentation, the impacting rock mass is distributed among the fragments, which are treated as new blocks with their kinematic conditions.

The most recent version of RockGIS used in this study includes the following updates regarding the first version described in [40]: the code base was moved from python to c++ to improve performance, the kinematics of the blocks are described as in [37], and rotational velocity is also considered. The contact detection algorithm was modified to increase performance and the fractal fragmentation model was improved and completed [66]. This code has been developed within the frame of the Rockmodels research project as part of the PhD thesis of the leading (first) author. The code runs in Linux and will be made available on an open source basis at https://rockmodels.upc.edu/en once the research project is closed. The following sections describe the details of the main improvements in the RockGIS model.

### 2.1. Topographic Model

A high-resolution digital elevation model (DEM) is used. This consists of a grid containing information on the height of the surface in each cell. It is a simplification of the slope's topographical surface that has some limitations. For example, overhangs cannot be considered in this approach, since only one Z value can be assigned to a single pair of planimetric X,Y coordinates. Some authors have prepared models that can work with point clouds [38]. These can use extremely detailed models obtained from laser scanning or aerial photogrammetry, which overcome the DEM limitations. However, the use of a regular DEM to describe the topography makes it easier and faster to numerically account for the interaction between particles and the ground surface.

The Z-value of the terrain at certain X,Y coordinates is calculated using a bilinear interpolation between the four nearest neighboring cells. This approach gives a continuous interpolation of the surface based on the digital elevation model cells. In the code, a function called height to ground (H2G) gives the height of the block with respect to the slope surface. This function is used to detect contact between a flying block and the terrain.

## 2.2. Block Kinematics

Blocks are considered as points in space with all the mass concentrated (lumped mass approach) and they have, as state variables, a position $\vec{R} = (x, y, z)$, linear velocity $\vec{V} = (v_x, v_y, v_z)$, rotational velocity $\vec{W} = (w_x, w_y, w_z)$ and volume. This approach does not explicitly account for the shape of the blocks except for the rebound model in which the blocks are assumed to be spheres (hybrid approach). Due to this simplification, some kinematic behaviors conditioned by the shape of the blocks may not be represented in a fully accurate way and may affect the result of the simulations. This deficiency is overcome by a thorough calibration process. Other variables, such as information regarding the parent fragment or the current motion state in the simulation algorithm are stored for numerical purposes. Blocks are subject to the gravity acceleration $\vec{a} = (0, 0, -g)$ and by integrating the movement equations with a certain time discretization, $\Delta t$, the parabolic trajectories are obtained. Considering an initial position, the linear and rotational velocity of a block in each time step of the simulation keeps producing a parabolic flight until contact with the terrain, mitigation structures, or virtual control sections are detected. During the interaction of the terrain, the rebound and fragmentation modules are applied and the resulting fragments and their reflected velocities are determined. Then, each fragment is treated as a new individual block and the flying phase is restarted.

## 2.3. Contact Detection

The contact detection between blocks and the terrain is computed by the bisection method, which is frequently used in photogrammetry [73]. At every time step, the block moves according to its velocity and the value of H2G is checked. If the value is less than zero, it means that the block is located under the ground surface. Then, an iterative process, using the bisection method, determines the exact time step that makes the block intersect with the slope surface with a certain tolerance. This tolerance is always on the positive side of H2G to ensure that (numerically) the block never penetrates the ground.

## 2.4. Rebound Model

Once impact with the terrain is detected, a rebound algorithm is applied to compute the reflected velocity of the block. The first version of RockGIS used the model described in [34]. The version presented in this study implements the approach proposed by [37]. To determine the reflected velocity, this approach considers the incidence velocity with respect to the normal vector of the surface, its rotational velocity and restitution coefficients. It also considers a stochastic perturbation of the impact surface to account for the variability of the process. The restitution coefficients can be estimated using different approaches. In this study, the normal and tangential restitution coefficients are computed at each impact using Wyllie [74] and Gischig et al's [37] equations, respectively. After each rebound, the amount of remaining normal kinetic energy is evaluated to determine whether the block fragments or not.

## 2.5. The Fragmentation Model

RockGIS can be used to consider both the disaggregation of the initial rock mass and the breakage of the blocks during propagation. The disaggregation of the IBSD is assumed in all cases and the trajectory of each of the blocks that is involved is modelled individually. A specific module is called every time a block hits the ground to check for the breakage criterion. This module decides whether the block remains intact or breaks. In the case of breakage, the module generates the new fragment size distribution based on the Rockfall Fractal Fragmentation Model [66].

The previous version of the code [40] considered invariable power law parameters at each impact for the entire simulation. In the upgraded version, the power law parameters depend on impact conditions and are specific for each impacting rock block. Thus, the way mass is distributed after the breakage is specific according to the kinematic conditions of the impacting block [66].

The fragment volume distribution after breakage is generated by Equation (1). The fragment generation process ends when one of these two conditions are satisfied: (1) the last generated fragment is smaller than a user-defined minimum volume. In this study, this value was set to the minimum fragment volume measured in the field. This avoids a mathematically infinite loop reaching senselessly small fragment sizes, or (2) the sum of all generated fragments reaching the initial block volume. In this case, the last fragment is the difference between the sum of all previous generated fragments and the initial block volume.

$$V_n = V_0 \times L_{max} \times n^{\frac{-1}{D_f}} \tag{1}$$

where:

$V_n$ volume of the fragment "n";
$V_0$ initial block volume;
$n$ number of fragments, running from 1 to infinite;
$L_{max}$ largest generated fragment;
$D_f$ the fractal dimension.

$D_f$ controls the shape of the fragment distribution. Both $L_{max}$ and the $D_f$ depend on the model parameters $b$ and $q$, as defined in Equations (2) and (3) (Perfect, 1997).

$$L_{max} = q \times b^n \tag{2}$$

$$D_f = 3 + \frac{log(1-q)}{log(b)} \tag{3}$$

where:

$b$ the proportion between the fragment size generated and the initial volume;
$q$ the probability of survival, expressed as the proportion of the block that breaks to create new fragments.

These two model parameters, $b$ and $q$, vary at each impact depending on the kinematic conditions. At each impact, the new surface area generated by breakage is estimated as a function of the normal impacting kinetic energy (Equation (4)).

$$Na = a_1 \times Ek_n{}^{a_2} \tag{4}$$

where:

$Na$ new generated surface area [m$^2$];
$Ek_n$ kinetic energy in normal impact direction [J];
$a_1, a_2$ model parameters to calibrate.

This equation involves the impacting angle and block dimensions. The parameters a1, a2 can be estimated from the potential energy of first impacts of the inventoried rockfall. Ruiz-Carulla and Corominas [66] found a relation between the new generated surface area and the initial area for each impact (Equation (5)), which can be related to the power law parameters ($b$ and $q$) that control fragment distribution (Equations (6) and (7)).

$$\frac{Na}{Ta} = \frac{Na}{Ia + Na} \tag{5}$$

$$b = b_1\left(\frac{Na}{Ta}\right) + b_2 \tag{6}$$

$$q = q_1\left(\frac{Na}{Ta}\right) + q_2 \tag{7}$$

where:

*Na* new generated surface area [m$^2$];

*Ta* total surface area [m$^2$];

*Ia* initial surface area [m$^2$];

$b_1$, $b_2$ linear model parameters controlling *b*; must be calibrated;

$q_1$, $q_2$ linear model parameters controlling *q*; must be calibrated.

### 2.6. Energy Transfer to the Fragments

Finally, by adding a certain degree of stochasticity, the simulator defines the trajectories of the new fragments that are generated. The fragments are distributed within a cone of a given angle around the expected trajectory of the unbroken block. This approach is based on field observations (Figure 1).
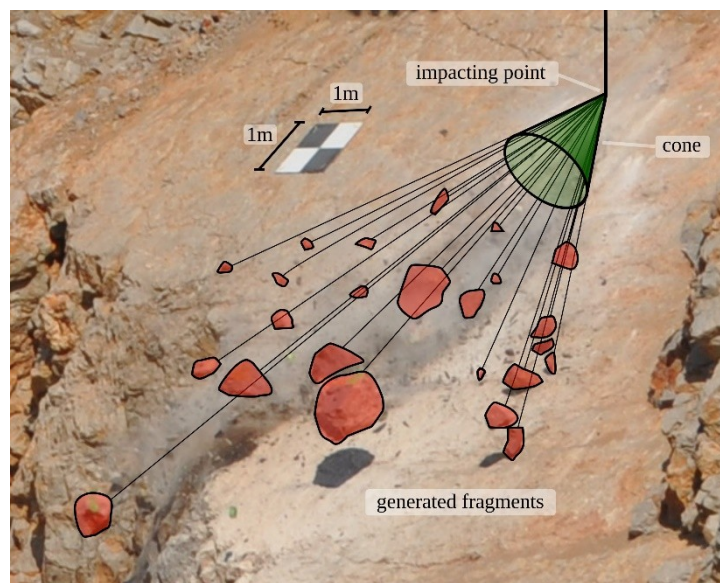


**Figure 1.** Example of a cone-shaped distribution of fragments produced after the impact of a block against a 42.4° inclined slope surface during a real-scale test performed in this study.

Once the list of generated fragments has been computed, linear and rotational velocities must be assigned to each fragment. The values estimated for energy loss during the fragmentation process in Giacomini et al. [5] are used. The knowledge on energy transferred between fragments is still in its early stages and for simplicity, in this study, it is assumed that the energy is distributed throughout fragments proportionally to mass, which leads to the equal post-fragmentation velocity of all fragments. These velocities are assumed to remain within a cone whose revolution axis is on the outcome velocity computed by the rebound model. The aperture of the cone is defined by the angle θ. Normal unitary vectors are randomly computed inside the cone, following Hall's [75] method. These unitary vectors are multiplied by the outcome velocity and assigned to each of the generated fragments. From this point, each fragment is treated as a new block with its own state variables.

## 3. Experimental Testing

### 3.1. Experimental Site

To verify the performance of the code and validate the results, a set of real-scale rockfall fragmentation tests were carried out in a quarry in Vallirana municipality (41.3635 N, 1.9067 E), Barcelona, Spain. The lithology of the rock blocks is massive limestone. Six samples were extracted and tested in the laboratory resulting in an average density of 2650 kg/m$^3$ and uniaxial compressive and tensile strengths of 103 MPa and 4.1 MPa, respectively.

The testing profile was selected inside the quarry in a zone of the steep slope bench where the rock was barely fractured, to ensure enough stiffness to break the blocks. The selected profile consists of a 42.4° inclined plane, which coincides with a natural discontinuity surface of the rock mass and where the first impacts after releasing the blocks were expected. An almost horizontal platform extends at the foot of the slope. The difference in height between the foot of the slope and the crown is 19 m (Figure 2). The impact surface in the inclined plane is high resistance rock, and no main discontinuities were observed. In the horizontal platform at the foot of the slope, a thin layer of fine-grained soil (a few centimeters thick) overlays the rock mass.
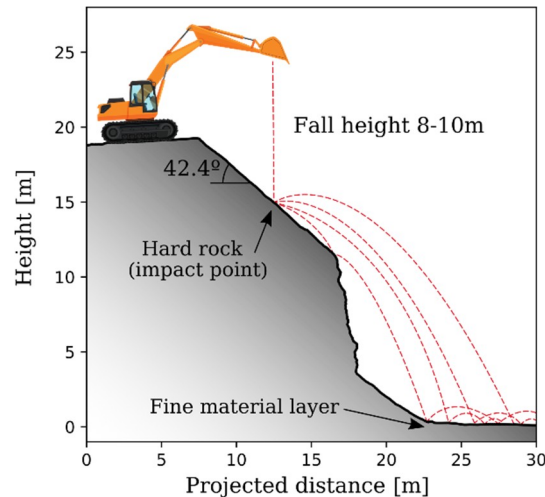


**Figure 2.** Testing profile.

### 3.2. Testing Set Up

A total of 21 massive limestone rock blocks were selected for this experiment and the methodology proposed in Gili et al. [46] was followed. During the preparation of the test, three ellipses following the major axis of each block were painted to improve their visibility in the videos. All blocks were hand-measured using a tape measure to obtain an initial estimation of their volumes, which ranged between 0.5 and 2.25 cubic meters. To allow easier visual identification of the fragments that were generated, the fragments were removed after each release, so that the accumulation area was clear for the next release.

A backhoe was used to release the blocks from the top of the slope. Two marks painted on the edge defined the space in which blocks had to be released by the engine. The height at which each block was released depended on the operator's criterion, for stability reasons. It ranged between 8 and 10 meters with respect the first impact point. Once the security protocol had been checked, the blocks were released (Figure 3).

For georeferencing purposes, a total of 29 ground control points (GCP, targets and crosses painted on rock outcrops) were distributed throughout the scene. They were surveyed using GNSS technology to provide scale and georeference photographs and video images.

Photogrammetric techniques using drones were applied to obtain a 3D geometric reconstruction of the test scenario. The drone device used was a DJI Inspire 2 with a X5S camera ($5280 \times 3956$ pixels sensors). About 150 pictures in zenithal and oblique orientations were taken at a distance of 30 meters from the ground, obtaining a resolution or Ground Sample Distance (GSD) of 7 mm/px. The GCP surveyed were used to georeference the model as well as to optimize the alignment of the cameras. The error in the control points was between 1.2 cm and 1.6 cm in planimetry and under 3 cm in altimetry. For the photogrammetric reconstruction, the software Agisoft Photoscan was used to obtain a dense point cloud of $74 \times 10^6$ points and the derived products, like a 3D mesh (Figure 4), the Digital Elevation Model (DEM) of 20 cm/px and the orthophoto of 7 mm/px resolution.

**Figure 3.** Example of the release of a block. The time step between selected frames is 0.33 s.
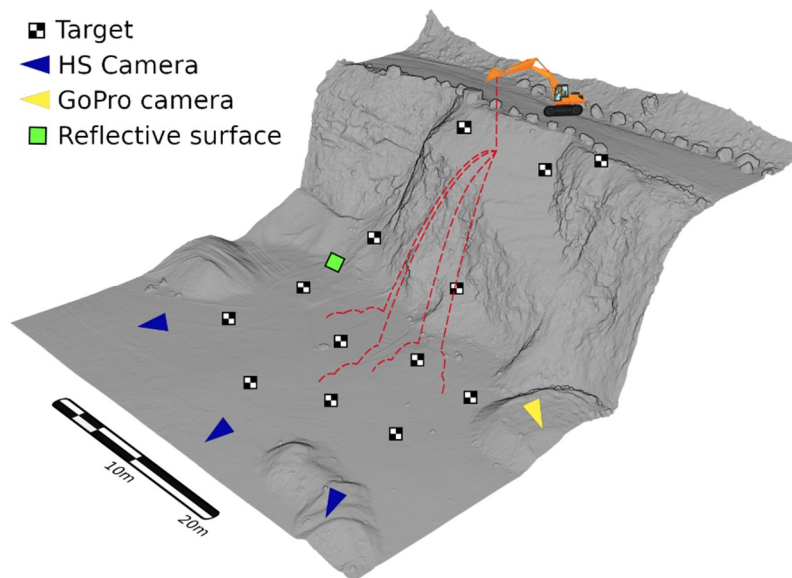


**Figure 4.** Photogrammetric model with the position of some of the targets used as ground control points and the positions of the high-speed video cameras recording the scene.

Each test was recorded using three high-speed video cameras recording at 400 fps in full-HD definition ($1920 \times 1080$ pixel) placed at about 60 m from the base of the slope and distributed so that they formed approximately a 40° angle. Since it was technically unfeasible to directly synchronize the cameras, a flashlight was placed at the bottom of the slope pointing to a reflective surface so that it was seen in the frame of the three cameras. The flash was fired several times during each release, to allow frame synchronization during the post-processing of the footage with a minimal error of 1/400 seconds. The tests were also recorded from a drone at 24 fps in 4K definition ($3840 \times 2160$ pixel) flying above the scene, and once all the fragments had stopped, the drone was used to capture a set of photographs of the fragments scattered across the platform in order to build a 3D photogrammetric model of each deposit.

The next section describes the post-processing that was used to extract additional data from the field experiments that were required to calibrate the model. Finally, the calibration procedure for the multiple parameters controlling the simulation is explained.

### 3.3. Data Acquisition

After the photogrammetric flight and when the conditions were safe again, all the fragments were hand-measured using a tape measure to check the 3D model obtained by photogrammetry.

The data that were directly collected during the experimental campaign include: the volume of each block prior to release, measured with a tape measure; the height of the release point for each test using a total station; and three lengths defining the volume of the fragments generated by the impact and subsequent breakage. The latter will provide the RBSD for each test and the relation between the area and volume of the fragment (Equation (8)). This procedure is similar to that followed by Su and Yan [76] to estimate the 3D sizes of particles from projected 2D images.

Manual georeferencing of the location of each fragment in the field was not possible since it would have been extremely time-consuming, considering that the volume of 1242 fragments was measured. The runout of each fragment was measured in the orthophoto provided by the UAV flights. The minimum fragment size measured was $8 \times 10^{-6}$ m$^3$, which corresponds to a $2 \times 2 \times 2$ cm fragment. The location and the projected area of each block in the orthophoto was measured and then the volume of each fragment was calculated from Equation (8).

$$V_{frag} = 0.453 \times Pa_{frag}^{1.494} \tag{8}$$

where:

$$V_{frag} = 0.453 \times Pa_{frag}^{1.494}$$

$V_{frag}$ estimated volume of measured fragments in the field;
$Pa_{frag}$ the projected area of measured fragments on the orthophoto.

The distances traveled by fragments were calculated on the orthophotos as the distance between the average release point and the centroids of the polygons that represent the fragments.

Once this correlation had been applied, a volume (Vfrag) could be assigned to each fragment drawn on the orthophoto to obtain the cumulative volume distribution as a function of the runout. Figure 5a shows the polygons of the fragments produced by tested block #10 measured on the orthophoto and the estimated volume for each fragment. After estimating each fragment volume, the RBSD of block #10 can be obtained (Figure 5b).
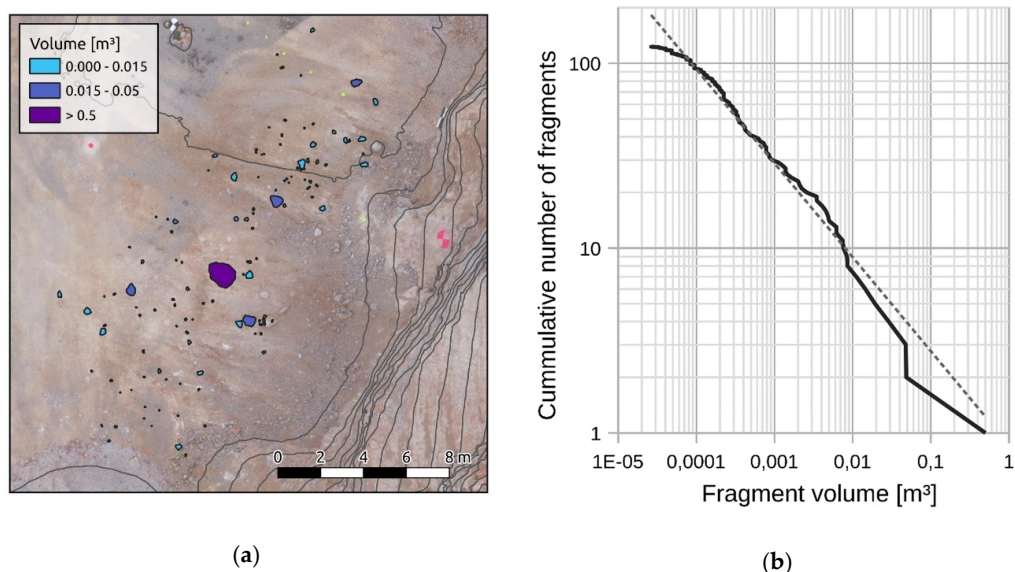


(a)                    (b)

**Figure 5.** This figure shows an example of the data obtained in tested block #10: (**a**) fragments generated by breakage. The area of the projected fragment was measured on the orthophoto was measured. The volumes were estimated from the correlation equation (Equation (8)); (**b**) fragment volume distribution produced. The fractal behavior is described by the power law that is drawn.

The aperture of the cone (θ) must be set in the fragmentation model. To estimate the ranges for this parameter, we measured, using video triangulation, the aperture of the most divergent fragments for each test [69]. The values of the aperture ranged between 25° and 145°, with an average value of 75°. Note that these measurements were made in the three-dimensional space, not using a 2D projection of the cone on the orthophoto.

## 4. Calibration Procedure

The calibration phase of the model was challenging in this study, since several parameters concerning the rebound and fragmentation models had to be adjusted to make the results match the field observations. The selected goodness of fit indicators were the similarities of the simulation results to the field experiments for three criteria: (1) the RBSD obtained for all blocks, (2) the runout distribution, and (3) the cumulative spatial distribution of the volume of the fragments as a function of distance from the release point. When these three criteria had been obtained from the field experiments, the calibration process consisted of a trial and error iterative process.

Just one seeder was considered in the average position of the release position of the blocks during the experiments. A horizontal velocity of 0.2 m/s was imposed to consider the initial momentum given to the blocks due to the movement of the backhoe shovel during the release. The digital elevation model used in this study was obtained from a UAV flight prior to the execution of the tests performed on the slope with a resolution of 0.2 × 0.2 meters. Just one material was considered on the entire slope, since the fine layer over the bedrock at the base of the slope, which was used to make the surface even, was estimated to be around 2–5-cm thick. One simulation event consists of the release of the 21 tested blocks along with their respective fragment volumes measured in place. Note that, in the simulation, the rock fragments do not interact during propagation. Having set these initial conditions, the calibration procedure could begin.

First, a list of parameter combinations was generated using combinatorics. To achieve this, testing value ranges obtained from an iterative heuristic trial and error process were imposed for each parameter. The combination of all possible parameter values gives a total $N = \prod^{i} n_i$ cases to be tested, where $n_i$ is the number of intervals of each parameter and $i$ is the number of considered parameters. Considering 10 parameters (Table 1) and 20 intervals for each one, a total of $2.56 \times 10^{10}$ possible cases had to be simulated.

**Table 1.** List of parameters considered for the model calibration.

| Parameter | Description |
|---|---|
| Kna | Multiplier of the power law relating the normal impact velocity with the normal restitution coefficient [75]. |
| Knb | Exponent of the power law relating the normal impact velocity with the normal restitution coefficient [75]. |
| Kta | Parameter that controls the hyperbolic curve of the tangential restitution coefficient with the tangential impact velocity [37]. |
| $a_1$ | Multiplier of the power law relating the normal impact remaining energy and the new area (Equation (4)). |
| $a_2$ | Multiplier of the power law relating the normal impact remaining energy and the new area (Equation (4)). |
| $b_1$ | Multiplier of the power law relating the fractal dimension and the new area (Equation (6)). |
| $b_2$ | Exponent of the power law relating the fractal dimension and the new area (Equation (6)). |
| $q_1$ | Multiplier of the power law relating the probability of survival with the new area (Equation (7)). |
| $q_2$ | Multiplier of the power law relating the probability of survival with the new area (Equation (7)). |
| cone | Angle defining the cone in which fragments may propagate after breakage (in degrees) |

For each set of parameters, 1000 rockfall propagation simulations were run, varying the stochastic seed. The seed determines the random numbers used during the stochastic processes in the simulation and may change the results of a single simulation if modified. The results of the simulations are averaged to obtain a mean behavior representative of the parameter set that is independent of the initial randomness seed. If just one simulation is performed, the calibration would only be meaningful for a specific seed. Once averaged, the resultant distributions were compared against the experimental data.

The goodness of the optimization for each one of the three calibration criteria is evaluated as a function of the residuals. The statistic $\varepsilon$ (Equation (9)) computes a mean error between two discrete distributions by considering the squared distance between simulation and measurement results and dividing by the total number of checkpoints.

$$\varepsilon = \frac{1}{n} \sum_{}^{n} \frac{(O_i - E_i)^2}{E_i} \tag{8}$$

where:

$n$ total number of checkpoints;
$E_i$ expected value on the checkpoint (field data);
$O_i$ observed value on the checkpoint (simulation result).

To evaluate the experimental and simulated distributions at the same points, n = 1000 samples were examined between the maximum and minimum range of both distributions using linear interpolation between points.

The optimization of the calibration consists of finding the combination of parameters that minimizes the value of $\varepsilon$ for the three considered criteria. To achieve this, both the product and the sum of the resulting $\varepsilon$ were compared between parameter sets and the lowest value was selected. Figure 6 shows the workflow for the entire calibration process.
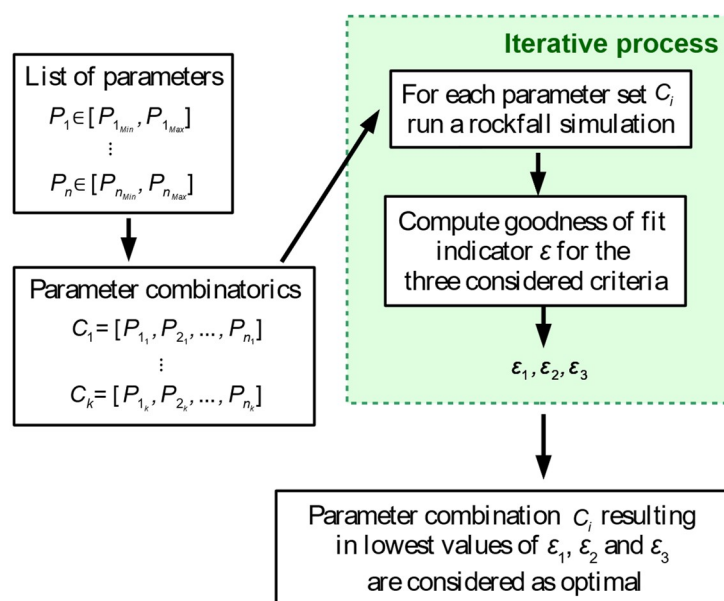


**Figure 6.** Workflow of the calibration process used to adjust the volume, runout and cumulative volume distributions of the field tests.

To perform the huge amount of simulations, a parallelization script has been written so that a full simulation can be run in the RockGIS program for the 21 blocks, considering a specific parameter set in multiple CPU cores at a time. Each thread stored the $\varepsilon$ values and, when all sets were tested, the best fitting ones were chosen. This entire process was run on an HPC using 24 cores. It took about 24 h.

## 5. Results and Discussion

After the calibration process, a set of parameters minimizing $\varepsilon$ was obtained for each of the criteria. Figures 7–9 show the resultant volume, runout and cumulative volume distributions of the 1000 simulations performed with the optimized parameter set and using different seeds. The average curve of all simulations (blue) adjusted with values of $\varepsilon$ of 0.028, 0.0015 and 0.4 for the three criteria, respectively. The values of the parameters resulting from the calibration are: na1 = 0.0031, na2 = 0.7562, b1 = −1.6125, b2 = 2.4875, q1 = −0.5125, q2 = 1.0, Kna = 19.54, Knb = −1.03, Kta = 22.6 and cone = 83°.
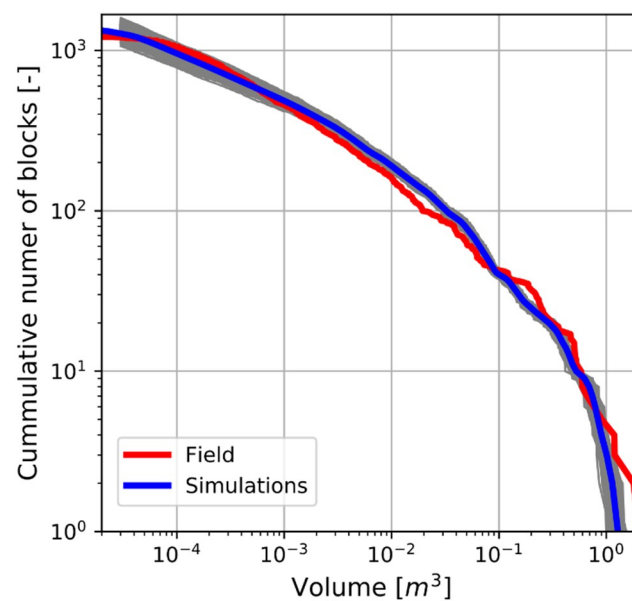


**Figure 7.** Comparison of rockfall block size distribution measured in real-scale tests with the average of the simulation results. Results of each individual simulation are shown in gray, while the average behavior is in blue.
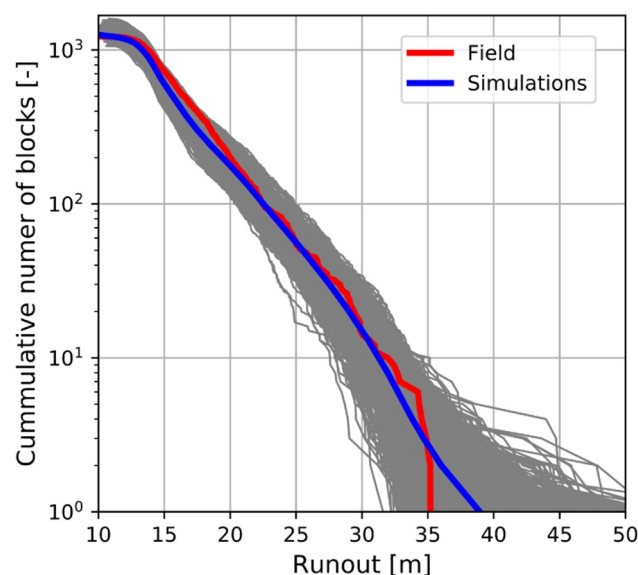


**Figure 8.** Comparison of rockfall runout distribution measured in real-scale tests with the average of the simulation results. Results of each individual simulation are shown in gray, while the average behavior is in blue.
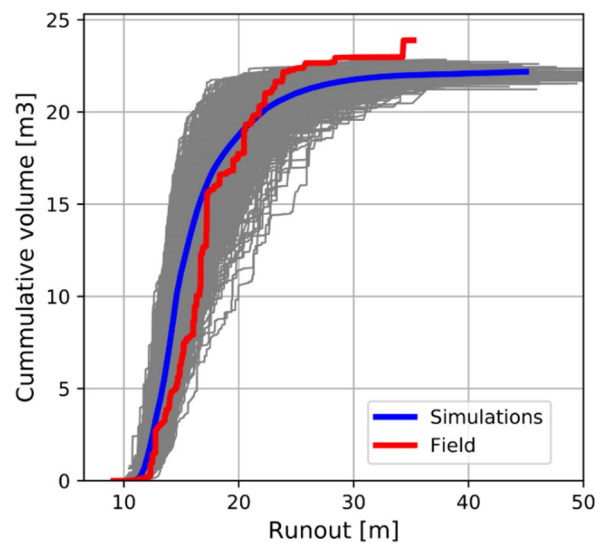
**Figure 9.** Deposited cumulative volume as a function of the runout distance from the release point. The results of each individual simulation are shown in gray, while the average behavior is in blue.

The average volume distribution fits well with the field measurements (Figure 7). The least accurate part of the distribution is the tail, corresponding to the biggest blocks. The biggest fragment measured in the tests corresponded to a block that nearly did not break and measured 2.03 m$^3$, while the biggest fragment obtained in the simulations measured 1.53 m$^3$. The average volume of the maximum fragment produced in the simulations was 1.28 m$^3$. Each of the volume distributions produced by a single simulation remained within the average curve, which means that the volume distribution showed little sensitivity to seed changes. Fragmentation parameters depended on kinematic incident conditions and seed changes only affected the small stochastic perturbations applied to the terrain to account for the variability of the phenomena.

Regarding the runout distribution, the average curve of all simulations also matched the measured distribution well, although the maximum runout was slightly overestimated (Figure 8). In the tests, the maximum measured runout distance was 35.2 m, while the average obtained in the simulations was 38.9 m. This distribution is more sensitive to the seed, as shown in Figure 8, where simulations resulted in distributions that differed from the average curve. The variability of ejecting velocities after fragmentation, which were randomly assigned inside a cone, made some blocks follow high parabolic trajectories, while others were ejected almost tangentially to the surface. This variability explains why, in some simulations, the blocks may travel significantly long distances.

The cumulative volume curve (Figure 9) shows that the model tends to accumulate more volume at the bottom of the slope than that observed in the tests. Furthermore, some big blocks traveled longer distances than in the simulations. After analyzing in depth the videos of all fragments greater than 0.3 m$^3$ that traveled a runout distance of more than 20 m, we qualitatively observed that they acquired high rotational speeds and ended their propagation by a rolling motion. Although our model accounts for rolling in a simplified way by small jumps, and considering its rotational motion on the rebound algorithm, the shape effect seems to allow some of the blocks to travel a few more meters.

The trajectory divergence of the simulations corresponded with that observed in the tests. The velocity of each 3D trajectory obtained from one simulation of the entire test with 21 blocks is shown in Figure 10 on the 3D photogrammetric model. Deposited fragment size and projected trajectories of the same example of simulation are shown in Figure 11.

Field and simulation fragment deposit density was analyzed by computing closed contours containing a defined percentage of fragments. From these contours, a map containing a specific percentage of blocks was obtained by iteratively counting the number of blocks inside each successive contour line. The resulting sets of lines for field data and simulations are shown in Figure 12. As in

the cumulative volume curve, the simulation tended to accumulate more fragments in the base of the slope, but the overall shape of the curves was qualitatively similar. Note that test results show more dispersion, for example on contours of 60%, where the width of the test polygon is 50% greater than the simulation width. This higher dispersion may be explained by the variability of the backhoe when blocks were released, since there was between 1–2 m of margin in the release operation.
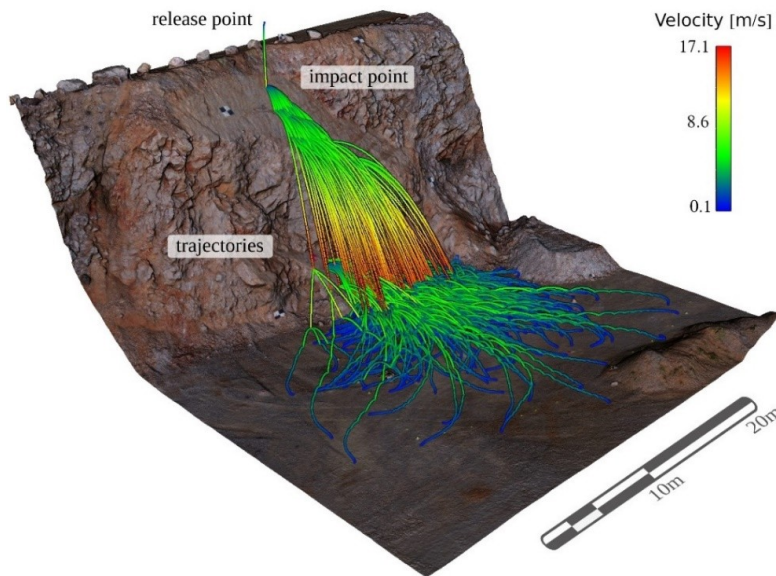


**Figure 10.** Trajectories of all fragments produced during one simulation of the entire test (21 blocks released).
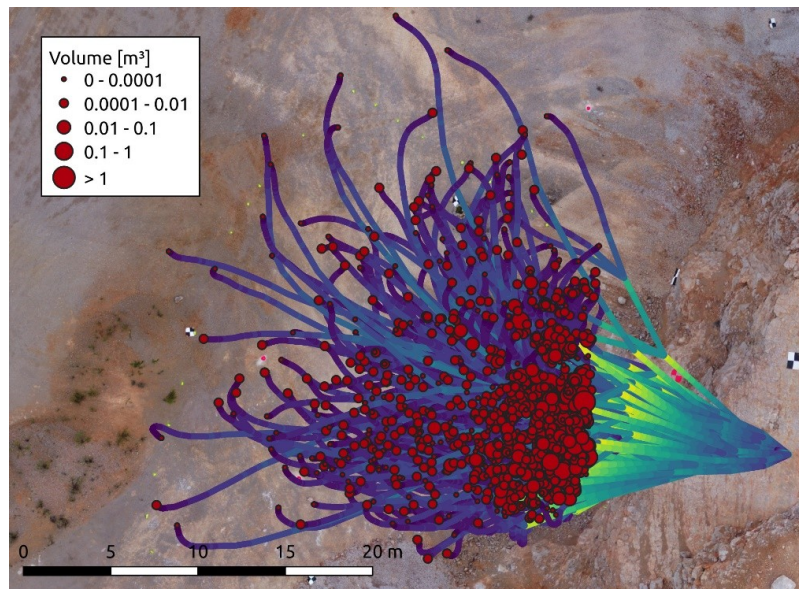


**Figure 11.** Fragment stopping points and trajectories of one run of the test (21 blocks simulated).

All measured fragments in the field are shown classified by volumes in Figure 13. The contours containing a defined percentage of total cumulative volume are also plotted. Note that a large fragment traveled a very long runout distance (the blue block shown on the left of Figure 13). This corresponds to an initial released block of 1.8 m$^3$ that, after fragmenting on the first impact, projected the 0.9 m$^3$ fragment at an almost horizontal angle and with significant rotational velocity. This fragment travelled the last 6–8 m of its trajectory by rolling. However, most of the fragments remained within the 95% volume contour.
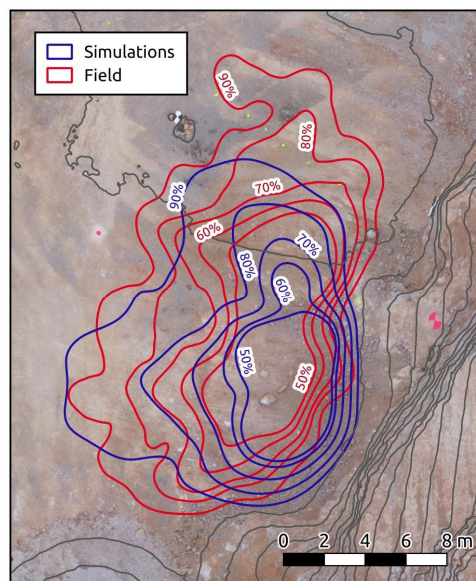
**Figure 12.** Contours containing a certain percentage of stopped fragments for both field measurements and simulation results.
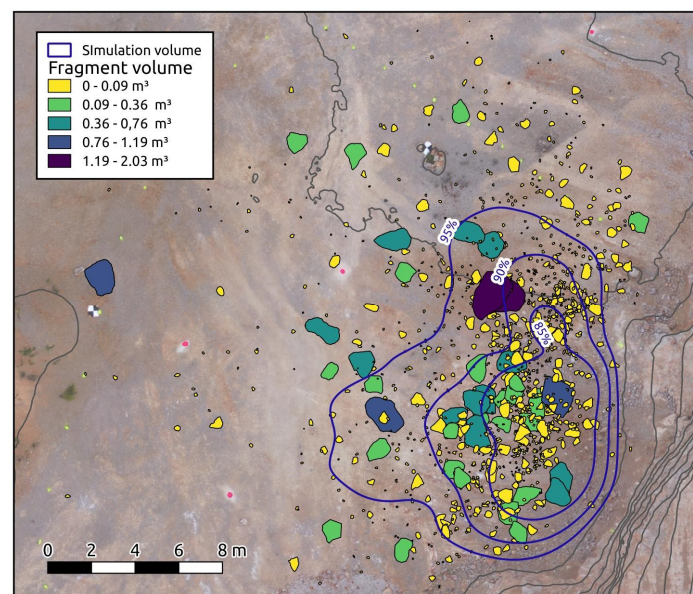


**Figure 13.** Contours containing a certain percentage of deposited volume and measured fragments on the orthophoto obtained from the simulations.

## 6. Sensitivity Analysis

A set of simulations was performed to assess the sensitivity of results in relation to the variability of the model parameters. Only one parameter was modified within a testing range for each simulation, while all the others were fixed.

The parameter set considered as a reference was the result of the calibration process. Each plot in Figure 14 a–j shows the values of the three $\varepsilon$ statistics of each one of the calibration criteria (Figures 7–9), as a function of the tested parameter. The simulations showed high sensitivity to the pairs of parameters controlling fragmentation: na1, na2; b1, b2; and q1, q2 (Figure 14a–f). Each pair displayed similar behavior within the testing range, as expected. Slight variations in the shape of these pairs of curves was due to discretization of the evaluation interval in each case. Note that b1, b2 and q1, q2 define a

line, so the shape of the distributions must be very similar regardless of the parameter that varies (but with its corresponding value interval). In the case of *b*, with a focus on runout only, two minimums could be found in the optimization curve but the volume curve showed a clear minimum around b1 = −1.6 and b2 = 2.49. The same occurred with *q* where the optimum value was found to be around q1 = −0.54 and q2 = 1. A focus on the interval of values that give, for example, a value of the indicator $\varepsilon$ smaller than one in the case of runouts reveals that the range of acceptance of na1, b1 and q1 represents respectively 29%, 8% and 7% variation with respect to the optimum value, while for parameters na2, b2 and q2, the values are, respectively, 5%, 2% and 1.3%. As expected, slight changes in the exponent of the potential function controlling the new generated area and the slopes of the lines controlling b and q were found to have more influence on the final result.
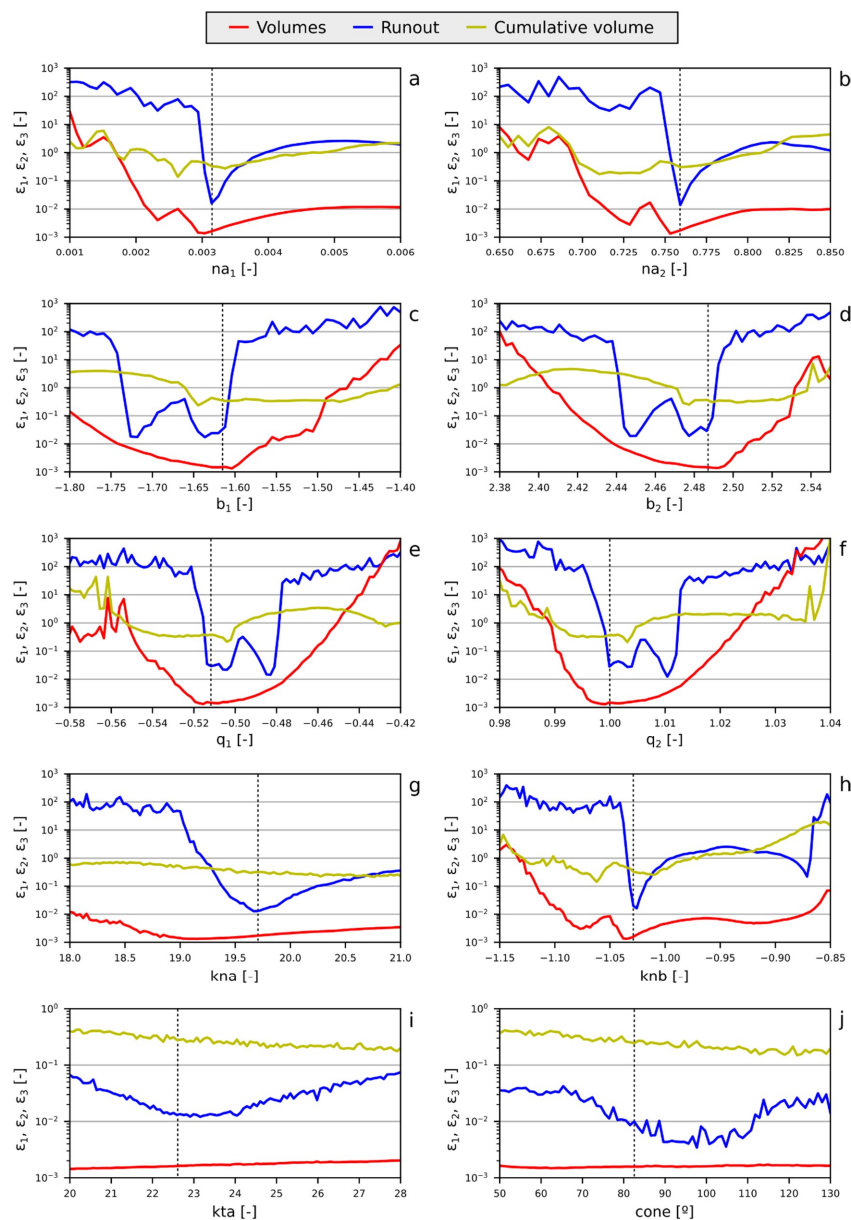


**Figure 14.** Results of the sensitivity analysis. Each plot shows the evolution of the three calibration criteria (volumes, runout and cumulative volume versus runout) within the testing range for each one of the tested parameters. The dashed vertical lines mark the optimal value of the parameter. (**a**–**f**): fragmentation law parameters; (**g**–**h**): parameters controlling normal restitution coefficients; (**i**): tangential restitution coefficient parameter and (**j**) cone aperture when fragmentation occurs.

Parameters that mostly control runout yield clear minima regarding the runout optimization curve. The optimum for *Kna* is 19.5 on the runout curve and 19.3 on the volume one. *Knb* (Figure 14g,h), which is the exponent of the function, is extremely sensitive and departs from the minimum found at −1.03, affecting the results significantly.

Despite showing a clear minimum, the parameter *Kta*, controlling the hyperbolic curve of the tangential restitution factor, was found to be more robust than those controlling normal restitution (Figure 14i). The optimum value is around 23 in the case of the runout criterion and did not have a significant influence on the volume or cumulative volume criteria.

Finally, the aperture angle of the cone when a block fragment showed an optimum value around 95°, which is inside the range measured in the field (25°–145°), but differs a little from the average measured (75°). However, the values of the cone were found to be robust in relation to slight changes.

## 7. Conclusions

In this study, a rockfall simulation model including fragmentation RockGIS was calibrated to numerically reproduce real-scale rockfall fragmentation tests performed in a limestone quarry. A new continuous approach was implemented in the RockGIS trajectories simulator to account for rock fragmentation upon impact, which depends on the impact conditions (based on fractal theory).

The results of 21 real-scale rockfall tests provided the data to calibrate the model. The initial block volumes and the final distribution of fragments after their breakage were measured with a combination of techniques including a tape measure, photogrammetry from a UAV platform and video triangulation. Data collection was a slow process due to the large number of fragments, which easily exceeded 50 fragments on a single block release.

A statistical approach was considered for the calibration, as each set of parameters could give different results depending on the initial stochastic seeds. The calibration was performed with the mean behavior of a parameter set, considering 1000 simulations with random seeds. The calibration criteria considered the runout distance and the size distributions of all generated fragments and was performed stochastically. Both runout and volume experimental cumulative curves were properly reproduced using these approaches. The parametric analysis showed that the model is very sensitive to parameters that control the fragmentation process. The parameters that most affect the volume criterion are b1, b2, q1 and q2, which control the fractal laws applied for mass distribution after breakage. In the case of runout criteria, the parameters that most affect this are na1 and na2, controlling the new generated area after fragmentation, and kta and ktb, controlling the normal restitution coefficient after rebound. The cumulative volume versus runout criteria turned out not to be very sensitive to parameter variations. Finally, we should keep in mind that rockfalls, as well as fragmentation, are stochastic phenomena. To use our approach for risk analysis and the design of protective measures, a precise calibration is required to ensure the parameters are appropriate for the case study considered.

**Conflicts of Interest:** The authors declare no conflict of interest.

## References

1. Varnes, D. Slope movement types and processes. In *Landslides, Analysis and Control*; Schuster, R.L., Krizek, R.J., Eds.; Transportation Research Board, Special Report No. 176; National Academy of Sciences: Washington, DC, USA, 1978; pp. 11–33.

2. Hungr, O.; Leroueil, S.; Picarelli, L. The Varnes classification of landslide types, an update. *Landslides* **2014**, *11*, 167–194. [CrossRef]

3. Chau, K.T.; Wong, R.H.C.; Liu, J.; Lee, C.F. Rockfall Hazard Analysis for Hong Kong Based on Rockfall Inventory. *Rock Mech. Rock Eng.* **2003**, *36*, 383–408. [CrossRef]

4. Guzzetti, F.; Reichenbach, P.; Wieczorek, G.F. Rockfall hazard and risk assessment in the Yosemite Valley, California, USA. *Nat. Hazards Earth Syst. Sci.* **2003**, *3*, 491–503. [CrossRef]

5. Giacomini, A.; Buzzi, O.; Renard, B.; Giani, G.P. Experimental studies on fragmentation of rock falls on impact with rock surfaces. *Int. J. Rock Mech. Min. Sci.* **2009**, *46*, 708–715. [CrossRef]

6. Thoeni, K.; Giacomini, A.; Lambert, C.; Sloan, S.W.; Carter, J.P. A 3D discrete element modelling approach for rockfall analysis with drapery systems. *Int. J. Rock Mech. Min. Sci.* **2014**, *68*, 107–119. [CrossRef]

7. Crosta, G.B.; Agliardi, F.; Frattini, P.; Lari, S. Key issues in rock fall modeling, hazard and risk assessment for rockfall protection. In *Engineering Geology for Society and Territory—Volume 2: Landslide Processes*; Lollino, G., Giordan, D., Crosta, G.B., Corominas, J., Azzam, R., Wasowski, J., Sciarra, N., Eds.; Springer International Publishing: Cham, Switzerland, 2015; pp. 43–58.

8. Mitchell, A.; Hungr, O. Theory and calibration of the pierre 2 stochastic rock fall dynamics simulation program. *Can. Geotech. J.* **2017**, *54*, 18–30. [CrossRef]

9. Asteriou, P.; Tsiambaos, G. Empirical Model for Predicting Rockfall Trajectory Direction. *Rock Mech. Rock Eng.* **2016**, *49*, 927–941. [CrossRef]

10. Mavrouli, O.; Corominas, J.; Ibarbia, I.; Alonso, N.; Jugo, I.; Ruiz, J.; Luzuriaga, S.; Navarro, J.A. Integrated risk assessment due to slope instabilities in the roadway network of Gipuzkoa, Basque Country. *Nat. Hazards Earth Syst. Sci.* **2019**, *19*, 399–419. [CrossRef]

11. Hoek, E. Analysis of rockfall hazards. In *Practical Rock Engineering*; Hoek, E., Ed.; 2000; pp. 141–165. Available online: https://www.rocscience.com/assets/resources/learning/hoek/Practical-Rock-Engineering-Full-Text.pdf (accessed on 7 May 2020).

12. Lu, P.; Latham, J.-P. Developments in the Assessment of In-situ Block Size Distributions of Rock Masses. *Rock Mech. Rock Eng.* **1999**, *32*, 29–49. [CrossRef]

13. Elmouttie, M.K.; Poropat, G.V. A Method to Estimate in Situ Block Size Distribution. *Rock Mech. Rock Eng.* **2012**, *45*, 401–407. [CrossRef]

14. Ruiz-Carulla, R.; Corominas, J.; Mavrouli, O. A fractal fragmentation model for rockfalls. *Landslides* **2017**, *14*, 875–889. [CrossRef]

15. Evans, S.G.; Hungr, O. The assessment of rockfall hazard at the base of talus slopes. *Can. Geotech. J.* **1993**, *30*, 620–636. [CrossRef]

16. Corominas, J.; Mavrouli, O.; Ruiz-Carulla, R. Rockfall Occurrence and Fragmentation. In *Advancing Culture of Living with Landslides*; Sassa, K., Mikoš, M., Yin, Y., Eds.; Springer International Publishing: Cham, Switzerland, 2017; pp. 75–97.

17. Jaboyedoff, M.; Dudt, J.P.; Labiouse, V. An attempt to refine rockfall hazard zoning based on the kinetic energy, frequency and fragmentation degree. *Nat. Hazards Earth Syst. Sci.* **2005**, *5*, 621–632. [CrossRef]

18. Hantz, D. Quantitative assessment of diffuse rock fall hazard along a cliff foot. *Nat. Hazards Earth Syst. Sci.* **2011**, *11*, 1303–1309. [CrossRef]

19. Bunce, C.M.; Cruden, D.M.; Morgenstern, N.R. Assessment of the hazard from rock fall on a highway. *Can. Geotech. J.* **1997**, *34*, 344–356. [CrossRef]

20. Hungr, O.; Evans, S.G.; Hazzard, J. Magnitude and frequency of rock falls and rock slides along the main transportation corridors of southwestern British Columbia. *Can. Geotech. J.* **1999**, *36*, 224–238. [CrossRef]

21. Ferlisi, S.; Cascini, L.; Corominas, J.; Matano, F. Rockfall risk assessment to persons travelling in vehicles along a road: The case study of the Amalfi coastal road (southern Italy). *Nat. Hazards* **2012**, *62*, 691–721. [CrossRef]

22. Macciotta, R.; Martin, C.D.; Morgenstern, N.R.; Cruden, D.M. Quantitative risk assessment of slope hazards along a section of railway in the Canadian Cordillera—A methodology considering the uncertainty in the results. *Landslides* **2016**, *13*, 115–127. [CrossRef]

23. Corominas, J.; Copons, R.; Moya, J.; Vilaplana, J.M.; Altimir, J.; Amigó, J. Quantitative assessment of the residual risk in a rockfall protected area. *Landslides* **2005**, *2*, 343–357. [CrossRef]

24. Agliardi, F.; Crosta, G.B.; Frattini, P. Integrating rockfall risk assessment and countermeasure design by 3D modelling techniques. *Nat. Hazards Earth Syst. Sci.* **2009**, *9*, 1059–1073. [CrossRef]

25. Mavrouli, O.; Corominas, J. Vulnerability of simple reinforced concrete buildings to damage by rockfalls. *Landslides* **2010**, *7*, 169–180. [CrossRef]

26. Ferrero, A.M.; Migliazza, M. *Landslide Transportation Network and Lifelines: Rockfall and Debris Flow BT—Landslide Science and Practice: Volume 6: Risk Assessment, Management and Mitigation*; Margottini, C., Canuti, P., Sassa, K., Eds.; Springer Berlin Heidelberg: Berlin/Heidelberg, Germany, 2013; pp. 161–170. ISBN 978-3-642-31319-6.

27. Volkwein, A.; Schellenberg, K.; Labiouse, V.; Agliardi, F.; Berger, F.; Bourrier, F.; Dorren, L.K.A.; Gerber, W.; Jaboyedoff, M. Rockfall characterisation and structural protection—A review. *Nat. Hazards Earth Syst. Sci.* **2011**, *11*, 2617–2651. [CrossRef]

28. Lambert, S.; Bourrier, F.; Toe, D. Improving three-dimensional rockfall trajectory simulation codes for assessing the efficiency of protective embankments. *Int. J. Rock Mech. Min. Sci.* **2013**, *60*, 26–36. [CrossRef]

29. Copons, R.; Vilaplana, J.M.; Linares, R. Rockfall travel distance analysis by using empirical models (Solà d'Andorra la Vella, Central Pyrenees). *Nat. Hazards Earth Syst. Sci.* **2009**, *9*, 2107–2118. [CrossRef]

30. Jaboyedoff, M.; Labiouse, V. Technical Note: Preliminary estimation of rockfall runout zones. *Nat. Hazards Earth Syst. Sci.* **2011**, *11*, 819–828. [CrossRef]

31. Guzzetti, F.; Crosta, G.; Detti, R.; Agliardi, F. STONE: A computer program for the three-dimensional simulation of rock-falls. *Comput. Geosci.* **2002**, *28*, 1079–1093. [CrossRef]

32. Crosta, G.B.; Agliardi, F. A methodology for physically based rockfall hazard assessment. *Nat. Hazards Earth Syst. Sci.* **2003**, *3*, 407–422. [CrossRef]

33. Dorren, L.K.A.; Berger, F.; Putters, U.S. Real-size experiments and 3-D simulation of rockfall on forested and non-forested slopes. *Nat. Hazards Earth Syst. Sci.* **2006**, *6*, 145–153. [CrossRef]

34. Lan, H.; Derek Martin, C.; Lim, C.H. RockFall analyst: A GIS extension for three-dimensional and spatially distributed rockfall hazard modeling. *Comput. Geosci.* **2007**, *33*, 262–279. [CrossRef]

35. Bourrier, F.; Dorren, L.; Nicot, F.; Berger, F.; Darve, F. Toward objective rockfall trajectory simulation using a stochastic impact model. *Geomorphology* **2009**, *110*, 68–79. [CrossRef]

36. Leine, R.I.; Schweizer, A.; Christen, M.; Glover, J.; Bartelt, P.; Gerber, W. Simulation of rockfall trajectories with consideration of rock shape. *Multibody Syst. Dyn.* **2014**, *32*, 241–271. [CrossRef]

37. Gischig, V.S.; Hungr, O.; Mitchell, A.; Bourrier, F. Pierre3D: A 3D stochastic rockfall simulator based on random ground roughness and hyperbolic restitution factors. *Can. Geotech. J.* **2015**, *52*, 1360–1373. [CrossRef]

38. Noël, F.; Cloutier, C.; Turmel, D.; Locat, J. Using point clouds as topography input for 3D rockfall modeling. In *Landslides and Engineered Slopes. Experience, Theory and Practice*; CRC Press: Boca Raton, FL, USA, 2018; pp. 1531–1535. ISBN 9781315375007.

39. Li, L.; Lan, H. Probabilistic modeling of rockfall trajectories: A review. *Bull. Eng. Geol. Environ.* **2015**, *74*, 1163–1176. [CrossRef]

40. Matas, G.; Lantada, N.; Corominas, J.; Gili, J.A.; Ruiz-Carulla, R.; Prades, A. RockGIS: A GIS-based model for the analysis of fragmentation in rockfalls. *Landslides* **2017**, *14*, 1565–1578. [CrossRef]

41. Ritchie, A.M. Evaluation of rockfall and its control. *Highw. Res. Rec.* **1963**, *17*, 13–28.

42. Chau, K.T.; Wong, R.H.C.; Wu, J.J. Coefficient of restitution and rotational motions of rockfall impacts. *Int. J. Rock Mech. Min. Sci.* **2002**, *39*, 69–77. [CrossRef]

43. Labiouse, V.; Heidenreich, B. Half-scale experimental study of rockfall impacts on sandy slopes. *Nat. Hazards Earth Syst. Sci.* **2009**, *9*, 1981–1993. [CrossRef]

44. Spadari, M.; Giacomini, A.; Buzzi, O.; Fityus, S.; Giani, G.P. In situ rockfall testing in New South Wales, Australia. *Int. J. Rock Mech. Min. Sci.* **2012**, *49*, 84–93. [CrossRef]

45. Volkwein, A.; Klette, J. Semi-automatic determination of rockfall trajectories. *Sensors (Switzerland)* **2014**, *14*, 18187–18210. [CrossRef]

46. Gili, J.A.; Ruiz, R.; Matas, G.; Corominas, J.; Lantada, N.; Núñez, M.A.; Mavrouli, O.; Buill, F.; Moya, J.; Prades, A.; et al. Experimental study on rockfall fragmentation: In situ test design and first results. In *Landslides and Engineered Slopes: Experience, Theory and Practice: Proceedings of the 12th International Symposium on Landslides, Napoli, Italy, 12–19 June 2016*; CRC Press: Boca Raton, FL, USA, 2016; Volume 2, pp. 983–990. ISBN 9781138029880.
47. Asteriou, P.; Saroglou, H.; Tsiambaos, G. Geotechnical and kinematic parameters affecting the coefficients of restitution for rock fall analysis. *Int. J. Rock Mech. Min. Sci.* **2012**, *54*, 103–113. [CrossRef]
48. Asteriou, P.; Tsiambaos, G. Effect of impact velocity, block mass and hardness on the coefficients of restitution for rockfall analysis. *Int. J. Rock Mech. Min. Sci.* **2018**, *106*, 41–50. [CrossRef]
49. Corominas, J.; Matas, G.; Ruiz-Carulla, R. Quantitative analysis of risk from fragmental rockfalls. *Landslides* **2019**, *16*, 5–21. [CrossRef]
50. Lilly, P. An Empirical Method of Assessing Rockmass blastability. In Proceedings of the Large Open Pit Mine Conference, Queensland, Australia, October 1986; pp. 89–92.
51. Hudaverdi, T.; Kuzu, C.; Fisne, A. Investigation of the blast fragmentation using the mean fragment size and fragmentation index. *Int. J. Rock Mech. Min. Sci.* **2012**, *56*, 136–145. [CrossRef]
52. Wang, Y.; Tonon, F. Discrete element modeling of rock fragmentation upon impact in rock fall analysis. *Rock Mech. Rock Eng.* **2011**, *44*, 23–35. [CrossRef]
53. Bourrier, F.; Hungr, O. Rockfall Dynamics: A Critical Review of Collision and Rebound Models. In *Rockfall Engineering*; John Wiley & Sons, Inc.: Hoboken, NJ, USA, 2013; pp. 175–209. ISBN 9781848212565.
54. Sala, Z.; Jean Hutchinson, D.; Harrap, R. Simulation of fragmental rockfalls detected using terrestrial laser scans from rock slopes in south-central British Columbia, Canada. *Nat. Hazards Earth Syst. Sci.* **2019**, *19*, 2385–2404. [CrossRef]
55. Luo, G.; Xiewen, H.; Yingjin, D.; Jiankang, F.; Xuefeng, M. A collision fragmentation model for predicting the distal reach of brittle fragmentable rock initiated from a cliff. *Bull. Eng. Geol. Environ.* **2019**, *78*, 579–592. [CrossRef]
56. Davies, T.R.; McSaveney, M.J.; Hodgson, K.A. A fragmentation-spreading model for long-runout rock avalanches. *Can. Geotech. J.* **1999**, *36*, 1096–1110. [CrossRef]
57. Davies, T.R.; McSaveney, M.J. Dynamic simulation of the motion of fragmenting rock avalanches. *Can. Geotech. J.* **2002**, *39*, 789–798. [CrossRef]
58. Crosta, G.B.; Frattini, P.; Fusi, N. Fragmentation in the Val Pola rock avalanche, Italian Alps. *J. Geophys. Res. Earth Surf.* **2007**, *112*. [CrossRef]
59. De Blasio, F.V.; Crosta, G.B. Extremely Energetic Rockfalls: Some preliminary estimates. In *Landslides and Engineered Slopes. Experience, Theory and Practice*; CRC Press: Boca Raton, FL, USA, 2016; Volume 2, pp. 759–764. ISBN 9781138029880.
60. De Blasio, F.V.; Crosta, G.B. Simple physical model for the fragmentation of rock avalanches. *Acta Mech.* **2014**, *225*, 243–252. [CrossRef]
61. De Blasio, F.V.; Dattola, G.; Crosta, G.B. Extremely Energetic Rockfalls. *J. Geophys. Res. Earth Surf.* **2018**, *123*, 2392–2421. [CrossRef]
62. Macciotta, R.; Martin, C.D. Remote structural mapping and discrete fracture networks to calculate rock fall volumes at Tornado Mountain, British Columbia. In Proceedings of the 49th US Rock Mechanics/Geomechanics Symposium, San Francisco, CA, USA, 28 June–1 July 2015.
63. Mandelbrot, B.B. *The Fractal Geometry of Nature*; W. H. Freeman: New York, NY, USA, 1982.
64. Turcotte, D.L. Fractals and fragmentation. *J. Geophys. Res.* **1986**, *91*, 1921–1926. [CrossRef]
65. Marchelli, M.; De Biagi, V. Optimization methods for the evaluation of the parameters of a rockfall fractal fragmentation model. *Landslides* **2019**, *16*, 1385–1396. [CrossRef]
66. Ruiz-Carulla, R.; Corominas, J. Analysis of Rockfalls by Means of a Fractal Fragmentation Model. *Rock Mech. Rock Eng.* **2019**, 1–23. [CrossRef]
67. Ruiz-Carulla, R.; Corominas, J.; Mavrouli, O. A methodology to obtain the block size distribution of fragmental rockfall deposits. *Landslides* **2015**, *12*, 815–825. [CrossRef]
68. Mavrouli, O.; Corominas, J. Comparing rockfall scar volumes and kinematically detachable rock masses. *Eng. Geol.* **2017**, *219*, 64–73. [CrossRef]

69. Prades, A.; Matas, G.; Núñez-Andrés, A.; Buill, F.; Nieves, N.; Corominas, J. Determinación de trayectorias de bloques rocosos en ensayos mediante videogrametría. In Proceedings of the Primer Congreso en Ingeniería Geomática, Valencia, España, 5–6 July 2017; pp. 34–40.

70. Zhao, T.; Crosta, G.B.; Dattola, G.; Utili, S. Dynamic Fragmentation of Jointed Rock Blocks During Rockslide-Avalanches: Insights from Discrete Element Analyses. *J. Geophys. Res. Solid Earth* **2018**, *123*, 3250–3269. [CrossRef]

71. Ye, Y.; Thoeni, K.; Zeng, Y.; Buzzi, O.; Giacomini, A. A novel 3D clumped particle method to simulate the complex mechanical behavior of rock. *Int. J. Rock Mech. Min. Sci.* **2019**, *120*, 1–16. [CrossRef]

72. Ye, Y.; Thoeni, K.; Zeng, Y.; Buzzi, O.; Giacomini, A. Numerical Investigation of the Fragmentation Process in Marble Spheres Upon Dynamic Impact. *Rock Mech. Rock Eng.* **2019**, *53*, 1287–1304. [CrossRef]

73. Sheng, Y. Theoretical Analysis of the Iterative Photogrammetric Method to Determining Ground Coordinates from Photo Coordinates and a DEM. *Photogramm. Eng. Remote Sens.* **2005**, *71*, 863–871. [CrossRef]

74. Wyllie, D.C. Calibration of rock fall modeling parameters. *Int. J. Rock Mech. Min. Sci.* **2014**, *67*, 170–180. [CrossRef]

75. Hall, D.C. Sampling random directions within an elliptical cone. *Comput. Phys. Commun.* **2017**, *219*, 87–90. [CrossRef]

76. Su, D.; Yan, W.M. Prediction of 3D size and shape descriptors of irregular granular particles from projected 2D images. *Acta Geotech.* **2019**. [CrossRef]